SCIENCE

TOMSK STATE UNIVERSITY

V.P. Yakubov
S.E. Shipilov
D.Ya. Sukhanov
A.V. Klokov

WAVE TOMOGRAPHY

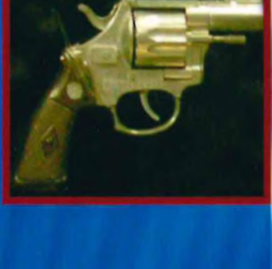
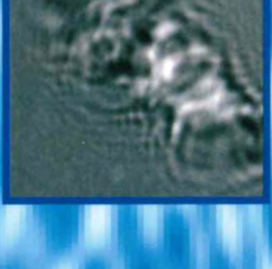


National Research
Tomsk State University

**V.P. Yakubov, S.E. Shipilov,
D.Ya. Sukhanov, A.V. Klokov**

WAVE TOMOGRAPHY

TOMSK
"Scientific Technology
Publishing House"
2017

UDC 621.391.244
W35

W35 **Yakubov V. P., Shipilov S. E., Sukhanov D. Ya., Klokov A. V.**
WAVE TOMOGRAPHY / ed. by V. P. Yakubov. – Tomsk: Scientific Technology Publishing House, 2017. – 248 p.

ISBN 978-5-89503-588-7

The monograph presents new methods in radio-wave tomography viewed as a remote sensing technique for imaging the three-dimensional structure of semi-transparent media and the shapes of opaque objects based on multi-angle wave sounding data. All of the techniques presented are analyzed on the basis of a common approach which is called radio-wave tomosynthesis. Several tomography variations, such as transmission, Doppler, incoherent, magnetic, and ultrasonic tomography, are considered in detail. Most of the proposed solutions were validated by numerical simulation and real-world experiments such as in-ground (subsurface) tomography (anti-personnel landmines, soils), tomography of land covers (forests, buildings), and tomography of objects hidden under clothes, in hand luggage, inside building walls.

The monograph can be considered as a study guide for a Master's program in radio-wave tomography. In addition, the authors hope that the monograph will be useful for young researchers and for specialists and experts working in different fields of science and technology, and for designers of new technologies related to wave processes.

UDC 621.391.244

Examiner: **V.A. Banakh**, Doctor of Science,
Laboratory Chief, Institute of Atmospheric Optics
of the Siberian Branch of the Russian Academy of Sciences.

ISBN 978-5-89503-588-7

INTRODUCTION

The main subject of research presented in this monograph is the development of radio-wave tomography methods as a means of remote non-destructive testing, diagnostics of the internal structure of semi-transparent media, and reconstruction of the shapes of opaque objects based on multi-angle sounding. Considering the meaning of the word tomography, note that it derives from two Greek words: τομος – a layer and γραφειν – to write. Thus, tomography means literally "to write a layer," i.e., to investigate a structure layer-by-layer. The difference between tomography and other computational diagnostic methods is that information from the same test element is recorded in multiple integral projections, i.e., many times from different angles relative to the imbedded inhomogeneities.

It has been over 50 years now since researchers in this field learned how to "clear up" these projections and recover the structure of inhomogeneities layer-by-layer. For the most part, this became possible, thanks to the development of new computational methods and computer technologies. Huge dataflows were "smoothly" layered as images of "crosscuts" of the internal structure of objects in a non-destructive fashion. At the present time, computer tomography is rightfully considered as an "absolute" diagnostic technique in medicine. Radio-wave tomography is similar to X-ray and magnetic resonance tomography, but it deals with electromagnetic radiation in the radio-frequency band. In this case, the wavelength is comparable to the size of the inhomogeneities, and diffraction effects and effects of multiple interactions hold much significance. For that reason, this form of tomography is sometimes called diffraction tomography. Without dwelling on all the different methods and approaches of diffraction tomography that are currently available, let us focus instead on active location (detection) wave tomography, which is of vital importance, e.g., for security systems.

In recent years, the use of manufactured and homemade improvised explosive devices in acts of terrorism and local armed conflicts has become more frequent. There have been numerous reported cases of the transportation of such devices and other prohibited items in hand luggage and under clothes in airports, and also in stadiums and other crowded places. Put very simply, the problem of designing a highly efficient means for remote detection of prohibited devices and articles is of urgent interest. It is of particular importance in view of different public events being held on Russian territory.

Radio wave systems are preferable in the development of contactless detection devices for a variety of reasons. In the first place, radio waves are practically harmless to human health. This is their crucial difference from ionizing X-rays. Second, the potential range of application of these systems is quite wide: in crowded public places, in special-forces raids for detection and tracking of people hiding behind walls, detection of injured persons after emergency events, etc. There is also a great demand for contactless and computer-aided systems for quality control in building construction, timber processing, and other industries.

The variety of physical processes involved in radio wave detection, taking place in natural and simulated complex environments and involving complex objects, underlies the complexity of the mathematical descriptions of such processes and the urgency of solutions of the tomography problem as well.

The main object of this monograph is to describe physical-mathematical models of systems designed to reconstruct images of hidden objects, based on tomographic processing of multi-angle remote measurements of scattered radio and acoustic (ultrasonic) wave radiation. One way or another, radio-wave tomography is based on the ray-focusing effect (Chapter 1), which enables the inverse transformation of wave projections of test objects and the propagation medium. It is safe to say that almost all of the methods that are available or under development right now may be considered under this aspect. Multiple effects (scattering and diffraction) of interactions of the wave fields with inhomogeneities of the propagation medium can be considerably reduced by the use of spatiotemporal radiation focusing.

In the course of research on this problem a number of working laboratory tomographs have been developed together with the associated software, which assist in the assessment of the potential of the system and its key parameters such as resolution, range of action, and response time. The fact that the development of a radio-location tomograph is possible is not in doubt – it has been demonstrated by numerous published results [1–45] and by our own research. The American millimeter-band radio vision system SafeScout (Fig. I.1) in use at the Domodedovo airport (Moscow, Russia) is solid evidence of this fact. General Electric, Smiths, Philips, as well as Rapiscan and Diehl, are considered to be essential players in the safety system market. L-3 Communications offers their own effective and proven system ProVision/SafeView.

The latest advanced screening system by Smiths Heimann is presented in Fig. I.2. From the looks of it, the microwave sounding sensor panel is a multi-element array of controllable reflective elements.

Fig. I.1. SafeScout 100 Scanner.

Fig. I.2. The Latest Screening System Model by Smiths Heimann.

Inspection of the figure reveals that radio-frequency electromagnetic sounding is combined with a magnetic induction system for screening hidden metallic objects. This is a real-time working system. As the screening is provided just from the side of the sensor panel, so the subject is asked to perform a 180-degree turn in the center of the monitored area (the highlighted circle in Fig. I2) with hands raised. The screening of one person in this way takes 10–30 sec and the resolution obtained is no better than 1 cm. The complexity of this system plus its substantial cost and low resolution are the main disadvantages of this setup.

The drawbacks of most current safety systems designed for crowded places and areas with heavy human traffic are as follows:

- Microwave systems are very time consuming as things stand, it takes a lot of time to screen people as the antennas are moved mechanically.

- The subject being screened must remain motionless for several seconds. Therefore, a doorway or a cabin is required which interrupts the constant human stream.

- It is not difficult to obstruct such a system, e.g., by wetting your outer garments with mineral water because the system operates in the millimeter wavelength band.

It should be noted that this interference is neutralized in ultra-wideband (UWB) systems where the working frequency spectrum lies within the range from 100 MHz to 18 GHz (Chapter 2). The use of UWB signals is considered to be the most promising approach from the standpoint of applications.

The development of a domestic radio-detection UWB tomograph requires the solution of a number of problems. The following systems are worthy of note: the Israeli scanner Raptor-1600 (Fig. I.3), which is able to monitor the movement of large objects, e.g., a person moving behind a wall, and the Russian scanner Dannik developed by MAI (Fig. I.4)

However, this does not exhaust all of the currently available possibilities. The development of an optimal antenna array configuration is, of necessity, the first step in this process. This development would include the relative placement of the receiving and transmitting antennas and a determination of their minimum number required for tomographic imaging. The solution of this problem is one of the objectives of ongoing research. This includes a determination of the optimal sequence of radar measurements to provide the required data digitization in a short period of time. Moreover, considerable attention must be paid to the development of fast algorithms for real-time 3D image restoration of scanned objects based on radio sounding data.

The antenna array optimization problem alluded to above also arises from the need to minimize the number of antennas in order to reduce antenna array costs while holding the number of artefacts to a minimum. From the latter half of the 20th century onward, several methods of antenna array optimization for radio astronomy and aircraft detection have been developed. The antenna array optimization problem is a natural outgrowth of the problem referred to as antenna array design with minimum redundancy. Accordingly, the antennas should be arranged in such a way as to avoid similar measurement data from each antenna for a given search angle of the radar.

Over the past few decades a great deal of research has been conducted and field-proven results have been obtained in the far-field zone of narrowband antenna arrays. However, a subject of particular interest to the authors

Fig. I.3. The Raptor-1600 Scanner. Through Wall Radar Life Detector.

Fig. I.4. Dannik-5 Scanner, developed by Moscow Aviation Institute (MAI).

is antenna arrays for ultra-wideband radiation, which are designed to characterize objects located in the array focusing area. So far, this issue has not been investigated as there has not been any urgency to research the near-field zone of antenna arrays. In this context, the near-field zone is considered as the region of space at a distance on the order of the dimensions of the array. In other words, this refers to the Fresnel diffraction zone.

The next problem is the development of efficient mathematical support to reconstruct tomograms from the wave projections of probed scenes containing hidden objects. In this context, the two following requirements come to the forefront: adequate restoration accuracy and real-time performance of the system. There is some contradiction here, which is formulated as "Fast is not always best." According to domestic and foreign experts, a resolution that is not worse than 1 cm is an appropriate value for safety systems. Reconstruction should be performed in real-time mode, for instance, in a minute. The task is complicated when it is impossible to obtain complete measurement data. This situation arises when the scanning is performed non-equidistantly, in motion, or when the object to be detected is hidden inside a building or under clothing near the body. This and related kinds of problems stipulate the necessity of a consistent theoretical study, backed up, of course, by experimental work. In other words, the mathematical (theoretical) part cannot be separated from the experimental (measurement) part.

It is critical to stress that wave tomography must utilize phase information from wave projections of the examined objects in an essential way. A phase information record is provided by radio-frequency holography, in which the result of interference of the background wave and the object wave is recorded. The wave projection record is in fact a radio-hologram record. From general considerations it is clear that large aperture synthesis is the preferable method for post-processing these projections since it provides the highest spatial resolution. There are now a large number of variations of this method under continuous development.

Electromagnetic radiation interacts with electrophysical inhomogeneities in the propagation medium. In contrast to electromagnetic radiation, acoustic radiation interacts mainly with density inhomogeneities. In this context, using ultrasound for tomography of an inhomogeneous medium provides a wide range of additional possibilities, particularly for determining the type of material that the hidden items are made of. Combining radio-wave and acoustic sounding creates interesting possibilities, e.g., for detection of explosive materials (EMs).

The current state of research on remote ultrasonic sounding has revealed that practically all of these methods are based on contact measurements. This is evidenced, for example, by the topic of the All-Russia Scientific Conference "Session of the Scientific Council of the Russian Academy of Sciences for Acoustics and XXIVth Session of the Russian Acoustical Society" held on September 2011 in Saratov. The reason is that ultrasound is strongly attenuated by air. The only ultrasonic sounding system (sonovision) which is actually efficient in air is bat echolocation. Some insects also generate ultrasound, but rather for scaring and masking from bats. The practical use of ultrasound in a liquid medium or through immersion liquids (e.g., in metal working, medicine, etc.) is well known. Preliminary studies hold out the hope for the effective use of ultrasound for purposes of near-field tomography in air (Chapter 10).

The general purpose of this work is to develop

- physical and mathematical models of an image reconstruction system for an inhomogeneous medium based on tomographic processing of multi-angle projection records of scattered radio-wave and acoustic radiation;
- key elements of the modeling system;
- subsystems and elements of a multi-angle measuring tool;
- experimental measurement techniques;
- evaluation of potential and actual performance-based specifications for a detecting tomograph with different measurement and sounding schemes.

The wide practical application of UWB tomography is still limited, on the one hand, by considerable engineering problems in generating and receiving UWB radiation, and by complications, on the other hand, that arise when describing and interpreting simultaneously manifested physical phenomena of the interaction of the radiation with matter. These phenomena include multiple scattering, diffraction, wave interference and absorption of ultra-wide-bandwidth radiation from arbitrarily placed and randomly oriented inhomogeneities of different size. A multitude of combinations of these effects hinders solution of the direct problem – a description of the integral effects of the wave disturbance. It should be noted, however, that direct problems, even of high complexity, are solved by nature itself as waves reach the observation points in one way or another. Solution of the inverse problem and reconstruction of the distribution of inhomogeneities in the tested volume is problematic under such conditions in any event. Researchers have no choice but to solve such inverse problems. These tasks are generally referred as ill-posed problems, which require the use of regularizing algorithms. The most stable inverse problems are the simplest ones, which account for the dominant mechanisms of the interaction of waves with the propagation media and make it possible to single out (identify) such mechanisms (Chapters 1–3).

Inverse problems are of crucial importance for applications such as sounding the optically opaque media. When radio-frequency radiation penetrates into such a medium, analysis of the transmitted and scattered fields makes it possible to reconstruct its internal structure. This internal structure consists in the spatial distribution of the permittivity. Steep permittivity gradients are typical for interfaces and for immersed objects (Chapter 5). A typical example is searching for hidden archaeological graves, underground cables, or anti-personnel landmines (Chapter 6) and ground covers (Chapter 7) as well as detection and identification of prohibited items in stowed luggage and in hand-carried items. Problems of this sort are not simple, but a great number of efficient solutions have been developed for them based on radiation focusing. With regard to a radio-opaque object, radiation hardly penetrates it, so the solution of the inverse problem in this case reduces to reconstructing the shape of the object on the basis of an analysis of scattered (reflected) radiation (Chapter 4).

Interesting directions for the future development of radiotomography include techniques for implementing incoherent radiation (Chapter 8) and low-frequency magnetic fields (Chapter 11). These and other examples of the use of radiotomographic methods, presented in this monograph, far from exhaust the full spectrum of potential applications. Radiotomography, especially using UWB radiation, is in a state of continuous intensive development. One thing that is new here is the use of UWB radiation for nonlinear radiodetection (Chapter 9). The development of visualization techniques for tomographic imaging is of great relevance for applications (Chapter 12).

A large body of experimental data and their interpretation was obtained within the framework of international collaboration with leading scientists from Magdeburg University (Magdeburg, Germany), the Institute for Non-Destructive Testing (Saarbrücken, Germany), and Tohoku University (Sendai, Japan). The authors are deeply indebted to Professors A. Omar, M. Kroning, and M. Sato for their collaboration, and also to their colleagues. This monograph incorporates the most interesting results of other authors but is focused primarily on original in-house research which was conducted through the kind offices of S.A. Slavgorodsky, I.S. Fedyanin, R.N. Satarov, I.Yu. Kuzmenko, T.R. Muksunov, K.V. Zavyalova, E.S. Berzina, A.A. Muravyova, M.D. Sovpel, A.A. Kozik, N.N. Yerzakova, I.S. Tseplyayev, and many more. The authors extend their appreciation to everyone…

Chapter 1

FUNDAMENTALS OF WAVE DETECTION TOMOGRAPHY

The chapter is based on summary results of papers [2, 4–10].

1.1. The method of Fourier synthesis from shadow projections

Fourier synthesis (FS) is the main method for tomogram reconstruction in modern computer tomography. It is based on a layer-by-layer reduction of multi-angle shadow projections of a tested object using the direct and inverse fast Fourier transforms (FFT and IFFT). Let us clarify the principle of this method. When a shadow projection is made, the measured quantity $f(y,\varphi)$ – the absorbed radiation intensity – is measured as a result of building up the absorbed radiation intensity along a straight line:

$$f(y,\varphi)=\int_{-\infty}^{\infty} g(x\cos\varphi-y\sin\varphi,\, x\sin\varphi+y\cos\varphi)\,dx\,. \tag{1.1}$$

This straight line (scanning direction) is drawn at the angle φ to the initial coordinate system (Fig. 1.1).

In the terminology of integral geometry the shadow function $f(y,\varphi)$ is an integral projection of the density distribution of the sounded object $g(X,Y)$. If we now calculate the FFT of the shadow function

$$F(\kappa,\varphi)=\int_{-\infty}^{\infty} \exp\{i\kappa y\}\, f(y,\varphi)dy\,, \tag{1.2}$$

the function obtained follows directly the spatial spectrum (SS) of the sounded object $g(X,Y)$,

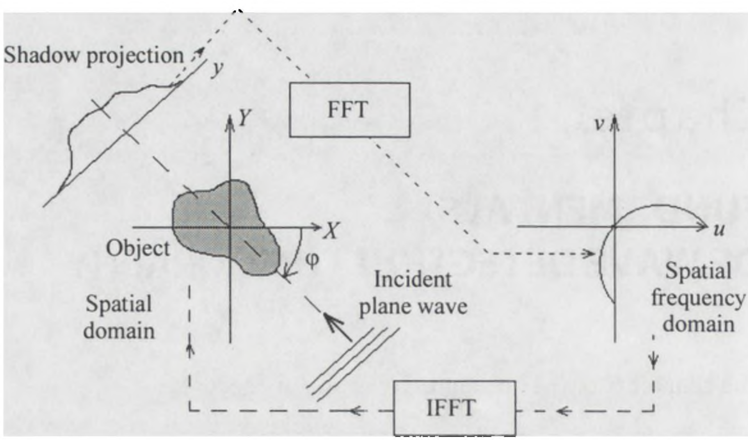

Fig. 1.1. Problem of Fourier synthesis.

$$F(\kappa,\varphi) = G(u = -\kappa\sin\varphi, v = \kappa\cos\varphi),$$

which is defined as

$$G(u,v) \equiv \int_{-\infty}^{\infty}\int_{-\infty}^{\infty} \exp\{iuX + ivY\}\, g(X,Y) dXdY.$$

The only difficulty lies in the fact that one spectrum $(F(\kappa,\varphi))$ is represented in the polar coordinate system, and the other one $(G(u,v))$ – in a Cartesian system. Simple interpolation from one coordinate system to the other overcomes this difficulty. Then the required characteristic object function (CF) is evaluated with the help of the two-dimensional IFFT:

$$g(X,Y) \equiv (2\pi)^{-2} \int_{-\infty}^{\infty}\int_{-\infty}^{\infty} \exp\{-iuX - ivY\} G(u,v) dudv. \tag{1.3}$$

Expression (1.1) corresponds to the solution of the direct problem, and transformations (1.2) and (1.3) correspond to the inverse problem. Such an approach is widely used in X-ray and magnetic resonance tomography where phase information is discounted and collimating measurement systems for shadow projections are implemented. The above-described operations are presented in Figs. 1.2–1.5 by the example of tubular test object.

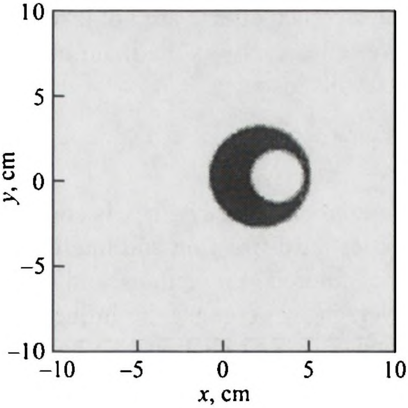

Fig. 1.2. Initial characteristic function of the object $g(x,y)$.

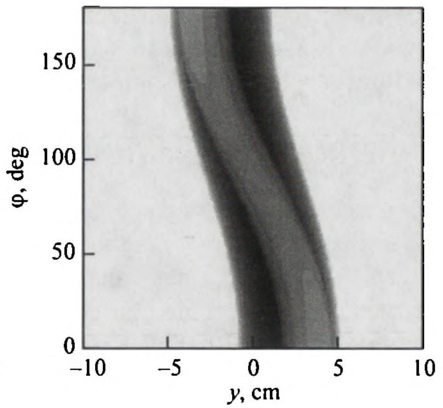

Fig. 1.3. Shadow function of the object $F(\kappa,\varphi)$.

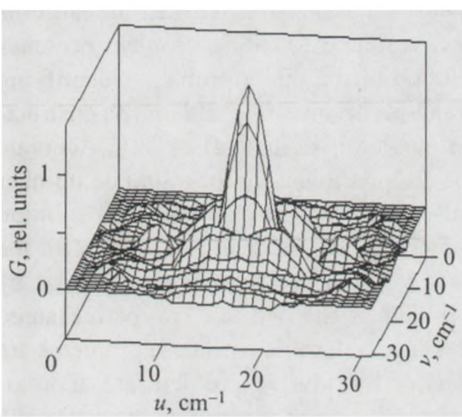

Fig. 1.4. Reconstructed spatial frequency spectrum for the object $G(u,v)$.

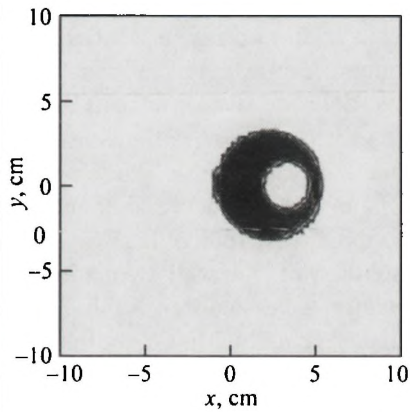

Fig. 1.5. Reconstructed characteristic function of the object $g(x,y)$.

It must be emphasized that all of the required operations are performed using fast algorithms in real time. This is the main advantage of Fourier synthesis. The given example assumes that the object is semi-transparent; however, all of the above results are applicable to opaque objects as well. In this context, transmission radiography of test objects is considered, i.e., the situation in which the receiver and radiation points are located on opposite sides of the object, and diffraction and interference effects are not taken into account. Neglect of these effects for wave tomography is the main obstacle for direct application of Fourier synthesis in this instance.

1.2. Double focusing method

In radio-wave tomography, when the radiation wavelength λ is comparable to the dimensions of the inhomogeneities ℓ, diffraction and interference effects become important and cannot be ignored. Projections and reconstructed images become blurred. Moreover, in this context the influence of multiple interactions and absorption (attenuation) of radiation also has to be reckoned with. Sounding is not necessarily of a transmission nature, but can also be multipositional and more often radar based, when the radiation and receiving points coincide but only their common position relative to the sounded object varies.

In the general case, sounding is most often multi-angle, i.e., the target is viewed from different spatial perspectives. The sounding problem becomes quite complicated in reference to solution of the direct problem (identifying the field for given sources and media) and the inverse problem (reconstructing the distribution of sources and/or medium parameters) as well. Accurate analytical solutions of these problems are possible only for a limited number of canonical objects and environments. However, the existence of a solution to the direct problem is always guaranteed by the uniqueness theorem for the solution of Maxwell's equations. This problem itself is uniquely solved by nature – the solution of the direct problem is the one that can be measured experimentally. This is not the case for inverse problems. These problems are solved manually. In general, solutions of the inverse problem are approximate in any case. A criterion of applicability of an approximation is the degree to which it conforms to the experimental data. As a rule, a solution of the inverse problem corresponds to a certain approximate solution of the direct problem. The more accurately this problem considers the dominant mechanisms, the more accurate the solution of the corresponding inverse problem is.

Let us elucidate the statement of the problem. If $j(\mathbf{r}_1)$ is the distribution of radiation sources (currents) localized in a certain volume V_1, then the field generated by these currents at the point $\mathbf{r}$ in a homogeneous medium is defined as

$$E(\mathbf{r}) = \iiint_{V_1} j(\mathbf{r}_1) G_0(\mathbf{r}_1 - \mathbf{r}) d^3\mathbf{r}_1 . \tag{1.4}$$

This is a convolution equation. Here $G_0(\mathbf{r}) = \exp(ik|\mathbf{r}|)/4\pi|\mathbf{r}|$ is the free-space Green's function, in other words, the solution of the free-space Helmholtz equation:

$$\Delta G_0(\mathbf{r}) + k^2 G_0(\mathbf{r}) = -\delta(\mathbf{r}) . \tag{1.5}$$

The quantity $k = 2\pi\sqrt{\varepsilon}/\lambda = 2\pi f\sqrt{\varepsilon}/c$ is the associated wave number, $\varepsilon = \varepsilon' + i\varepsilon''$ is the complex permittivity of the background medium, f is the frequency of monochromatic radiation or the spectral frequency in the case of pulsed radiation. Determination of the field $E(\mathbf{r})$ is a simple direct problem. The inverse problem involves solution of integral equation (1.4) and reconstruction of the distribution $j(\mathbf{r}_1)$ from measured values of $E(\mathbf{r})$. If this field was measured at all points in space, then the solution would be obtained by the simple operation of deconvolution. Usually, the field $E(\mathbf{r})$ is measured on some given surface S. In this situation, inverse radiation focusing is implemented to reconstruct the distribution of currents $j(\mathbf{r}_1)$ when the received radiation is focused (gathered) on some point in space $\mathbf{r}_F$ as a result of integration:

$$U(\mathbf{r}_F) = \iint_S W(\mathbf{r}_F, \mathbf{r}_s) E(\mathbf{r}_s) dS = \iiint_{V_1} j(\mathbf{r}_1) Q(\mathbf{r}_F, \mathbf{r}_1) d^3\mathbf{r}_1 , \tag{1.6}$$

where $W(\mathbf{r}_F, \mathbf{r}_s)$ is some focusing function, and

$$Q(\mathbf{r}_F, \mathbf{r}_1) = \iint_S W(\mathbf{r}_F, \mathbf{r}_s) G_0(\mathbf{r}_s - \mathbf{r}_1) dS$$

is the kernel of the new integral equation for $j(\mathbf{r}_1)$. This function $Q(\mathbf{r}_F, \mathbf{r}_1)$ is the system instrument function (SIF), in other words, it describes the response of the system to a point source: $j(\mathbf{r}_1) = \delta(\mathbf{r}_1 - \mathbf{r}_0)$. Here $\mathbf{r}_0$ is the actual position of this point source. This function is called the point spread function (PSF) in optics.

When the focusing function $W(\mathbf{r}_F,\mathbf{r}_s)$ is successfully (optimally) chosen, the kernel $Q(\mathbf{r}_F,\mathbf{r}_1)$ should be well localized in the vicinity of the point $\mathbf{r}_F=\mathbf{r}_1$, or at least depend on the difference between the points $\mathbf{r}_F$ and $\mathbf{r}_1$: $Q(\mathbf{r}_F,\mathbf{r}_1)\approx Q(\mathbf{r}_F-\mathbf{r}_1)$. In the case, equation (1.6) is a convolution equation:

$$U(\mathbf{r}_F)\approx\iiint_{V_1} j(\mathbf{r}_1)Q(\mathbf{r}_F-\mathbf{r}_1)d^3\mathbf{r}_1, \tag{1.7}$$

which is solved by standard means, for example, by implementing Wiener filtering with regularization. The best result will be obtained when the kernel of equation (1.6) is close to a δ-function:

$$Q(\mathbf{r}_F-\mathbf{r}_1)\approx\delta(\mathbf{r}_F-\mathbf{r}_1),$$

then it can be written as

$$j(\mathbf{r}_1)\approx U(\mathbf{r}_F).$$

This is the desired solution of the inverse tomography problem. There is just one thing left to do – figure out how to define the focusing function $W(\mathbf{r}_F,\mathbf{r}_s)$.

As is shown in Appendix 1, the function [2]

$$W(\mathbf{r}_F,\mathbf{r}_s)\equiv\frac{4}{i}\frac{dG_*(\mathbf{r}_F-\mathbf{r}_s)}{dn}=W(\mathbf{r}_F-\mathbf{r}_s)$$

should be taken as the focusing function in the case of monochromatic radiation with wave number k, where $G_*(\mathbf{r})=\exp(-ik|\mathbf{r}|)/4\pi|\mathbf{r}|$ corresponds to a so-called convergent wave while the function $G_0(\mathbf{r})$ is referred to as a divergent wave. This function is the second independent solution of the Helmholtz equation (1.5). It is important here that

$$\oint\!\!\oint_S G_0(\mathbf{r}_1-\mathbf{r}_s)W(\mathbf{r}_F-\mathbf{r}_s)dS_1=$$

$$=\frac{4}{i}\oint\!\!\oint_S G_0(\mathbf{r}_F-\mathbf{r}_s)\frac{dG_*(\mathbf{r}_F-\mathbf{r}_s)}{dn}dS\equiv\delta_k(|\mathbf{r}_1-\mathbf{r}_F|).$$

The integration is performed here over a closed surface that encloses the points $\mathbf{r}_F$ and $\mathbf{r}_1$, and the surface normal is chosen to be the inwardly-pointed one. In this case, the so-called *spread* δ-function arises

$$\delta_k(|\mathbf{r}_1 - \mathbf{r}_F|) = \frac{\sin(k|\mathbf{r}_1 - \mathbf{r}_F|)}{\pi|\mathbf{r}_1 - \mathbf{r}_F|},$$

which transforms in the limit to the ordinary one-dimensional δ-function:

$$\lim_{k\to\infty} \delta_k(|\mathbf{r}_1 - \mathbf{r}_F|) = \delta(|\mathbf{r}_1 - \mathbf{r}_F|).$$

Figure 1.6 illustrates this point.

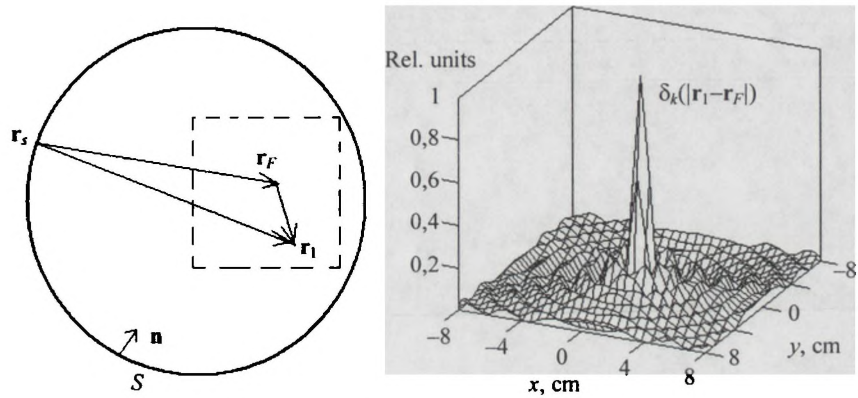

Fig. 1.6. SIF in the case of complete focusing by a closed aperture – the *spread* δ-function.

When the integration surface (the scanning aperture of the receiving antenna) is open, localization will be partial and maximized (take a stretched form) in the direction normal to the aperture surface (Fig. 1.7). Thus, the SIF takes the form

$$Q(\mathbf{r}_F, \mathbf{r}_1) = \frac{4}{i}\iint_S G_0(\mathbf{r}_s - \mathbf{r}_1)\frac{dG_*(\mathbf{r}_F - \mathbf{r}_s)}{dn}dS.$$

The above-described choice of the focusing function $W(\mathbf{r}_F, \mathbf{r}_s)$ is physically justified and corresponds to inverse focusing where radiation incoming from a given point in space – the focusing point $\mathbf{r}_F$ – is summed in-phase. To align the phases of incoming partial waves the convergent Green's function $G_*(\mathbf{r}_F - \mathbf{r}_s)$ is used.

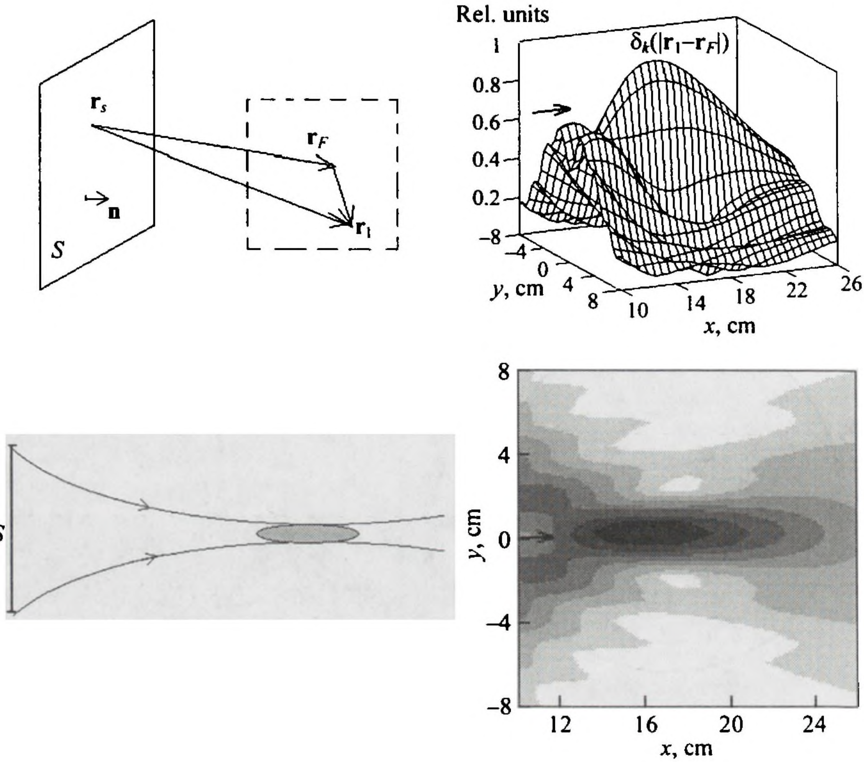

Fig. 1.7. SIF in the case of partial focusing by an aperture of finite size.

It should be noted that the form of the SIF is the result of recording the interference pattern in the vicinity of the focusing point. The SIF will take a stretched form (Fig. 1.7) if monochromatic radiation and a receiving aperture of finite size are used for sounding. This means that the best resolution is achieved in the cross direction ($\sim \lambda = c/f$), and the worst resolution, in the longitudinal direction. In general, the SIF depends on the sounding radiation frequency, which determines the oscillating nature of the SIF and its spatial variation. By using pulsed (multifrequency) radiation, localization of the SIF can be increased, and the spatial resolution will be increased as well, particularly with distance.

Using the reciprocity principle, it may be noted that similar focusing can be performed by the radiating aperture. The cross focusing obtained in this way provides good localization of radiation or, more accurately, localization of the radiation-matter interaction (Fig. 1.8). Implementing cross focusing considerably weakens the role of multiple interactions between radiation and matter.

Under double focusing, the resultant signal is proportional to the intensity of inhomogeneities in the intersection region of focusing of the radiation field and focusing of the received field. The localization region is found by taking the product of the corresponding focusing functions.

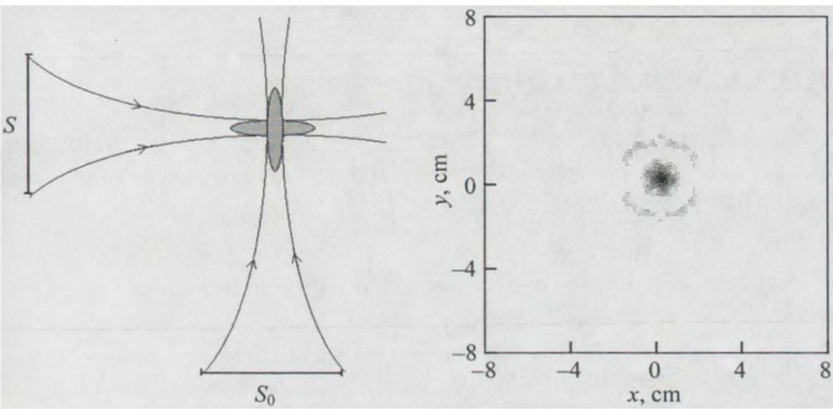

Fig. 1.8. Cross focusing of radiation.

It should be noticed straight away that focusing of the two fields is possible at the hardware level using lenses, mirrors, and prisms as well as at the computer post-processing stage when the phase distribution is recorded. The wave phase is crucial for the realization of focusing. When waves interfere in the focal region, the partial waves add together in-phase (coherently), amplifying the intensity of the resulting wave. Outside of the focal region the partial waves add together out of phase and there is only partial or rather no amplification of the wave intensity. All of this is compatible with bringing Fresnel zones into the picture in the analysis of a zone that is significant for wave propagation.

If the transmitting and receiving apertures of the sounding system are collocated (monostatic location), multiple interactions are also decreased in this case but only in the direction transverse to the sounding direction (Fig. 1.7). Longitudinal multiple interactions can be attenuated either by increasing the aperture size, for example, by using synthetic aperture radar (SAR) or by pulsed radiation. Monostatic sounding (tomography) is most interesting in practice and is used the most often.

Note that direct realization of the described focusing method is a time-consuming operation because of mechanical scanning or multiple multi-dimensional summations. It should also be emphasized that in defining the focusing function $W(\mathbf{r}_F, \mathbf{r}_s)$ it is crucial to assign the phase correctly in order to ensure that the waves from the focal point add together in-phase. The amplitude of this function is not important for focusing.

1.3. Radio-wave tomosynthesis technique

The radio-wave tomosynthesis technique (RWTS) is a generalization of FS to the case of wave fields. Formally, the method reduces to re-expressing relation (1.7) in the spectral representation

$$\hat{U}(\boldsymbol{\kappa}) = \hat{j}(\boldsymbol{\kappa})\hat{Q}(\boldsymbol{\kappa})$$

and proceeding from there to deconvolution with regularization

$$j(\mathbf{r}) = \frac{1}{(2\pi)^3}\iiint \hat{j}(\boldsymbol{\kappa})\exp(i\boldsymbol{\kappa}\mathbf{r})d^3\boldsymbol{\kappa},$$

where
$$\hat{j}(\boldsymbol{\kappa}) = \frac{\hat{Q}^*(\boldsymbol{\kappa})}{\hat{Q}(\boldsymbol{\kappa})\hat{Q}^*(\boldsymbol{\kappa}) + \alpha}\hat{U}(\boldsymbol{\kappa}). \tag{1.8}$$

The following spatial spectra are introduced here:

$$\hat{j}(\boldsymbol{\kappa}) \equiv \iiint j(\mathbf{r})\exp(-i\boldsymbol{\kappa}\mathbf{r})d^3\mathbf{r},$$

$$\hat{Q}(\boldsymbol{\kappa}) \equiv \iiint Q(\mathbf{r})\exp(-i\boldsymbol{\kappa}\mathbf{r})d^3\mathbf{r},$$

$$\hat{U}(\boldsymbol{\kappa}) \equiv \iiint U(\mathbf{r})\exp(-i\boldsymbol{\kappa}\mathbf{r})d^3\mathbf{r},$$

where α is a regularization parameter that depends on the measurement noise level.

The solution in the form (1.8) is rarely used owing to laboriousness and weak localization of the result of focusing in the longitude direction. A similar, but much simpler, solution is the one based on two-dimensional spectral analysis of the radiation distribution in the form (1.4).

If the Green's function in formula (1.4) is represented in the form of a two-dimensional plane-wave spectrum, then, according to Weyl's formula

$$G_0(\mathbf{r}) = \frac{1}{(2\pi)^2} \int_{-\infty}^{\infty} \int_{-\infty}^{\infty} \frac{i}{2\kappa_z} \exp(i\boldsymbol{\kappa}\mathbf{r}) d^2\boldsymbol{\kappa}_\perp , \tag{1.9}$$

$$\boldsymbol{\kappa} = (\kappa_x, \kappa_y, \kappa_z), \ \boldsymbol{\kappa}_\perp = (\kappa_x, \kappa_y), \ \kappa_z = \sqrt{k^2 - \kappa_x{}^2 - \kappa_y{}^2} = \sqrt{k^2 - \kappa_\perp{}^2} ,$$

for the field in the z plane (Fig. 1.9) it is possible to write

$$E(\mathbf{r}) = \frac{1}{(2\pi)^2} \int_{-\infty}^{\infty} \int_{-\infty}^{\infty} \frac{i}{2\kappa_z} \exp(i\boldsymbol{\kappa}\mathbf{r}) \hat{j}(\boldsymbol{\kappa}) d^2\boldsymbol{\kappa}_\perp .$$

Taking the two-dimensional Fourier transform of this field results in the simple expression

$$\hat{E}(\boldsymbol{\kappa}_\perp, z) = \int_{-\infty}^{\infty} \int_{-\infty}^{\infty} \exp(-i\boldsymbol{\kappa}_\perp \mathbf{r}) E(\mathbf{r}) d^2\mathbf{r}_\perp = \frac{i}{2\kappa_z} \exp(i\kappa_z z) \hat{j}(\boldsymbol{\kappa}) .$$

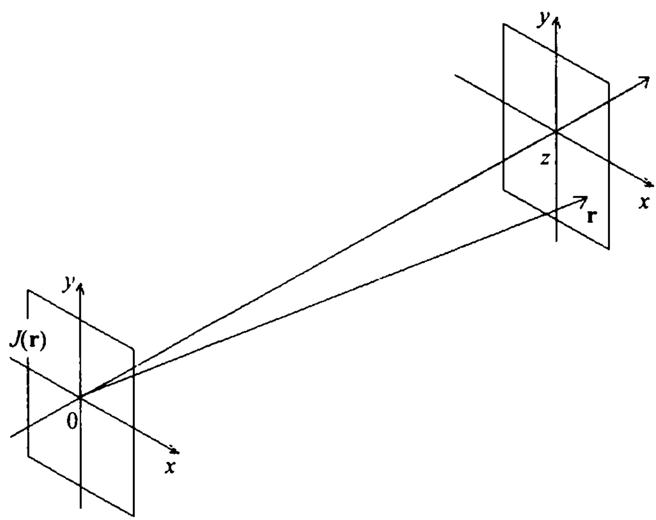

Fig. 1.9. Planes of radiation sources and receivers.

It follows that the three-dimensional spatial spectrum of the distribution of radiation sources (currents) is expressed in terms of the two-dimensional spectrum of the observed field:

$$\hat{j}(\boldsymbol{\kappa}) = \iiint\limits_{V_1} j(\mathbf{r}_1)\exp(-i\boldsymbol{\kappa}\mathbf{r}_1)d^3\mathbf{r}_1 = \frac{2\kappa_z}{i}\exp(-i\kappa_z z)\hat{\mathrm{E}}(\boldsymbol{\kappa}_\perp, z).$$

It must be borne in mind that the third spectral component is expressed in terms of the first two components:

$$\kappa_z = \sqrt{k^2 - \kappa_x{}^2 - \kappa_y{}^2} = \sqrt{k^2 - \kappa_\perp{}^2}.$$

In other words, the 3-D vector of spatial frequencies lies on a sphere of radius k:

$$\kappa_x{}^2 + \kappa_y{}^2 + \kappa_z{}^2 = k^2.$$

It is necessary to cover all wave numbers $k = 2\pi f/c$ and, equivalently, all frequencies f of the recorded radiation to fill out the spatial frequency spectrum. Next, the spatial frequency spectrum of the quantity $\hat{j}(\boldsymbol{\kappa})$ must be converted from the (κ_x, κ_y, k) coordinate system into the Cartesian system $(\kappa_x, \kappa_y, \kappa_z)$ by interpolation. The desired 3-D source distribution is then reconstructed as follows:

$$j(\mathbf{r}) = \frac{1}{(2\pi)^3}\iiint \hat{j}(\boldsymbol{\kappa})\exp(i\boldsymbol{\kappa}\mathbf{r})d^3\boldsymbol{\kappa}.$$

Fast algorithms are available to perform this inverse Fourier transform.

The considered approach generalized and combines the two approaches addressed in Sections 1.1 and 1.2. For brevity, we shall call it the RVTS technique. In the final count, the idea formulated above lies at the basis of all tomographic methods, including the Stolt method [I.28].

The central idea of this method is to get the spatial spectrum of the received signal in a given aperture to be directly proportional to the spatial spectrum of the sources. How this result is achieved becomes clear if we turn to the Huygens – Fresnel principle.

Let the wave field distribution $E_0(\mathbf{r})$ be defined in the plane $z = 0$ (Fig. 1.10). According to the Huygens–Fresnel principle, the field in the z plane can be calculated using the formula

$$E(\mathbf{r}) = 2\iint\limits_S E_0(\mathbf{r}_s)\frac{dG_0(\mathbf{r} - \mathbf{r}_s)}{dn}dS,$$

where $dS = dxdy$, $\mathbf{r}_s = (x, y, z = 0)$, and $\mathbf{r} = (x, y, z)$.

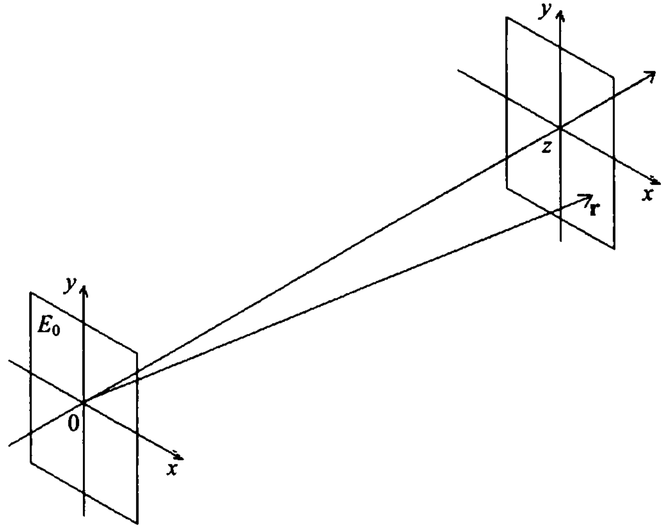

Fig. 1.10. Field transfer from one plane to another.

Using Weyl's formula (1.9), the two-dimensional spectra of the field can be written as

$$\hat{E}(\boldsymbol{\kappa}_\perp, z) = \int_{-\infty}^{\infty}\int_{-\infty}^{\infty} \exp(-i\boldsymbol{\kappa}_\perp \mathbf{r}) E(\mathbf{r}) d^2\mathbf{r}_\perp = \exp(i\kappa_z z)\hat{E}_0(\boldsymbol{\kappa}_\perp, z=0).$$

Of importance here is the exponential factor, which is the transfer function of free space (the background medium):

$$H(\boldsymbol{\kappa}) = \exp\{i\kappa_z z\}.$$

Thus, reconstruction of the spatial spectrum of the sources reduces to elimination of this factor, which physically means inverse radiation focusing (see Section 1.2). Multiplication of the obtained expression by the phase factor

$$H_*(\boldsymbol{\kappa}) = \exp\{-i\kappa_z z\}$$

eliminates the spatial field divergence and corresponds to inverse focusing in the plane $z=0$. According to this focusing method, this operation is effected by convolution of the field with the focusing function

$$W(\mathbf{r}_F, \mathbf{r}_s) = \frac{4}{i}\frac{dG_*(\mathbf{r}_F - \mathbf{r}_s)}{dn}.$$

1.4. Location tomography

1.4.1. Inverse focusing

As noted above, implementing radiation focusing reduces the effects of diffraction and multiple interactions so that the dominant wave interactions can be described in the single-scattering approximation. We write an expression for the singly scattered field in the so-called Born approximation where a point source located at the point $\mathbf{r}_0$ generates secondary currents in an inhomogeneous medium in the form

$$j(\mathbf{r}_1) = k^2 \Delta\varepsilon(\mathbf{r}_1) G_0(\mathbf{r}_1 - \mathbf{r}_0),$$

where $\Delta\varepsilon(\mathbf{r}_1)$ is the spatial distribution of the permittivity disturbance in the propagation medium. In this case, expression (1.4) transforms to

$$E(\mathbf{r},\mathbf{r}_0) = k^2 \iiint\limits_{V_1} \Delta\varepsilon(\mathbf{r}_1) G_0(\mathbf{r}_1 - \mathbf{r}_0) G_0(\mathbf{r}_1 - \mathbf{r}) d^3\mathbf{r}_1. \qquad (1.10)$$

This field corresponds to the so-called bistatic location scheme. The generating point coincides with the receiving point $\mathbf{r}_0 = \mathbf{r}$ in monostatic location, so that the received radiation is described by the expression

$$E(\mathbf{r}) = k^2 \iiint\limits_{V_1} \Delta\varepsilon(\mathbf{r}_1) G_0^{\,2}(\mathbf{r}_1 - \mathbf{r}) d^3\mathbf{r}_1. \qquad (1.11)$$

The spatial distribution of the quantity $\Delta\varepsilon(\mathbf{r}_1)$ is of interest for tomography. There are some peculiarities in the solution of this problem pertinent to the approach discussed above: a change in the position of the receiving point is realized simultaneously with a change in the position of the source.

Using the pulse signal

$$S_0(t) = \int \hat{S}_0(2\pi f) \exp(-i2\pi f t) df$$

in bistatic as well as in monostatic location generates a response of the form

$$S(\mathbf{r},\mathbf{r}_0,t) \cong \int E(\mathbf{r}) \hat{S}_0(2\pi f) \exp(-i2\pi f t) df \cong$$

$$= k_0^{\,2} \iiint\limits_{V_1} \Delta\varepsilon(\mathbf{r}_1) \frac{S_0\left(t - \dfrac{|\mathbf{r}_1 - \mathbf{r}_0| + |\mathbf{r}_1 - \mathbf{r}|}{c}\right)}{(4\pi)^2 |\mathbf{r}_1 - \mathbf{r}_0| |\mathbf{r}_1 - \mathbf{r}|} d^3\mathbf{r}_1.$$

Here $k_0 = 2\pi f_0/c$ is the wave number corresponding to some average frequency of the signal spectrum. In the case of a point-like inhomogeneity

$$\Delta\varepsilon(\mathbf{r}_1) = \Delta\varepsilon_0 \delta(\mathbf{r}_1 - \mathbf{r}_{10})$$

the integral is evaluated as follows:

$$S(\mathbf{r},\mathbf{r}_0,t) \equiv k_0{}^2 \Delta\varepsilon_0 \frac{S_0\left(t - \dfrac{|\mathbf{r}_{10} - \mathbf{r}_0| + |\mathbf{r}_{10} - \mathbf{r}|}{c}\right)}{(4\pi)^2 |\mathbf{r}_{10} - \mathbf{r}_0||\mathbf{r}_{10} - \mathbf{r}|},$$

and generates the characteristic pattern depicted in Fig. 1.11. Time t is plotted along the vertical axis, and the coordinate $\mathbf{r}$ of the observation point is plotted horizontally. The pulse waveform in each vertical cross-section is represented as a gray-scale image. Such a pattern is called a diffraction hyperbola.

Fig. 1.11. Diffraction hyperbola.

In our opinion, out of the entire set of existing approaches the focusing synthesis technique is the most promising. In this technique localization of the radiation-matter interaction can be realized in series or in parallel. This approach is reminiscent of the inverse projection method, which is widely known amongst mathematical tomography methods, but, in contrast to it, this approach deals with predominantly coherent radiation. As its final result, it delivers a significant gain in spatial resolution and computation speed. Synthesis of focusing is based on the idea of representing the act of focusing as the result of multi-beam interference of coherent waves, when these wave fields interfere in-phase at a selected point – the focal point ($\mathbf{r}_F$). In the case of monochromatic radiation (1.10) this operation is performed by multiplying the complex amplitude of the received field at each receiving point $\mathbf{r}_m$ for each transmitting point $\mathbf{r}_{0,n}$ by the focusing function

$$M(\mathbf{r}_F,\mathbf{r}_m,\mathbf{r}_{0,n})=\exp\left\{-ik\left(\left|\mathbf{r}_F-\mathbf{r}_m\right|+\left|\mathbf{r}_F-\mathbf{r}_{0,n}\right|\right)\right\}.$$

As a result, we obtain the following function:

$$U(\mathbf{r}_F)=\sum_m\sum_n M(\mathbf{r}_F,\mathbf{r}_m,\mathbf{r}_{0,n})E(\mathbf{r}_m,\mathbf{r}_{0,n}). \tag{1.12}$$

The central idea of this operation is to interfere all possible waves in-phase at a given focal point $\mathbf{r}_F$. Scanning the sounded region with the focusing point delivers the distribution of inhomogenities in space. If sounding is performed at a set of frequencies f_k, i.e., at a set of values of the wave number $k=2\pi f_k/c$, summation (superposition) of the set of interference patterns $U(\mathbf{r}_F,k)$ will decrease the level of side lobes and increase the magnitude of the central peak at the focusing point. Mathematically, this can be written as

$$U(\mathbf{r}_F)=\sum_k U(\mathbf{r}_F,k). \tag{1.13 a}$$

If pulsed radiation is used, the last equation means that focusing should be over both space and time:

$$U(\mathbf{r}_F)=\sum_m\sum_n S(\mathbf{r}_m,\mathbf{r}_{0,n},t_{m,n}), \tag{1.13 b}$$

where $$t_{m,n}=\frac{\left|\mathbf{r}_F-\mathbf{r}_m\right|+\left|\mathbf{r}_F-\mathbf{r}_{0,n}\right|}{c}.$$

In the case presented in Fig. 1.11, the focusing procedure is equivalent to integration (summation) over a hyperbola. So this focusing method is called the (diffraction) hyperbola summation method in some papers [6]. This approach is, by its definition and realization, equivalent to using spatiotemporal matched filtering, where the focusing function acts as the transfer function of the matched filter. We call this approach the inverse focusing method (IFM).

Note that the contribution by weight of each term in sums (1.12) and (1.13) is important to enhance the quality of the focused images, but correct phasing of the terms plays a much larger role. Amplitude weighting of the terms influences the side-lobe level and the possible appearance of artifacts.

Radiation focusing alone as an interference phenomenon can be realized in two ways: physically or mathematically. Physically, this means the use of physical equipment such as lens, mirrors, prisms, phased antenna arrays. Mathematically, it means using computer software. The latter is of particular interest because, on the one hand, it affords to analyze the experiment data in deferred processing mode as thoroughly as it needed, and, on the other hand, to perform such analyses quickly by the use of fast algorithms.

A wave field, which is formed as the result of focusing, is a quasi-parallel (collimated) beam of electromagnetic radiation. According to calculations, the phase and amplitude of a wave-front in the focusing region are close to a plane wave. So, the interaction of focused radiation, including UWB pulses, with media and objects imbedded in them can be considered in the approximation of a collimated beam. Let us consider some peculiarities of location sounding, i.e., sounding with one-sided access to the object being inspected.

1.4.2. Single focusing on environmental boundary

Let us suppose that the measurements at the frequency $f = ck/2\pi$ result in a scattered field distribution $E(\boldsymbol{\rho}_0, f)$ over a certain plane above the surface of the sounded medium (Fig. 1.12).

The method of synthesized aperture radar makes it possible to reconstruct the volume distribution of inhomogeneities by inversion of integral (1.10). To obtain this distribution, we focus the field at some point on the interface of the media $\boldsymbol{\rho}_F$. As is well known, the operation of focusing consists in the in-phase interference of scattered field amplitudes at the chosen focusing point. To provide such interference, it is necessary to compensate the phase differences from the transmitting antenna to the focusing point and from the focusing point to the receiving antenna.

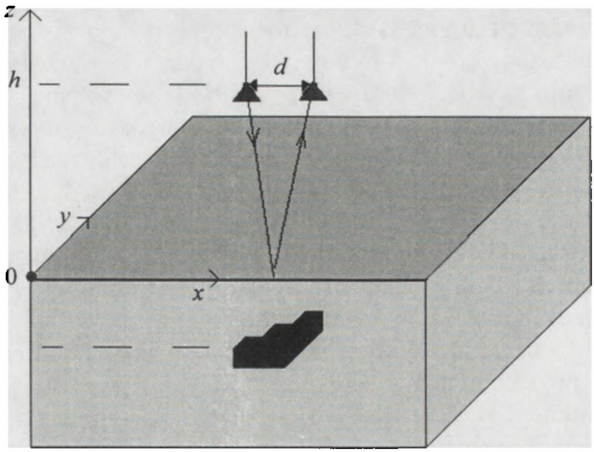

Fig. 1.12. Detection of hidden inhomogeneities.

The result of focusing of the scattered field at some point $\boldsymbol{\rho}_F$ on the surface can be written with the help of a convolution integral

$$F(\boldsymbol{\rho}_F,f)=\iint\limits_S E(\boldsymbol{\rho}_0,f)M(\boldsymbol{\rho}_F-\boldsymbol{\rho}_0,f)d^2\boldsymbol{\rho}_0\,,$$

where $M(\boldsymbol{\rho},f)=\exp\left\{-ik_0\left(2\sqrt{\rho^2+h^2}\right)\right\}$ is the simplest form of the corresponding weighting function (focusing function), and the integration is performed over the entire observation plane S, which is the synthetic aperture plane. The hidden object, or inhomogeneity, is located in the lower half-space with refraction index n.

With regard to representation (1.10), the focused field can be written as

$$F(\boldsymbol{\rho}_F,f)=\iiint\limits_{V_1}\Delta\varepsilon(\boldsymbol{\rho}_1,z_1)Q(\boldsymbol{\rho}_1,\boldsymbol{\rho}_F,z_1,f)d^3\mathbf{r}_1\,, \qquad (1.14)$$

where

$$Q(\boldsymbol{\rho}_1,\boldsymbol{\rho}_F,z_1,f)=k_1^2\iint\limits_S G_0^{\,2}(\boldsymbol{\rho}_1-\boldsymbol{\rho}_0,z_1)M(\boldsymbol{\rho}_F-\boldsymbol{\rho}_0,f)d\boldsymbol{\rho}_0 \qquad (1.15)$$

is the system response to a point-like inhomogeneity located at the point $\mathbf{r}_1$, i.e., this is an instrument function at the frequency f for focusing at the point $\boldsymbol{\rho}_F$ on the surface.

Note that the field in the focusing region becomes homogeneous in the case of a large aperture S, and integral (1.14) transforms to an integral of convolution type, and thus can be approximately written as

$$Q(\boldsymbol{\rho}_1, \boldsymbol{\rho}_F, z_1, f) \approx Q(\boldsymbol{\rho}_F - \boldsymbol{\rho}_1, z_1, f).$$

This allows the instrument function for one focusing point to be applied approximately for other points. Only the displacement between these two points $\boldsymbol{\rho} \equiv \boldsymbol{\rho}_F - \boldsymbol{\rho}_1$ is important here. Figure 1.13*a* presents gray-scale plots of numerical calculations of the instrument function $Q(\boldsymbol{\rho}, z, f)$ for free space

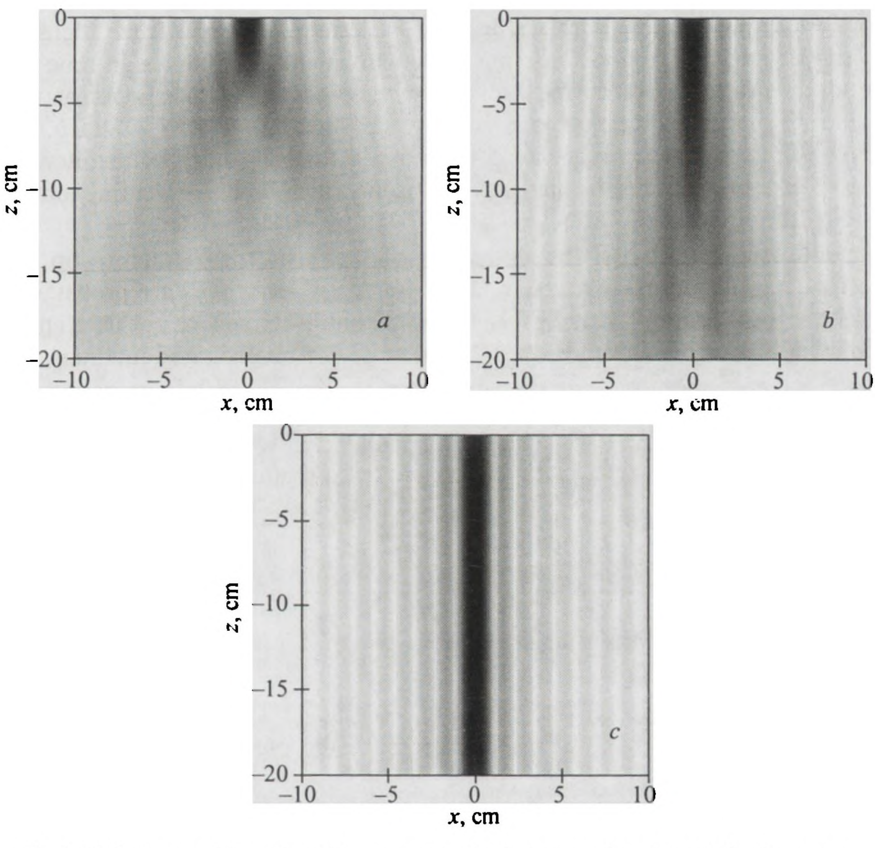

Fig. 1.13. Instrument function of the system in the frequency domain: *a* is for free space; *b* is for a medium with $n = 3$; *c* is in the transverse approximation for a medium with $n = 3$.

($n=1$) at the frequency $f=10$ GHz, when the synthetic aperture is 50 cm and its height $h=30$ cm. Darker regions correspond to the larger amplitude values. The amplitude of the instrument function for a medium with refraction index $n=3$ is shown in Fig. 1.13*b*. It can be seen that the region of maximum response of the medium to the point scatterer will be extended vertically if the refraction index of the lower medium n is increased. In other words, increasing the electric phase difference relative to its geometrical path results in a marked extension of the focusing region in lower medium.

It should be stressed that such focusing will localize the inhomogeneities in the horizontal plane only, and vertical focusing is not possible at this stage. From general considerations, it would clearly be more appropriate to select a focusing point directly in the investigated medium. However, such focusing is connected with cumbersome mathematical calculations and high time expenditures for data processing as well, for example, up to four hours, as was mentioned in paper [1]. As can be observed in Figures 1.13 *a* and *b*, the wave-refraction effect will extend the surface focusing into the medium, at least for points that are located not too deeply. The higher the refraction index n, the stronger this effect becomes.

With due regard for the extension of the instrument function in the vertical direction, let us suppose that refracted plane waves are propagated in the lower medium transversely to the medium boundary. Let us emphasize that the higher the refraction index n of the investigated medium, the more accurate the approximation becomes. In this case, the expression for κ_{1z} simplifies: $\kappa_{1z}=\sqrt{k^2n^2-\kappa_\perp^2}\approx kn=k_1$, and the factor $\exp(ik_1z)$, which appears in Eq. (1.15), can be taken outside the integral:

$$G_0(\rho,z)\approx\exp(ik_1z)\int_{-\infty}^{\infty}\int_{-\infty}^{\infty}\frac{iT(\mathbf{k})\exp[i(\mathbf{k}_\perp\rho+\kappa_z h)]}{2(2\pi)^2\kappa_z}d^2\mathbf{k}_\perp\equiv$$
$$\equiv\exp(ik_1z)G_\perp(\rho),\qquad(1.16)$$

where $T(\mathbf{k})$ is the transmission coefficient of a plane wave through the boundary of the two media [3].

Reversing the order of integration in integrals (1.14) and (1.15) and employing approximation (1.16), the expression for the focused field can be written as

$$F(\rho_F,f)=\int_{-\infty}^{0}\exp(i2knz_1)\iint\Delta\varepsilon(\rho_1,z_1)Q_\perp(\rho_F-\rho_1,f)d^2\rho_1dz_1,\qquad(1.17)$$

where
$$Q_\perp(\boldsymbol{\rho}_F - \boldsymbol{\rho}_1, f) = Q(\boldsymbol{\rho}_F - \boldsymbol{\rho}_1, z_1 = 0, f) = \\ = \iint_S M(\boldsymbol{\rho}_F - \boldsymbol{\rho}_0, f) G_\perp^2(\boldsymbol{\rho}_1 - \boldsymbol{\rho}_0) d\boldsymbol{\rho}_0$$

acts as the transverse instrument function of the system at the frequency f. Figure 1.13 *c* presents a gray-scale plot of a numerical calculation of the transverse instrument function $Q_\perp(\boldsymbol{\rho}, f)$ for the frequency $f = 10$ GHz. It can be seen that this function duplicates the instrument function quite accurately for the refraction index $n = 3$ down to a certain depth $z_{\max}$, then the approximation is no longer applicable. Localization of the instrument function $Q_\perp(\boldsymbol{\rho}, f)$ over $\boldsymbol{\rho}$ determines the potential resolution of the system in the horizontal plane.

To obtain the three-dimensional instrument function, we apply the Fourier transform to the focused field (1.17) at all frequencies at which the measurements are performed. As a result, we can write

$$\tilde{F}(\boldsymbol{\rho}_F, t) \equiv \int F(\boldsymbol{\rho}_F, f) \exp(-i2\pi f t) df = \\ = \iiint_{V_1} \Delta\varepsilon(\boldsymbol{\rho}_1, z_1) \tilde{Q}_\perp\left(\boldsymbol{\rho}_F - \boldsymbol{\rho}_1, \frac{ct}{2n} - z_1\right) d^2\boldsymbol{\rho}_1 dz_1, \tag{1.18}$$

where

$$\tilde{Q}_\perp\left(\boldsymbol{\rho}_F - \boldsymbol{\rho}_1, \frac{ct}{2n} - z_1\right) \equiv \int Q_\perp(\boldsymbol{\rho}_F - \boldsymbol{\rho}_1, f) \exp[-i2\pi f(t - 2nz_1/c)] df$$

the instrument function of the system in the space-time domain. Numerical calculation for the frequency band from 0.5 to 17 GHz has revealed that the function $\tilde{Q}_\perp$ is localized in three dimensions (Fig. 1.14). The calculation was performed under the assumption that the depth of point-like inhomogeneity z_1=2.5 cm.

Within the framework of the adopted approximations, it is sufficient to write the solution of the convolution equation (1.18) to reconstruct the spatial distribution of the inhomogeneities $\Delta\varepsilon(\rho_1, z_1)$. This is a well-known problem, which is usually solved by using Wiener filtering with regularization. However, the established fact of good localization of the instrument function of the system makes it possible in the first approximation to assume that

$$\Delta\varepsilon(\rho_F, z_F) \sim \tilde{F}(\rho_F, 2nz_F/c) =$$
$$= \int_{-\infty}^{\infty} \exp(-i2knz_F) \iint_S E(\rho_0, f) M(\rho_F - \rho_0, f) d^2\rho_0 df. \qquad (1.19)$$

The accuracy of the resolution in this case is determined by the scale of localization of the instrument function of the system.

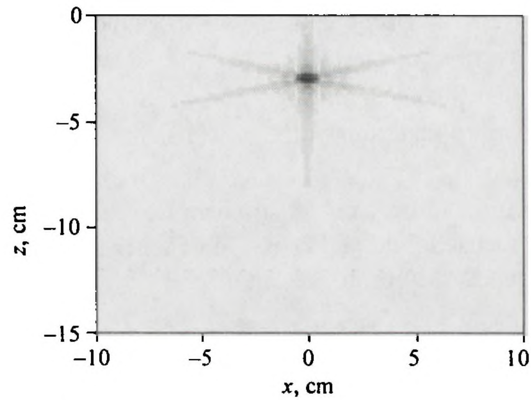

Fig. 1.14. Three-dimensional instrument function of the system.

Taking the adopted approximations into account, solution of the inverse problem reduces to focusing of radiation at a point of the medium near the surface and taking the inverse Fourier transform over frequency. The fast Fourier transform makes it possible to significantly speed up data processing.

The proposed algorithm was successfully implemented for tomography of antipersonnel landmines buried in moist sand (see Chapter 6).

1.4.3. Two-step focusing approach

The method of fixed focusing onto the medium interface, presented above, is especially efficient if the lower medium is strongly refracting [4]. In this case, the lower medium acts as a refractive prism, which keeps the radiation focused like on the surface. This situations change in the case of a weakly refracting medium or if the refraction index of the lower medium is lower that that of the upper medium. Partially focused radiation bergins to diverge in the lower medium. This happens, for example, when sound propagates from air into water. To correct this situation, additional focusing (second focusing) is needed. Let us consider how that can be done.

We assume that the monochromatic wave radiator and receiver move in parallel to plane medium interface at some distance from it. Location sounding of the medium is performed by monochromatic waves with a definite step, and the radiation point coincides with the receiving point and is located at a constant height h = const in the air above the surface of the medium.

Let us suppose that focusing at a certain point on the medium boundary has been performed. To correct the situation, the additional (second) focusing should be performed. We do this using the convolution integral

$$F_1(\boldsymbol{\rho}_{F1},h_1,f)=\iint\limits_S F(\boldsymbol{\rho}_F,f)M_1(\boldsymbol{\rho}_{f1}-\boldsymbol{\rho}_F,h_1,f)\left(d^2\boldsymbol{\rho}_F\right), \qquad (1.20)$$

where $M_1(\boldsymbol{\rho}_F,f)=\exp[-ikn2\sqrt{\boldsymbol{\rho}_F{}^2+h_1{}^2}\,]$ is the weight function of focusing; $\mathbf{r}_1=(\boldsymbol{\rho}_F,h_1)$ is the focusing point in the lower half-space; S is the plane of the medium boundary, which is also the plane of the second synthetic aperture. It is assumed that the refractive index is known. The function M_1 in Eq. (1.20) depends only on the difference of arguments by virtue of the assumed uniformity of the synthetic aperture.

Taking Eq. (1.17) into account, the focused field can be written as

$$F_1(\boldsymbol{\rho}_{F1},h_1,f)=\iiint\limits_{V_1}\Delta\varepsilon(\boldsymbol{\rho}_1,z_1)Q_1(\boldsymbol{\rho}_1,\boldsymbol{\rho}_{F1},h_1,f)\left(d^2\boldsymbol{\rho}_1\right)dz_1, \qquad (1.21)$$

where

$$Q_1(\boldsymbol{\rho}_1,\boldsymbol{\rho}_{F1},h_1,f)=\iint Q(\boldsymbol{\rho}_1,z_1,\boldsymbol{\rho}_F)M_1(\boldsymbol{\rho}_{F1}-\boldsymbol{\rho}_F,h_1)(d^2\boldsymbol{\rho}_F) \qquad (1.22)$$

corresponds to the system response to a point-like inhomogeneity located at the point $\mathbf{r}_1$, i.e., it is the instrument function of the system at the frequency f for focusing on the point $\boldsymbol{\rho}_{F_1}$ below the medium boundary.

If the aperture S is large, the integrals transform into convolution integrals, then it is possible to write

$$Q_1(\boldsymbol{\rho}_1,\boldsymbol{\rho}_{F1},z_1,h_1)=$$
$$=k_1^2\iint G_0{}^2(\boldsymbol{\rho}_1-\boldsymbol{\rho}_0,)M(\boldsymbol{\rho}_F-\boldsymbol{\rho}_0,f)d^2\boldsymbol{\rho}_0\iint M_1(\boldsymbol{\rho}_{F1}-\boldsymbol{\rho}_F,h_1)(d^2\boldsymbol{\rho}_F). \qquad (1.23)$$

Of course, this is an approximate result. Making the substitution

$G_0^2(\boldsymbol{\rho}_1 - \boldsymbol{\rho}_0) = g(\boldsymbol{\rho}_1 - \boldsymbol{\rho}_0)$, equation (1.20) can now be written as follows:

$$Q_1(\boldsymbol{\rho}_1, \boldsymbol{\rho}_{F1}, z_1, h_1) = \\ = k_1^2 \iint g(\boldsymbol{\rho}_1 - \boldsymbol{\rho}_0) M(\boldsymbol{\rho}_F - \boldsymbol{\rho}_0) M_1(\boldsymbol{\rho}_{F1} - \boldsymbol{\rho}_F)(d^2\boldsymbol{\rho}_0)(d^2\boldsymbol{\rho}_F). \quad (1.24)$$

Carrying out this integration, we obtain

$$Q_1 = k^2 \frac{1}{2\pi} \int \tilde{g}(-\boldsymbol{\kappa}_{2\perp}) \tilde{M}(\boldsymbol{\kappa}_{3\perp}) \tilde{M}_1(\boldsymbol{\kappa}_{3\perp}) \exp(i\boldsymbol{\kappa}_{3\perp}(\boldsymbol{\rho}_{F1} - \boldsymbol{\rho}_1))(d^2\boldsymbol{\kappa}_{3\perp}) = \\ = Q_1(\boldsymbol{\rho}_{F1} - \boldsymbol{\rho}_1, h_1, z_1), \quad (1.25)$$

where $\tilde{g}(-\boldsymbol{\kappa}_{2\perp})$, $\tilde{M}(\boldsymbol{\kappa}_{3\perp})$, and $\tilde{M}_1(\boldsymbol{\kappa}_{3\perp})$ are the spatial spectra of the functions $g(\boldsymbol{\rho}_1 - \boldsymbol{\rho}_0)$, $M(\boldsymbol{\rho}, h, f)$, and $M_1(\boldsymbol{\rho}_f, f)$, respectively.

On the basis of Eq. (1.25), integral (1.21) transforms into a convolution integral and can now be approximately written as

$$F_1(\boldsymbol{\rho}_{f1}, h_1, f) = \iiint_{V_1} \Delta\varepsilon(\boldsymbol{\rho}_1, z_1) Q_1(\boldsymbol{\rho}_1 - \boldsymbol{\rho}_{f1}, h_1, f) d\mathbf{r}_1 .$$

The function $Q_1(\boldsymbol{\rho}, h_1, f)$ acts as the instrument function in the focusing system with double synthesis of the focusing effect. Figure 1.15*a* presents a 2-D gray-scale plot of the system instrument function when two-step focusing is performed at a depth of 10 cm below the medium boundary.

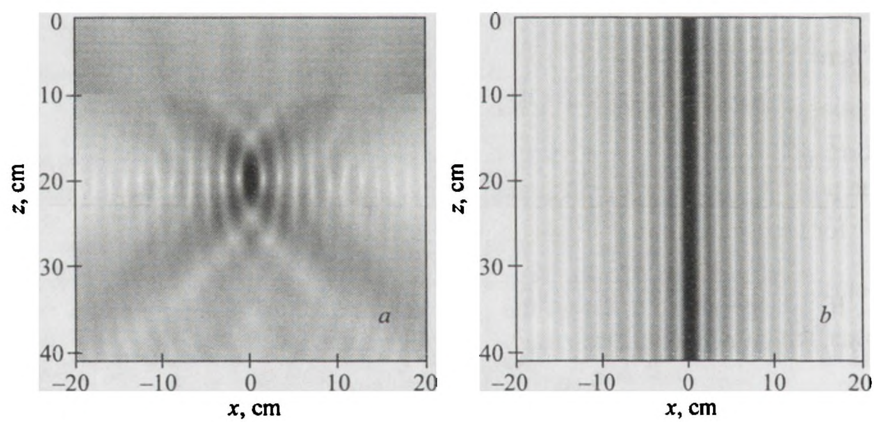

Fig. 1.15. Instrument Function (IF): *a* – in two-step focusing; *b* – approximate representation.

Let us admit the approximation in which the waves propagate along the normal to the surface in some region near the focusing point. This region will be localized in the horizontal plane and extend vertically to a great height h_1. In the given region it is possible approximately to write the instrument function as

$$Q_1 = Q_1(\boldsymbol{\rho}_{F1} - \boldsymbol{\rho}_1, z_1 - h_1) \approx Q_{1\perp}(\boldsymbol{\rho}_{F1} - \boldsymbol{\rho}_1)\exp(2ikn[z_1 - h_1]).$$

With this taken into account, the focusing field takes on the following form:

$$F(\boldsymbol{\rho}_F, h_1) = \iint (d^2\boldsymbol{\rho}_1)dz_1\Delta\varepsilon(\boldsymbol{\rho}_1, z_1)Q_{1\perp}(\boldsymbol{\rho}_{F1} - \boldsymbol{\rho}_1)\exp(2ikn[z_1 - h_1]),$$

where $k = \omega/c$. If we now transform from the frequency domain to the time domain by means of the inverse Fourier transform, it is possible to obtain depth resolution and approximately recover the image of the scattering inhomogeneities $\Delta\varepsilon(\boldsymbol{\rho}_f, z_f)$:

$$\int F_1(\boldsymbol{\rho}_{F1}, h_1)\exp(-2iknz_F)df \approx$$
$$\approx \int d\boldsymbol{\rho}_1 dz_1\Delta\varepsilon(\boldsymbol{\rho}_1, z_1)Q_{1\perp}\delta[z_F - [z_1 - h_1]]2\pi/(2n/c) \approx \Delta\varepsilon(\boldsymbol{\rho}_F, z_F),$$

where z_F is the focusing depth, and $t_F = 2nz_F/c$ is the time it takes for the wave to travel to the focusing point and back.

The obtained formula solves the tomography problem by implementation of two-step focusing.

1.4.4. Group focusing approach

The two-step focusing method can prove to be insufficient in a number of situations, for example, in a multilayer background medium or, on the contrary in a homogeneous medium. The focusing should be performed in such a case in series or parallel at all distances. Let us elucidate the essence of the proposed solution in the particular case of a homogeneous background medium in the single scattering approximation

$$E(\boldsymbol{\rho}_0, f) = k_1^2 \iiint_{V_1} \Delta\varepsilon(\boldsymbol{\rho}_1, z_1)G_0{}^2(\boldsymbol{\rho}_1 - \boldsymbol{\rho}_0, z_1)d^2\boldsymbol{\rho}_1 dz_1. \qquad (1.26)$$

Here $k_1 = k = 2\pi f/c$ is the wave number corresponding to the background medium. The Green's function is written in this case as a spherical wave field:

$$G_0(\boldsymbol{\rho}_1-\boldsymbol{\rho}_0,z_1)=\exp\left\{ik\sqrt{(\boldsymbol{\rho}_1-\boldsymbol{\rho}_0)^2+z_1^{\;2}}\right\}\Big/4\pi\sqrt{(\boldsymbol{\rho}_1-\boldsymbol{\rho}_0)^2+z_1^{\;2}}\ .$$

If we differentiate equation (1.26), we can write

$$\frac{d}{dk}\left\{\frac{E(\boldsymbol{\rho}_0,f)}{k^2}\right\}=\iiint\limits_{V_1}\Delta\varepsilon(\boldsymbol{\rho}_1,z_1)G_2(\boldsymbol{\rho}_1-\boldsymbol{\rho}_0,z_1)d^2\boldsymbol{\rho}_1 dz_1,$$

where

$$G_2(\boldsymbol{\rho}_1-\boldsymbol{\rho}_0,z_1)\equiv\exp\left\{i2k\sqrt{(\boldsymbol{\rho}_1-\boldsymbol{\rho}_0)^2+z_1^{\;2}}\right\}\Big/4\pi\sqrt{(\boldsymbol{\rho}_1-\boldsymbol{\rho}_0)^2+z_1^{\;2}}\ .$$

This function admits a plane-wave decomposition of the spectrum (Weyl's formula):

$$G_2(\boldsymbol{\rho}_1-\boldsymbol{\rho}_0,z_1)=\frac{i}{(2\pi)^2}\iint\frac{\exp\{i(\boldsymbol{\kappa}_\perp(\boldsymbol{\rho}_1-\boldsymbol{\rho}_0)+\boldsymbol{\kappa}_z z_1)\}}{2\boldsymbol{\kappa}_z}\left(d^2\boldsymbol{\kappa}_\perp\right),$$

where $\boldsymbol{\kappa}_z=\sqrt{(2k)^2-\boldsymbol{\kappa}_\perp^2}$. Taking this representation into account, we can write

$$E_1(\mathbf{u}_\perp,f)\equiv\iint\exp\{i\mathbf{u}_\perp\boldsymbol{\rho}_0\}\frac{d}{dk}\left\{\frac{E(\boldsymbol{\rho}_0,f)}{k^2}\right\}d^2\boldsymbol{\rho}_0=$$

$$=\iiint\limits_{V_1}\Delta\varepsilon(\boldsymbol{\rho}_1,z_1)\frac{\exp\{i(\mathbf{u}_\perp\boldsymbol{\rho}_1+u_z z_1)\}}{2i\mathbf{u}_z}d^2\boldsymbol{\rho}_1 dz_1, \tag{1.27}$$

where $\mathbf{u}_z=\sqrt{(2k)^2-\mathbf{u}_\perp^2}$. This expression implies that the spatial frequency spectrum of the inhomogeneities coincides with the obtained expression for $E_1(\mathbf{u}_\perp,f)$ to within a constant factor:

$$\Delta\varepsilon(\mathbf{u}_\perp,\mathbf{u}_z)\equiv\iiint\limits_{V_1}\Delta\varepsilon(\boldsymbol{\rho}_1,z_1)\exp\{i(\mathbf{u}_\perp\boldsymbol{\rho}_1+\mathbf{u}_z z_1)\}d^2\boldsymbol{\rho}_1 dz_1=$$

$$=2i\mathbf{u}_z E_1(\mathbf{u}_\perp,f). \tag{1.28}$$

In the final count, the three-dimensional inverse Fourier transform remains to be performed to recover the spatial distribution of the inhomogeneities. There is only one calculational peculiarity here if expression (1.27) is used, and that is the need to transform from time frequencies f to the corresponding spatial frequencies

$$u_z = \sqrt{(2k)^2 - \mathbf{u}_\perp^2} = \sqrt{(4\pi f/c)^2 - \mathbf{u}_\perp^2}\,, \tag{1.29}$$

which is realized by interpolation. Expression (1.28) realizes the idea of the focusing method at all distances.

Figure 1.16 displays the result of simulation when the above-described group focusing method was used. The result of numerical simulation of the distribution of the real part of the radio-location response from a point-like inhomogeneity with the coordinates $x = 20$ cm, $y = 0$ cm, and $z = 150$ cm is presented in the upper part of Fig. 1.16.

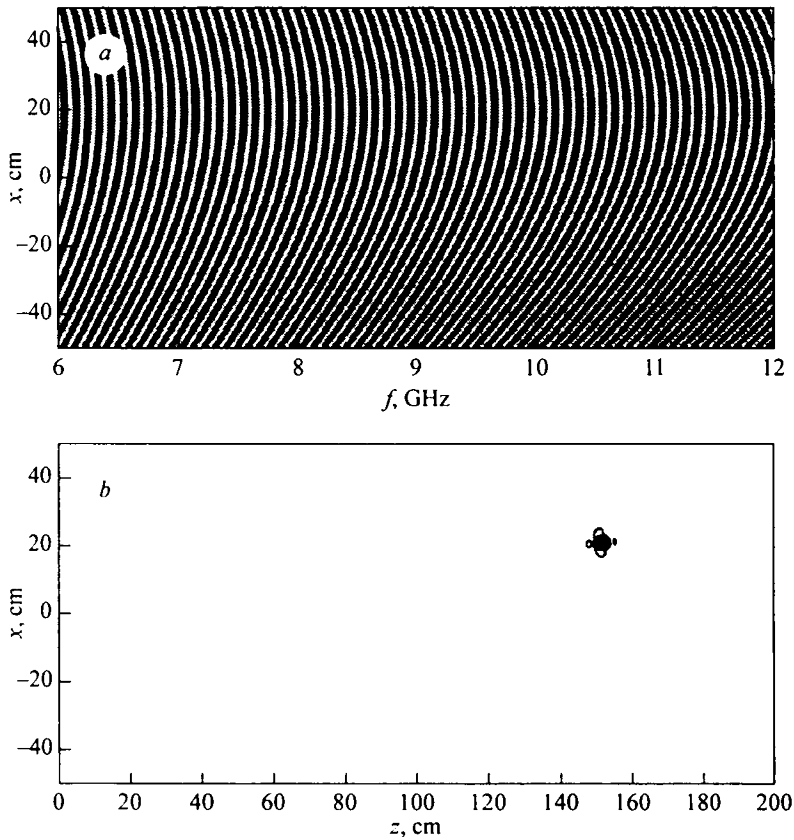

Fig. 1.16. Location sounding problem: a – simulation modeling; b – result of reconstruction a point-like inhomogeneity using the group focusing method.

Sounding was performed within the limits ± 50 cm along the x axis, in the plane $y = 0$ cm in the frequency band 6–12 GHz. The solution result, the tomogram reconstructed in the plane $y = 0$ cm, is shown as a gray-scale plot in Fig. 1.16*b*. It is obvious that the prescribed inhomogeneity is restored unambiguously.

Here and below, the problem of large aperture synthesis with radiation focusing is called radio-wave tomosynthesis. Equation (1.28) in this case is a generalization of the Stolt method and it takes into account the difference between the functions $G_0(\boldsymbol{\rho}_1 - \boldsymbol{\rho}_0, z_1)$ and $G_2(\boldsymbol{\rho}_1 - \boldsymbol{\rho}_0, z_1)$. It should be noted that this substitution acts as a selection of the window function and does not affect the focusing procedure.

The proposed method is applicable in the case of a multilayer medium. It suffices, for this purpose, to replace the exponential factor $\exp\{i u_z z_1\}$ in formula (1.27) by the combined factor

$$\exp\left\{i\left(\sum_j u_{zj} z_j + u_z z_1\right)\right\},$$

which accounts for the phase difference for all previous layers with depths z_j and refractive indices n_j. The normal projection of the wave number in each of the layers is calculated as

$$u_{zj} \equiv \sqrt{(2kn_j)^2 - \mathbf{u}_\perp^2}\ .$$

As an experimental test of this approach, a model medium was constructed from three foam-concrete blocks with equal depth of 10 cm (Fig. 1.17*a*). A thin test layer made from five aluminum foil strips with equal width of 2 cm (Fig. 1.17*b*) was placed between the second and third blocks. The aluminum test layer is indicated by an arrow. The measured refractive index of the foam-concrete was $n = 1.44$. A radio image of the test layer obtained by the proposed method is shown in Fig. 1.17*b* as a gray-scale plot. Sounding was performed using UWB pulses with a pulse duration of 200 ps.

The radio image reproduces the actual size and positions of the aluminum strips with a resolution of at least 2 cm. If the background medium is inhomogeneous, the resolution will be a bit worse (see Chapter 2).

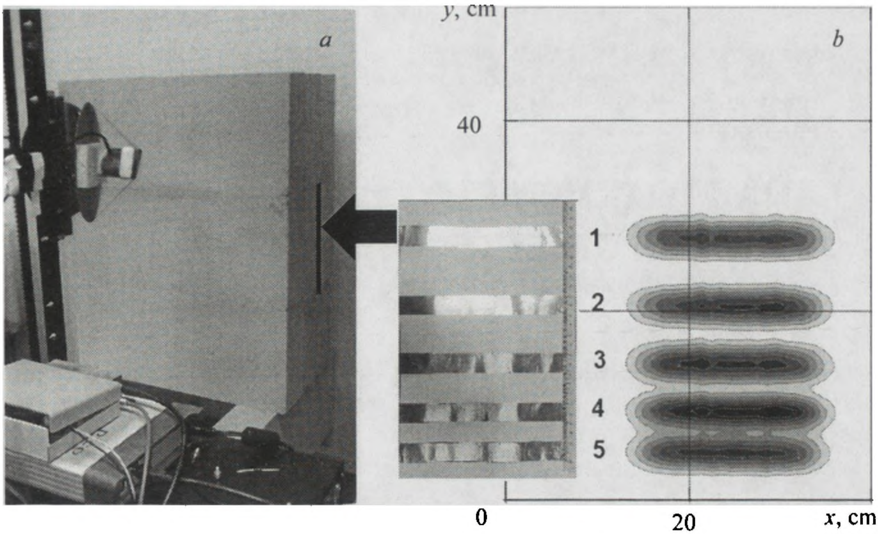

Fig. 1.17. Experiment to validate the group focusing approach: *a* – a wall made of foam-concrete blocks; *b* – test object inside the wall and its radio image.

1.5. Summary

The methods and approaches developed in this chapter form the basis of a common approach called radio-wave tomosynthesis. The fundamental idea of this approach is to develop a focusing effect as a result of partial wave interference. The connection between radio-wave tomosynthesis and multidimensional matched filtering and other methods has been pointed out.

It has been demonstrated that the focusing effect, which is the basis of wave tomography, significantly reduces the effect of multiple interactions and amplifies the role of the dominant mechanisms of the radiation-matter interaction.

The emphasis has been upon location sounding, where the radiation and receiving points are located in the same half-space. Many of the algorithms proposed for the solution of the inverse problem reduce to fast algorithms and admit of real-time operation.

Most of the solutions considered have been borne out by numerical simulation and real experiments.

Chapter 2

RADAR TOMOGRAPHY OF HIDDEN OBJECTS

The tomographic methods described in Chapter 1 were validated by numerical simulation. But their experimental testing is of greater interest. The aim of the present chapter is an objective assessment of these methods' resolution. The working models developed here may serve as prototypes of commercial radio-tomographs. Results of papers [1–6] are summarized in the present chapter.

2.1. Basic experimental setup

The basic setup for UWB radio-wave sounding includes: a scanner, an XY positioner (Fig. 2.1), a scanner control unit, a TMR8140 stroboscopic oscilloscope (Fig. 2.2), a personal computer, and a transceiver module (Fig. 2.3).

The transceiver module is worthy of note. The original design of the UWB antenna is implemented in this device (Fig.2.4). The antenna is constructed as a combined antenna which consists of two electric antennas (a TEM horn and an asymmetrical dipole) and a magnetic antenna of spiral shape. The overlap of the near-field zones of these unlike (electric and magnetic) antennas makes it possible to considerably reduce the presence of reactive fields and extend the bandwidth as a result. Figure 2.5 plots the frequency characteristic of the smallest of the antennas shown in Fig. 2.4. The bandwidth of this antenna is 1–18 GHz. The voltage standing wave ratio (VSWR), which is a specification used to rate antennas, does not exceed 2.

The displacement of the antenna phase center for the frequency spectrum does not exceed its diameter. The design of the antenna was developed by Associate Professor J. I. Buyanov.

Fig. 2.1. Scaled-up two-dimensional scanner for UWB measurements.

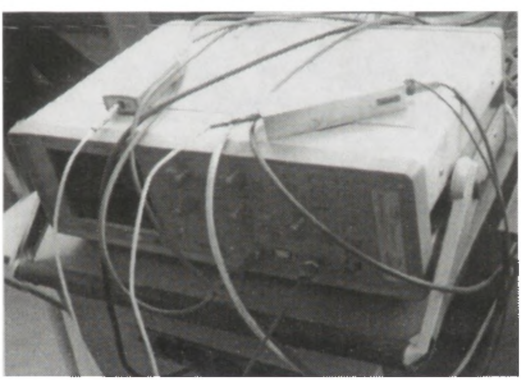

Fig 2.2. TMR8140 stroboscopic oscilloscope and bipolar pulse generator with a duration of 0.1 ns.

Fig. 2.3. Transceiver module.

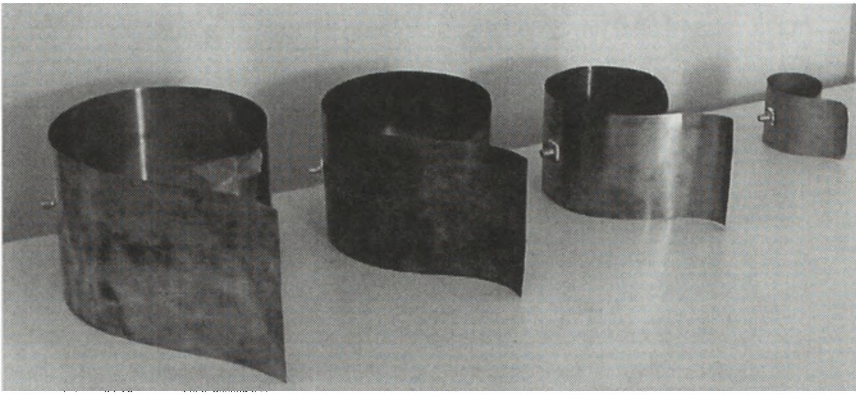

Fig. 2.4. UWB antennas of snail type.

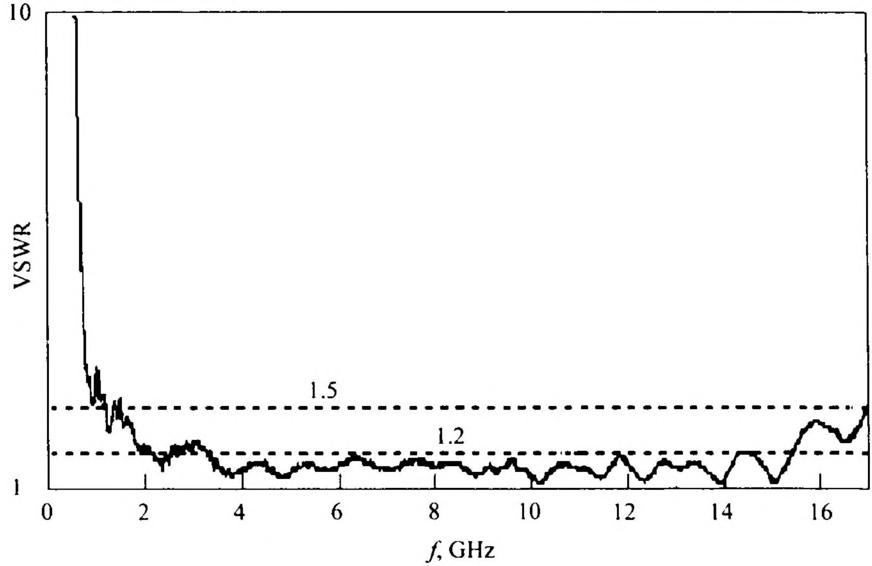

Fig. 2.5. VSWR frequency dependence of snail type antennas.

The directivity pattern of the antenna, by virtue of its small size, is quite wide in both the azimuthal and the elevation plane (30–70°). Directivity patterns (DPs) of the antenna, measured at two frequencies (3 GHz and 9 GHz), are shown in Fig. 2.6.

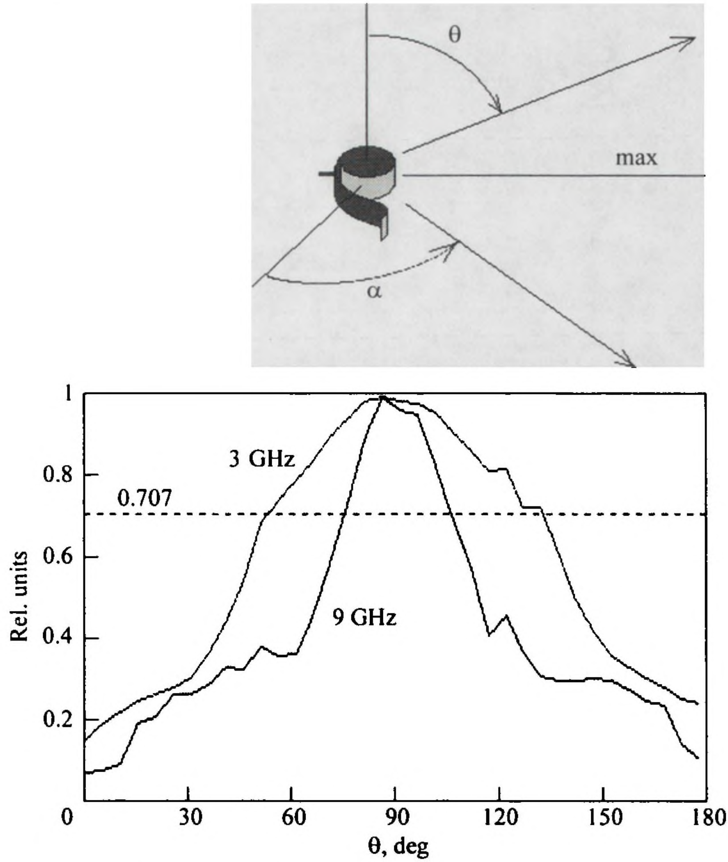

Fig. 2.6. Azimuthal DP of a snail type antenna.

Signals with durations of 100, 200, and 1500 ps were analyzed for radio-sounding. Equipment from TRIM, Ltd. – Research and Production Enterprise (St. Petersburg, Russia) (TRIM Ultrawideband Measurement Systems) was used to generate and receive the UWB signals. The pulse repetition rate of the strobe was 100 kHz. Analysis of signal forms and spectra (Fig.2.7) revealed that pulses with durations of 100 and 200 ps were most relevant for radio-tomography. These signals in particular should provide proper spatial resolution, and their spectra are well-matched to the chosen design of the transceiver antenna.

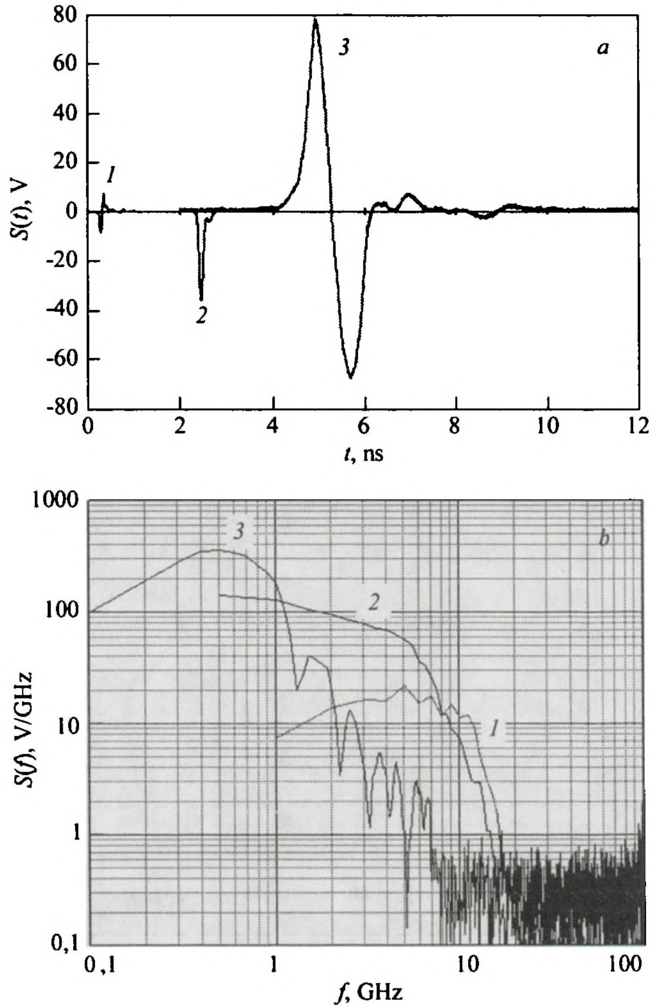

Fig. 2.7. UWB pulses of different duration (*a*) used for sounding, and their spectra (*b*): curve *1* – 100 ps; curve 2 – 200 ps; curve *3* – 1500 ps.

A typical signal with a duration of 100 ps, reflected from the test object, is shown in Fig. 2.8. The signal is of indented form, and the central peak is delayed by the travel time from the object to the antenna module.

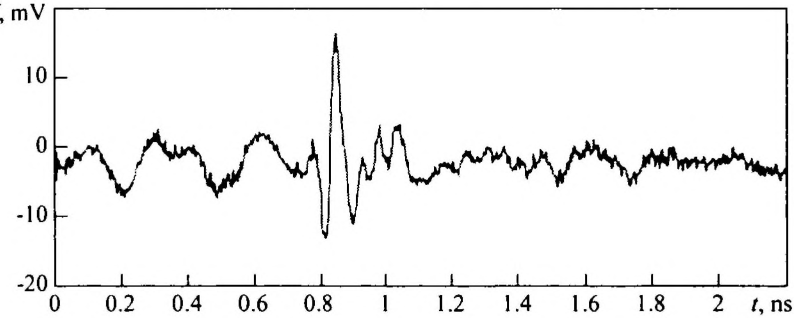

Fig. 2.8. A UWB signal reflected from the test object.

Figure 2.9 displays a sample raster image of recorded signals from scanning the test object. The line-by-line rasters presented here are set one above another. In this case, horizontal flyback of the scanner starts immediately after direct scanning of the previous line.

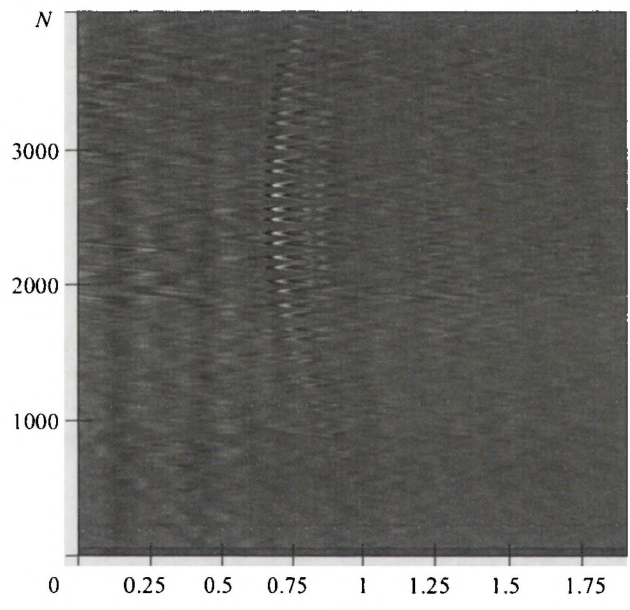

Fig. 2.9. Raw data of tested section.

This considerably shortens the scanning time. It is important that the characteristic diffraction hyperbola, which indicates the localization of the object, is distinctly visible at every step.

The scanner control unit contains a USB-to-COM converter based on the FTDI 245BM chip. This makes it possible to transform low-current USB command signals into eight binary output signals, which after being routed through matching amplifiers are directed to the stepper motor control of a two-coordinate scanner. There are four windings in each stepper motor, where the current in each of them assigns the motor state. The control unit makes it possible to position the scanner antenna module along two axes independently. In general, the experimental setup allows the transceiver antenna module to be repositioned within an 84×84 cm square region in the plane with an accuracy of 2 mm and a speed of up to 3 cm/s.

Employing monostatic radiometry methods to solve problems of tomography in most cases supposes the use of a single antenna for both reception and transmission in a way that facilitates more accurate reconstruction of the radio-wave image of the tested object, all other things being equal. In UWB tomography, use of a single antenna is complicated by technical difficulties associated with isolation of the transmitting and receiving antenna paths. It proved to be impossible to find suitable directional couplers providing isolation of not less than 30 dB in the UW frequency band. Development of a fast UWB switch is another independent task.

It was experimentally determined that the antennas must be separated by a distance of not less than 20 cm to get isolation of 25–30 dB between the receiving and transmitting antennas; however, this is unacceptable in UWB tomography.

To increase the decoupling from the transmitting antenna to the receiving antenna, a metallic screen was used, whose shape and geometric dimensions were determined experimentally. It turned out that an acceptable result was achieved when the screen had a shape close to that of an ellipse with major and minor semi-axes of 9 and 5 cm, respectively. A photograph of the assembly of antennas with screen is shown in Fig. 2.3.

2.2. UWB tomosynthesis of objects hidden in buildings and hand luggage

Figure 2.10 displays experimental data for a flat test object in the shape of a metal-coated stepped triangle. Each step is 5 cm (Fig. 2.10*a*). Processing of the radio-scanning data was performed by means of the algorithm described in Section 1.4.1. The result of single focusing at the actual distance to the object is presented in Fig. 2.10*b*. The object's shape is fully recovered, but there is outline blur, which is estimated as ≈ 2 cm.

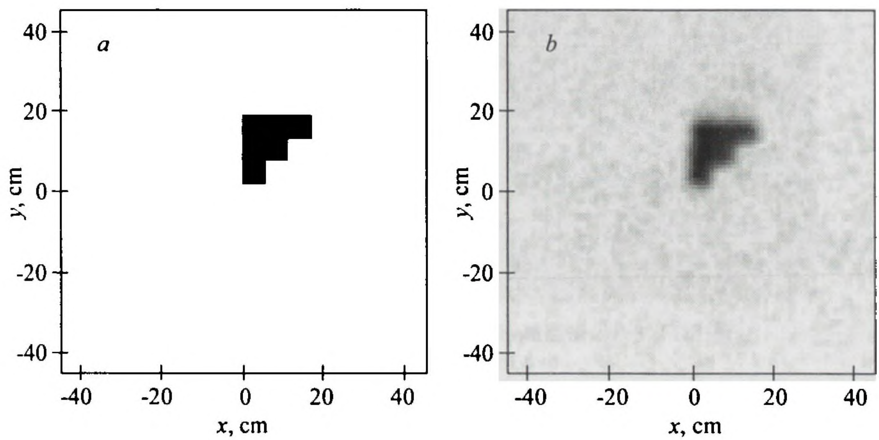

Fig. 2.10. Test object – stepped triangle:
a – true shape; *b* – reconstructed radio tomogram.

Research on the possibility of tomography of hidden objects is of prime interest from an applications point of view. An example of such an experiment is shown in Fig. 2.11, where an object of triangular shape, made of metallic foil glued on paper was placed between two foam-concrete blocks of thickness 10 cm each. The blocks and the object were situated at a distance of 80 cm from the scanner.

The observed location signals are plotted as a time series in Fig. 2.12, which is seen to fluctuate wildly. What we see here is multiple reflections caused by reflection from the medium boundaries and by reflections from the test triangle itself.

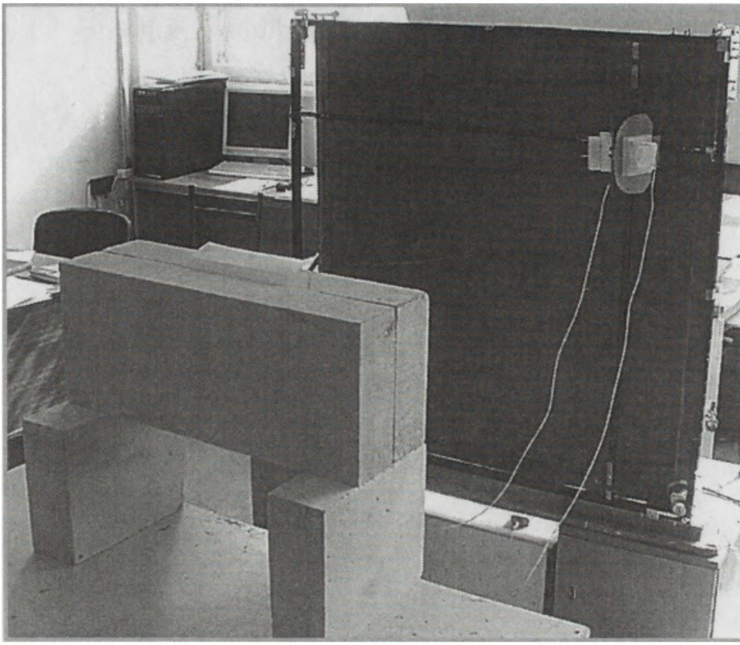

Fig. 2.11. Experiment on tomography of a thin metallic object in a foam-concrete wall.

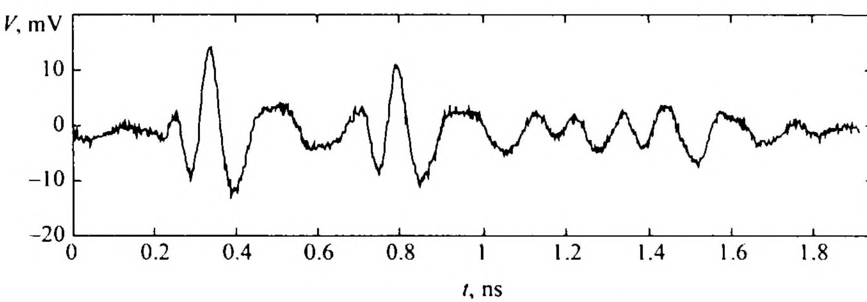

Fig. 2.12. Signal reflected from the wall and the hidden object inside it.

Fig. 2.13 displays results of a location radio-scan for a scene with a hidden object. Figure 2.14 presents results of reconstructing the image of the wall with the hidden object inside it. The object can be clearly made out, which means that there is range resolution.

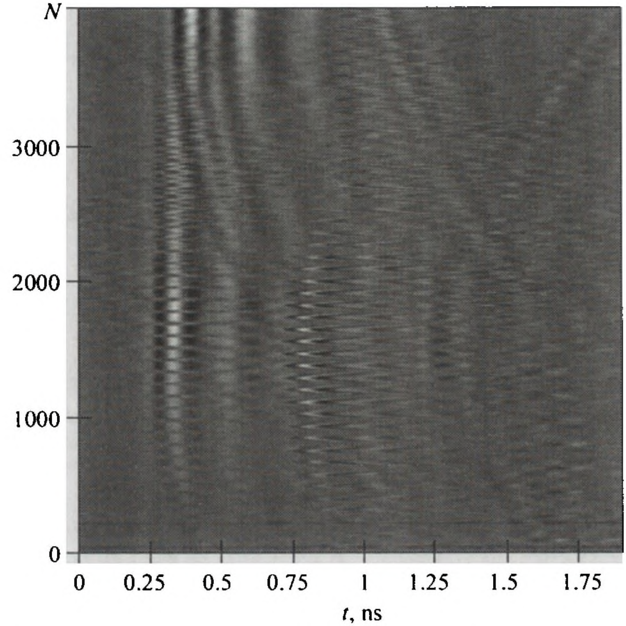

Fig. 2.13. Radio-wave scan of a scene with a hidden object.

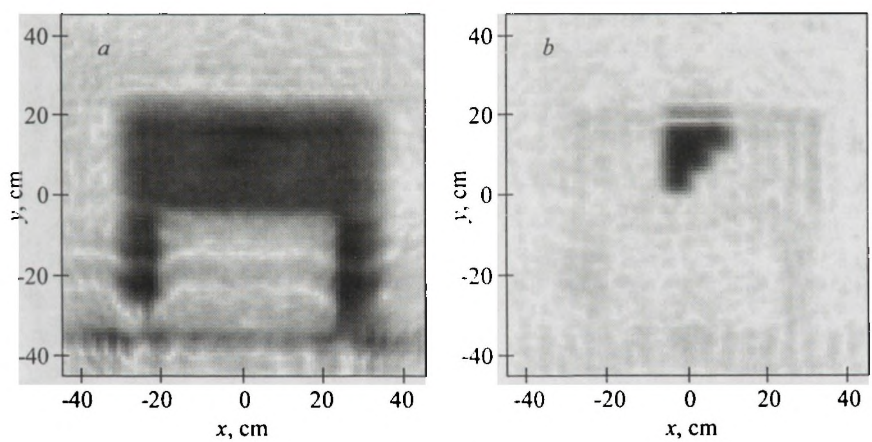

Fig. 2.14. Reconstructed image of the foam-concrete wall:
a – focusing on the foreground; *b* – focusing on the hidden object.

Thus, the possibility of visualizing hidden objects inside a wall by means of radio-waves has been demonstrated. It can be seen that the resolution of the hidden object has been degraded somewhat, and is close to 2–3 cm.

From physical considerations it is clear that the spatial resolution of wave tomographic images has a limit which is defined primarily by the size of the focusing area in the transverse direction and by the spatial extension of the applied pulses in the longitudinal direction. Let us clarify that.

We start with transverse localization. Focusing is possible within the so-called Fresnel diffraction zone, i.e., the zone in which the radiation point is observed with measured phase difference at different points of the recording aperture. If the size of the recording aperture is D, and $\Delta\varphi = \pi/16$ is the effective phase difference over the receiving aperture, then the depth of the Fresnel zone for radiation with the wave length λ is defined as the distance

$$H_F = 4D^2/\lambda\,.$$

Focusing degrades as the distance r approaches the limiting depth H_F by an amount proportional to the ratio $\gamma \equiv r/H_F$. If the diameter of best focusing on the center of the closed aperture is defined by the localization value $\delta_k(\rho)$ and is equal to the wavelength λ, i.e., the diffraction limit (see Section 1.2), then it will be increased by an amount that is proportional to γ as the boundary of the Fresnel zone is approached:

$$\rho_\perp = \lambda(1+\gamma) \equiv \lambda(1+\lambda r/4D^2)\,. \tag{2.1}$$

For example, if the frequency $f = 12$ GHz and $r = 90$ cm and $D = 84$ cm, the resolution will be estimated as $\rho_\perp = 2.52$ cm. This is close to the experimentally observed value. But this estimate is approximate.

Let us turn now to the case of longitudinal resolution. It is defined by the efficient pulse duration τ or by pulse frequency bandwidth $\Delta f \sim 1/\tau$, so that the longitudinal resolution is estimated by the relation

$$\rho_{||} = c\tau/2 \equiv c/2\Delta f\,.$$

This estimate gives the value $\rho_{||} = 1.5$ cm for a pulse with a bandwidth on the order of 10 GHz. This corresponds to the observed values.

An experiment with two metallized cylinders was performed to assess the loss of spatial resolution with increasing distance to the object. The cylinders were separated by a distance of 6 cm in the transverse direction (Fig. 2.15).

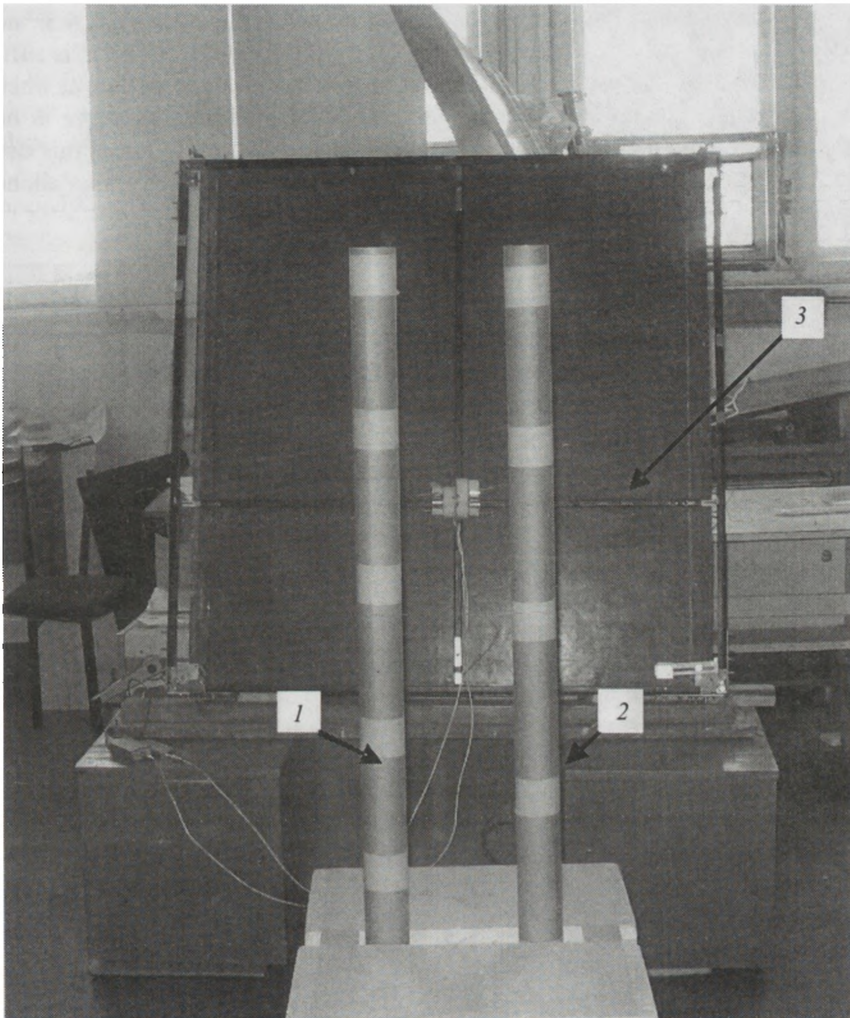

Fig. 2.15. Experiment with metallized cylinders:
1, *2* – cylinders, *3* – scanner.

The test objects were placed at distances $r = 90$, 135, and 180 cm. The tomograms obtained are displayed in Fig. 2.16. The positions of the cylinders are marked by the numbers *1* and *2*, and an artefact is indicated by the number *3*. The single cell size is 5×5 cm. According to formula (2.1), the estimates of the transverse resolution for these ranges are $\rho_{\perp} = 2.8, 4.3$, and 5.7 cm, respectively. It is seen that the resolution at short distances is sufficient to observe inhomogeneities, but as the distance is approached at which resolution is lost ($r = 180$ cm), the likelihood of artefacts appearing in the image increases. It is interesting that the longitudinal resolution in this case does not vary since the working bandwidth remains unchanged – after all, the sounding pulse is one and the same.

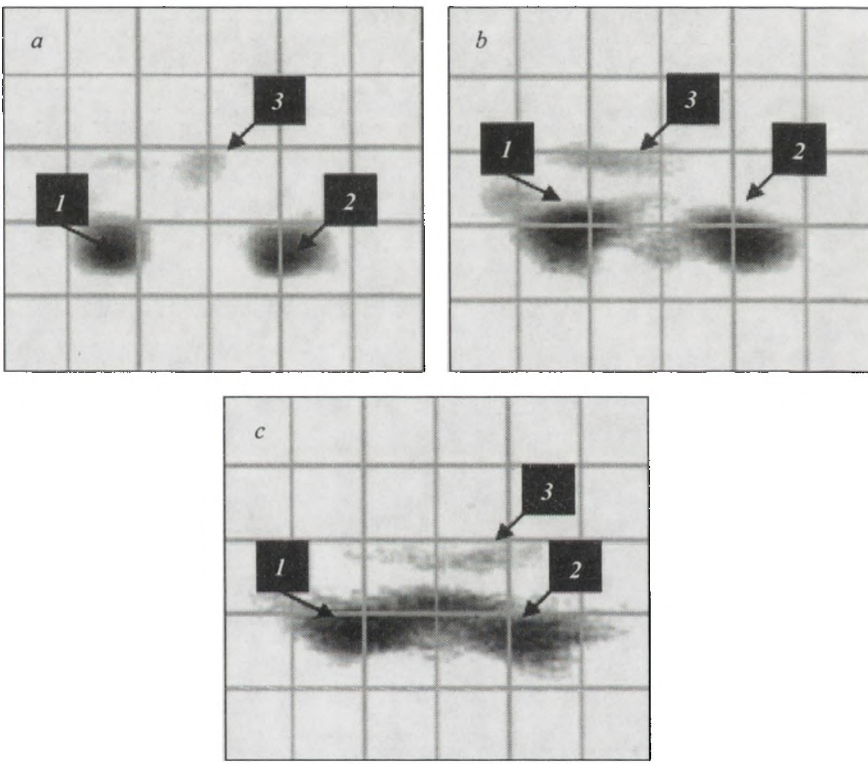

Fig. 2.16. Estimation of degradation of spatial resolution at different distances to the test cylinders, cm: *a* – 90; *b* – 135; *c* – 180.

Practical implementation of the proposed technique for the tomography of building structures is of special interest. A plastered brick wall, which separates two rooms, was chosen for the experiment. The wall is 16 cm thick and gives the appearance of having a smooth surface. Layer-by-layer scanning revealed that the inner structure of the wall is considerably nonuniform (Fig. 2.17).

First, electric circuit wiring was detected hidden under plastering. It shows up in Fig. 2.17*a* as a blurred vertical inhomogeneity with an extended shape. The wiring leads to a socket, which is located at the bottom of a picture. Current flows through the wire. It can be seen that the wiring is laid improperly and does not lie entirely in the same plane considering that it is hidden deeper in the upper part of the wall. Second, the bricklaying is not uniform at all, mortared brick layers are readily visible (Fig. 2.17*b*). Partitions inside the hollow bricks are visible as well.

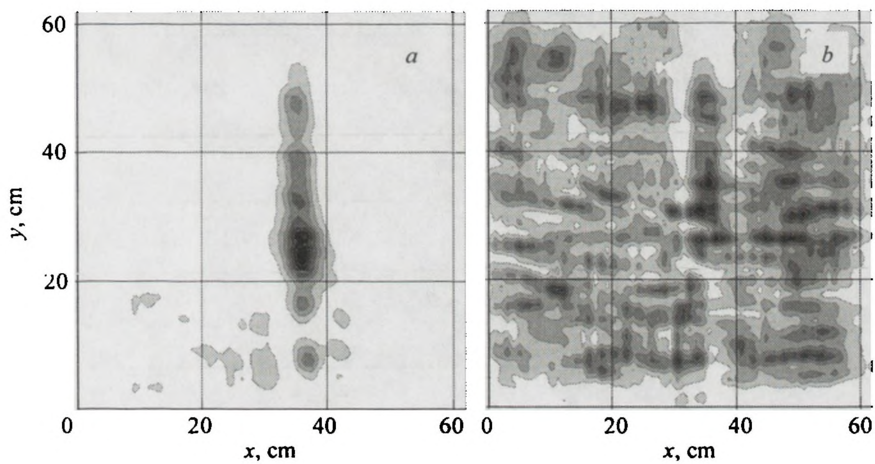

Fig. 2.17. Radiogram of inhomogeneities inside a plastered brick wall that is 16 cm thick: *a* – cross section depth is 2 cm; *b* – cross section depth is 9 cm.

To estimate the resolving power of the radiotomograph, an attempt to visualize a special test inhomogeneity was made. This inhomogeneity consisted of a set of five parallel metallized strips, each of which was 2 cm wide (see the left side of Fig. 2.18). The strips were fastened to the back side of the wall. Traces of the strips are clearly distinguished in the tomogram of the corresponding layer (look at the central part of Fig. 2.18). Inhomogeneities inside the wall act as local prisms which deform (distort) the image in both the vertical and the horizontal direction. This can be seen by looking at strips *4* and *5* in the tomogram which appear to be shifted lower from the set of strips *1–3* by about 1–2 cm. Moreover, strips *4* and *5* are shifted left by 2 cm. The image of strip 5 is nearly out of the vision plane of this layer of the tomogram by 16 cm. It bears noting that surface irregularities of the back side of the wall are visible in the figure as well (see the right-hand side and the upper part of Fig. 2.18).

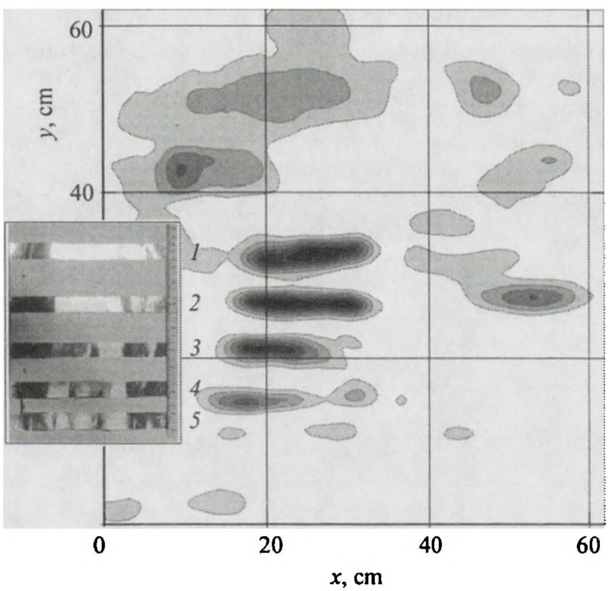

Fig. 2.18. Radio tomogram of metallized strips fastened to the back side of a brick wall with thickness 16 cm.

An experiment with the same metallized strips (Fig. 2.19) in air was performed to estimate the resolving power of the tomograph in a homogeneous medium. As could be expected, the result was impressive (Fig. 2.20). The transverse spatial resolution was at least 2 cm. UWB pulses of 200 ps duration were used for sounding, and the distance from the scanned plane to the strips was 40 cm.

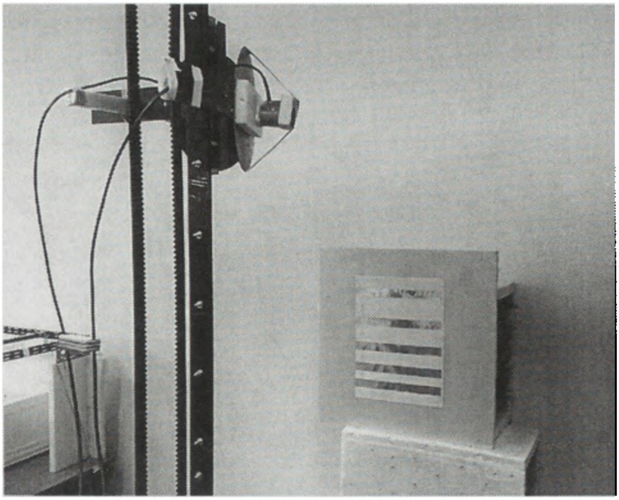

Fig. 2.19. The experimental scene with metallized strips in air.

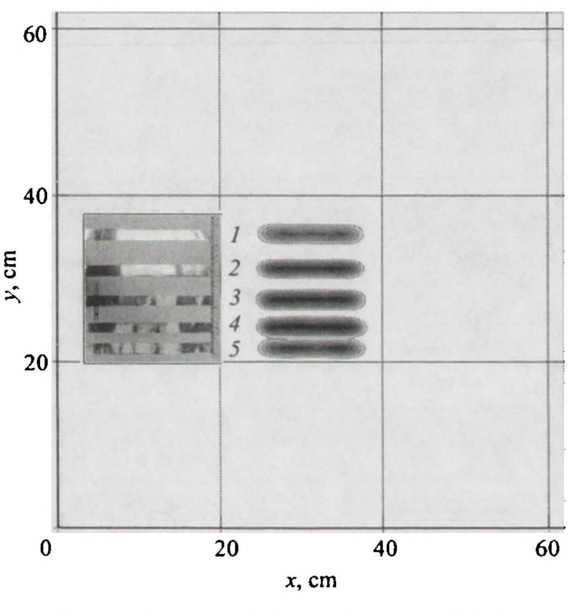

Fig. 2.20. Radio tomogram of metallized strips set in an open space in front of a brick wall.

UWB tomography is especially effective for luggage inspection. A plastic suitcase with a plastic gun and a bottle of water inside it is shown in Fig. 2.21. Figure 2.22 presents the tomography of this scene.

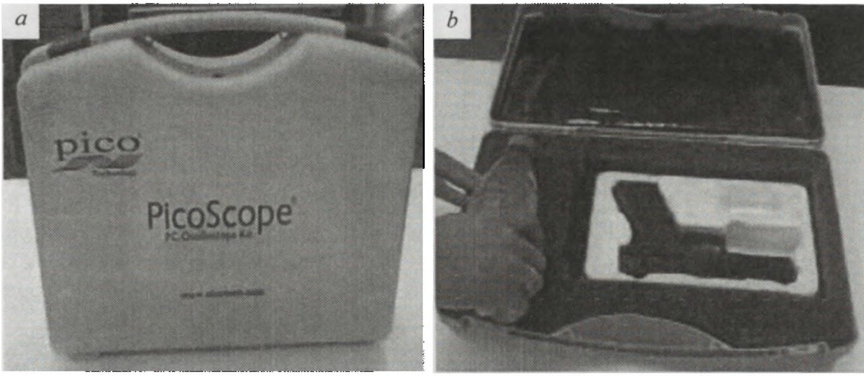

Fig. 2.21. Plastic suitcase (*a*) and case contents (*b*).

Fig. 2.22. UWB tomogram of case contents.

2.3. The results of UWB tomosynthesis of objects in media with metallic inclusions

The experimental setup described above (see Fig. 2.1) was used for tomosynthesis of images of hidden objects in media with metallic inclusions. First off, a wooden carrying box reinforced with metal bands was sounded (Fig. 2.23). The dimensions of the box were 47×41×19 cm.

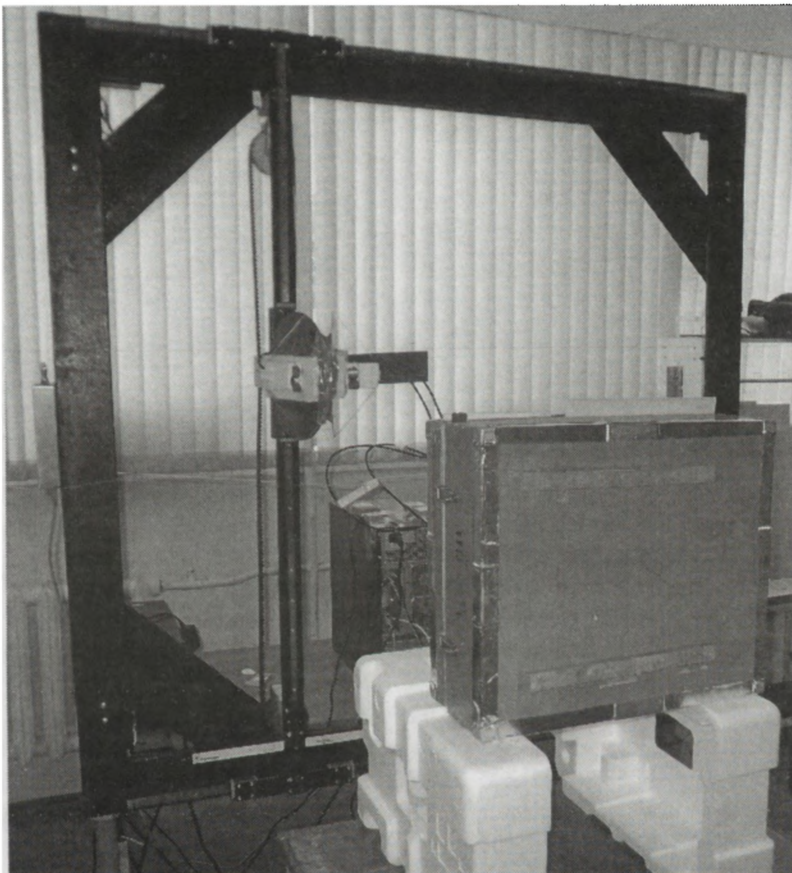

Fig. 2.23. UWB-scanner and carrying box.

A metal-coated stepped triangle was placed in the box. Each step of the triangle was 5 cm in length. There was a 2×2 cm square hole in the center of the triangle (Fig. 2.24).

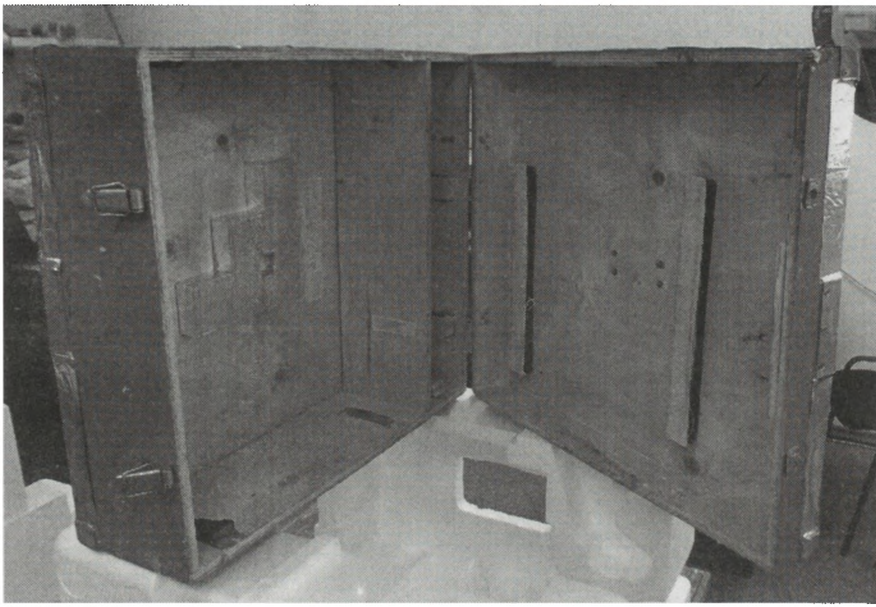

Fig. 2.24. Test object inside the box.

Scanning was performed by moving the transceiver antenna module in the *OXZ* plane with a step of 1 cm. The scanning area had dimensions 60×50 cm. The test object was fastened to the bottom of the box at a range of 39 cm, as shown in Fig. 2.24. Range is reckoned in the *OZ* direction from the transceiver antenna module.

As a result of UWB-scanning and data processing a 3D-tomogram of the contents of the box was obtained (Fig. 2.25). Cross-section (*a*), which corresponds to the upper cover of the box at a range of 18.5 cm, reveals the reinforcing tape along the perimeter of the cover and a metal handle in the center of the cover.

Wooden latches at the back side of the front of the box can be observed in cross-section (*b*), which corresponds to a range of 21.5 cm. Cross-section (*c*) corresponds to a range of 22.5 cm. The same inhomogeneities are visible in it.

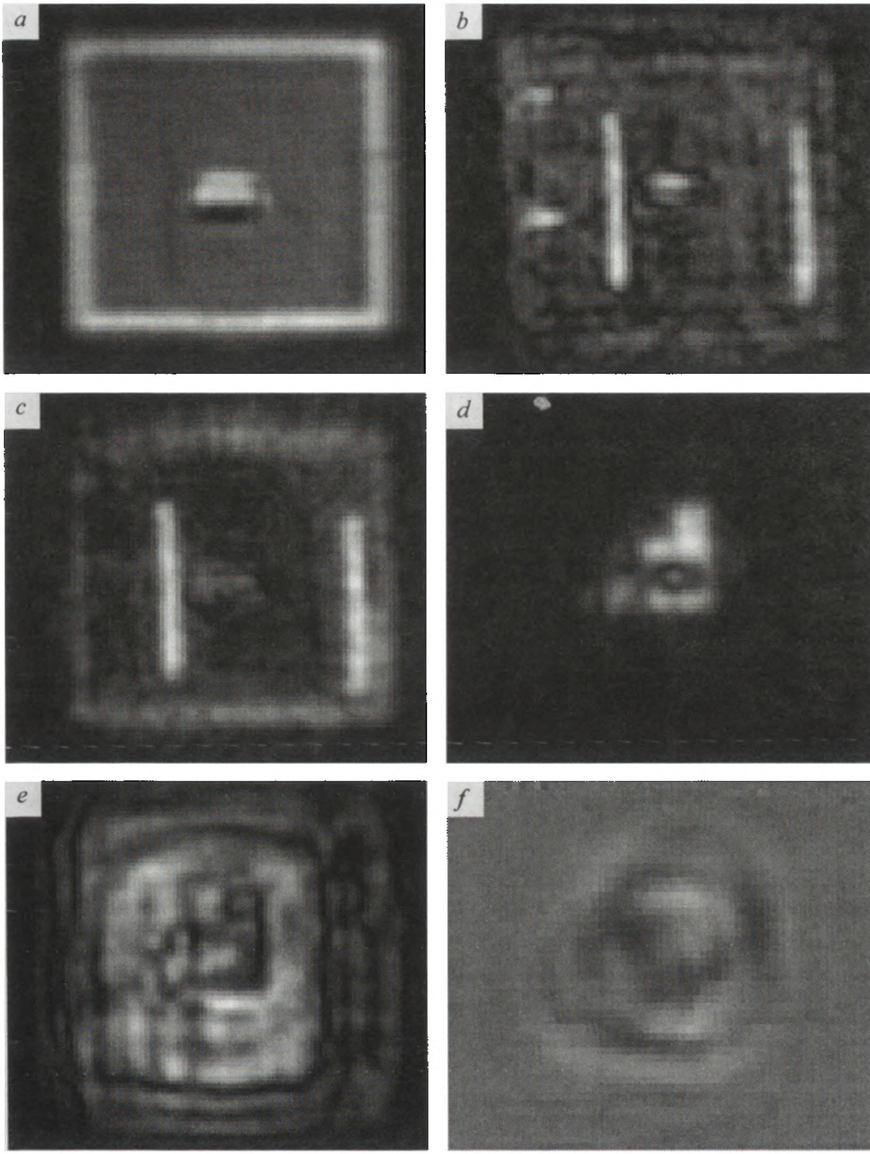

Fig. 2.25. Tomogram of metal-band reinforced wooden box and contents.

The test object, a triangle with a central hole, is visible in cross-section (*d*) corresponding to a range of 39 cm. Cross-section (*e*) at a range of 42 cm corresponds to the back of the box. The back of the box and a radio shadow from the test object are clearly visible in cross-sections (*e*) and (*f*).

A radio shadow appears since the test object is metal-coated and therefore radio opaque.

According to the results of the experiment, it may be concluded that implementation of tomosynthesis algorithms makes it possible to tune out interference caused by echo signals reflected from the reinforcing elements. The obtained tomogram allowed us to determine the depth of the test object with an accuracy better than 0.5 cm and visualize its shape as well.

Next, let us consider experimental results of visualization of an object placed in an open metal container. A metal safe with dimensions 64×48×41 cm was used for this purpose (see Fig. 2.26). The door of the safe was taken off its hinges. Figure 2.27 shows the safe from behind.

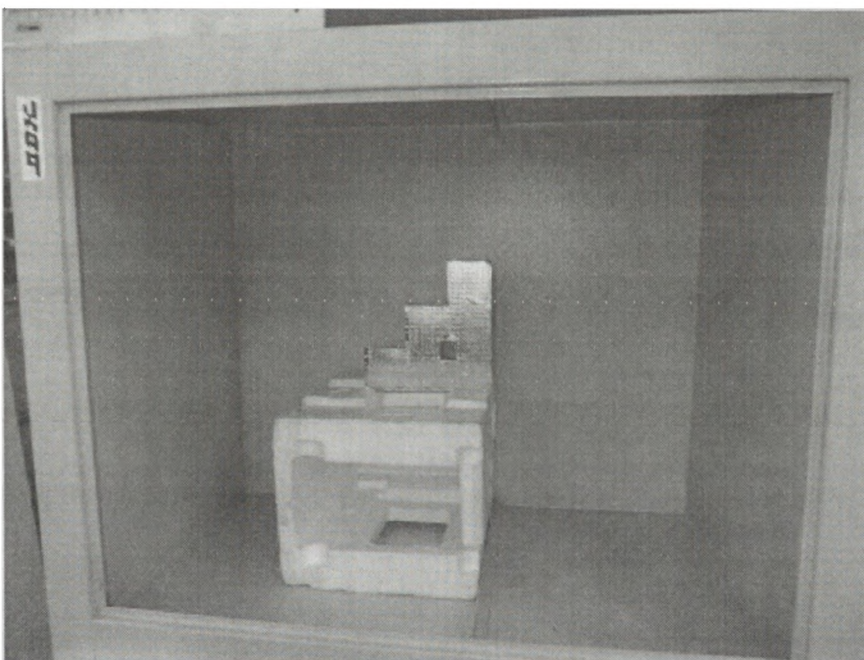

Fig. 2.26. Test object inside the metal safe.

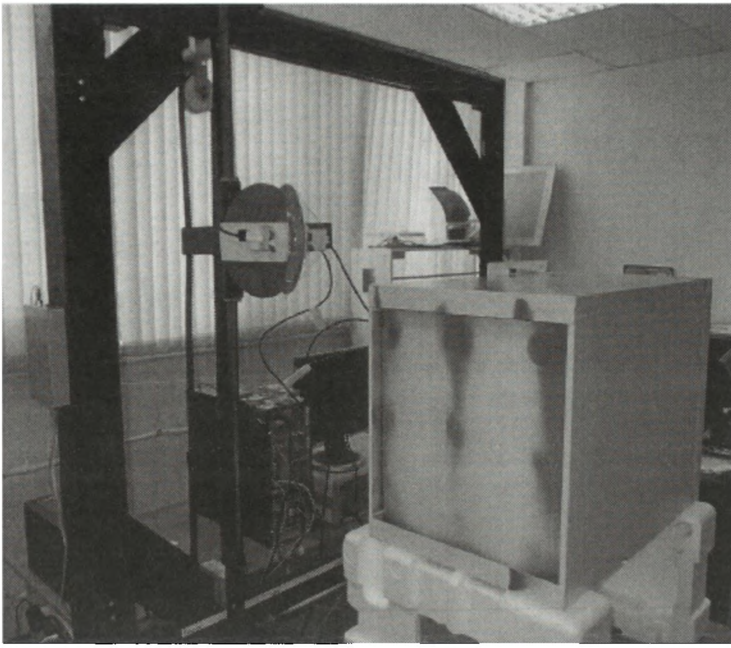

Fig. 2.27. Back view of the safe.

On completion of scanning a tomogram was obtained which showed the distribution of inhomogeneities in the tested space. Radio images of cross-sections at different ranges are presented in Fig. 2.28. Figure 2.28*a* presents a cross-section corresponding to the upper cover of the safe at a range of 18.5 cm. The front frame of the safe stands out distinctly in the tomogram. The cross-section corresponding to a range of 19 cm is shown in Fig. 2.28*b*. This tomogram demonstrates the sunken frame used to hang the door. The cross-section corresponding to a range of 53 cm is shown in Fig. 2.28*c*. In this tomogram the test object with central hole is distinctly visible. The cross-section at a range of 62 cm is shown in Fig. 2.28*d*. This cross-section images the back wall of the safe.

Based on the experimental results, it may be concluded that implementing tomosynthesis algorithms makes it possible to tune out interference caused by echo signals reflected from the walls and bottom of the metal container. The obtained tomogram allows the depth of test object to be determined and the shape of the object to be visualized as well.

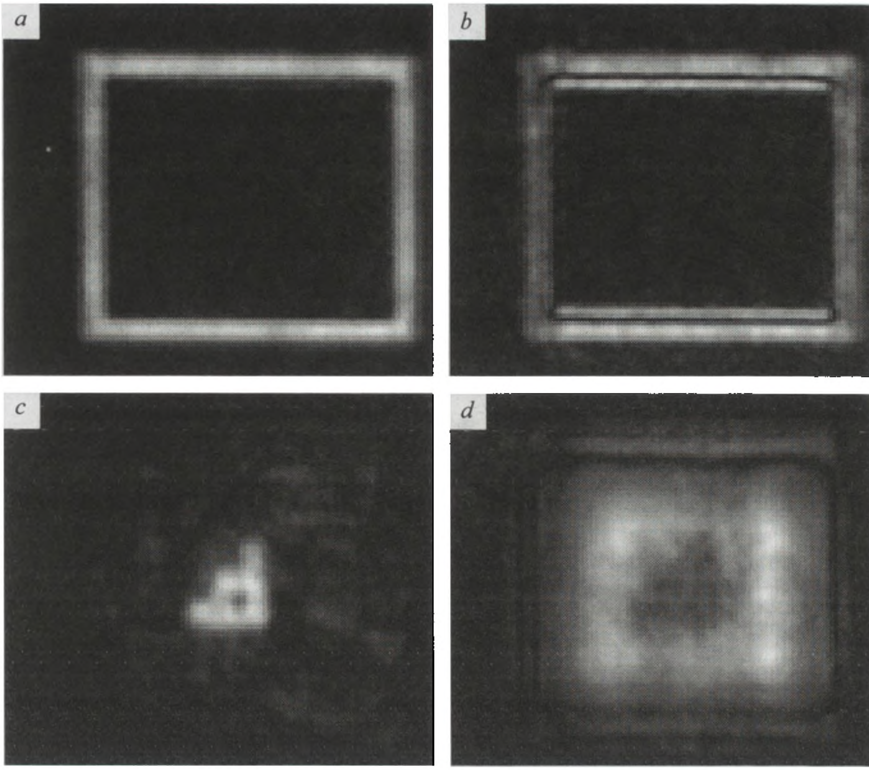

Fig. 2.28. Radio images of sounded area at different distances.

Big trucks inspection in order to prevent the transportation of prohibited articles such as weapons, explosives, etc. is a major problem at access control points (ACPs). There are special-purpose X-rays detectors for that purpose, but it is not possible to equip all of the critical ACPs owing to the high cost of the equipment. A relatively cheaper radio-wave system for detecting and visualizing hidden objects can be implemented to search dump trucks and similar vehicles. It is depicted in Fig. 2.29.

The system is basically a clocked array of UWB-antennas, which are switched by electromechanical switching devices. When a truck moves through this system at low speed, it will be possible to sound the truck body in order to detect hidden objects under the load (soil, sand, etc.) A prototype of this system is shown in Fig. 2.30.

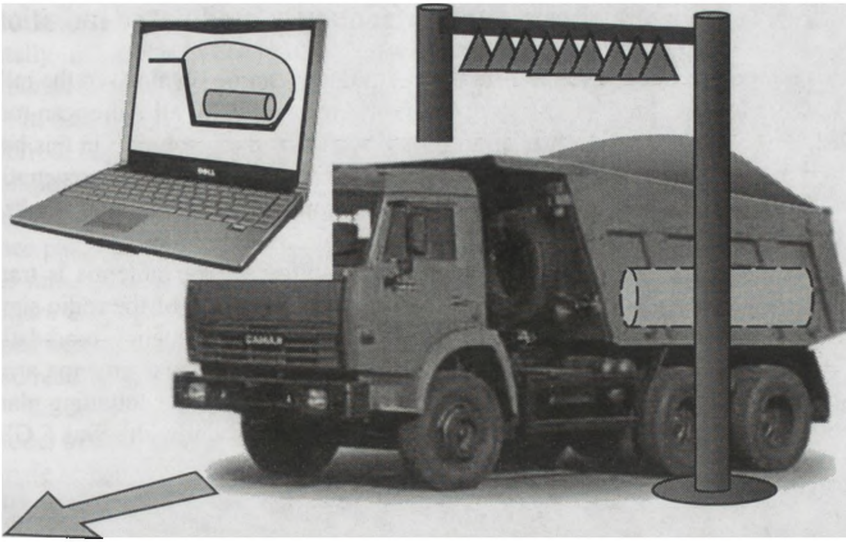

Fig. 2.29. Advanced system for detecting and visualizing hidden objects at ACPs.

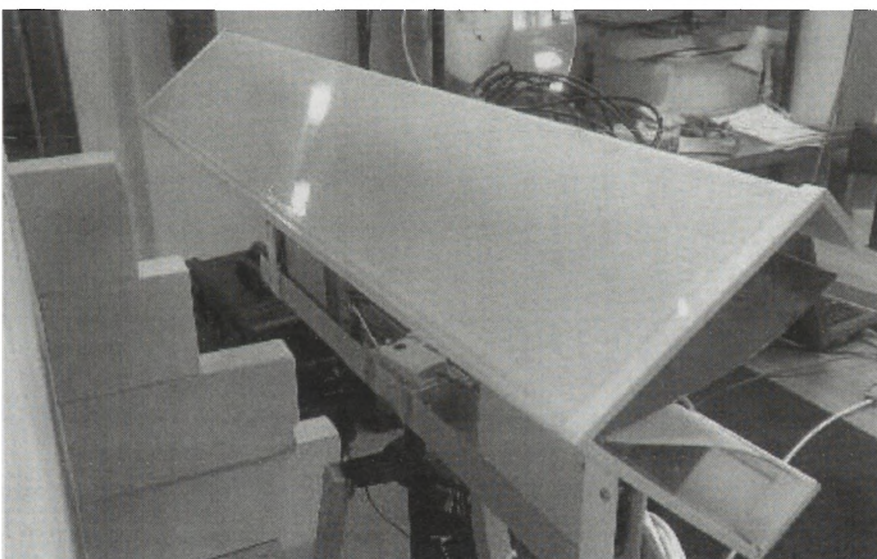

Fig. 2.30. Clocked array of UWB-antennas.

2.4. Tomography using linearly frequency-modulated radiation

The best possible resolution in the radio range can be obtained in the millimeter frequency range. This is the range where practically all American radio scanner prototypes work. It is an important fact that the resolution in this band is usually sufficient to recognize fine details of an object, while the penetration remains on a reasonable level. Let us get down now to experimental results to determine the potential and actual capabilities of this technique.

We consider a sounding scheme where the transceiver antenna is translated in the xOy plane (Fig. 2.31). Emission and reception of the radio signal are frequency-stepped with a fixed step using linear frequency modulation (LFM). This sounding scheme fully simulates using a planar antenna array. The test object was placed at a fixed range (30 cm) from the sounding plane. The central frequency was 94 GHz and the deviation bandwidth was 5 GHz.

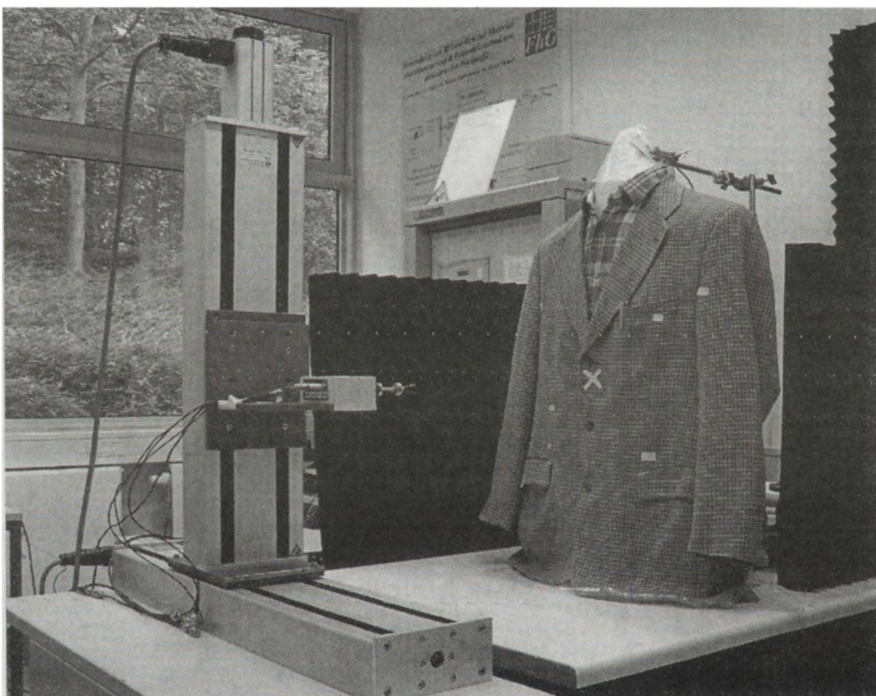

Fig. 2.31. Experimental setup for radar sounding of objects hidden under clothes.

The horn antenna directivity was wide enough to cover the sounding field totally from any sounding point. The experiment was carried out at the Fraunhofer Institute for Nondestructive Testing (IZFP, Germany).

In accordance with expectations, the obtained radio-image was severely blurred. Figure 2.32*a* presents the spatial distribution of one of the quadrature components of the received signal at the moment of maximum contrast. In this particular case a plastic revolver was sounded. A haloing of the interference pattern is clearly visible in the image, which was obtained with a step of 1.5 mm. This confirms the information content of the obtained radio-images. Figure 2.32*b* presents the reconstructed tomogram using the algorithm developed below, together with a photograph of the object, so ignore this for now and read further.

To develop a SAR-based algorithm for data processing, let us turn to a model of the interaction of the waves and the medium inhomogeneities in the single scattering approximation of (see Eq. (1.11))

$$E(\boldsymbol{\rho}_0, f) = k^2 \iiint\limits_V \Delta\varepsilon(\boldsymbol{\rho}_1, z_1) G_0^2(R, f) d^2\boldsymbol{\rho}_1 dz_1,$$

where $G_0(R, f) = \exp\{ikR\}/4\pi R$ is the free-space Green's function for radiation at the frequency f and $k = 2\pi f/c$, $R = \sqrt{(\boldsymbol{\rho}_0 - \boldsymbol{\rho}_1)^2 + z_1^2}$. The quantity $\Delta\varepsilon$ characterizes the distribution of sounded inhomogeneities in the volume V.

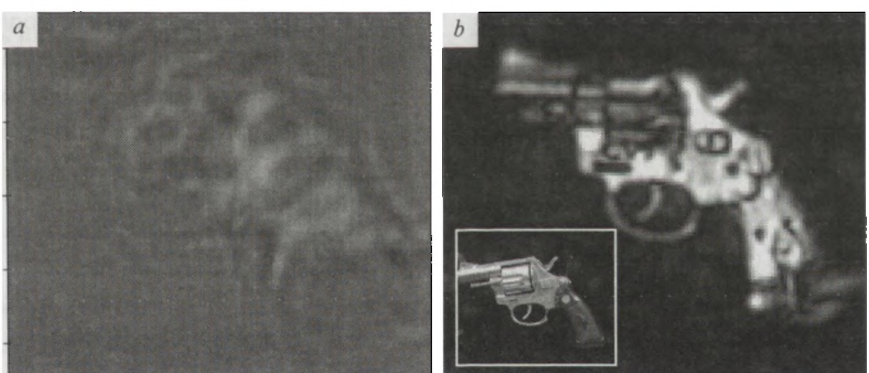

Fig. 2.32. Radiotomography of a hidden revolver: *a*) original radio image, *b*) photograph and reconstructed radio tomogram of the object.

If a narrow-band LFM signal is used

$$S_0(t) = A(t)\exp\{2\pi i(f_0 + \alpha t/2)t\}$$

the mixer output signal for any location point $\boldsymbol{\rho}_0$ is written as

$$S(\boldsymbol{\rho}_0,t) \approx \left(k_0 A(t)\right)^2 \iiint\limits_V \Delta\varepsilon(\boldsymbol{\rho}_1,z_1) G_0^2(R, f_0 + \alpha t) d^2\boldsymbol{\rho}_1 dz_1 .$$

Here $k_0 = 2\pi f_0/c$. If, using the Fourier transform, we now transform to the spectral domain, then we can write

$$S(\boldsymbol{\rho}_0,f) \equiv \int\limits_{-\infty}^{\infty} S(\boldsymbol{\rho}_0,t)\exp\{i2\pi f t\}dt \approx$$

$$\approx k_0^2 \iiint\limits_V \Delta\varepsilon(\boldsymbol{\rho}_1,z_1) \mathrm{G}_0^2(R,f_0)\delta_A(\nu - 2\alpha R/c) d^2\boldsymbol{\rho}_1 dz_1,$$

in the case of a sufficiently wide bandwidth of the sounding signal, where the function

$$\delta_A(f) = \int\limits_{-\infty}^{\infty} A^2(t)\exp\{i2\pi f t\}dt$$

is the *smeared* δ-function in frequency. Thus, a particular range from the source point to the sounding point under the integral will be associated with some specific frequency ν.

We next perform the operation of image focusing in the transverse coordinates of the observation points $\boldsymbol{\rho}_0$, which is performed by successive summation, with wave phase compensation , of the received signals which are scattered by a point with prescribed coordinates $(\boldsymbol{\rho}_F, z_F)$. This operation is performed using two-dimensional convolution in the plane of the equivalent antenna array:

$$S(\boldsymbol{\rho}_F,z_F,f) = \iint\limits_{S_0} S(\boldsymbol{\rho}_0,f)\exp\left\{-2\pi i k_0 2\sqrt{(\boldsymbol{\rho}_0 - \boldsymbol{\rho}_F)^2 + z_F^2}\right\} d^2\rho_0 .$$

Reversing the order of integration, the integral is rewritten as follows:

$$S(\boldsymbol{\rho}_F,z_F,f) = \iiint\limits_V \Delta\varepsilon(\boldsymbol{\rho}_1,z_1) Q(\boldsymbol{\rho}_1,\boldsymbol{\rho}_F,z_1,z_F,f) d^2\boldsymbol{\rho}_1 dz_1 ,$$

where

$$Q(\mathbf{\rho}_1,\mathbf{\rho}_F,z_1,z_F,f)\equiv$$
$$\equiv k_0^2\iint\limits_{S_0} G^2(R,f_0)\delta_A(f-2\alpha R/c)\exp\left\{-2\pi i k_0 2\sqrt{(\mathbf{\rho}_0-\mathbf{\rho}_F)^2+z_F^2}\right\}d^2\mathbf{\rho}_0.$$

Calculations show that for a sufficiently large observation area and the frequency assigned as $f=f_F\equiv 2\alpha z_F/c$, this function will be homogeneous in its arguments, so that

$$Q(\mathbf{\rho}_1,\mathbf{\rho}_F,z_1,z_F,f_F)\approx Q_\perp(\mathbf{\rho}_1-\mathbf{\rho}_F,z_F)\delta_A(z_1-z_F).$$

The following notation was introduced

$$Q_\perp(\mathbf{\rho}_1-\mathbf{\rho}_F,z_F)\equiv k_0^2\iint\limits_{S_0} G^2(R_F,f_0)\exp\left\{-2\pi i k_0 2\sqrt{(\mathbf{\rho}_0-\mathbf{\rho}_F)^2+z_F^2}\right\}d^2\mathbf{\rho}_0,$$

$$R_F=\sqrt{(\mathbf{\rho}_0-\mathbf{\rho}_1)^2+z_F^2}.$$

As a result, we can write

$$S(\mathbf{\rho}_F,z_F,f_F)=\iint\Delta\varepsilon(\mathbf{\rho}_1,z_F)Q_\perp(\mathbf{\rho}_1-\mathbf{\rho}_F,z_F)d^2\rho_1.$$

The kernel of this integral is localized so that we can write approximately

$$\Delta\varepsilon(\mathbf{\rho}_F,z_F)\approx S(\mathbf{\rho}_F,z_F,f_F)/q(z_F),\quad q(z_F)=\iint Q_\perp(\mathbf{\rho}_1,z_F)d^2\rho_1.$$

In fact, this representation delivers the solution of the inverse problem. It is in full conformity with SAR technology.

To provide a step-by-step demonstration of the feasibility of this method, we carried out a numerical simulation of LFM-sounding of a scene consisting of three point scatterers. Figure 2.33*a* schematically depicts their locations. The simulation was performed for the case in which $f_0=94$ GHz, $\alpha=1.2\cdot10^{13}$ s^{-2}, and the measurement time is 5.1 ms. The result of numerical simulation of the real part of $S(\mathbf{\rho}_0,t)$ is shown in Fig. 2.33*b*.

Figure 2.34 presents a gray-scale plot of the real part (cosine quadrature) of the function $S(\mathbf{\rho}_0,t)$, obtained by taking the Fourier time transform (*a*), and the final tomogram of the test scene (*b*). It can be seen that the spatial resolution in depth is markedly poorer than the transverse resolution. An identical result was obtained by processing real experimental data for three metal rods.

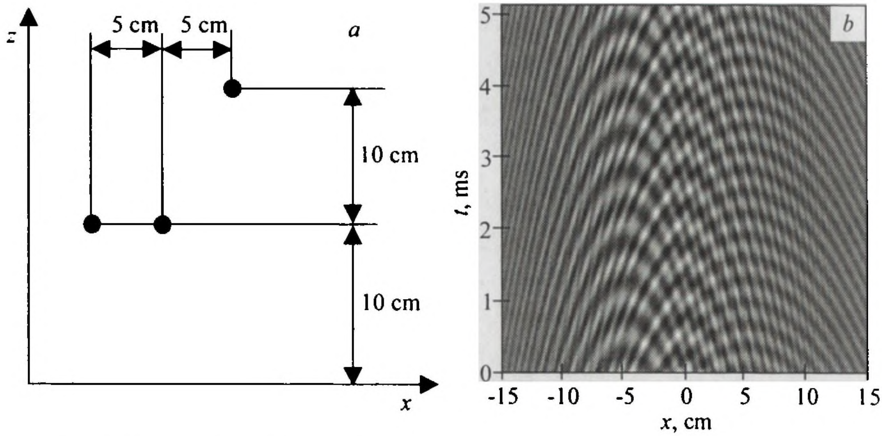

Fig. 2.33. Location of three point scatterers (*a*) and their initial radio-image (*b*).

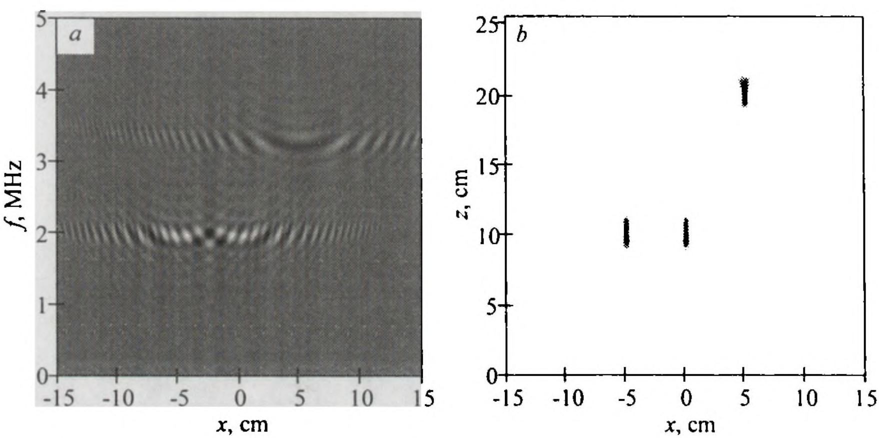

Fig. 2.34. Source image spectrum of test objects (*a*) and its radiotomogram (*b*).

The result of applying the proposed algorithm to actual experimental data with a plastic toy revolver is displayed in Fig. 2.32*b*. It can be seen that a resolution on the order of 2–3 mm has been achieved, which is sufficient for detailed detection of the revolver. Similar results were obtained with a ceramic knife and other objects.

Thus, numerical simulation results confirm the feasibility of the proposed technique for reconstructing the distribution of medium inhomogeneities by implementing an LFM-signal. The developed algorithm is encoded as the application RADIO IMAGE in C++ with a user-friendly interface. It is currently in use for interactive data processing at the Fraunhofer Institute for Nondestructive Testing (IZFP, Germany). Thanks to algorithms based on the fast Fourier transform (FFT), the total image processing time does not exceed 30 s.

2.5. Summary

The experimental research described above demonstrates the prospects of the techniques proposed in Chapter 1 for radio-wave tomography of the internal structure of hidden semi-transparent objects and the external form of opaque objects as well.

The unified technology lying at the basis of these techniques, itself based on synthesis of the focusing effect in the spectral domain and the time domain, has been confirmed by numerous practical examples. Especially worthy of note is the use of UWB radiation.

The design elements and modeling setups proposed in this chapter can be considered as prototypes for development of commercial systems of radio vision. Use of the step-scan technique allowed us to reveal the potential and actual capabilities –and estimate the limits – of radio tomography to obtain maximum spatial resolution.

Chapter 3

TRANSMISSION TOMOGRAPHY

Transmission radio-tomography is tomography that is concerned with end-to-end scanning of the test area. A particular case of this tomography is shadow projection tomography and the Fourier synthesis method described in Section 1.1. As noted above, in contrast to X-ray and NMR-tomography the wave projections that arise here cannot be considered as purely shadow projections. Wave diffraction and interference, as well as multiple wave interactions, are nearly always important for radio-waves. Using the double focusing method, which is described in Section 1.2, makes it possible to reduce the influence of multiple interactions, but not completely. Such phenomena as diffraction and interference cannot be described solely within the framework of single interactions; and this fact must be taken into account in any effort to invert wave projections and solve the tomography problem, at least in any description of the dominant effects. As will be shown below, ray-optical phenomena such as an increase in the phase taper (eikonal) of partial waves must be taken into account when scanning semitransparent objects and media, and that means multiple interactions, but on individual rays. So as not to complicate the problem, we immediately point out that we have in mind here the so-called phase approximation of the Huygens–Kirchhoff method, which is, in our opinion, the most efficient and simple approach in the transmission wave tomography of semitransparent media. Chapter 3 integrates the results of papers [1–6]. The approximation of the physical theory of diffraction suffices to describe the transmission tomography of the shapes of opaque objects. This will be discussed in Chapter 4.

Let us start from a description of experimental setup for transmission tomography and primary data processing.

3.1. Experimental Setup

The setup provides direct focusing as well as inverse focusing at the hardware level. The basic optical circuit and a photograph showing the external appearance of the transmission tomography setup are shown in Fig. 3.1. The current system makes it possible to measure the complex transmission coefficient of the wave channel. Measurements of the amplitude and the phase of the radiation penetrating the object were performed using a P4–36 panoramic transmission coefficient meter. This meter is outlined by the dashed rectangle in Fig. 3.1*a*.

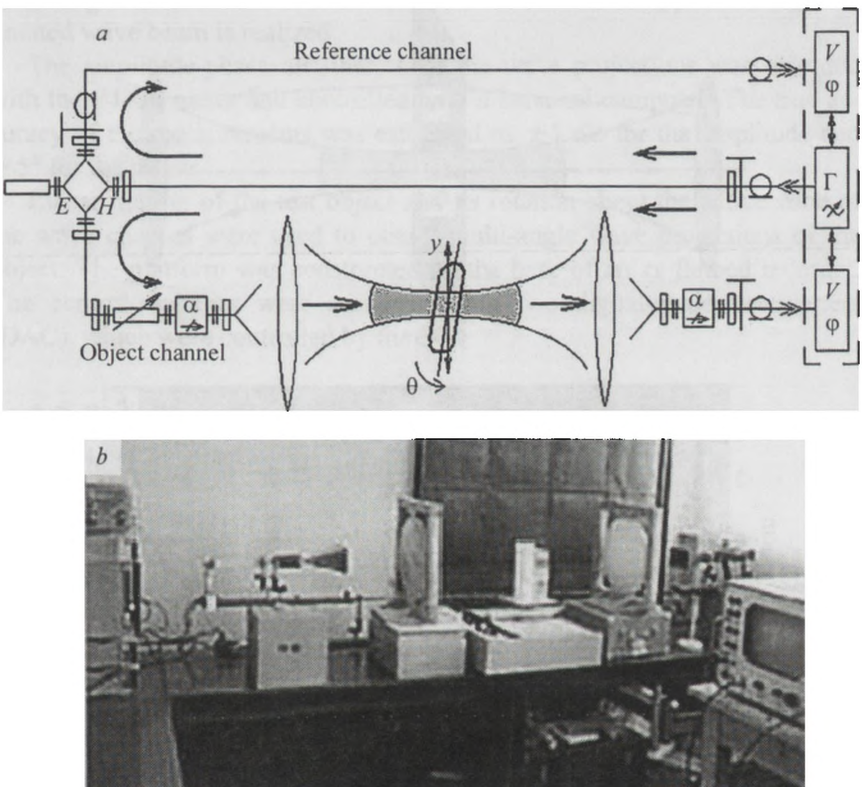

Fig. 3.1. Basic optical circuit (*a*) and photograph (*b*) of the transmission tomography setup.

To improve the accuracy of measurement of the phase values of the recorded field (i.e., of the scanned area), a reference channel and an information channel are included in the circuit. The setup operates in the range 8–12 GHz with mid-frequency 10GHz. Vertical wave polarization was applied.

The radiation was focused with two lenses made of plaster. Each lens is 32 cm in diameter, and the focal distance is 16 cm. The focusing system and amplitude-phase distribution of the field in the focusing area are depicted in Fig. 3.2. The point of combined focusing of both lenses is denoted as $\mathbf{r}_F$.

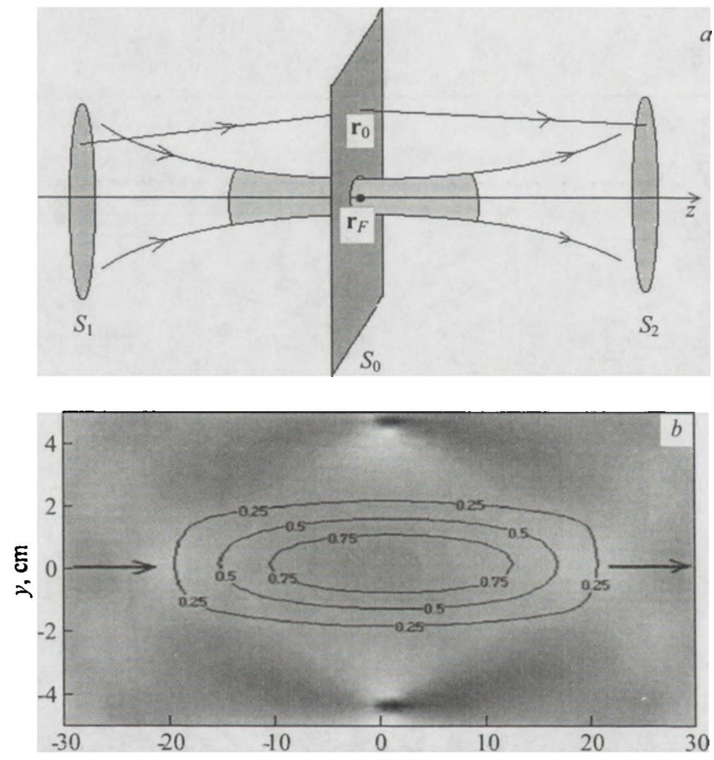

Fig. 3.2. Focusing system (*a*) and computed amplitude-phase distribution of the field in the focusing area (*b*).

The region of localization of focusing has the shape of a solid of revolution 3 cm in diameter and 30 cm in length. Figure 3.2*b* depicts the distribution of the calculated values of the phase and amplitude of the focusing field in the case when the transmitting and receiving apertures are separated by 90 cm. Intensity contours, which define the active zone of the wave channel, are displayed in the middle of the figure. The active zone, which is important for propagation of radiation, is the region of maximum interaction of the field with the propagation medium. Of course, this is true for relatively weak interactions. The distribution of phase values is represented in gray-scale. The field in the focusing region has approximately a planar phase front and small phase shifts across the wave channel. In other words, an approximately collimated wave beam is realized.

The amplitude-phase distribution of the wave projections was recorded with the P4–36 meter and controlled with a personal computer. The true accuracy of the measurements was estimated as $\pm$ 1 dB for the amplitude and $\pm$ 5° for the phase.

Linear motion of the test object and its rotation about the active zone of the wave channel were used to obtain multi-angle wave projections of the object. The platform was constructed on the base of an *xy* flatbed recorder. The control voltages were assigned using two digital-analog converters (DAC), which were controlled by the PC.

3.2. Tomography of semitransparent objects in the phase approximation of the Huygens – Kirchhoff method

Tomographic scanning of an inhomogeneous test scene was performed by means of the setup described above. The test scene consisted of two semitransparent figures – two cylinders, one of circular cross section and the other, of square cross section, filled with polystyrene beads.

Full-angle images of the distribution of the amplitude attenuation and phase disturbance of the wave field are displayed in Fig. 3.3. Variation of the measured values are displayed in gray scale. The areas that are darker gray correspond to more intense amplitude attenuation and greater phase disturbance, respectively. The axial symmetry of two figures reflects the double redundancy of the obtained projections because rotation of the object by 180° should not change these projections. The observed differences of opposite projections indicate a good level of measurement accuracy. The differences can be averaged during processing.

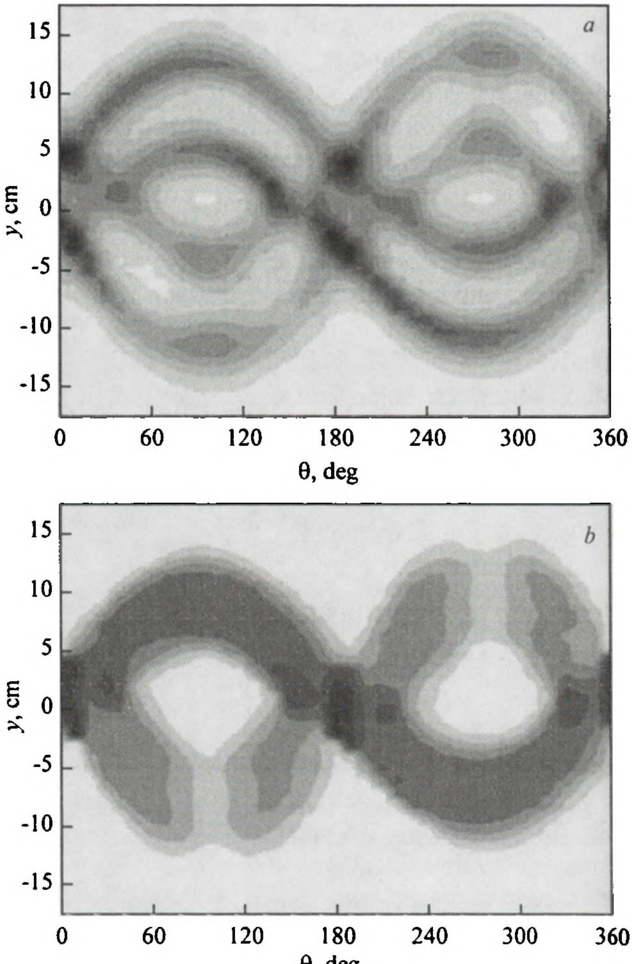

Fig. 3.3. Full-angle images of the distribution of amplitude attenuation (*a*) and phase disturbance (*b*) of the wave field when the test scene is scanned.

The shape of the scanned objects is depicted in Fig. 3.4*a*. It should be noticed that an abrupt (nonmonotonic) attenuation of the amplitude of the transmitted radiation is observed when a focused ray is transmitted through the side boundaries of the object, and then the amplitude increases. This is shown in Fig. 3.3*b* and can be explained by the ray refraction effect at the side boundaries. Everything varies monotonously in the phase image – ray transmission through the side boundary does not cause nonmonotonic changes in the phase (Fig. 3.3*b*). Note the smaller phase disturbance due to the rectangular cylinder in contrast to the circular cylinder. A distinctive characteristic here is the horseshoe-shaped gaps in the images, which is explained by passage of the focused ray through the space between the cylinders.

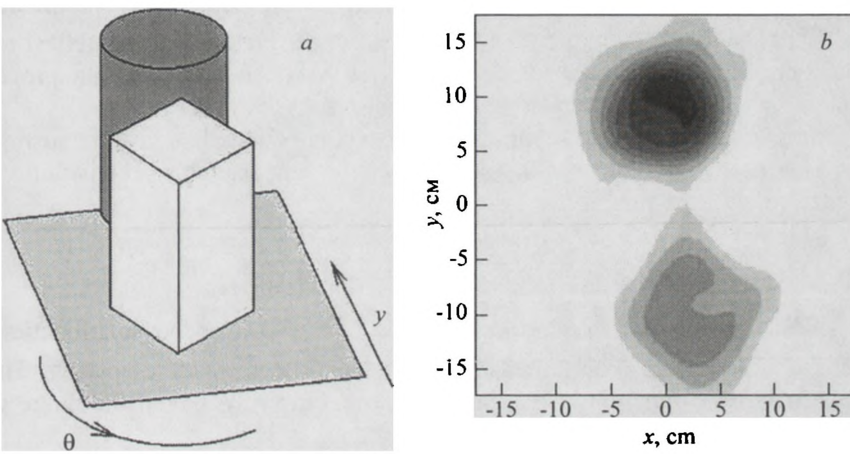

Fig. 3.4. Shape of test scene objects (*a*) and reconstructed tomogram (*b*).

One way or another, the obtained wave projections (Fig. 3.3) do not resemble to the shapes of the test objects (Fig. 3.4*a*). For adequate reconstruction of the tomogram, dominant effects of the interaction of radiation with the propagation medium must be taken into account. Let us consider an analytical model of wave projections.

If the source of the sounding wave is a point source, then we can write for the field in the observation plane S_2 (see Fig. 3.2*a*)

$$E(\mathbf{r}_2,\mathbf{r}_1)=2\iint_{S_0} G_0(\mathbf{r}_{s0}-\mathbf{r}_1)\frac{dG_0(\mathbf{r}_2-\mathbf{r}_{s0})}{dn}dS_0 .$$

The phase approximation of the Huygens–Kirchhoff method (PAHKM) is founded on the physical assumption that the main contribution to the radiation disturbance transmitted through an object comes from phase differences in medium. It is assumed that these differences can be described in the geometrical optics approximation so that the wave projection of the medium inhomogeneities can be written as

$$E(\mathbf{r}_2,\mathbf{r}_1)=2\iint_{S_0} G_0(\mathbf{r}_{s0}-\mathbf{r}_1)\frac{dG_0(\mathbf{r}_2-\mathbf{r}_{s0})}{dn}\exp\left\{ik\int \Delta n(x')dx'\right\}dS_0,$$

where the integration in the exponential factor is performed along the line $\mathbf{r}_2-\mathbf{r}_{s0}$, and Δn is the disturbance of the refraction index relative to the homogeneous background medium. Numerous experimental and theoretical results confirm the considerable capabilities of PAHKM to describe the propagation of short waves in inhomogeneous media.

Implementing double (counter) lens focusing of radiation at the transmitting and receiving ends of the sounding trace reduces to two convolutions with the focusing functions

$$W_1(\mathbf{r}_F,\mathbf{r}_1)=\frac{4}{i}\frac{dG_*(\mathbf{r}_F-\mathbf{r}_1)}{dn} \text{ and } W_2(\mathbf{r}_F,\mathbf{r}_s)=\frac{2}{i}G_*(\mathbf{r}_F-\mathbf{r}_2).$$

The focusing point $\mathbf{r}_F$ lies in the plane S_0. The role of focusing functions in the experiments is provided by lenses which were made of plaster. The *smeared-out* δ-functions appearing here (see Eq. (1.8)) bound the range of integration in the transverse direction, and thus

$$U(y,\theta)\equiv\iint_{S_1}\iint_{S_2} E(\mathbf{r}_2,\mathbf{r}_1)W_1(\mathbf{r}_F,\mathbf{r}_1)W_2(\mathbf{r}_F,\mathbf{r}_2)dS_1dS_1\approx$$
$$\approx\exp\left\{ik\int\Delta n(x')dx'\right\}. \tag{3.1}$$

This result delivers the solution to the problem of wave transmission tomography. It now suffices to extract the eikonal in the obtained result

$$f(y,\theta)\equiv\int\Delta n(x')dx'=\frac{1}{k}\arg(U(y,\theta));$$

the problem then reduces to the canonical problem of Fourier synthesis discussed in Section 1.1.

Figure 3.4*b* presents the result of processing of experimental data which were processed in this way. As can be seen, the obtained results are in good agreement with the shape and geometrical dimensions of the sounded objects. For a central wavelength of 3 cm, the resolution of object details is estimated to be about 1 cm.

3.3. Summary

Transmission radio-wave tomography is a direct development of X-ray and NMR-tomography, but, in contrast to these methods, it takes account of the wave nature of radiation, which is manifested in multiple diffraction and interference interactions.

It has been shown that double counter focusing provides effective localization of the interaction of radiation with matter, and reduces the impact of multiple interactions. It has been established that phase relations are of particular importance here, and that the phase approximation of the Huygens–Kirchhoff method provides an efficient means with which to describe them. It has been demonstrated that obtaining the phase portrait of the wave projections in this approximation reduces the inverse problem to shadow projection tomography.

All of the results presented in this chapter have been validated with numerical simulations and confirmed experimentally.

Chapter 4

RADIO-TOMOGRAPHY OF OPAQUE OBJECTS

When sounding radiopaque objects, the radiation does not penetrate them, so the main information provided consists in their shapes. Of course, surface reflectivity is also an important factor, but the recovery of object shapes provides far more information about the object. This information is essential, e.g., for identification of hidden objects, and for estimation of their integrity and dynamics. All metallic objects and living beings come under the heading of such objects. The water content of dielectric objects renders them opaque. Object in radio-location (radio-detection) makes it possible to specify type of aircraft, its purpose and weapon systems, and also to detect underground cables and other underground structures. The range of possible applications is extremely wide. Chapter 4 summarizes working results of papers [1–7].

4.1. Transmission tomography of the shape of opaque object

Let us start out with transmission tomography. In transmission scanning of radiopaque objects the radiation is presented as a diffraction field. This problem is approximately described by the method of physical diffraction theory, according to which the diffraction field is evaluated as (see Eq. (1.11))

$$E(\mathbf{r}) = 2 \iint\limits_{S_{\text{out}}} E_0(\mathbf{r}_s) \frac{dG_0(\mathbf{r}-\mathbf{r}_s)}{dn} dS \, .$$

The integral is taken here over the illuminated part of the surface S_{out}, which is perpendicular to the direction of sounding of the primary wave $E_0(\mathbf{r}_s)$ (Fig. 4.1). According to Babinet's principle, this same field can be represented as $E(\mathbf{r}) = E_0(\mathbf{r}) + E_1(\mathbf{r})$, where the integral

$$E_1(\mathbf{r}) \equiv -2\iint\limits_{S_{in}} E_0(\mathbf{r}_s)\frac{dG_0(\mathbf{r}-\mathbf{r}_s)}{dn}dS =$$

$$= -2\int\limits_{-\infty}^{\infty}\int\limits_{-\infty}^{\infty} F(\mathbf{r}_s)E_0(\mathbf{r}_s)\frac{dG_0(\mathbf{r}-\mathbf{r}_s)}{dn}dS \qquad (4.1)$$

is the secondary field (response field) produced by the opaque object. The function $F(\mathbf{r}_s)$ bounds the integration area lying inside the terminator plane created by the primary wave $E_0(\mathbf{r}_s)$. In other words, $F(\mathbf{r}_s) = 1$ inside the terminator, and $= 0$ outside of it.

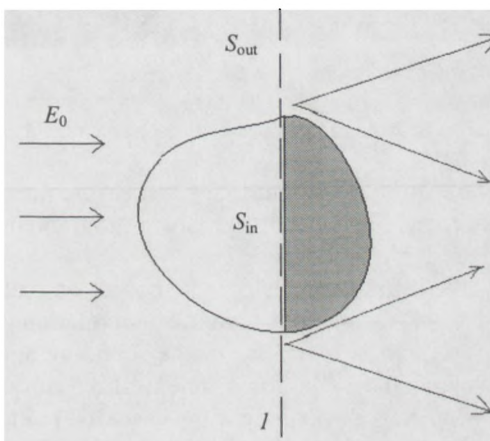

Fig. 4.1. Wave scattering on an opaque object:
1 – terminator plane.

All possible terminators create a set of shadow projections, whose inversion is possible by means of the Fourier synthesis technique described in Section 1.1. The characteristic function of the terminator $F(\mathbf{r}_s)$ can be reconstructed by the method of radio-wave tomosynthesis described in Section 1.3. The inverse focusing method (Section 1.4.1) is an equivalent technique for reconstructing the characteristic function of an object.

The following modeling experiment (Fig. 4.2) was performed to illustrate the proposed approach. An opaque object was placed on a turntable *3*.

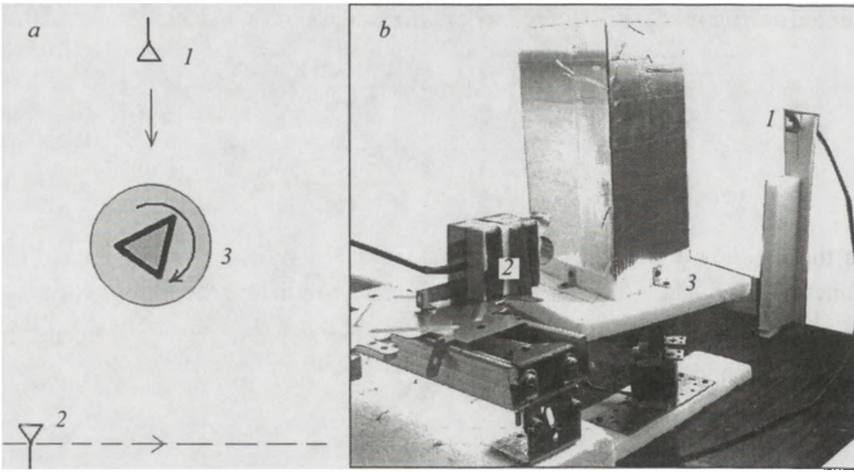

Fig. 4.2. Scheme (*a*) and photograph (*b*) of experimental setup for transmission tomography of an opaque object.

This makes it possible to perform multi-angle measurements of the diffraction field. The object was illuminated by transmitting antenna *2*, which was moved behind the object along a straight line.

Simulation of the diffraction field was based on calculation of the Kirchhoff integral (4.1). The result of numerical simulation of the diffraction field in the scalar approximation for one of the sounding angles is presented in Fig. 4.3. Here the spatial distribution of one of the quadratures of the field for a frequency of 18 GHz is displayed for the case of a point source which is 50 cm distant from the center of the simulation area. Shadow and penumbral areas are clearly seen. A similar picture is obtained for other sounding angles as well.

Data obtained by numerical simulation of the field along the line segment $y = 25$ cm were treated as measurement data. The object was rotated by 360° with a step of 360°/64. Thus, 64 measurements were simulated at different sounding angles.

The inverse problem – the problem of tomography – was solved by the inverse focusing technique described in Chapter 1. If $E(x,\varphi)$ is the complex amplitude of the diffraction field behind the object at different coordinate values of the sampling point (x) within the interval L for different angles of

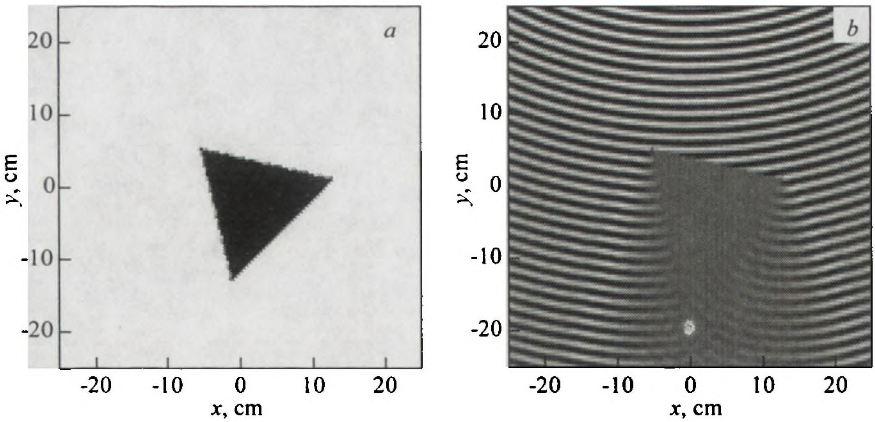

Fig. 4.3. Cross section of opaque triangular cylinder (*a*) and its (calculated) diffraction field (*b*).

rotation of the object (φ) relative to the measurement system, then the problem reduces to finding the integral

$$U(x_F, y_F) = \int_{-\pi}^{\pi} d\varphi \int_{L} dx M(x_F, y_F; x, \varphi) E(x, \varphi) . \tag{4.2}$$

The focusing function is defined as

$$M(x_F, y_F; x, \varphi) =$$
$$= \exp\left\{ -ik\left(\sqrt{(x_F - X)^2 + (y_F - Y)^2} + \sqrt{(x_F - x_0)^2 + (y_F - y_0)^2}\right)\right\},$$

$$X \equiv R\sin\varphi + x\cos\varphi \,, \; Y \equiv -R\cos\varphi + x\sin\varphi \,,$$

$$x_0 = -R_0 \sin\phi \,, \; y_0 = R_0 \cos\phi \,,$$

where R and R_0 are the distances from the scanning line L and from the radiation source to the center of rotation, and (x_0, y_0) are the coordinates of the radiation point. The coordinates of the focusing point are reckoned with respect to the stationary object (Fig. 4.4).

Reconstruction of the shape of a test object in the form of a triangular cylinder was simulated. Results are presented in Fig. 4.5. It can be seen that the angular areas of the test object are quite sharp, but the faces of the object

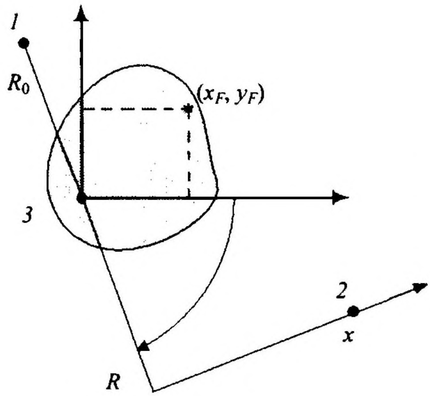

Fig. 4.4. Coordinate system.

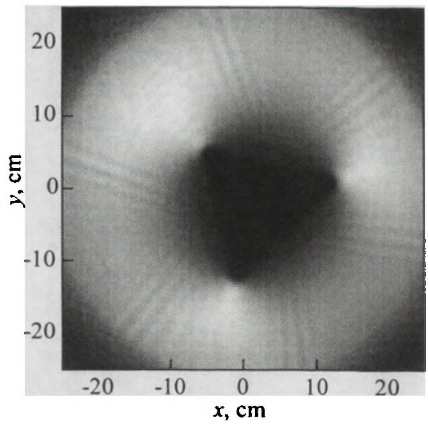

Fig. 4.5. Tomogram of test object (calculation).

are slightly blurred. This latter result is caused by the fact that the faces fall in the shadow or penumbra area in most transmission projections. It should also be noted that this method does not allow visualization of objects that have concavities, because the concave areas always fall in the shadow area.

The numerical simulation results were completely confirmed by experiment. The experiment was performed according to the scheme depicted in Fig. 4.2*a*. The experimental setup included: a fixed radiating antenna 1, a mobile receiving antenna 2, and a turntable 3 on which the test object was placed. The turntable was mounted to the line scanner and could be moved in a straight line. The range of motion of the receiving antenna was $L = 60$ cm, the distance from the center of rotation of the object to the line of antenna movement was $R = 23$ cm, and the signal frequency was 18 GHz. The widths of the sides of the triangular cylinder (side lengths of its triangular face) were 195, 185, and 155 mm. UWB antennas described in Section 2.1 were used as the receiving and transmitting antennas. The object was rotated on the turntable in the angular range from 0° to 180° in 32 positions. The shadow image (tomogram) of the object displayed in Fig. 4.6 was reconstructed by processing the measured field using formula (4.2).

It can be seen that the shape of the object was reconstructed, however with some distortions which are associated with measurement noise and the finite value of the wavelength ($\lambda = 1.7$ cm). Increasing the frequency (decreasing the wavelength) of the sounding radiation should increase the resolution of the image of the object and thereby present its shape more clearly. This can be checked most easily with ultrasound. Ultrasonic transceiver sensors operating at a frequency of 40 kHz are widely available. Noting that the speed of ultrasound in air is $v = 330$ m/s, we obtain the value $\lambda = v/f = 8.25$ mm for the wavelength. We decreased the wavelength by about a factor of two. The experimental setup used was the same, but we shortened the scanning interval to $L = 37.5$ cm.

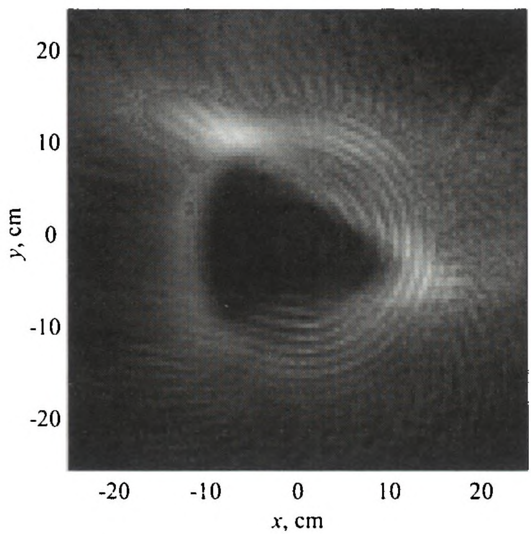

Fig. 4.6. Reconstructed tomogram of triangular cylinder.

Results of measurements of one of the quadratures of the wave projection for the triangular cylinder are presented in Fig. 4.7, and results of reconstruction of its shape are shown in Fig. 4.8. It can be seen that the spatial resolution has been substantially improved even though the scanning interval was shortened somewhat.

The experiment with ultrasonic transmission tomography was repeated with two test objects of different shapes: a square cylinder with a side length of 57 mm and a round cylinder 28 mm in diameter. Corresponding results are presented in Figs. 4.9 and 4.10. It can be seen that the objects differ from each other, the object separation is about 7 cm, and one object is twice as large as the other one. However, the shape of the square cylinder is hardly discernible, and the spatial resolution achieved is no better than 3 cm. Arguably, it can be said that the method of shadow transmission wave projections is not efficient at reconstructing the shapes of objects that produce self-shadowing and mutual-shadowing effects.

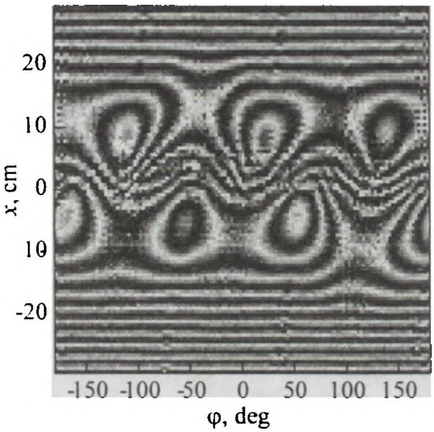

Fig. 4.7. Measurement results for wave projection of triangular cylinder

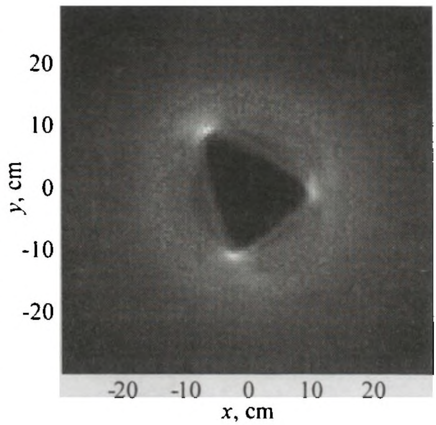

Fig. 4.8. Ultrasonic tomogram of triangular cylinder

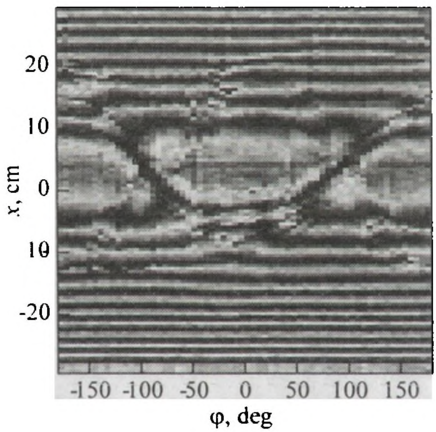

Fig. 4.9. Measurement results for wave projection of a square and a round cylinder.

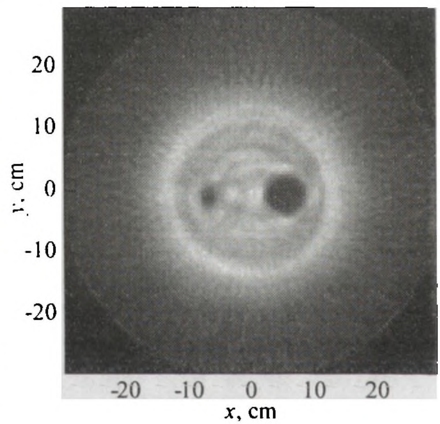

Fig. 4.10. Ultrasonic tomogram of a square and a round cylinder.

4.2. Multi-angle tomography of radiopaque object shapes

The location sounding scheme that is the most efficient at reconstructing the shapes of opaque objects is the one in which the radiating and transmitting antennas are located on the same side of the object. First, this scheme is the easiest to realize, and second, there is no shadowing at most of the sounding angles. As was pointed out above, this last circumstance has a significant effect on the accuracy of reconstruction of the shape of an opaque object.

The main mathematical methods of inverting wave projections for radiolocation purposes were considered in Section 1.4. However, there are a number of peculiarities in the scanning of opaque objects. Let us consider them.

First of all, let us consider how the surface integral for the field scattered by an opaque object with an uneven surface can be converted into a volume integral. The initial integral for the field backscattered by a perfectly reflecting object is given by

$$E(\mathbf{r}) = -2\iint_S G_0(\mathbf{r}-\mathbf{r}_s)\frac{dG_0(\mathbf{r}-\mathbf{r}_s)}{dn}dS$$

or

$$E(\mathbf{r}) \equiv -\iint_S \frac{dG_0{}^2(\mathbf{r}-\mathbf{r}_s)}{dn}dS .$$

Here the vector $\mathbf{r}_s = (x', y', Z_s(x', y'))$ has as its third component the function $z' = Z_s(x', y')$, which describes the shape of the upper (visible) part of the object (see Fig. 4.11). If we now introduce the function $\delta(z' - Z_s(x', y'))$ under the integral, we can write

$$E(\mathbf{r}) = -\iiint_V \delta(z' - Z_s(x', y'))(\mathbf{N}\nabla')G_0{}^2(\mathbf{r}'-\mathbf{r})dx'dy'dz' ,$$

where the vector $\mathbf{N} = (-\partial Z_s/\partial x', -\partial Z_s/\partial y', 1)$ describes the direction of the normal to the visible surface of the object. We now introduce the characteristic function of the object $F(\mathbf{r})$ equal to 1 and 0 inside and outside the object, respectively. This is simply the Heaviside step function:

$$F(\mathbf{r}) = \chi[Z_s(x,y) - z] = \iiint_V \delta(\mathbf{r}-\mathbf{r}')d^3\mathbf{r}' .$$

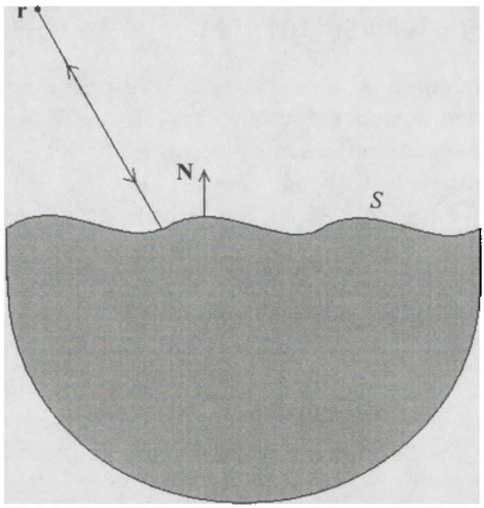

Fig. 4.11. Defining the characteristic function of the object.

This integral for the field can now be written as

$$E(\mathbf{r}) = \iiint_V (\nabla' F(\mathbf{r}')\nabla') G_0{}^2(\mathbf{r}' - \mathbf{r})dx'dy'dz' .$$

Integration by parts gives

$$E(\mathbf{r}) = -\iiint_V F(\mathbf{r}')\Delta G_0{}^2(\mathbf{r}' - \mathbf{r})dx'dy'dz' .$$

In the case of sufficiently high-frequency signals, ($k|\mathbf{r}| \gg 1$) it follows (see Appendix 2) that

$$E(\mathbf{r}) = (2k)^2 \iiint_V F(\mathbf{r}') G_0{}^2(\mathbf{r}' - \mathbf{r})dx'dy'dz' . \tag{4.3}$$

This relation is similar to Eq. (1.11), but the characteristic function $F(\mathbf{r})$, which describes the shape of the opaque object, acts as the unknown function here.

In the case of partial *scanning* of the object by the sounding point, the form of the characteristic function is uniquely determined only for the illuminated areas, so the shape of the object can be reconstructed for those areas only. Panoramic scanning of the object from all sides is required for complete reconstruction of the shape of an opaque object (Fig. 4.12).

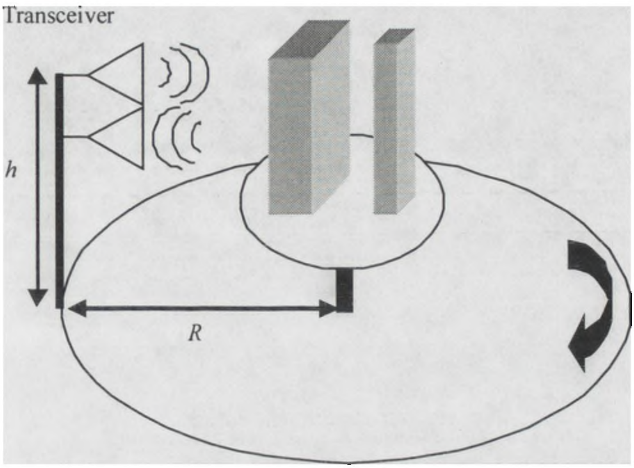

Fig. 4.12. Object viewed from all sides.

The inverse focusing technique described in Section 1.4.1 can be implemented to reconstruct the characteristic function. Toward this end, it suffices to apply formulas (1.12) and (1.13) in sequence. In the case of cylindrically shaped objects (Fig. 4.12) and circular scanning with some radius R, the calculations using these formulas reduce to the following operations: convolution over the angular position of the sounding system and summation over all sounding frequencies. Both operations are realized by means of FFT algorithms, i.e., fast algorithms operating in real time. Figure 4.13 displays the result of numerical simulation of tomography of the scene depicted in Fig. 4.12, for circular scanning, as depicted in the figure, with radius $R = 30$ cm in the frequency bandwidth from 1 to 18 GHz. The image is presented as its negative for illustrative purposes: the darker areas correspond to higher values of the tomogram. There is good agreement in dimensions and mutual arrangement of both rectangular cylinders. The resolution achieved here is 1–2 cm. The observed peripheral artefacts are due to edge effects caused by a non-optimal choice of the time window in the FFT.

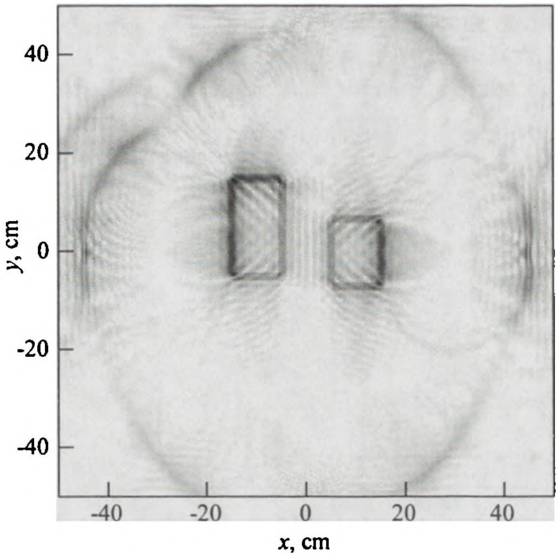

Fig. 4.13. Result of numerical simulation using the inverse focusing method.

Experiments were performed on the setup shown in Fig. 4.2 with the triangular cylindrical object used previously. The measurements were performed using the R4M–18 vector network analyzer produced by MICRAN, Russian Research and Production Company (Tomsk). The scanning radius was $R = 67$ cm, and the frequency bandwidth was 1–18 GHz. The distribution of one of the quadratures of the radar response is presented in Fig. 4.14 as a function of scanning angle and scanning frequency. It can be clearly seen that the distribution is sharper in the high-frequency range.

The corresponding spatial spectrum of the radar responses (the real part), converted into Cartesian coordinates, is displayed in Fig. 4.15*a*. The reconstructed shape of the characteristic function of the object is shown in Fig. 4.15*b*.

It can be seen that the spatial resolution of the obtained images is on the order of 1.5 cm. This sharp resolution is achieved thanks to a wide frequency bandwidth of 1–18 GHz. In contrast to the transmission scheme, there are no shadowing effects in multi-angle location sounding.

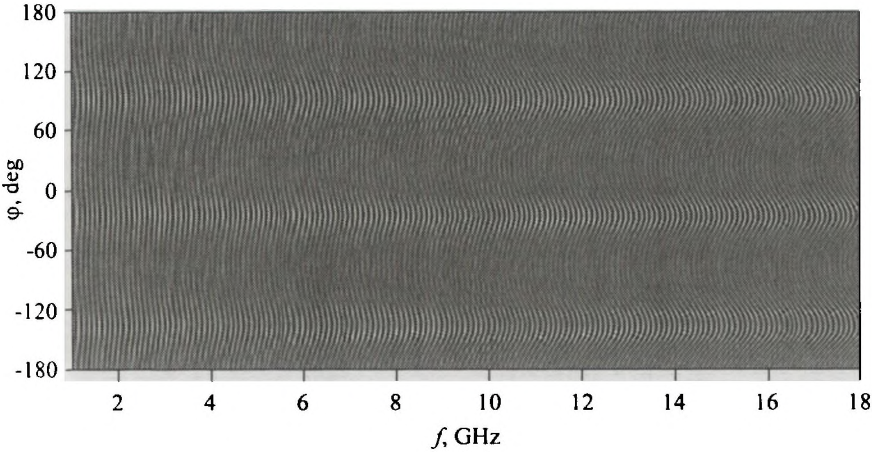

Fig. 4.14. Measured distribution of the radar response of a triangular cylindrical object.

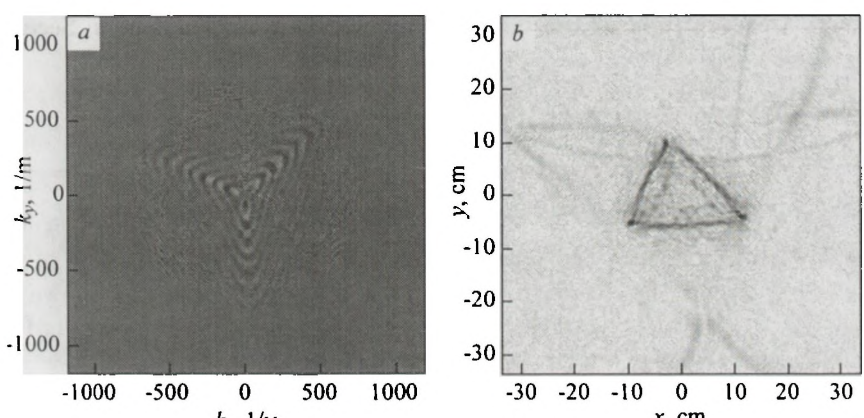

Fig. 4.15. Spatial spectrum (*a*) and reconstructed tomogram (*b*) of the test object.

4.3. Unilateral location tomography of the shapes of radiopaque objects

Let us consider the situation where location (detection) of an opaque object is performed at a certain frequency in some plane S. We make use of the inverse focusing method in the form (1.12). As a result, we can write the result of focusing as

$$U(\mathbf{r}_F)=\sum_m\sum_n M(\mathbf{r}_F,\mathbf{r}_m,\mathbf{r}_{0,n})E(\mathbf{r}_m,\mathbf{r}_{0,n})=\iint_S dSM(\mathbf{r}_F,\mathbf{r}_s)E(\mathbf{r}_s)\,, \tag{4.4}$$

where the focusing function is expressed as

$$M(\mathbf{r}_F,\mathbf{r}_s)=\exp\{-2ik|\mathbf{r}_F-\mathbf{r}_s|\}\,.$$

Changing the order of integration in (4.4), we have

$$U(\mathbf{r}_F)=\iiint_V F(\mathbf{r}')Q(\mathbf{r}',\mathbf{r}_F)dx'dy'dz'\,.$$

With a sufficiently large area of synthesis of focusing ($k^2S\gg 1$), the instrument function can be represented in simplified form as was done in Section 1.4.2:

$$Q(\mathbf{r}',\mathbf{r}_F)\equiv(2k)^2\iint_S M(\mathbf{r}_F,\mathbf{r}_s)G_0{}^2(\mathbf{r}'-\mathbf{r}_s)dS\approx$$

$$\approx Q(\mathbf{r}'-\mathbf{r}_F)=Q_\perp(\boldsymbol{\rho}'-\boldsymbol{\rho}_F,f)\exp\{2ik(z'-z_F)\}\,,$$

where $Q_\perp(\boldsymbol{\rho}'-\boldsymbol{\rho}_F,f)$ is the transverse instrument function defined in formula (1.14). The reason for this is the physical fact that the wavefront in the focusing region takes a form similar to a collimated beam, as shown in Fig. 1.7. If good transverse localization of AFTS is achieved, then the following approximate equality can be assumed to hold

$$U(\mathbf{r}_F)\equiv U(\boldsymbol{\rho}_F,z_F)=\exp\{2ik[Z_s(\boldsymbol{\rho}_F)-z_F]\}\iint dxdy\,Q_\perp(\boldsymbol{\rho},f)\,,$$

$$\boldsymbol{\rho}=(x,y)\,.$$

This expression is in fact the solution of the inverse problem of reconstructing the shape of the illuminated part of an opaque object:

$$Z_s(\boldsymbol{\rho}_F)-z_F=\frac{1}{2k}\arg\frac{U(\boldsymbol{\rho}_F,z_F)}{U(\mathbf{0},z_F)}\,. \tag{4.5}$$

The higher the sounding frequency, the greater will the localization of radiation be for transverse focusing, and the more accurately will the shape of the opaque object's surface be reconstructed.

Two important points should be noticed here:

1) since the function $\arg(z)$ in expression (4.5) is a multivalued function, reconstruction of the total phase should be performed on neighboring segments of the phase profile;

2) the best result is obtained by averaging multi-frequency measurements.

The solution obtained here was checked by numerical simulation in the example of reconstruction of the surface of a parabolic mirror. The solution of the direct problem of reflection of a plane wave from a parabolic mirror was obtained in the approximation of the Kirchhoff method. Figure 4.16*a* displays the distribution of one of the quadratures of the field at a frequency of 1 GHz in the receiving aperture, which is located above a perfect parabolic mirror with a diameter of 5 m. The focus is located 1.8 m from the mirror vertex, and the sounding aperture is shifted upwards from the focus by 40 cm. The field of the reflected wave has good rotational symmetry. In the presence of a deformation (Fig. 4.16*b*), the symmetry is degraded.

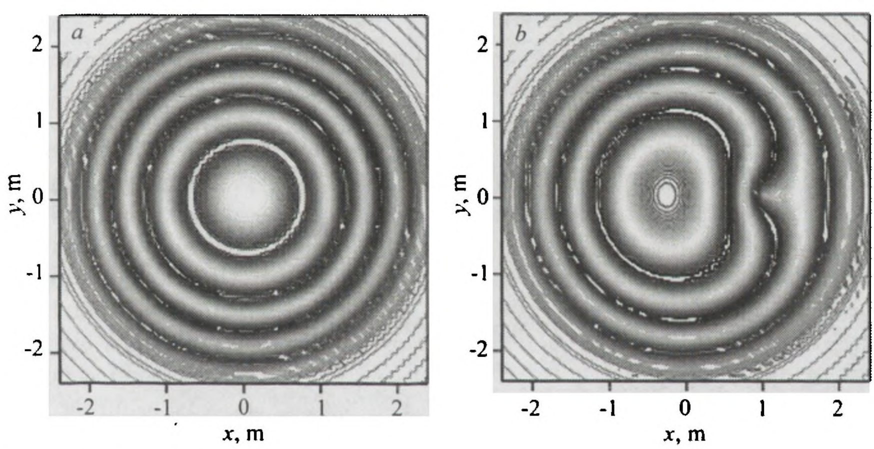

Fig. 4.16. The distribution of one of the quadratures of a reflected wave field in the aperture of a parabolic reflector antenna in the absence (*a*) and in the presence (*b*) of a deformation.

Implementation of the solution (4.5) of the inverse problem enabled reconstruction of the profile of the parabolic mirror (Fig. 4.17) and detection of the shape and position of a small deformation in the mirror (indicated by the arrow) as well. Good agreement between the predefined and reconstructed shapes of the mirror was observed.

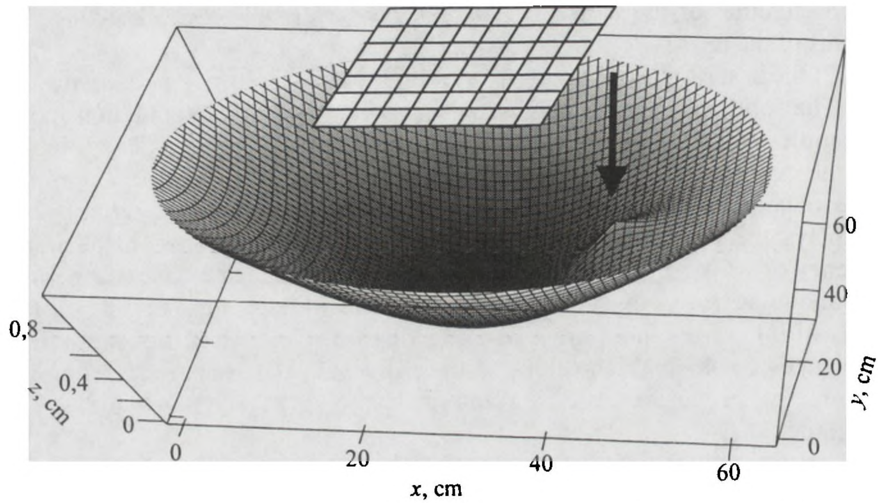

Fig. 4.17. Reconstructed shape of a parabolic mirror with a local deformation (indicated by the arrow) and aperture of the sounding antenna.

A dish antenna of 66 cm in diameter with a focal length of 30 cm was investigated to validate the method experimentally (Fig. 4.18*a*). The sounding distance was 56 cm. The antenna was scanned by ultrasound. The signal frequency was 40 kHz, which corresponded to a wave length of 0.82 cm and electromagnetic radiation with a frequency of 36 GHz. From the scattered field data, the shape of this paraboloid was reconstructed. It was found that the shape was nearly ideal. The distribution of detected deviations over the mirror surface is shown in Fig. 4.18*b*. The lighter areas correspond to downward deviations from the regular shape, and the darker areas, to upward deviations. It can be seen that the mirror antenna has smooth distortions of its shape extending over its entire surface and reaching 1 cm at its periphery, and local dimple-shaped non-uniformities up to 2 mm in depth. This is in good agreement with the positions of flaws indicated in Fig. 4.18*a*.

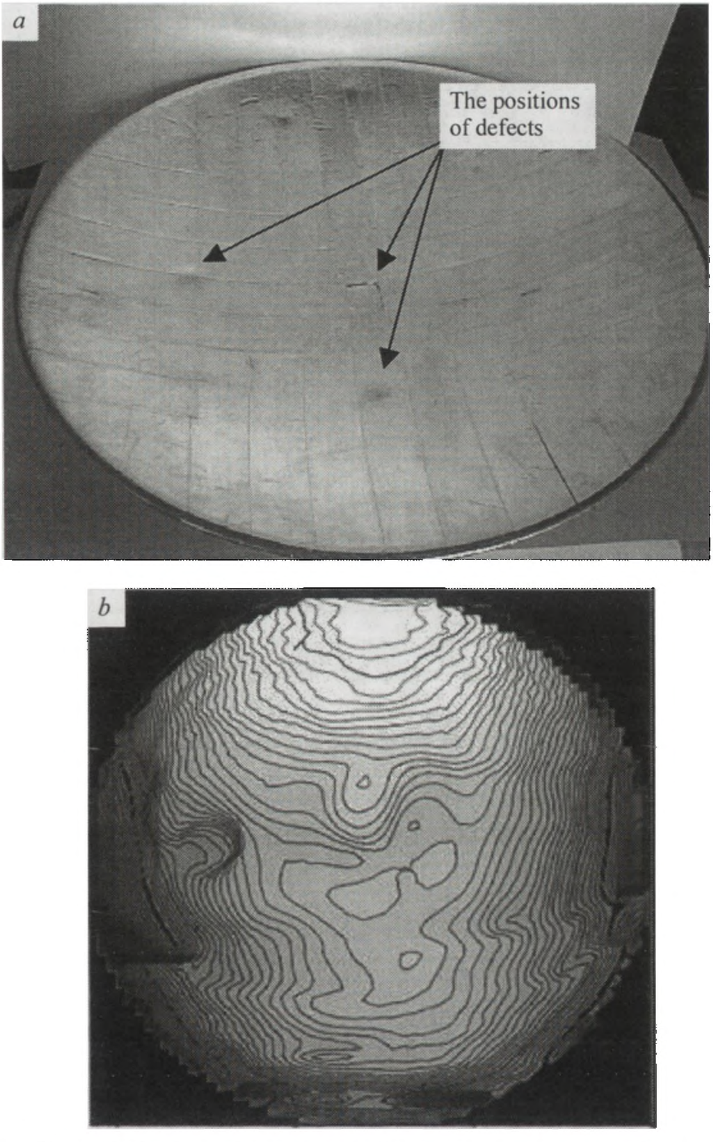

Fig. 4.18. Surface of a real parabolic antenna: *a* – external view; *b* – reconstructed distribution of deviations of its shape from that of a perfect mirror.

4.4. Recovery of the focusing properties of combined reflector antennas

Solution (4.5) for calculating the distortions of the surface of a reflector antenna, discussed in Section 4.3, is of practical significance. The point here is that systems in which surface distortions of the reflector antenna are present lose their ability to focus signals efficiently and, as a result, lose their ability to distinguish signals from background noise and distinguish signals coming from neighboring angular directions. There are a number of factors giving rise to defects on reflector antennas. These include thermal deformations, defects in the materials the antennas are made from, operational damage (damage incurred during the course of use), etc. All of these lead to degradation of system performance or even to complete system breakdown. Large antennas mounted on communication and remote sensing satellites are especially sensitive to distortions. Actual replacement of such antennas is hardly possible, and the devising of a curvature-correction systems is quite a difficult engineering task. Distortion of the optimal shape of a parabolic reflector ultimately results in partial or complete failure of the satellite system, which in turn leads to significant time and money lost on satellite repair.

The solution for tomographic measurement of the shape of a reflector antenna proposed above can be used to achieve additional focusing of signals in the antenna focal plane without resorting to mechanical correction of such distortions (deformations). Thus, the power gain of the antenna can be restored simply by suitable signal processing. Correcting for the effect of such deformations is possible on the mathematical level provided the phase-amplitude spatial distribution of the field is completely recorded by an antenna array located near the reflector focal plane (see Fig. 4.17). Thus, the problem that needs to be solved is split into two interrelated tasks: first, to define the geometrical surface flaws of the large satellite reflector antenna and second, to take these flaws into account when restoring the antenna power gain without resorting to mechanical correction of the reflector.

To solve the first problem it is proposed to use measurements of the field from a known reference source and radio-tomography to reconstruct the surface curvature of the reflector antenna. This problem is solved by applying the fast Fourier transform, followed by reconstruction of the reflector antenna flaws using the phase distribution of the spatial spectrum of the recorded field (see Section 4.3). At the basis of this solution lies the assumption that all distortions of the spatial distribution are caused by geometrical distortions of the reflector antenna surface, and also by a high residual localization of the field near the focus even in the presence of surface flaws.

The spatial frequency spectrum for the deformed mirror, calculated using the 2D Fourier transform, is shown in Fig. 4.19*a*. The asymmetry of the spectrum is caused by deformations. Using a perfect mirror here would give the spectrum shown in Fig. 4.19*b*. To reconstruct the shape of the deformed mirror, it is sufficient to recalculate the spatial frequency spectrum onto the aperture plane of the mirror and then, using the inverse Fourier transform, to reconstruct the distribution of the complex amplitude. The shape of the mirror is uniquely determined by the phase distribution of the complex amplitude over the aperture. In essence, this procedure is described in Section 4.3.

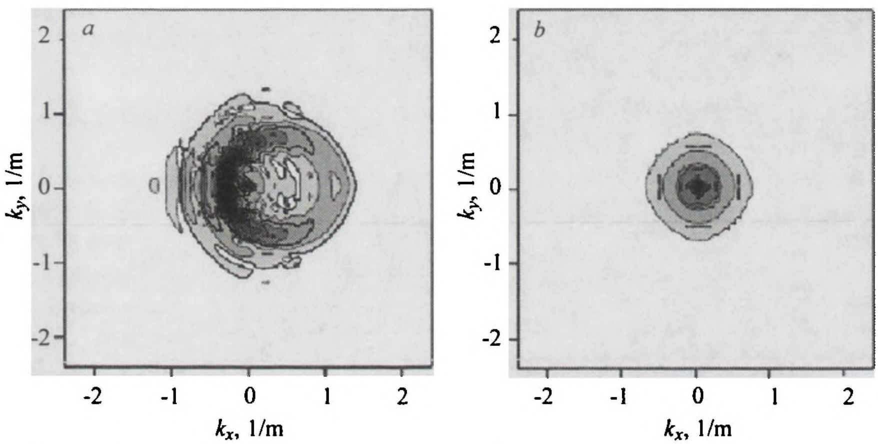

Fig. 4.19. Spatial frequency spectrum in the receiving array of a combined reflector antenna before (*a*) and after (*b*) correction for antenna surface deformation.

A reference source located near the mirror is considered to be a convenient tool to eliminate the effect of deformations. The corresponding spatial frequency spectrum in the receiving array is found by convolving the spectrum of the reference source (known) with the transfer function of the focusing system, which includes within itself the effect of geometrical distortions. In the case of any other source, the spatial frequency spectrum in the receiving array also results from convolution of its (unknown) spectrum with the same transfer function of the focusing system as mentioned above. Eliminating the imperfect transfer function of the focusing system from these relations makes it possible to calculate the actual spatial frequency spectrum of this source. Convolution of this spectrum with the transfer function of a perfect paraboloid yields maximum gain at the focal point. It is significant that all of this can be performed at the microprocessor level without resorting to any mechanical manipulations of the mirror surface. As a result, the antenna power gain can be restored to its maximum possible value. The equivalent directivity pattern (DP) of such an antenna is symmetric in contrast to the distorted initial DP (Fig. 4.20). As illustrated in the figure, the maximum value of the amplitude has been increased, and the width of the DP has been reduced.

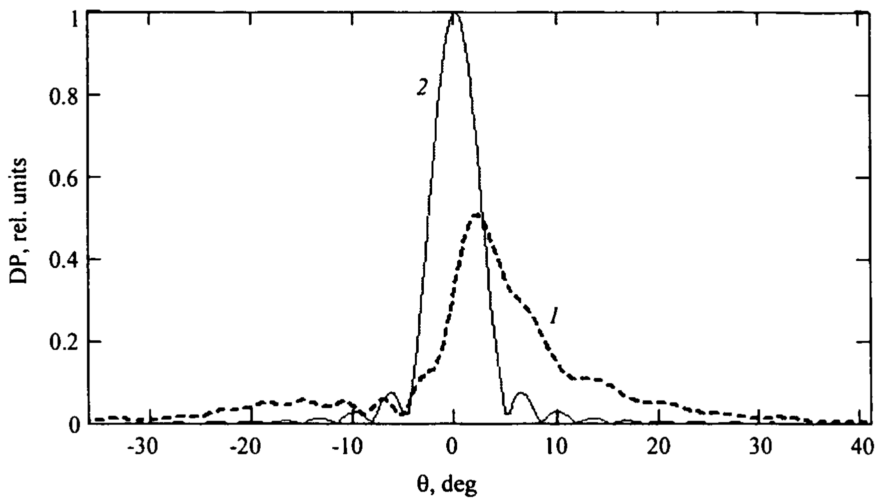

Fig. 4.20. Directivity pattern of reflector antenna before (curve *1*) and after (curve *2*) correction of surface deformation.

Thus it becomes possible to reconstruct the shape and restore the power gain of a satellite-based antenna without resorting to mechanical correction of the curvature of the mirror. Both problems are interrelated and solved using computer technologies and, what is most significant, they permit the use of fast algorithms, i.e., their solutions can be realized in real-time. The effect of focusing-defocusing on signal detection from different directions is illustrated in Fig. 4.21.

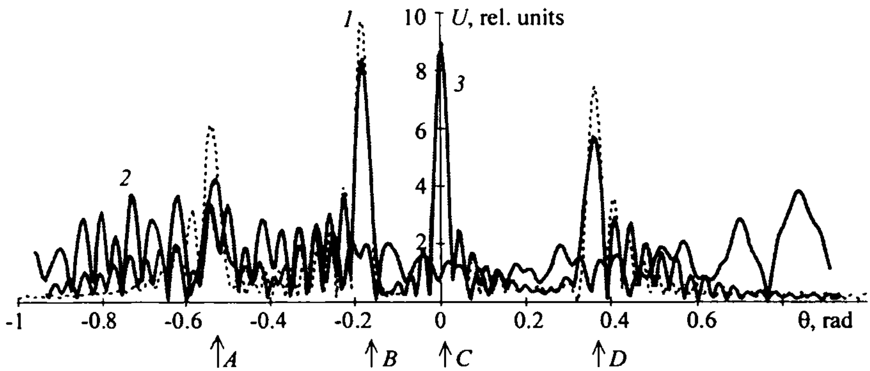

Fig. 4.21. Example of simultaneous reception of signals from different directions (*A–D*): *1* – perfect antenna, *2* – defocused antenna, *3* – restored (compensated) antenna.

4.5. Summary

Radio-tomography of radiopaque objects reduces to reconstruction of object shapes. Multi-angle wave sounding enables one to reconstruct their shapes and corresponding spatial frequency spectra.

Transmission tomography of the shapes of opaque objects is limited by the requirement that no area on the surface of the object overshadow other areas. There are fewer limitations due to shadowing requirements in unilateral location tomography. The approximation of geometrical diffraction theory suffices to describe the diffraction effects that arise.

The results obtained using these methods have a wide range of application. The reconstruction and correction of distortions of the curvature of large parabolic reflectors by means of wave sounding is one example.

Chapter 5

DOPPLER TOMOGRAPHY

As has already been pointed out, there are a number of advantages of using microwaves in remote detection of prohibited items concealed under clothing or in hand luggage over other forms of radiation. Thus, using high-intensity X-rays is potentially hazardous for individuals, and every time it is implemented it should be strictly regulated. This also pertains to particle radiation, i.e. neutrons, protons, electrons, etc. The use of ultrasound runs up against the fact that it is strongly attenuated as it penetrates air and clothing. The use of optical and infrared radiation is limited by their low ability to penetrate through clothes. The same disadvantages are encountered in the terahertz band and, moreover, the currently available element base for this band is not sufficiently developed and is not yet ready for extensive use. It follows that preference should be given to radio wave systems in the microwave band. In the first place, radio waves are almost completely safe and do not lead to negative health outcomes. This is their key distinction from X-rays. Secondly, the range of applications of radio waves is potentially quite wide: they have been successfully put to use in crowded spaces, during special-forces raids for detecting and tracking the movement of people hiding behind building walls, detecting people who have been injured in natural disasters, etc.

However, the microwave systems in current use are elaborate stationary systems of high cost – more than $250,000. Looking for an alternative approach based on Doppler measurements is the aim of this chapter. According to preliminary estimates, the alternate solution that we propose will cut the costs of such an equipment package by more than a hundredfold. Moreover, the working instrument can be rather compact and operate under any conditions, including field conditions. Chapter 5 integrates the results of papers [4–13].

5.1. Microwave Doppler sensor and location (detection) sounding

Let us consider the operation of a microcircuit that goes under the name of a microwave Radar based motion detection module (RMM) of the type CON-RSM1700 [1], which operates at a frequency of 24 GHz (Fig. 5.1). Sensor size is 25.0×25.0×6.2 mm, and its market price is about €10. The radiating power does not exceed 16 dBm (40 mW), so an RMM is absolutely safe from the perspective of human health. Such sensors can be easily combined into sensor arrays, thanks to their small size.

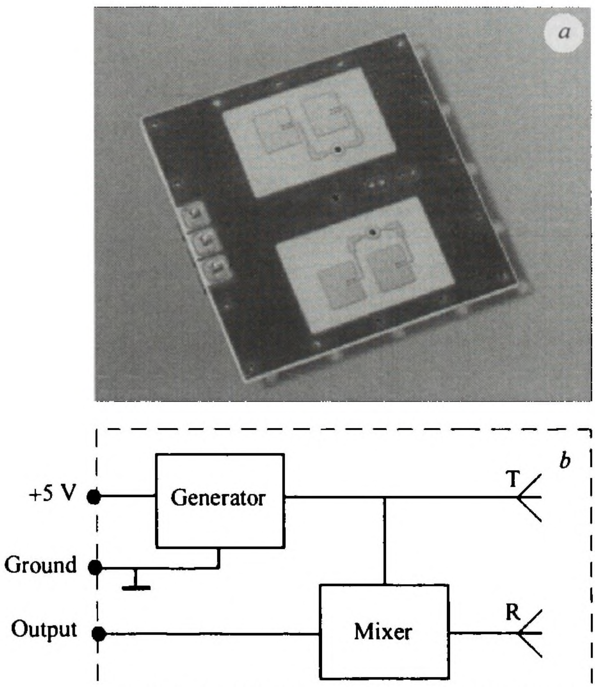

Fig. 5.1. Doppler motion sensor CON-RSM1700 (*a*) and its block diagram (*b*).

Basically, the sensor under discussion is a compact short-range radar station [2]. Key sensor elements are a reference-frequency generator, transmitting (T) and receiving (R) antennas, and a mixer (Fig. 5.1). The output signal is typically passed through a differentiating circuit. The reference-frequency generator produces a signal with frequency ω_0 of the form $u_0 = A_0 \cos(\omega_0 t)$, which is fed to the radiating antenna (T) and then, somewhat attenuated, to the mixer. The signal $u_1 = A\cos(\omega_0 t - 2kVt - \varphi)$ incoming from the receiving antenna (R) is sent to the second input of the mixer. A and φ here denote the amplitude and phase of the signal reflected from the test object, V is the velocity of the object relative to the sensor. Signal multiplexing and averaging are performed in the mixer:

$$U(t) = \overline{u_0 u_1} = \frac{1}{2} A_0 A \overline{[\cos(2kVt + \varphi) + \cos(2\omega_0 t - 2kVt - \varphi)]} =$$
$$= \frac{1}{2} A_0 A \cos(2kVt + \varphi).$$

After the output signal has passed through the differentiating circuit, it takes the following form:

$$\frac{dU}{dt} = -VkA_0 A \sin(2kVt + \varphi),$$

or, in the general case,

$$\frac{dU}{dt} = -\frac{dr}{dt} kA_0 A \sin(2kr + \varphi), \tag{5.1}$$

where $r = Vt$.

Depending on whether the RMM moves in the forward or the reverse direction relative to the test object, the factor $V = dr/dt$ will be either positive or negative, and the Doppler shift frequency will either increase or decrease (Fig. 5.2). The case was considered here when the test object has a sharp boundary. Reflections from long parts of the object do not result in a Doppler effect and are not detected by the sensor.

For a constant speed, expression (5.1), which describes the output signal of the RMM, coincides to within a constant factor with the quadrature component of the received signal

$$S(t) = A\sin(2kr + \varphi),$$

which contains information about amplitude and phase of the signal reflected from the test object. This is clearly demonstrated in Figure 5.2, *b*, where the signal records are antisymmetric in relation to reversing the direction of motion of the RMM. Thus, the microwave motion sensor provides an objective measurement of one of the quadratures of the field and can be used for sounding objects of different shapes. On this basis, it is proposed to apply the Doppler effect in the tomographic examination of hidden objects, and in the reconstruction of object shapes using the SAR technique.

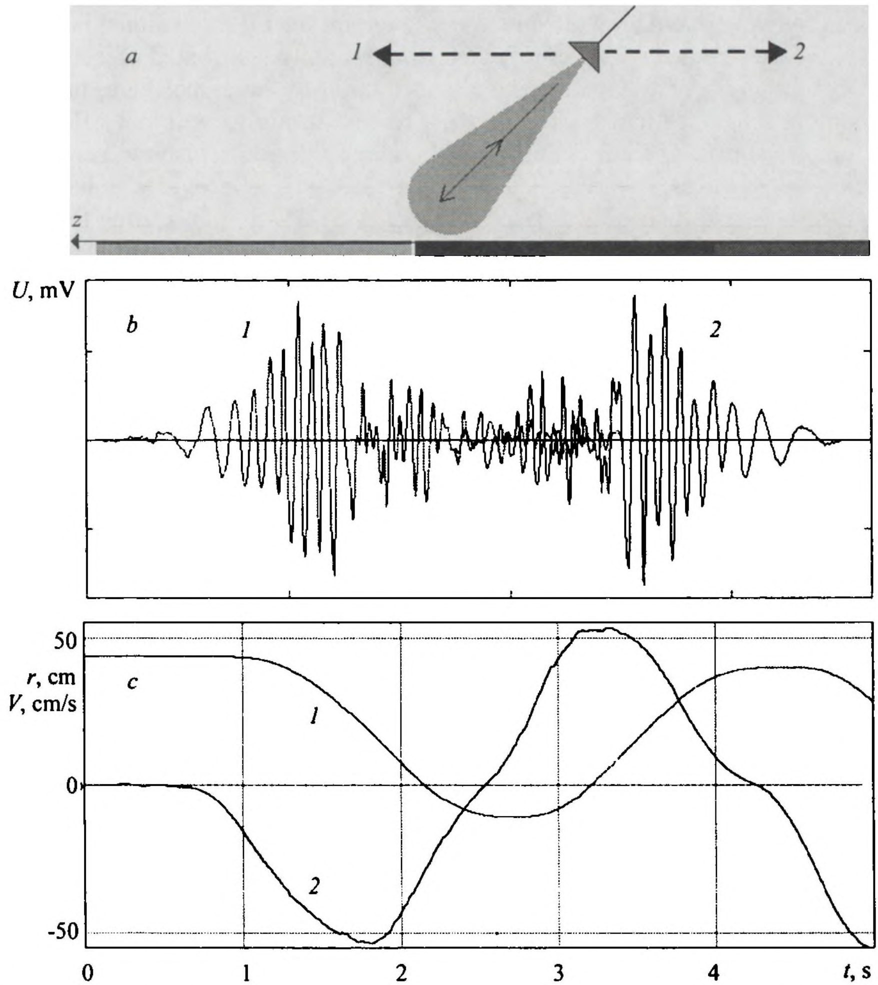

Fig. 5.2. Explanation of operating principle of an RMM: *a* – diagram of motions; *b* – actual signal records when the sensor moves forward (curve *1*) and backward (curve *2*); *c* – synchronous values of coordinates (curve *1*) and sensor velocity (curve *2*).

5.2. Simulation modeling

Thus, the basic idea of the method involves applying the Doppler effect as a means of continuous recording of information about the integral amplitude and the phase of a received radio signal along the trajectory of motion. For a location system with a wide directivity diagram, the received signal is the result of interference of waves reflected from spatially distributed objects. Only local inhomogeneities will make a contribution to the signal here, but long homogeneous segments, even if they reflect strongly, will not affect the Doppler signal, as their contribution falls into the non-registered zero Doppler frequencies. The recorded Doppler radio signal provides a basis for processing and reconstructing the inhomogeneity distribution using the SAR technique. The possibility exists to adjust the focusing depth and thereby to obtain the tomographic image. For processing of this type, the system instrument function (SIF) must be defined, which is the spatial and temporal location response to a point scatterer. The SIF analog in optics is the point spread function. Reconstruction of the SIF can be achieved either theoretically by simulation with trajectory parameters taken into account, or experimentally, when a local segment of the image is selected corresponding to a point scatterer.

Let us elucidate the model of formation of the SIF. If the location (detection) system moves at a velocity V along the Oy axis at a height H (Fig. 5.3a), and the point scatterer is located at a point with coordinates $\mathbf{r}_0=(x_0,y_0,0)$, then the signal received at the observing point at some specified time t is written as follows:

$$E_0(x,t)=A_0G^2\frac{\exp\left\{2ik\left[(x-x_0)^2+(Vt-y_0)^2+H^2\right]^{1/2}\right\}}{\left[(x-x_0)^2+(Vt-y_0)^2+H^2\right]}, \qquad (5.2)$$

where G is the antenna directivity diagram, A_0 is the reflection coefficient, $k=2\pi f/c$ is the wave number for radiation with central frequency f. The parameter x here is the coordinate of the antenna system transverse to the direction of motion, i.e., it is the coordinate of the position of the microwave sensor in the antenna array. The scanning direction is indicated by the arrow in Fig. 5.3. The function $E_0(x,t)$ calculated in this way can be interpreted as the system instrument function.

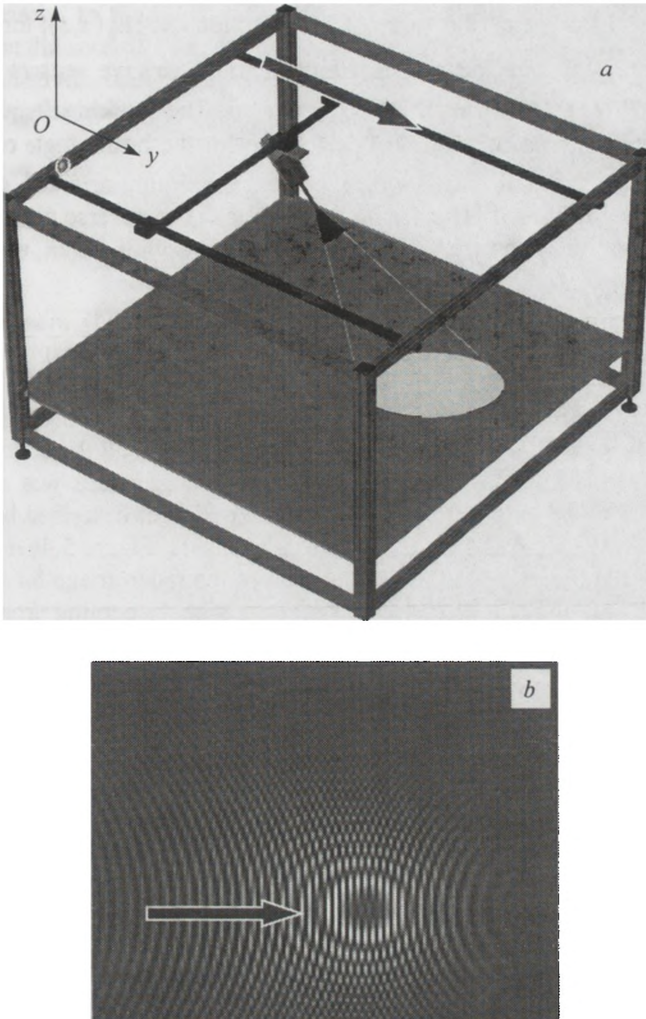

Fig. 5.3. Simulation modeling scheme (a) and calculated form of the SIF(b).

Figure 5.3*b* presents the form of the function $\mathrm{Re}\{E_0(x,t)\}$ for the point scatterer $\mathbf{r}_0 = (0,0,0)$ in location scanning with microwave sensors at the velocity $V = 30$ cm/s at a height of $H = 30$ cm. The working frequency was $f = 24$ GHz. The calculation was performed for the beam angle of the transceiving antenna equal to 36° with the beam maximum oriented at an angle of 45° to the horizontal. The scanning step for the transverse coordinate was chosen to be $\Delta x = 5$ mm. As expected for such a wide beam, the SIF was found to be weakly localized.

If there are several reflectors or the tested (sounded) inhomogeneities have a distributed character, the radar image (wave projection) is more complicated. The example of simulation modeling where four inhomogeneities (objects) are distributed diversely is presented in Fig. 5.4. Three of the inhomogeneities were assigned as point inhomogeneities, and the remaining one as a long rod (Fig. 5.4*a*). This scene with inhomogeneities was configured intentionally to be similar to the full-scale experiment described below. The simulation was calculated for the case of 32 sensors. Figure 5.4*b* displays the solution of the direct problem – calculation of the radar image for the chosen scene with inhomogeneities. Interference of signals coming from all four objects is clearly observed: traces of reflections from the rod are visible in the upper part of the image, and in the lower part, traces of the point-like inhomogeneities are seen. It is important that the influence of the directivity diagram of the microwave sensors was taken into account in the calculation. This is manifested in the asymmetrical intensity distribution of the reflections in the upper and lower parts of the image for the point-like inhomogeneities.

Processing the location signal $E(x,t)$ in the case of a complex distributed target can be performed with the SAR technique. It is sufficient to perform the computer aided inverse focusing of the received radiation, or, what is completely equivalent, to apply two-dimensional matched filtering using the SIF [3]. This operation is performed using double convolution with the complex-conjugate of the system instrument function:

$$W(x, y = Vt) = E(x,t) \otimes E_0^*(x,t). \tag{5.3}$$

Figure 5.4*c* shows the form of the function so obtained $|W(x,y)|$. All of the reflectors are located at the positions where they were assigned initially. The reason for the achieved effect is obvious: the SAR technique provides radiation focusing with a large aperture equal to the size of the scanning area or, more precisely, to the size of the spot that is illuminated by the directivity diagram on the sounded surface. A standard situation arises: the wider the directivity diagram, the more blurred is the source location imaging, but the better is the resolution for image processing using the SAR technique.

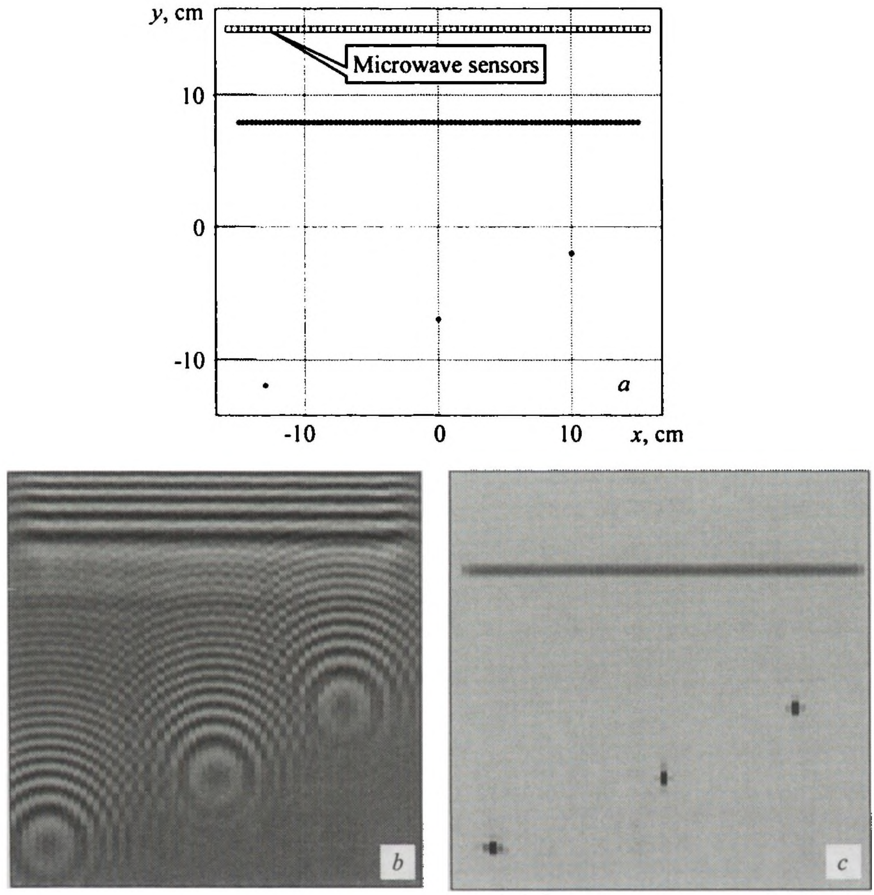

Fig. 5.4. Results of simulation modeling: *a* – source scene with four inhomogeneities; *b* – solution of the direct problem; *c* – solution of the inverse problem.

5.3. Positioning system and manually-operated Doppler scanner

To experimentally check the working efficiency of the proposed approach, Doppler measurements were conducted at a frequency of $f = 24\,\text{GHz}$. A scene with inhomogeneities chosen for this purpose is shown in Fig. 5.5*a*. A metallic rod 0.6 cm in diameter is located in the upper part of the scene, and three balls, which are 2.2 cm in diameter, are located in the lower part of the scene. The balls were taken from computer mouses. An array, which included 16 of the Doppler microwave sensors described above was used for the measurements. The polarization of the microwave sensors was horizontal. Motion of the array (scanning) was performed manually with a speed of about 50 cm/s. Manual scanning was implemented to evaluate the possibility of simplifying and economizing the developed tomography system. Scanning was effected from a height of 7 cm above the plane with the inhomogeneities. The scanning was performed many times in both the forward and backward directions. A typical scanning result – a wave projection of the test scene – is shown in Fig. 5.5*b*.

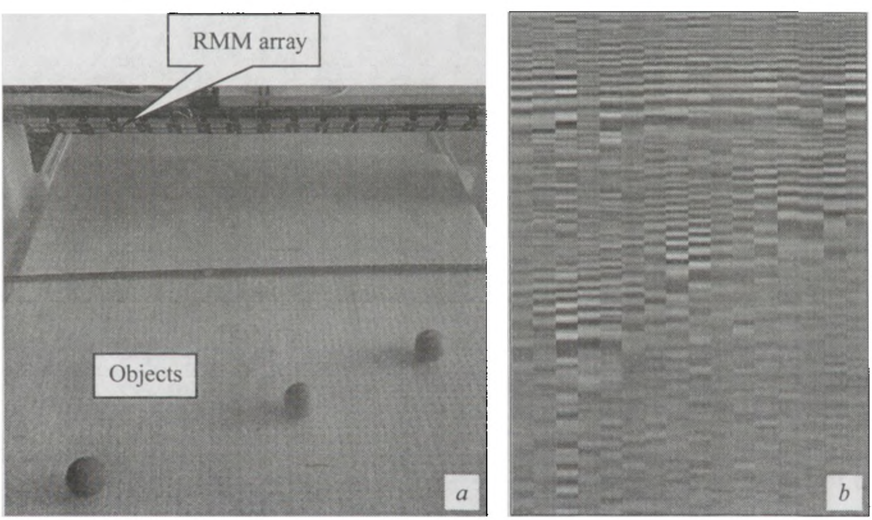

Fig. 5.5. Scene selected for physical experiment (*a*) and its measured wave projection (*b*).

As manual scanning cannot be perfect – uniform and rectilinear – so, this must be taken into account in the processing of the experimental data. For this purpose, a precise positioning system was used which monitored all six parameters of the motion of the linear array of microwave sensors: the three Cartesian coordinates of the center of the array and the three rotation angles of the array in space (Fig. 5.6). For positioning, a Wintracker III magnetic tracking system for 3D computer games was chosen. Judging from the experimental data, under conditions of manual scanning it is not possible using this system to reorient the motion of the array by an angle of less than 2°. However, the greatest impact on the quality of the location image was caused by irregular motion of the operator's hand at the beginning and end of each scan.

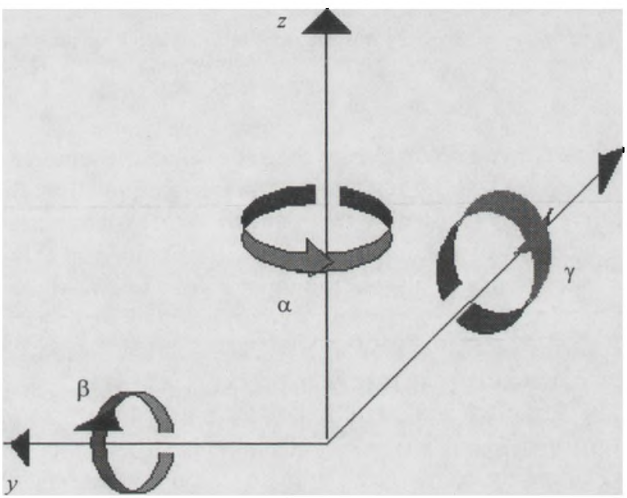

Fig. 5.6. Angular rotations of linear array of microwave sensors.

After the coordinates of each sensor were recorded, the experimental data were recalculated (reduced) to a uniform Cartesian grid by spline interpolation. A sample cross section of the obtained image (the central cross section) is plotted by curve 1 in Fig. 5.7*a*. The initial segment of this curve (for lesser values of y) plots the response to the central ball in the test scene, and the following segment (for larger values of y) plots the response to the metallic rod.

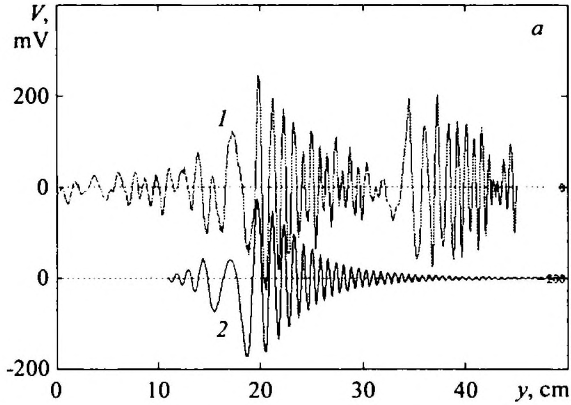

Fig. 5.7. Reconstruction of the SIF: *a* – distribution of central sensor signal along the *y* axis (curve *1* – measurement result, curve *2* – the calculated SIF); *b* – reconstructed two-dimensional SIF.

The presented cross-section or, to be more exact, a segment corresponding to the central ball in the test scene, can be interpreted as the SIF cross-section. Matching this segment with the function (5.1), it is possible to reconstruct the ideal form of the SIF. The ideal SIF obtained in this way has the cross-section displayed by curve *2* in Figure 5.7*a*. The two-dimensional form of the system instrument function is shown in Fig. 5.7*b*. It should be noted that the reconstructed SIF is similar to the SIF shown in Fig. 5.3*b* obtained by numerical simulation. The instrument function of the real system makes it possible using formula (5.3) to reconstruct the distribution of inhomogeneities in the test scene. Here $E(x, y)$ is understood as the reduced experimental data. The result of reconstructing the distribution of inhomogeneities in the test scene is presented in Fig. 5.8*a*.

As can be seen from Fig. 5.8*a*, the spatial distribution of inhomogeneities in the physical experiment has been faithfully reconstructed. Some of the errors in the image can be explained by the need to interpolate reduced data in the transverse cross section – spline interpolation was used to increase the number of points in the transverse cross section from 16 to 64, i.e., by a factor of four. Without resorting to interpolation, the transverse resolution could be increased by reducing the pitch between microwave sensors, for example, by a consecutive shift of the linear arrays, as shown in Fig. 5.9.

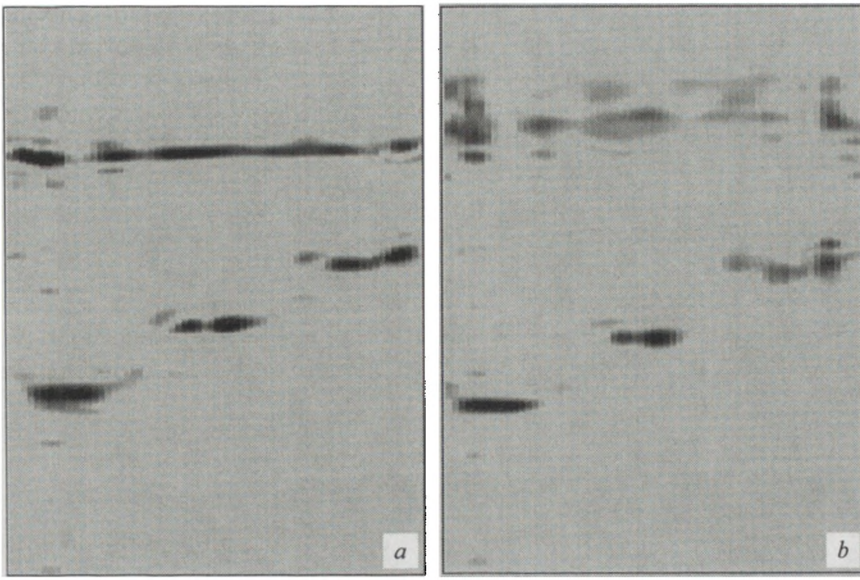

Fig. 5.8. Reconstructed image of the test scene:
a – with the positioning system; *b* – without the positioning system.

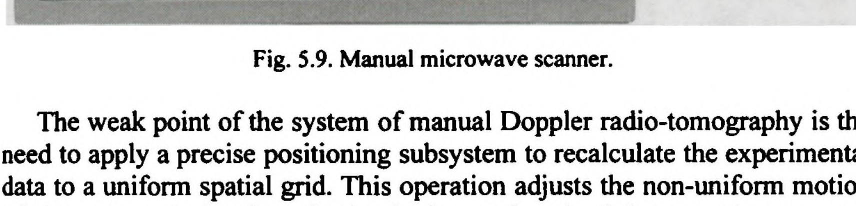

Fig. 5.9. Manual microwave scanner.

The weak point of the system of manual Doppler radio-tomography is the need to apply a precise positioning subsystem to recalculate the experimental data to a uniform spatial grid. This operation adjusts the non-uniform motion of the operator's hand at the beginning and end of the scanning process. However, if just the middle scanned segment is of interest, where the hand movement is almost uniform, then the positioning subsystem can be omitted. The average speed V of hand motion in the center of the tested scene can be calculated by comparing the calculated SIF with the experimental data.

In our case that speed was 52 cm/s. This makes it possible to recalculate the time scale of scanning into the coordinates in the direction of motion of the microwave sensor array. Then it is sufficient to apply procedure (5.3) aided by the obtained SIF. The result of this operation is presented in Fig. 5.8*b*. Here it is obvious that satisfactory quality is observed only in the central part of the scanned field, where the velocity of array motion is nearly uniform. But often this is entirely sufficient to come to a decision about the presence of hidden objects.

The technology of implementing Doppler microwave sensors proposed in this paper for the development of a manual radio-detection scanner is feasible and quite promising from the point of view of practical applications. We suppose that this system will find wide use, primarily in security applications.

5.4. Doppler subsurface tomography

For purposes of experimental testing of the applicability of the proposed approach for the tomography of inhomogeneities hidden under a planar interface of two media, a series of laboratory experiments was conducted at Frauenhofer Institute for Nondestructive Testing (IZFP, Germany). Sounding was performed at the frequency $f = 24$ GHz using the moving horn-type antenna shown in Fig. 5.10*a*. To eliminate clutter reflections as much as possible, the sounding height was lowered to $H = 30$ mm. Three different objects were sounded. Thus, Figure 5.10*b* presents the raw Doppler image of a wooden slat, a photograph of which is shown in Fig. 5.10*c*.

Data processing was performed at National Research Tomsk State University using the above-described technique incorporating large aperture synthesis. The result of SAR processing is shown in Fig. 5.10*d*. To reconstruct the SIF, a fragment was used containing the image of a small knot on the right-hand side of the slat. It can be seen that the image resolution has improved noticeably. The inhomogeneities hidden under the surface have become visible. The scanning direction is indicated by the arrow.

Similar results were obtained for metal plates with holes of different shapes (circular, triangular, and square holes, and slits) hidden under a plastic layer (Fig. 5.11). To increase the resolution of the shapes of the holes, multi-angle sounding of each plate was performed. The results of data processing for six sounding angles are presented in Fig. 5.11*b*. The obtained resolution is on the order of 1 cm.

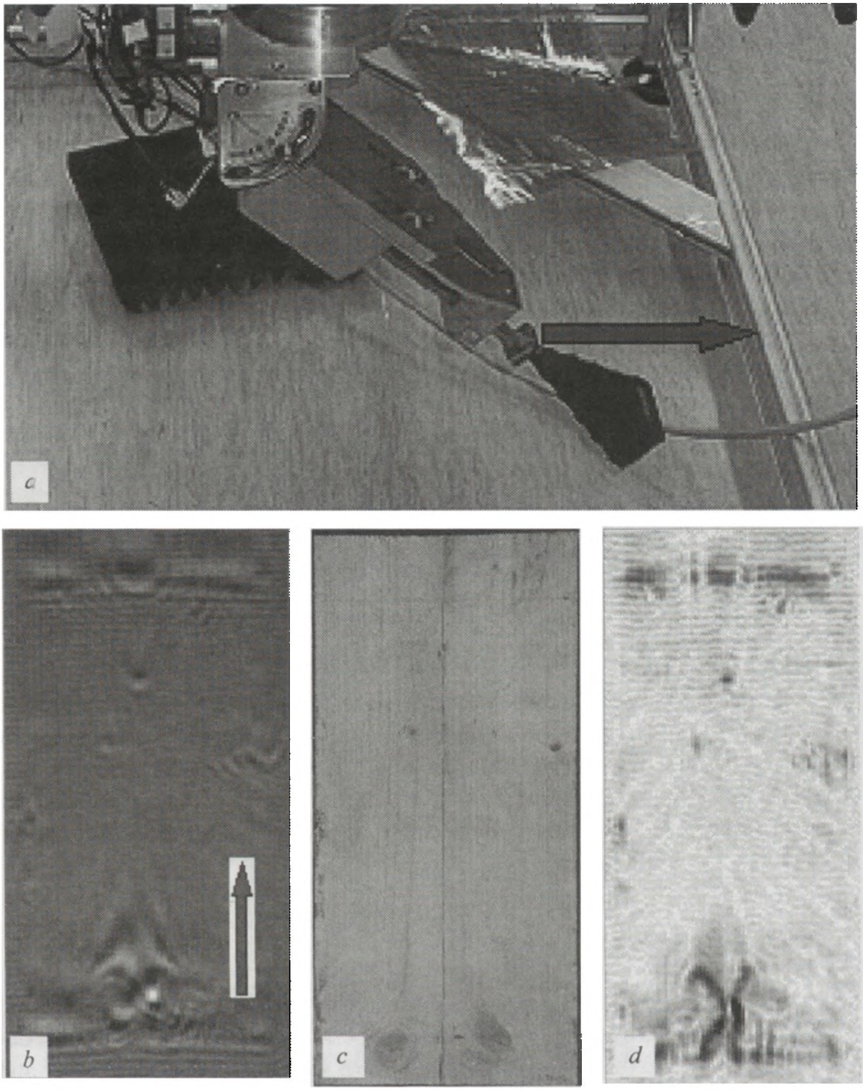

Fig. 5.10. The Doppler tomography of a wooden slat: *a* – measuring unit, *b* – raw radar image, *c* – photograph, *d* – result of SAR processing.

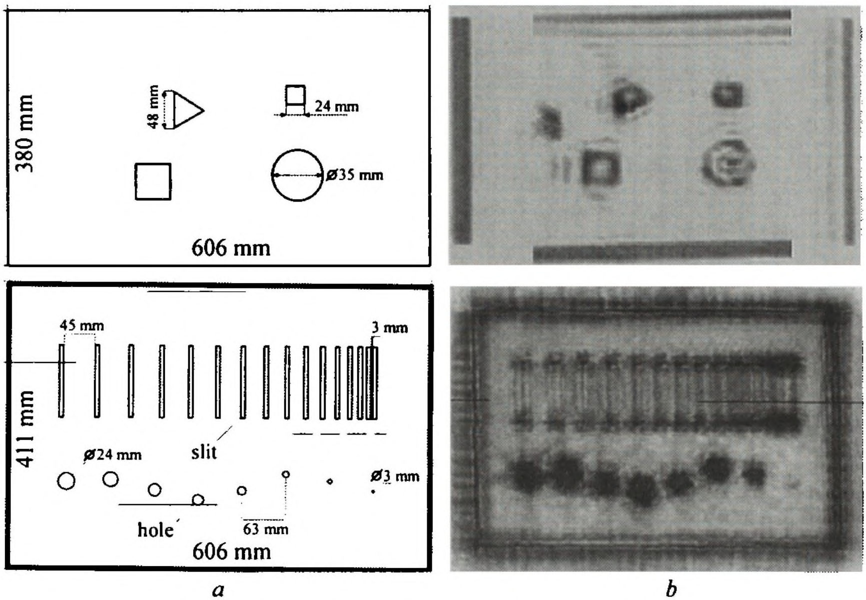

Fig. 5.11. Doppler SAR tomography of metal plates:
a – holes in plates, showing their shapes, *b* – their radio-images.

These latter results are applicable, e.g., in tomography and identification of hidden radio-electronics or for crack detection. A significant point here is that the proposed SAR-based data processing reduces to performing a two-dimensional convolution, and this is efficiently realized using the 2D fast Fourier transform. The time required for data processing does not exceed 30 seconds.

5.5. Summary

Doppler tomography is a special case of radio-wave tomography and mainly uses monochromatic radiation. The principal condition for signal detection in this type of tomography is relative motion of the transceiver and the object. The effect of the frequency shift that arises due to motion of the transceiver is used to select the information signal and disaggregate its quadrature components, which contain within themselves the amplitude phase of the reflected signal.

It has been demonstrated both theoretically and experimentally that radio-wave tomosynthesis allows reconstruction of the image of small inhomogeneities. A design for a manual radio-tomograph based on Doppler motion sensors has been proposed.

A disadvantage of Doppler tomography is the impossibility of radio vision of large, uniform, or stationary objects. Its relatively simple design, the possibility of using standard motion sensors, and its overall low cost are considered among its obvious advantages.

All of the obtained results were confirmed by numerical simulations and physical experiments.

Chapter 6

GEOTOMOGRAPHY

The tomographic techniques described in Chapter 1 have been validated by the results of numerical simulations. However, their experimental verification, which would provide the most objective estimation of current possibilities, is of far greater interest. The implementation of radio-tomographic techniques in the solution of various practical problems was described in Chapters 2–5. The present chapter addresses the testing of methods of location tomography in the context of problems of geolocation.

The problem of detecting dielectric inhomogeneities hidden underground or inside building walls has become an ever more urgent task at the present time. First of all, it relates to the widespread use of plastic antipersonnel mines, whose detection is impossible by means of standard magnetic induction mine detectors. Minefields remaining after various local conflicts on large terrains create a number of risks for peaceful human activity. A problem that was initially a military and technical task has become a humanitarian one. Using radio-wave ground-penetrating radars is considered as the most promising direction in subsurface detection of dielectric objects. These systems assist in nondestructive underground searches for industrial purposes such as detecting lost communication lines, monitoring the condition of gas and water-supply pipelines, groundwater detection, and prospecting for mineral resources. Ground penetrating radars are widely used for archaeological purposes: for studying archaeological ground layers, searching for artefacts, etc. However, a number of problems arise in connection with difficulties in describing the interaction of waves with the medium and scattering inhomogeneities in contactless radio-wave sounding. These include interference created by strong wave reflections at the medium interface and their attenuation in the ground, and also frequency dispersion and multiple scattering number.

This raises the question of fast and reliable processing of the data obtained from ground penetrating radars. A convenient tool for investigating inhomogeneities hidden underground is the SAR technique in the wide frequency band.

Scattered radiation in this sounding technique contains more definite information about scattering inhomogeneities in the medium. To obtain useful information from scattered radiation data, the inverse problem of subsurface location must solved, i.e., the distribution of inhomogeneities in the medium must be reconstructed on the basis of measurements of the scattered field and information about the scattering inhomogeneities. Focusing the reflected signals is the basic technique for underground data processing.

The use of ground penetrating radars dates back to 1971 when the first measurements of sea ice thickness were performed based on the video pulse method introduced by M.I. Finkelstein in 1969. Unflagging interest in subsurface sounding in dielectric media was manifested in the 1990s owing to the widespread use of personal computers. Ground penetrating radars are most widely used today in rail and road inspection, locating and monitoring communication lines and archaeological objects, in estimating snow and ice cover, in monitoring concrete structures, in horizontal directional drilling and geological surveys, and in searches for hidden objects [1–9]. The following problems in the agricultural and forest sectors are solved thanks to the ground penetrating radar: the location of drain pipes, the occurrence of ground water and hydric soils, determination of the productivity of land and the salinity level of soils, spatially variable fertilizer application control, watering control, location of sandy pockets, trunks and roots analysis, and visual representation of tree cross sections.

Despite 40 years of experience there are still bottlenecks and unexplored facts. As experts have noted, the accuracy of determination of depth depends directly on the accuracy of determination of the permittivity of layers. Location-based methods are not widely accepted in agricultural communities although these methods may be conducive to more efficient fertilizing, monitoring of soil consistency, early detection of the formation of plow sole, etc. Chapter 6 summarizes the results of papers [10–20].

6.1. Contactless sounding and detection of antipersonnel mines

Radio-location subsurface tomography of dielectric objectss, including antipersonnel mines, is a challenging problem, whose solution is complicated by a number of factors. First of all, only location sounding is possible, in other words, unilateral (one-sided) sounding. There is no possibility in this case of introducing receiving or transmitting devices under the mines. Moreover, sounding should be performed without contacts since any ground contact is connected with the danger of triggering the explosive device. Wave reflections at the medium interface, irregularities in the medium interface, and wave attenuation in the ground have a strong impact o this type of sounding, as do also frequency dispersion and multiple scattering. It is obvious that the problem can be solved only by using UWB radiation and the SAR technique to process the data.

To test the location method proposed in Chapter 1 for the reconstruction of the distribution of inhomogeneities, an experiment with four dielectric test objects buried at different depths was carried out. The experimental setup presented in Fig. 6.1 was developed at Magdeburg University (Magdeburg, Germany) in cooperation with the authors of this monograph.

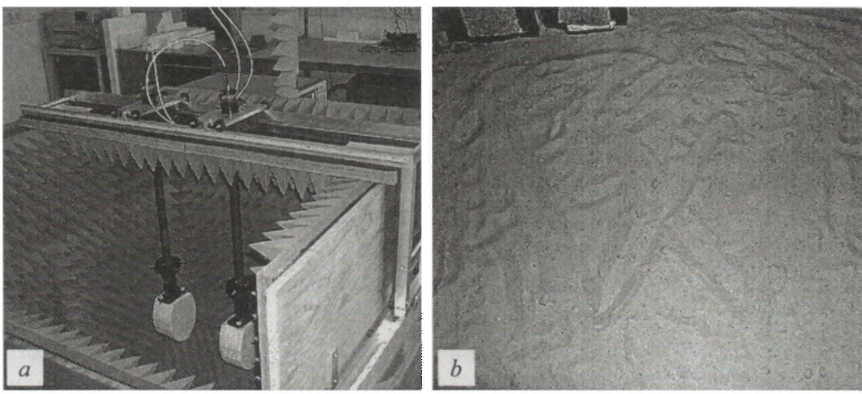

Fig. 6.1. Experimental set up: *a* – scanning system;
b – uneven relief of sand surface after burying the test objects.

Three cases of plastic antipersonnel mines and a foam polystyrene object of stepped configuration where each step was 5 cm in size, were placed in wet sand at a depth varying from 1 to 25 cm. Photographs of these objects are presented in Fig.6.2*a*. In the course of the measurements, frequency scanning in the range from 0.5 to 17 GHz was implemented. The system of receiving and transmitting antennas mounted 14 cm apart was moved over a 50×50 cm square test area in the horizontal plane with a step of 1 cm at a height of 30 cm above the sand surface. The results of reconstructing the shapes of the test objects and their location depths in cm are presented in Fig. 6.2*b*. It can be seen that the algorithm for reconstruction of the distribution of subsurface inhomogeneities (distribution of mines in wet sand) works as it should work, and the obtained resolution was about 2 cm, which is sufficient for such types of objects.

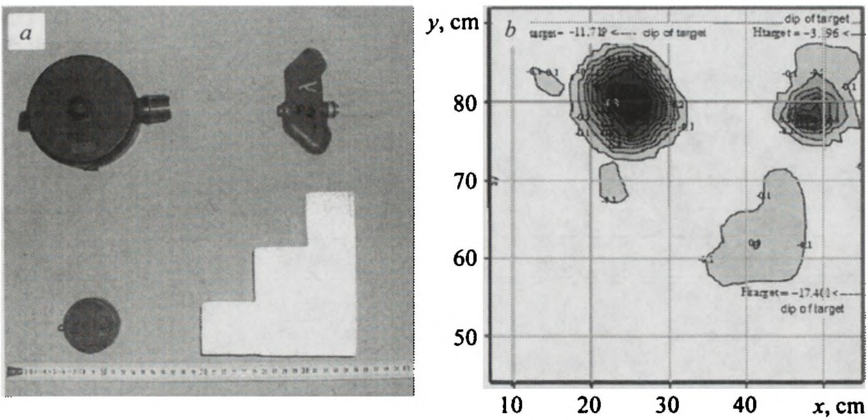

Fig. 6.2. Example of UWB-radio tomography of dielectric mines in wet sand, it the frequency range 0.5–17 GHz: *a* – photograph of test objects; *b* – radio tomogram of object.

6.2. Random and incomplete ground penetrating radar technology

The purpose of this section is to work up algorithms for reconstructing the radio-tomogram of hidden objects and media when the matrix of measured wave projections is not complete, i.e., when the measurements do not cover the area needed to apply fast reconstruction algorithms. This can happen, e.g., when measurements in certain areas are not possible or there is a need to speed up the scanning process. Partial failure of the sensor matrix or the intentional use of a sparse matrix are also related to this case. Experimental data obtained by the authors in 2011 at Tohoku University (Sendai, Japan) were used to verify the developed method.

6.2.1. Statement of problem and experimental data

The experiment was conducted in the laboratory test facility at the Center for Northeast Asian Studies, Tohoku University (Sendai, Japan) with standard ground sounding equipment operating in real time and augmented by an iGPS laser system for steady coordinate positioning (Fig. 6.3*a*). The coordinate positioning was effected with an accuracy not worse than 1 mm, which is one order of magnitude better than for determination of the phase center of the antenna. The radar unit was repositioned manually along a relatively arbitrary path (Fig. 6.3*b*).

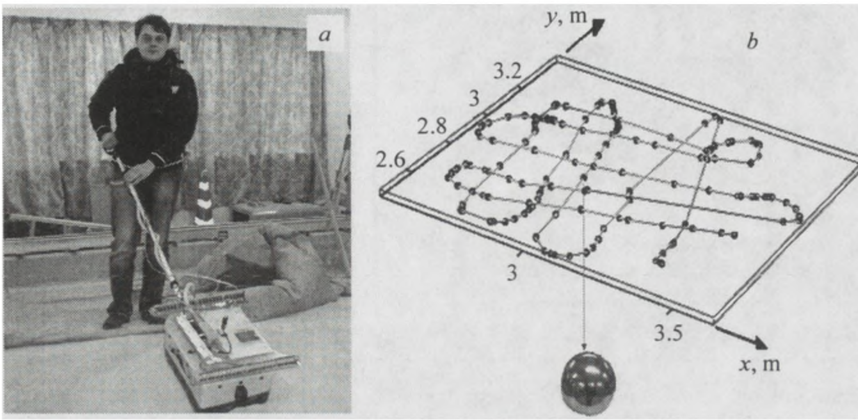

Fig. 6.3. Ground penetrating locator and measurement scheme.

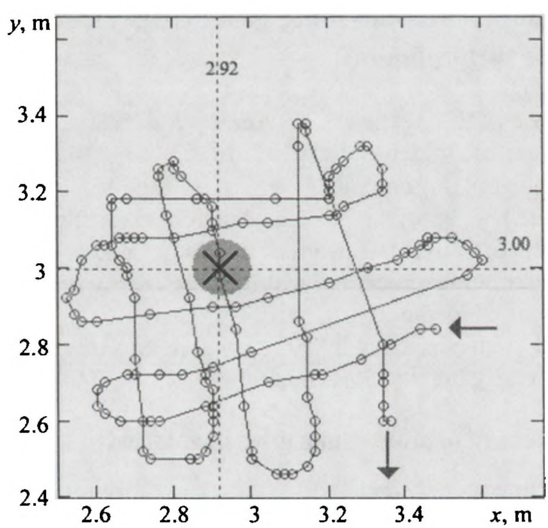

Fig. 6.4. Actual measurement path.

A metal ball 15 cm in diameter was selected as the test object, and was buried in sand at a depth of about 20 cm. The approximate location of the test object is marked in Fig. 6.4 by an ×. The shape of the reflected pulse signal was recorded at each point with a discretization of 512 points. The positions of the measurement points are marked with circles in Figs. 6.3*b* and 6.4. Typical shapes of the observed signal (*a*) and its spectrum (*b*) are shown in Fig. 6.5. As is well known, the initial (reference) shape and spectrum of the signal are determined by the choice of the type of radiation antenna and the characteristics of the radar driving oscillator. An antenna unit with a UWB antenna of bow-tie type was employed in the experiment. The selected signals need to provide sufficient spatial resolution (3–5 cm) and the necessary penetration depth of the radiation into sand (up to 1m).

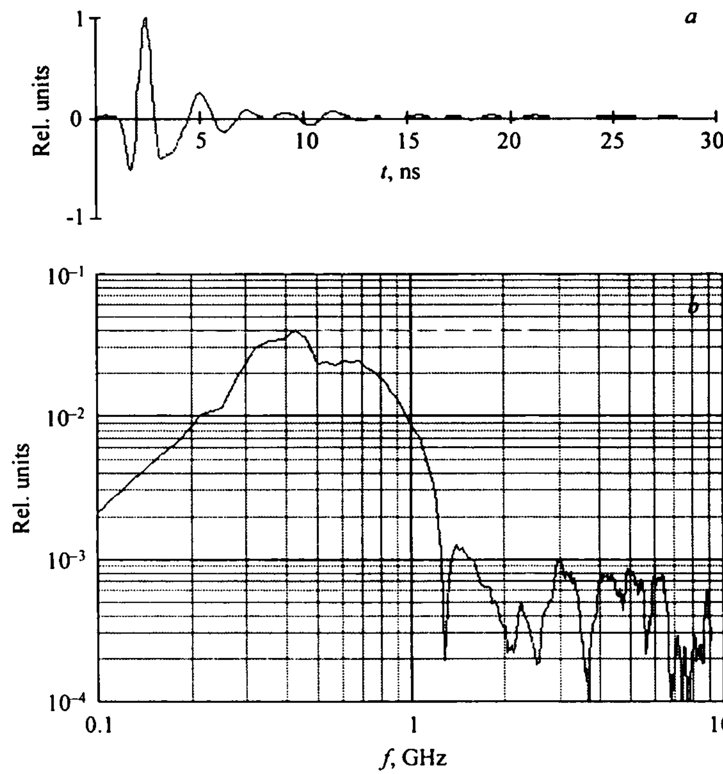

Fig. 6.5. Shape of detecting signal and its spectrum.

Since the selected sounding path is not a regular curve and does not completely cover the grid of observation points, as is needed in the standard SAR technique, the measurements can be considered as typical for incomplete measurements. The measured data are represented as gray-scale levels in Fig. 6.6 where they are plotted versus position along the measurement trajectory (horizontally) and time (vertically).

Figure 6.6*a* displays reflections from the air-sand interface (upper part of the figure) and traces from diffraction hyperbolas, which are caused by signal reflections from a test object hidden in the sand. The darker areas correspond to larger values, and the lightest ones – to smaller values. The reflections from the air-sand interface are the strongest, and against this background the reflections from test objects have lower contrast. A simple subtraction of the average signal from the air-sand interface can be applied to enhance the contrast of the reflections from the test object. The result of this operation is shown in Fig.6.6*b*. The time series of the signal records are halved by eliminating the less informative segments with a long time-delay.

Next, the transition to the amplitude image of the corresponding analytical responses was used at each measurement position to increase the contrast of the test image. Toward this end, all the time records of the signals $u(t)$ were subjected to the Hilbert transform, as a result of which the corresponding conjugate signals were calculated:

$$v(t) = \frac{1}{\pi} \int_{-\infty}^{\infty} \frac{u(\tau)}{\tau - t} d\tau ,$$

and the analytical signals $w(t) = u(t) + iv(t)$ were then calculated, where the signal amplitudes are defined as $A(t) = |w(t)|$. The resulting amplitude distribution of the analytical response is shown in Fig. 6.6*c*. The areas, where the GPR antenna moved directly above the test object stand out distinctly in the obtained image. One such area, which is the closest to the metallic ball, is indicated by the arrow in Fig 6.6*b*. The point marked by a cross in Fig. 6.4 falls in this position.

It is of interest now to get a picture of the distribution of the analytical response in the observation plane. This distribution is displayed as squares of different intensity in Fig.6.7*a*. It can be seen that the largest values fall in a region with central point $x = 2.9$ m and $y = 3.0$ m, i.e., in the area where the test object is placed. This can be traced out more clearly in Fig. 6.7*b* where the measured points have been interpolated over the selected area.

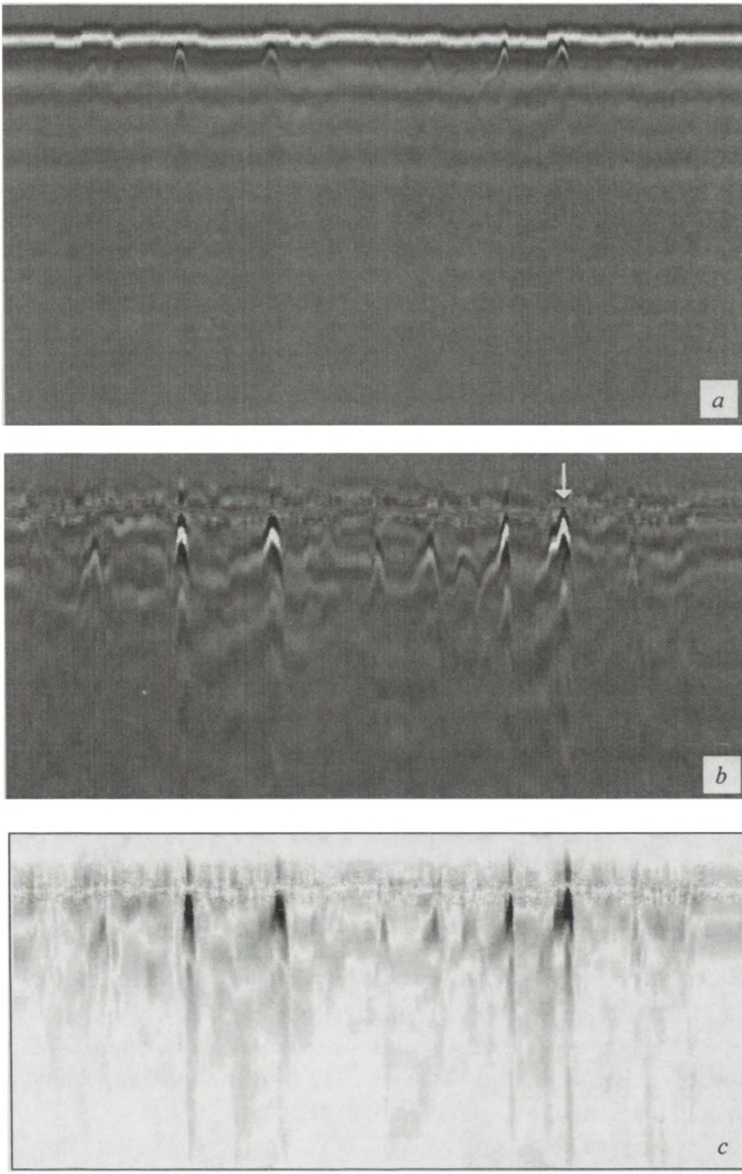

Fig. 6.6. Ground penetrating radar data.

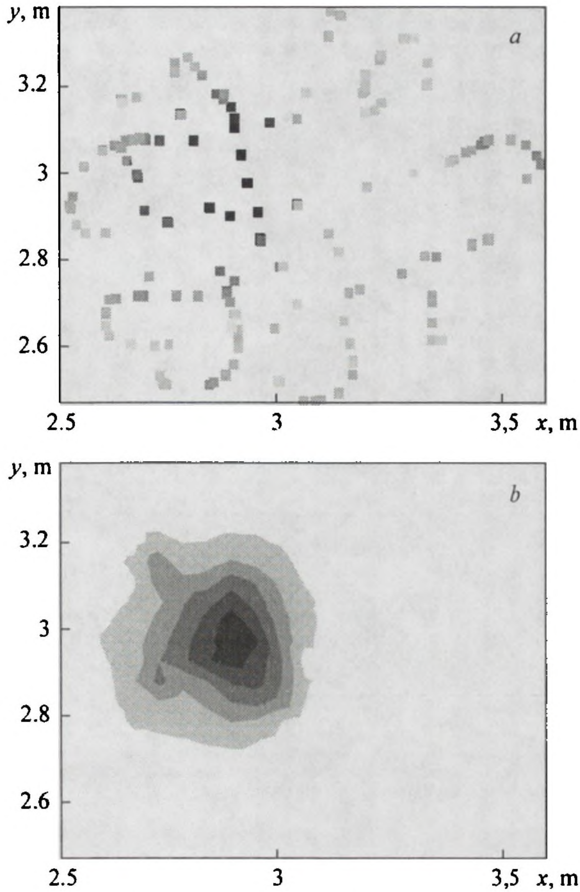

Fig. 6.7. Distribution of the analytic response amplitude over the observation plane.

Thus it turns out that the test object is located somewhere below the point with the assigned coordinates within a region with diameter 0.4–0.5 m. To improve the in-depth and in-plane resolution of the inhomogeneity, a focusing technique of any type should be implemented.

6.2.2. Theoretical background

Three currently existing focusing techniques have proved themselves to be the most efficient (Chapter 1). These are summation over diffraction hyperbolas (inverse focusing or diffraction summation method), multidimensional matched filtering implementing the system instrument function (focusing with learning), and the Stolt migration (group focusing). There are also other focusing techniques, e.g., algebraic methods of reducing the problems to systems of algebraic equations, but their efficiency remains relatively low. Each of these three techniques has its own advantages and disadvantages. Let us briefly enumerate them.

The summation over hyperbolas method is the simplest one. It performs a summation of the received signals introducing a signal delay to compensate for the return path to some chosen focusing point. The tomographic distribution of inhomogeneities can be reconstructed by searching through the certain spatial region layer-by layer with the focusing point. A disadvantage of this method is that the compensation is calculated individually for each point, so the total computation speed for testing large areas is low. Its advantages are: complete versatility and adaptability to monochromatic signals and random spatial scanning.

The Stolt migration employs the fundamental association between temporal frequencies and longitudinal spatial frequencies, which in the case of UWB signals enables fast transformation of signal time compression into longitudinal focusing using the fast Fourier transform. This is the main advantage of the method. The fact that this method is applicable only just to the UWB signals and to plane-parallel scanning geometry is its obvious disadvantage.

Matched filtering occupies an intermediate place between the first and third methods described above. It bears noting that all three methods require a-priori knowledge or step-by-step fitting of the background refraction index n, which is defined in terms of the wave propagation velocity $n = c/v$.

From the point of view of using incomplete or non-equidistant measurement data, only the first method – the sum over hyperbolas – is applicable as given, when the signal-to-noise ratio of the reconstructed image of the hidden objects is low. In the other two methods, interpolation of the source data over a uniform Cartesian grid is required.

Interpolation over missing points can be performed, of course, in different ways, e.g., by using spline interpolation or simple linear interpolation. But it is a time-consuming process. We propose to use a variant of Fourier interpolation, where points in the measurement matrix where data are lacking are filled in with zeros. Such a radar response (such as that displayed in Fig.6.7*a*) is transformed into the spatial frequency domain. Ungrounded (false) values appear at high frequencies (Fig. 6.8*a*) as a result of this zero filling. If those frequencies are filtered properly and the image is transformed back from the frequency domain to the spatial domain, this will provide the necessary interpolation. Only two fast operations are needed here, namely the forward and the inverse Fourier transform (FFT and IFT).

Selecting the required filter is quite a difficult problem, but it can be avoided if the system instrumental function is transformed to the frequency domain as well. There are no *spurious* higher frequencies in the spectrum of the full instrumental function. Now it suffices to multiply the spectra of the image and the instrument function together, of course after taking the complex conjugate (Fig. 6.8*b*). It then remains to take the inverse Fourier transform, so that both image interpolation and image focusing to the selected plane corresponding to the instrument function will be simultaneously realized. Thus, the described procedure of obtaining the tomogram with interpolation is accelerated by at least 20 fold in the scanning step, which is the slowest of all the required steps.

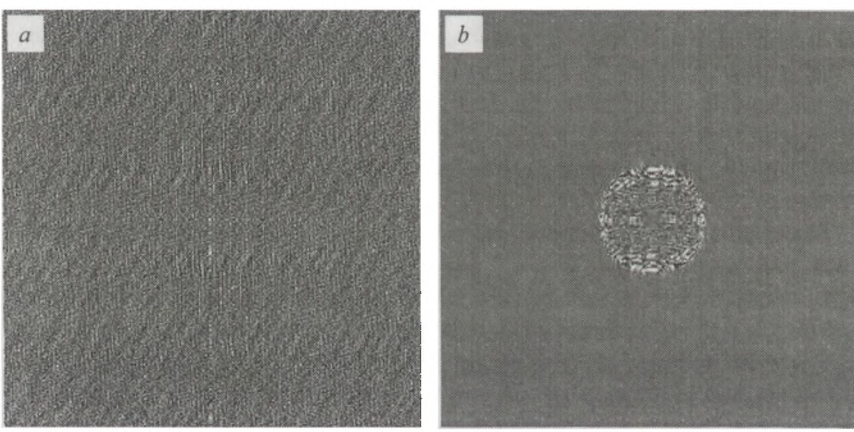

Fig. 6.8. Example of spatial frequency distribution of a radar image *a*) before and *b*) after multiplying by the corresponding spectrum of the instrument function.

Concerning the final goal – a three-dimensional tomogram of the subsurface inhomogeneities – there still remains the as-yet unperformed operation of constructing or measuring the system instrument function for each of the interesting layers. Here it must be borne in mind that the refractive index of the lower background medium n practically always has significant contrast in comparison with the refractive index of air, which is equal to 1. Since the sounding antenna is located in the air but the inhomogeneity is located in the lower medium, strong refraction of the wave occurs upon passage of the wave from the one half-space to the other. This phenomenon obeys Snell's law

$$n \sin \beta = \sin \alpha .$$

Still one more remark: if the possible depth of the inhomogeneities varies over a fairly narrow range, then in the construction of the instrument function, it is possible to use its value for some average depth, and not reconstruct for the entire range of depths.

6.2.3. Numerical simulation

The problem of incomplete data processing was simulated to provide a convincing demonstration of the efficiency of proposed solutions and to practice the algorithm for 3D-tomogram reconstruction as well. The sounding path shown in Fig. 6.9 (*a*, *b*) was selected. Four point-like inhomogeneities were tested, which were located in the same plane at a depth of 15 cm. The sounding procedure for a 1×1 m square test area was simulated in the frequency band 6–12 GHz.

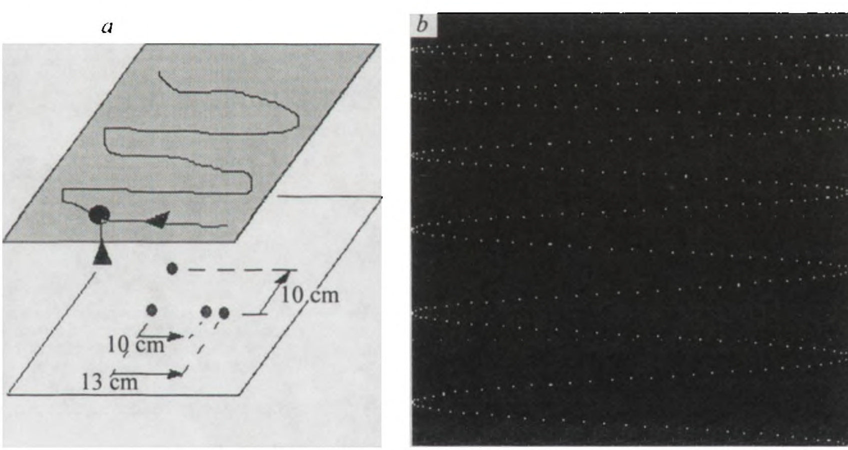

Fig. 6.9. Sounding path of four point-like inhomogeneities.

Figure 6.10*a* displays an image of the full radar response to the assigned group inhomogeneity. The measurements were simulated at a frequency of 10 GHz. A 256×256 image frame with a 4-mm step was recorded. If only 400 points are kept, that is, about 6% of all of the points marked in Fig.6.9*b*, then the radar response will be incomplete.

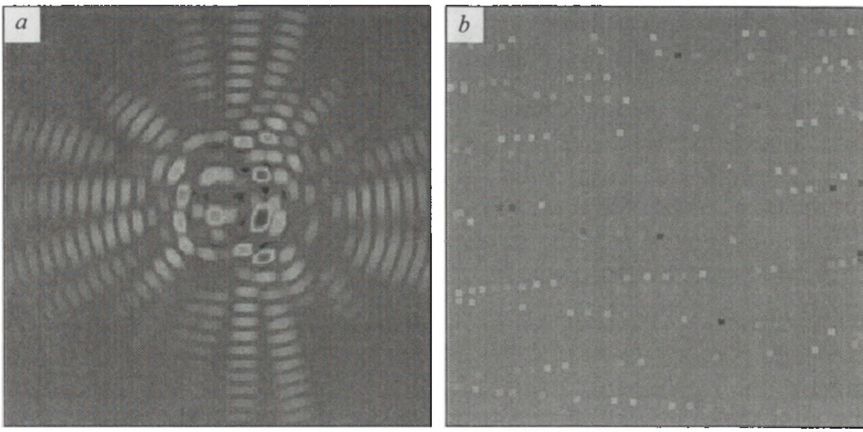

Fig. 6.10. Radar response to group uniformity with complete (*a*) and incomplete (*b*) data.

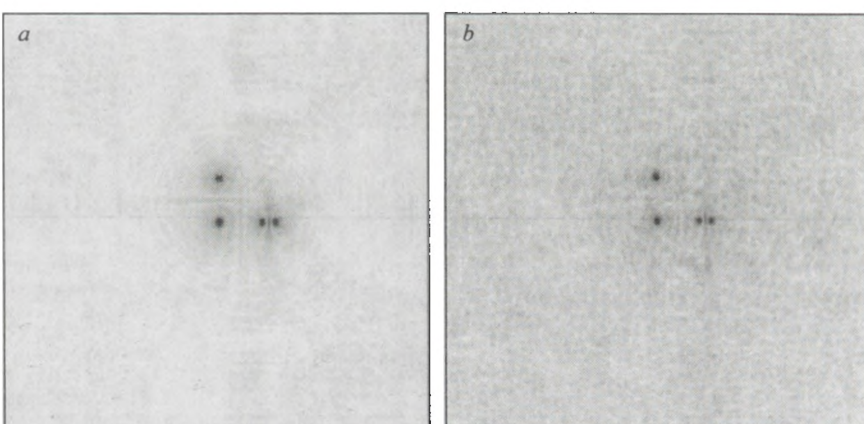

Fig. 6.11. Test tomogram over the complete (*a*) and incomplete (*b*) data.

Figure 6.11 presents an example of reconstruction of the tomogram over complete and incomplete data for the four assigned inhomogeneities using the combined technique of matched filtering and Fourier interpolation presented in the previous section. It is clear that a true reconstruction of the distribution of inhomogeneities is achieved, which confirms the adequacy of the proposed algorithm.

6.2.4. Processing of experimental data

Having convinced ourselves of the potential feasibility of the method, let us turn to the processing of actual experimental data. The developed technique was applied to the experimental data described at the beginning of the section. To use this technique, the system instrument function first had to be reconstructed. It would be better to perform special measurements over a sufficiently detailed grid of measurement points. However, this is not always possible in practice. In this situation, it is possible to use the most successful subset of the measurements. In our case, such a subset is indicated in Fig. 6.6*b*. The vertical part of the measurement path near the cross mark in Fig.6.4 corresponds to this subset. This segment of the overall image is presented in Fig. 6.12*a*. This segment can easily be interpreted as a diffraction hyperbola of the instrument function.

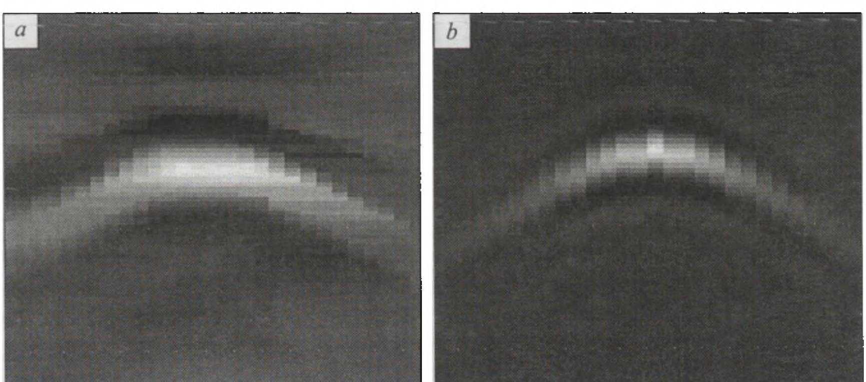

Fig. 6.12. Parts of experimental data (*a*) and calculated (*b*) system instrument function.

Using the technique presented above enabled us to determine the average refractive index of the background medium (sand) from the diffraction hyperbola of the instrument function. That value turned out to be about $n \approx 2.0$. The true depth ($h \approx 20.0$ cm) of the test object, a metallic ball, was evaluated next. Those data made it possible to calculate the form of the instrument function. The experimental and calculated data are in good agreement. The full form of the calculated instrument function is displayed in Fig. 6.13.

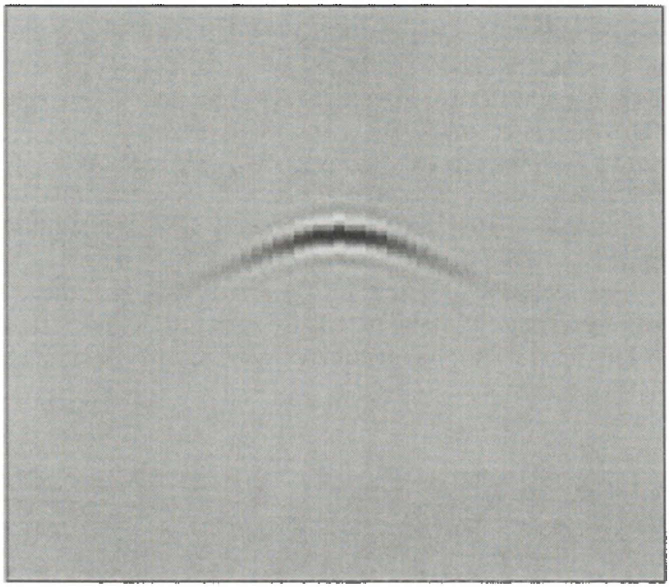

Fig. 6.13. Reconstructed instrument function of ground penetrating radar.

It now remains to perform the Fourier interpolation of incomplete data and matched filtering. Vertical and horizontal cross-sections of the reconstructed three-dimensional tomogram are shown in Fig. 6.14. In addition, the transition to the analytical signal was performed at each point of the xOy plane, and its modulus, the envelope of the signal, was taken. This increased the possibility of an unambiguous interpretation of the result. The data obtained are in good agreement with the results of direct measurements with a measuring rod.

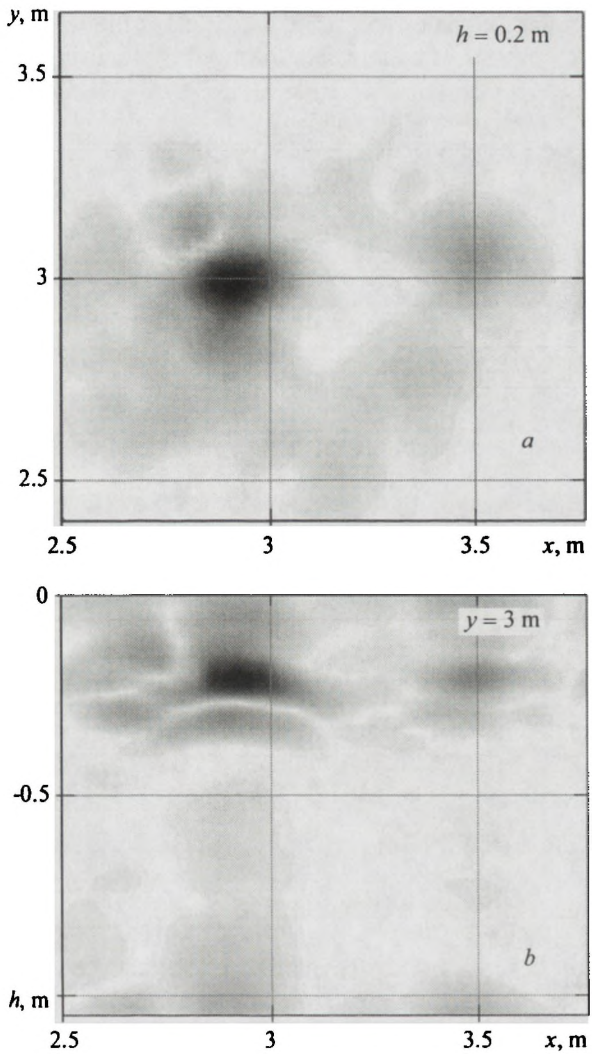

Fig. 6.14. Two orthogonal cross-sections of tomogram reconstructed over incomplete experimental data.

The described algorithm is presented in the form of a control flow chart in Fig. 6.15. The key element of the chart is the procedure for calculating and filtering the spatial frequency spectrum, which plays the role of interpolation of an incomplete matrix of source data followed by focusing of the image of the hidden object.

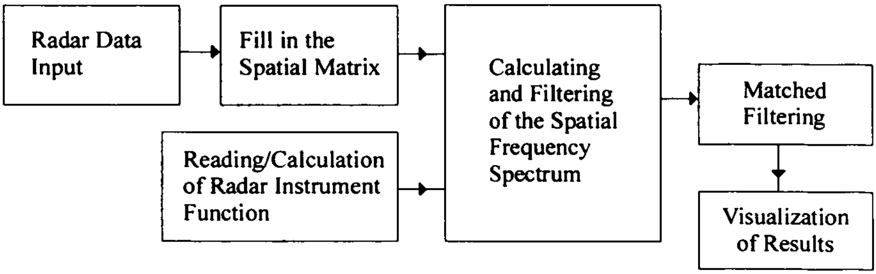

Fig. 6.15. Flow chart of tomography over incomplete data.

The studies conducted in this section confirm the efficiency of the developed method for 3-D tomogram reconstruction from incomplete experimental data using Fourier interpolation and multidimensional matched filtering. Also, the technique of using total internal reflection to determine the average refractive index of the background medium. This technique can be realized by using fast algorithms and can work in real time. The described technique can be applied to speed up the visualization of hidden objects in UWB sounding. Moreover, it can be directly employed in current geolocation systems and in advanced systems for radiotomography of hidden objects. Further gains in reduction of computation time are possible using the group focusing method.

6.3. Geolocation over a curved surface

This section describes three techniques for subsurface image reconstruction based on geolocation scanning over a curved (uneven) surface.

6.3.1. Inverse focusing

In this section we consider the profile of subsurface sounding shown in Fig. 6.16. It is assumed that the radiating and receiving antennas are integrated and move along the curved surface $h(x,y)$. The synthesized frequency bandwidth was taken to extend from 5 to 10 GHz.

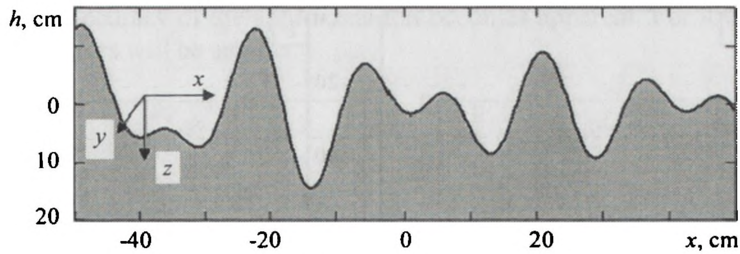

Fig. 6.16. Curved surface.

Two cases of inhomogeneities were considered: a) a single inhomogeneity and b) a group inhomogeneity. Corresponding radar responses are presented in Fig. 6.17. We note that the solution of the problem for a flat surface would be take the form of a diffraction hyperbola, but the radar response for a curved surface resembles the shape of the surface.

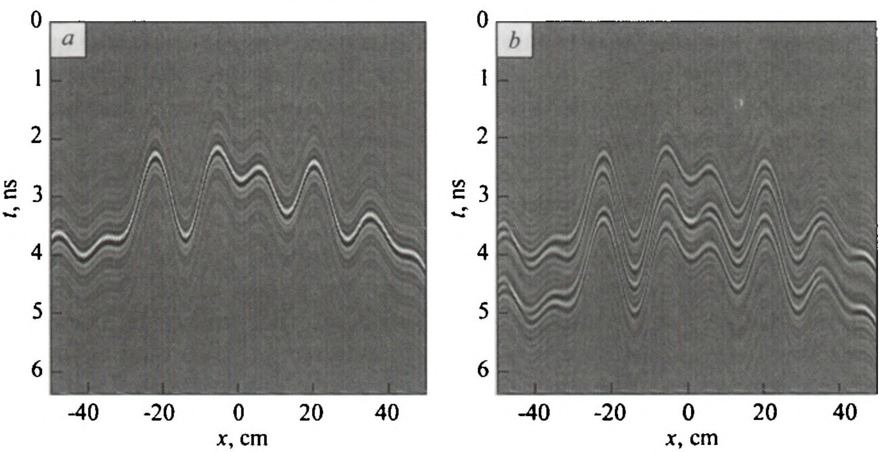

Fig. 6.17. Solution of the direct problem: *a* – for a single inhomogeneity; *b* – for four inhomogeneities.

Figure 6.18 presents the result of processing of the data displayed in Fig. 6.17 using inverse focusing (1.13). It can be seen that the transverse resolution is 3.5 cm and the longitudinal resolution is 6.8 cm. These values are close to the diffraction limit per the selected frequency bandwidth and the size of the synthesized aperture.

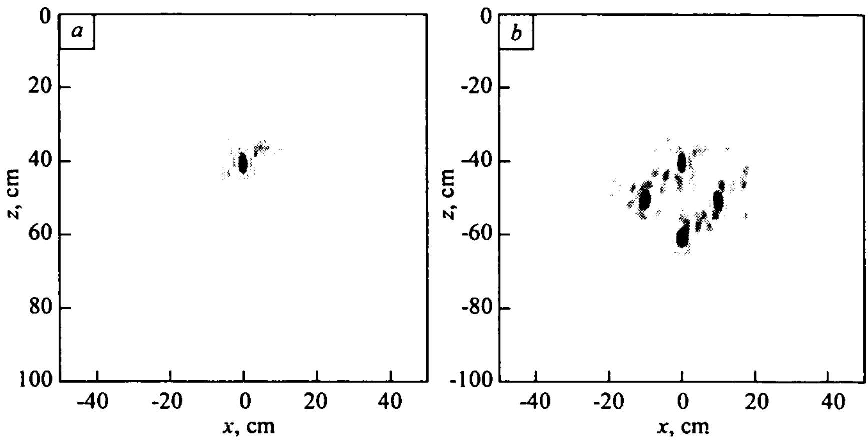

Fig. 6.18. Images of point-like inhomogeneities reconstructed by inverse focusing: *a* – for a single inhomogeneity; *b* – for four inhomogeneities.

Inverse focusing is a relatively universal and easy-to-use technique. It provides the opportunity to consider surface irregularities and different velocities of wave propagation in a stratified medium. The main drawback of this technique is the large volume of calculations.

6.3.2. The phase screen approximation

It is supposed in the phase screen approximation that the curvature of scanning surface is not high. In this case, the values of the field from a curved surface can be transferred to a relatively flat surface by correcting only the phase difference (by addition or subtraction) according to the following formula as if the wave were propagating along the normal to the average surface at each frequency:

$$E(\mathbf{r}) \to E(\mathbf{r})\exp\{-2iknh(x,y)\},$$

where $k = \omega/c$, and n is the refractive index of the lower medium.

Next, using the group focusing algorithm (analog of the Stolt migration) the tomogram of the distribution of scattering inhomogeneities in the lower medium can be calculated as if the medium interface were planar. The images so obtained are displayed in Fig. 6.19. The assigned distributions of inhomogeneities are reconstructed, but the level of artefacts has increased.

Here, the inaccuracy of the approximation becomes apparent. For lower curvature the errors will be smaller.

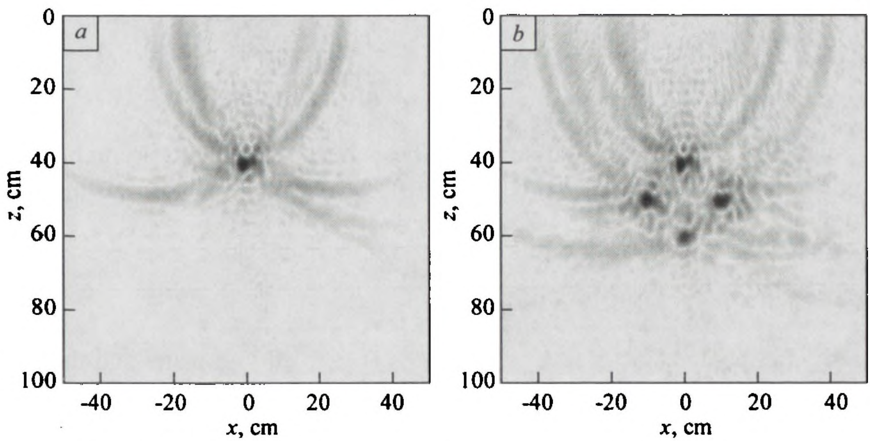

Fig. 6.19. Reconstructed images of point-like scatterers in the phase screen approximation: *a* – for a single inhomogeneity; *b* – for four inhomogeneities.

6.3.3. The Huygens–Fresnel interpolation

Interpolation based on the Huygens–Fresnel principle can be considered as the more accurate approximation. Let us consider it. The scattering inhomogeneities can be replaced by in-phase field sources at the doubled frequency if the measurements are performed with a transceiver in line with Eq. (1.11). This approximation does not take into account the falloff of the field with distance after the scattering; however, since this measurements is less critical than the phase differences, it can be neglected. Thus, the direct problem for the scattered field (1.11) is transformed into the problem of searching for the field sources:

$$E(\mathbf{r}) = \iiint_{V_1} j(\mathbf{r}_1) G_2(\mathbf{r}_1 - \mathbf{r}) d^3\mathbf{r}_1 , \tag{6.1}$$

where $j(\mathbf{r}_1) \approx k^2 \Delta\varepsilon(\mathbf{r}_1)/4\pi|\mathbf{r}_1 - \mathbf{r}|$ is interpreted now as the distribution of sources, whereas in fact it is the distribution of inhomogeneities; $G_2(\mathbf{r}) = \exp(ik2|\mathbf{r}|)/4\pi|\mathbf{r}|$ is the Green's function for the lower homogeneous space of the background medium at the doubled frequency, where $\mathbf{r}$ is the point of radiation and reception, which lies on the curvilinear surface.

Let us calculate the field $E(\mathbf{r}_0)$ on the average plane $z=0$ from the known field $E(\mathbf{r})$ on the curvilinear surface S using the Huygens–Fresnel principle as follows [4]

$$E(\mathbf{r}_0)=2\iint\limits_S E(\mathbf{r})\frac{\partial G_2(\mathbf{r}-\mathbf{r}_0)}{\partial n}dS, \tag{6.2}$$

where S is the curvilinear surface, where the measurements are to be performed. Here, without incurring great error, we can make the following substitution:

$$\frac{\partial G_2(\mathbf{r})}{\partial n}\approx\frac{\partial G_2(\mathbf{r})}{\partial z}.$$

It is important here that the field $E(\mathbf{r}_0)$ is defined in a plane and the fast algorithm of group focusing (analog of the Stolt migration) described above can be applied to this field. The images shown in Fig. 6.20 were obtained as a result of applying interpolation (6.1) and the group focusing algorithm. The quality of the reconstructed images is substantially improved and the level of artefacts has been reduced.

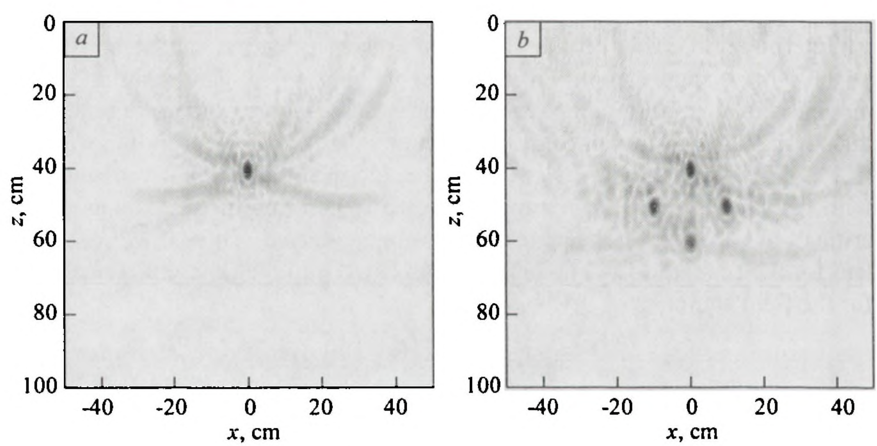

Fig. 6.20. Images of point-like inhomogeneities reconstructed by inverse focusing: *a* – for a single inhomogeneity; *b* – for four inhomogeneities.

The quality of the reconstructed image is comparable to the quality of the image obtained by applying inverse focusing. In other words, Huygens–Fresnel interpolation is actually equivalent in image quality to inverse focusing, but it allows the use of fast algorithms.

6.4. Geolocation of soil structure

This section describes the effectiveness of radar tomography for soil cover research. A comprehensive approach is proposed which combines the application of the OKO-2 ground penetrating radar (Fig. 6.21), the conventional method of cross sectioning applied in soil science, and relevant soil-testing parameters with mobile and laboratory research on the permittivity of hidden soil layers. The combination of several techniques enabled us to relate the electrical properties of soil to soil moisture and density and thereby detect the location of deep aquifers and reconstruct the actual local topography. This research was performed within the Timiryazevskoye forest district near the city of Tomsk.

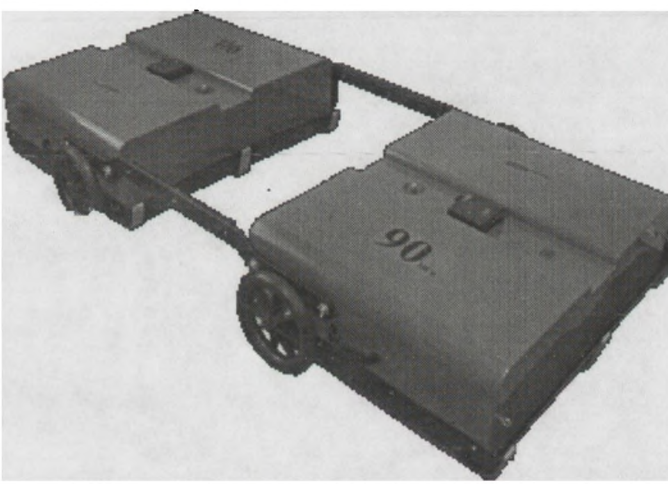

Fig. 6.21. Antenna unit of the OKO-2 ground penetrating radar with central frequency 90 MHz.

6.4.1. Contact measurements of soil characteristics

Several traces were cut under different soil conditions. Figure 6.22 presents one of the selected traces within the geomorphological slope with 3 m level difference in the Timiryazevskoye forest district near the city of Tomsk. The area is covered by green moss pine forest which is 80-90 years old, and the shrub layer consists of mountain ash undergrowth. Crown density is 40%. Soil cover includes bilberry, green moss, sedge, and several rare plants. Projective cover is 10-15%. Macrorelief is terrace above the Tom flood-plain. The mesorelief comprises the mid section and base of the slope with southern exposure, and the steepness is 3-5°. The parent material is pine forest sands.

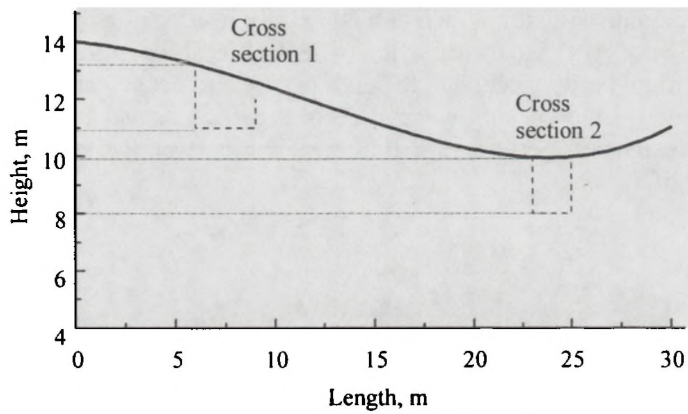

Fig. 6.22. Geomorphological slope profile and land view.

Fig. 6.23. Sod-podzolic soil profile (cross section 1).

Sod-podzolic soil with loamy sand prevails in the sounding field. This type of soil is characterized by a thin humus horizon. The organic layer here does not exceed 3-4%. Small amount of humus, lack of structural aggregates, predominance of sandy fraction in the soil texture predeteremine the high density of the structure of soil horizons over the entire soil profile. The firmest soils are illuvial horizons (B horizons) which contain pseudo-fiber layers. Pseudo-fibers consolidated by organic mineral colloids slow down the process of filtration of atmospheric moisture filtering and prevent water evaporation from deep horizons. There are short term regenerative conditions over the pseudo-fiber layers and under them. Morphologically, this is manifested by smoke-blue tones and ferrous iron staining, and also by increased humidity.

Two cross sections of soil were cut on this trace marked with a dashed line in Fig. 6.22. Figure 6.23 illustrates the morphology of sod-podzolic soil in the middle part of the slope (cross section 1). Soil samples were selected from genetic horizons of the cross section.

The complex permittivity of the samples was determined in a laboratory environment. The permittivity was measured by the waveguide-coaxial method with a P2M scalar network analyzer. The match between the calculated and measured values of the transmission coefficient and the standing wave ratio was monitored on a frequency of 90MHz. The temperature was

25°C. The density of samples in the measuring cell was taken into account. The value of the permittivity was renormalized for each sample with allowance for the density: first, it was divided into the density of the soil sample in the measuring cell, then it was multiplied by the dry density in the cross section. The dry density is the mass of a unit volume of absolutely dry soil in the undisturbed structure.

The soil moisture in the samples was measured by the dry-and-wet weight method in which the water content is calculated as the ratio of the weight of water in the sample to the dry weight of the sample. In this case, samples weighing from 10 to 25 g were dried in an oven at 105°C for 3 hours and then weighed. Then, they were oven dried once again for 3 hours and weighed once more. The weight difference between weighings was 0.004 g on average resulting in 0.1% error in the moisture measurement.

Figure 6.24 presents summary results of contact laboratory experiments for cross section 1. This cross section (Fig. 6.23) provides a clear view of three rust-colored pseudofiber layers 0.5–6 cm thick. They are distinguished by an increased value of the permittivity and density (Fig. 6.24). An increased moisture content between the layers can also be seen.

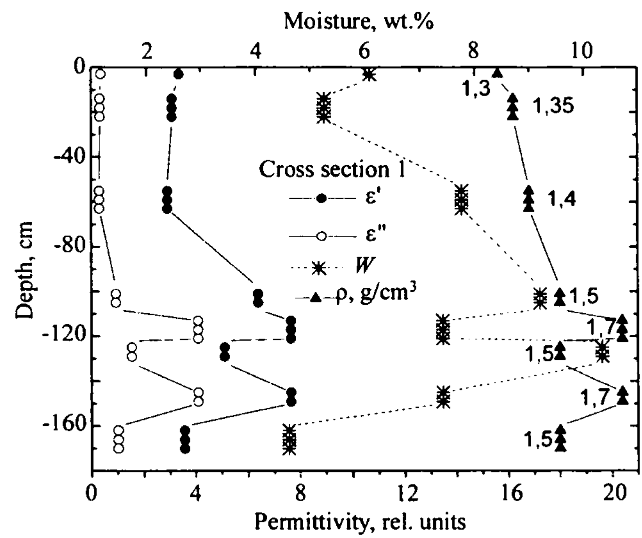

Fig. 6.24. Depth-wise distribution of moisture, dry density and permittivity for cross section 1.

Similar results were obtained for sod-podzolic soil from the dell (cross section 2). The results are shown in Figures 6.25 and 6.26.

Fig. 6.25. Sod-podzolic soil profile (cross section 2).

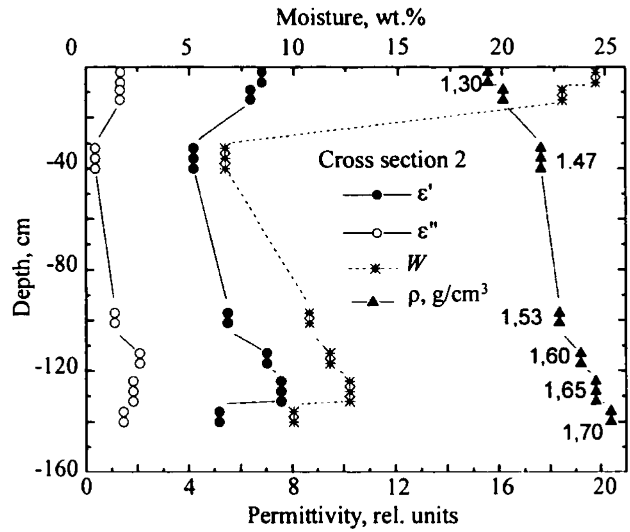

Fig. 6.26. Depth-wise distribution of moisture, dry density and permittivity for cross section 2.

6.4.2. Geolocation results

A georadar survey was conducted with an OKO-2 commercial GPR (LOGIS Ltd., Ramenskoye, Moscow Region, Russia). A subsystem with bipolar sound pulses with a central frequency of 90 MHz was decided on for soil sounding based on its penetrating power. Sounding was conducted straight in-line so that real cross sections were cut along this straight line (Fig. 6.22).

Since the profile was traced along the slope in a top-down way and sounding was conducted by a georadar set up directly on the ground, geometrical distortions showed up in the radar image (Fig. 6.27). Horizontal movement of the sounding antenna is plotted along the abscissa and the time delays of the reflected signals are plotted along the ordinate. The reflected signal intensity is plotted in grayscale. The level of the underground aquifer is shown by curve *1*. This curve was plotted using least-squares regression. The aquifer level should actually be horizontal. Correction for such distortions results in the image presented in Fig. 6.28. Here, curve *1* is turned into a horizontal line, and the upper edge of the reflected signals corresponds to the actual topography. Thus, the presence of an aquifer made it possible to reconstruct the actual local topography along the radar path.

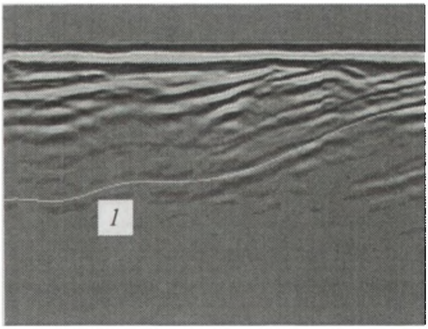

Fig. 6.27. Georadar reference profile.

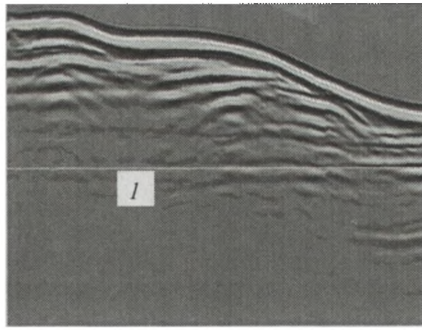

Fig. 6.28. Georadar profile taking topographic features (relief) into account.

The next stage in georadar data processing was to compress the images measured by wide-angle radar aperture. The external manifestation of this effect is the presence of the so-called *diffraction hyperbolas* in the images. The traces of these hyperbolas show up in Fig. 6.29 as curves *2* and *3*. The diffraction hyperbolas are the radar response to a point-like inhomogeneity and the analog of the point spread function in optics. The aperture angle of the hyperbolas depends on the average refractive index n of the medium in which the inhomogeneities occur. By varying the aperture angle of the approximating curves it is possible to determine the average refractive index of the soil. In this case, n has is seen to be approximately equal to ≈ 2.5. This value corresponds to a value of the permittivity equal to $\varepsilon' \approx 6.5$, which is close to the values presented in Figs. 6.24 and 6.26. Elimination of the point spread function is performed by large aperture synthesis or, what is equivalent, by two-dimensional matched filtering.

However, before matched filtering can be applied, another operation needs to be performed, namely correction for exponential attenuation of the radiation with penetration depth into the medium, i.e., into the soil. Of course, this can be done only on average for the background medium.

The sequence of operations is as follows: 1) for all positions of the antenna the time series (vertical records) are transformed into the amplitudes of the corresponding analytical signal; 2) the obtained amplitude profiles are averaged over all antenna positions. The average attenuation of the relative amplitude of the analytical signal, obtained by this method, is presented in Fig. 6.30. Its exponential approximation is represented by the dashed line.

Correction for attenuation makes it possible to increase the relative contribution of the response signals from the deep layers.

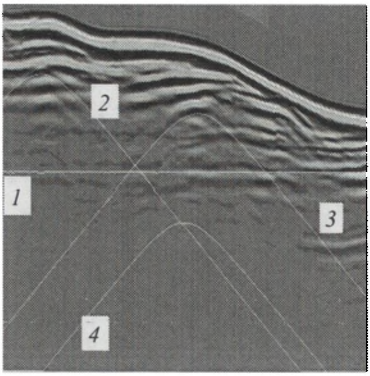

Fig. 6.29. Diffraction hyperbola traces.

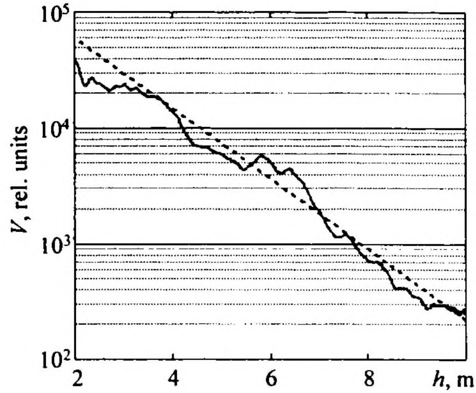

Fig. 6.30. Exponential attenuation of radiation.

Combined execution of the above-mentioned procedures (matched filtering and amplitude correction) delivers the final result – a vertical cross section along the radar path (Fig. 6.31). The results show that a number of features in the obtained cross section match up well with the results of contact measurement.

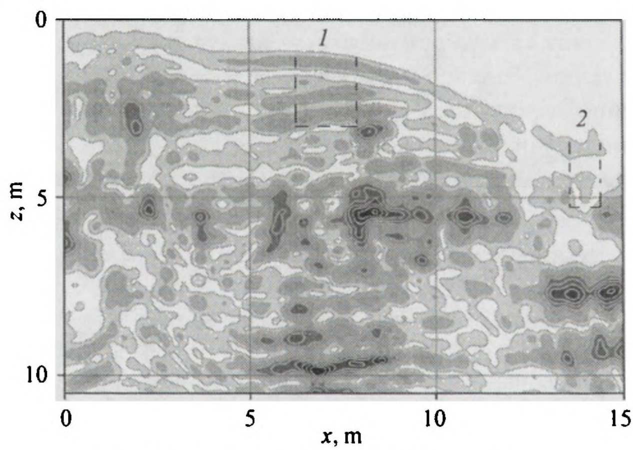

Fig. 6.31. Radar cross section of sounding path.

This work demonstrates a high correlation between the structural features revealed by radar non-destructive sounding and by contact measurement. The procedures required for correct processing of the radar data are

- data correction for relief (local topography);
- reconstruction of the average refractive index, and vertical positioning of the data;
- amplitude correction for attenuation of radiation with depth.

6.5. UWB-sounding of media in a petroleum reservoir

In our studies of the formation of radiation wave projections using different sounding techniques we showed that to solve the inverse problem, namely the problem of reconstructing the distribution of inhomogeneities, it is necessary, first of all, to localize the radiation in the propagation medium. Only under this condition does reconstruction of the structure of inhomogeneities become achievable, i.e., in real time and with acceptable accuracy. Realization of the localization effect can be achieved in two ways which are conceptually equivalent. These are computer-based focusing and physical focusing. A combination of both techniques is also possible. In this context, the requirement arises of developing a working model that could enable radiotomography of different inhomogeneities (objects) in the medium according to both schemes: the scheme with reflection (location) and the scheme with ray transmission. Of course, in this case localization of radiation is mandatory. To prove the efficiency of the working model we have used it in studies on simulated media which are typical for a petroleum reservoir.

A TMG-100010P01 bipolar generator was used as the transmission unit in the developed model radiotomograph with a pulse shape similar to one period of a sine wave with an amplitude of ±8 V and a duration of 100 ps at the 0.1 level of the amplitude with a pulse repetition rate of 100 kHz (signal 1 in Fig. 2.7). A TMR8140 stroboscopic oscilloscope was used to record the signals. A double mirror focusing system constructed in the Cassegrain configuration (Fig. 6.32) as used to localize the region of interaction of radiation with matter. Such a design delivers lateral localization of radiation on the order of 3–5 cm. The test substance (simulated medium) was placed into a measuring cell with planar boundaries.

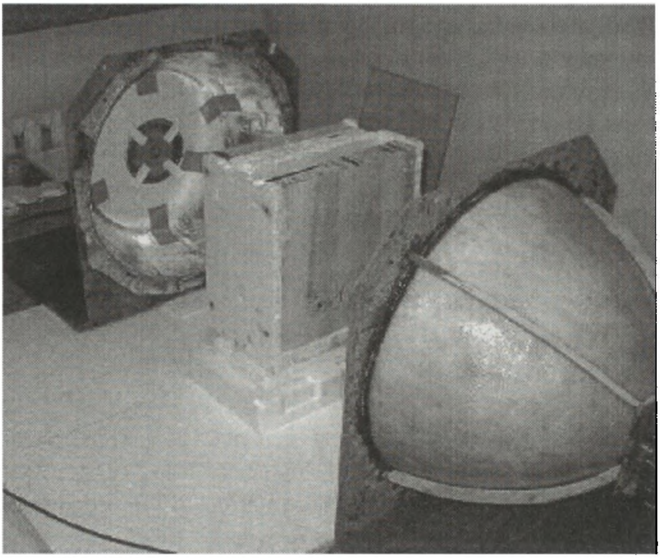

Fig. 6.32. UWB-radiotomograph setup for sounding simulated media of a petroleum reservoir.

Siliceous sand was used as the carrier fraction, and oil from the oil well № 418 of the Mirnoye field and from well № 11 of the Kazanskoye field, Tomsk Region, was used as the filling fraction. A salt solution was prepared from distilled water and table salt. The percentage amounts of all components were taken according to Table 6.1.

Table 6.1

Medium structure in a petroleum reservoir

№	Layer	Water, %	Salinity, g/l	Clay, %	Sand, %	Oil, %	Gas (methane), %	Depth, m
1	Water-Clay layer (oil well)	88	3	12	0	0	0	0.2
2	Oil-Bearing Stratum	6	17	0	85	9	0	5
3	Gas Cap	4.5	17	0	85	0	10.5	1
4	Clay Cap	3	17	97		0	0	2
5	Water-Bearing Stratum	15	17	0	85	0	0	3

The fundamental problem here is to investigate the pecularities of UWB pulse propagation in the specific media of a petroleum reservoir. The specific practical purpose is to investigate the propagation of UWB radiation in simulated media of a petroleum reservoir and evaluate the possible use of UWB radiation for well logging and navigation of drilling equipment in horizontal drilling.

Interest in such research has grown more intense all over the world and in Russia as well. It is assumed a- priori that the use of UWB radiation provides relatively deep penetration into oil-bearing media while maintaining sufficient spatial resolution. This research is based on the results of UWB experiments and should give a direct answer to the question of the realistic use of UWB techniques for radio-wave well logging in the exploitation of hydrocarbon deposits.

According to general ideas about the structure of the media of a petroleum reservoir, it was believed that the oil-bearing stratum lies between the gas cup and the water-bearing stratum, with the clay cap in between. It is supposed that radio-wave sounding should be performed within the oil-bearing stratum, i.e., directly from the horizontal water-injection borehole filled with water-clay sludge.

Using a collimated beam helps evaluate the actual penetrating ability of the UWB-radiation by comparing the forms of the incident and transmitted pulses and also evaluate the electrical properties of the test media. Two records of such signals are presented in Fig. 6.33.

The calculated spectra of the incident $S_x(f)$ and transmitted $S_y(f)$ signals enabled us to find the transfer function of a planar layer $W(f) = S_y(f)/S_x(f)$, and, in the case of a planar layer, to determine the complex permittivity of the filling substance $\varepsilon = n^2$ using the formula

$$W(f) = \frac{4n}{(n+1)^2 - (n-1)^2 \exp(2iknd)} \exp(iknd),$$

where d is the layer depth and $k = 2\pi f/c$ is the wave number for free space. This model considers all possible wave re-reflections which arise within the layer when a plane wave penetrates it. The obtained parameters of the main fractions can be used to determine the blend parameters (parameters of mixtures) according to the so-called refraction model, according to which

$$n = \sum_j n_j w_j,$$

where w_j is the volume fraction of the jth component with complex index n_j.

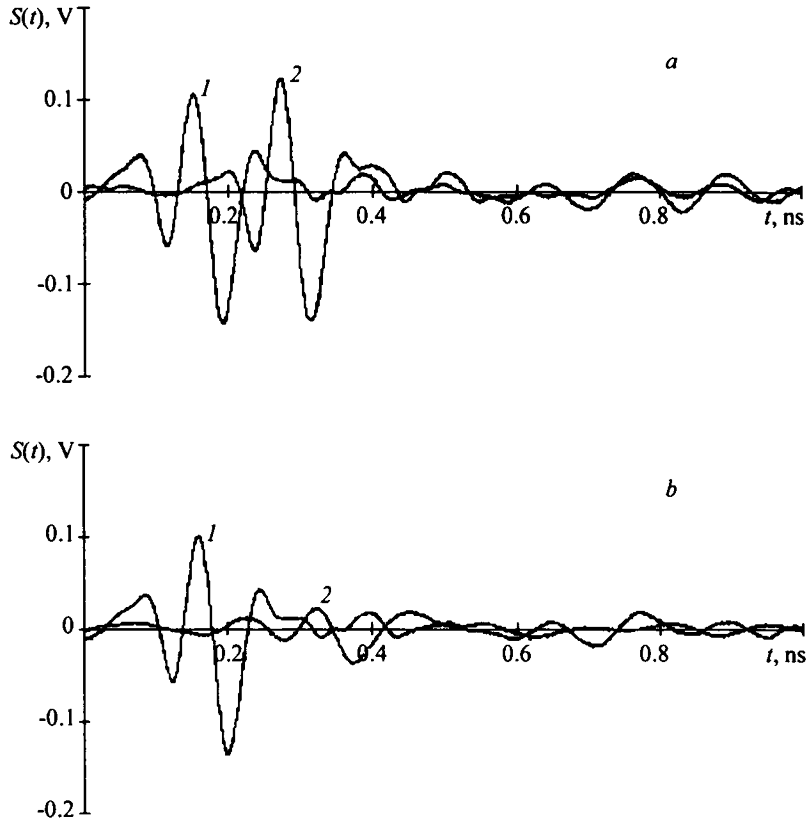

Fig. 6.33. Shape of collimated UWB-pulse with duration of 100 ps while empty cell (curve *1*) and cells (curve *2*) filled with sand (*a*) and with oil-bearing substance (*b*) were examined in the open space. The cell thickness was 50 mm.

Figure 6.34 plots the permittivity values of the main media in a petroleum reservoir as a function of frequency.

The obtained spectra of complex blend permittivity (permittivity of mixtures) can be used to estimate pulse transmission and reflection within pure layers and any of their combinations as well. Calculated attenuation of a radiation pulse is plotted in Fig. 6.35 as a function of penetration depth in a simple oil-bearing stratum. The signal envelope M (amplitude envelope) is understood to be the modulus of the corresponding analytical signal.

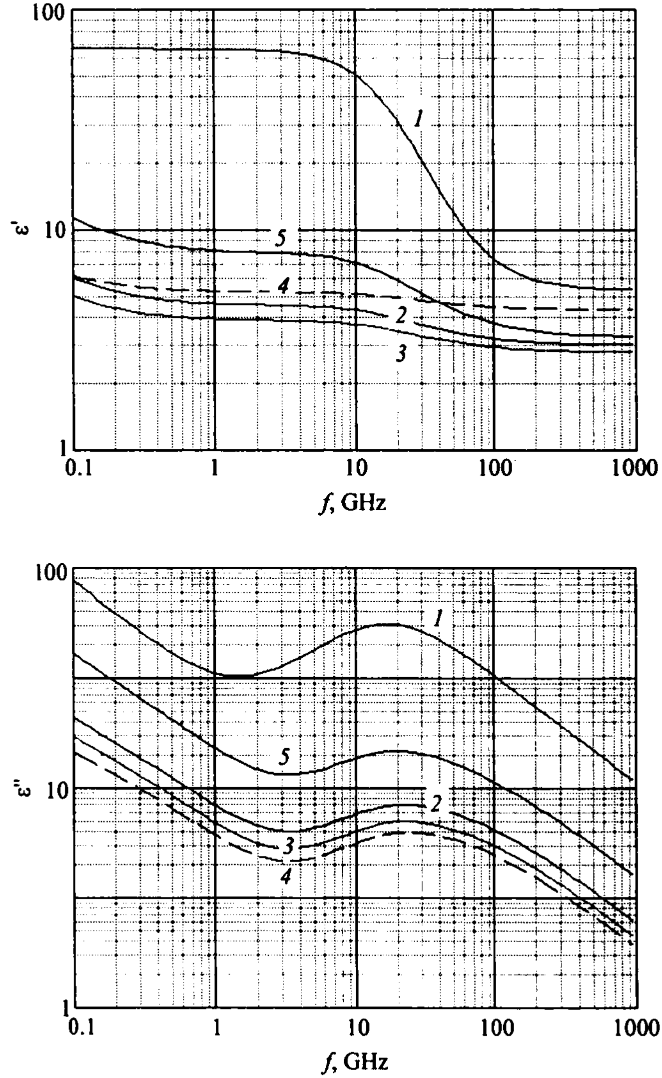

Fig. 6.34. Real and imaginary parts of medium permittivity in a petroleum reservoir: curve *1* – water-clay layer (well), curve *2* – oil-bearing stratum; curve *3* – gas cap; curve *4* – clay cup; curve *5* – water-bearing stratum.

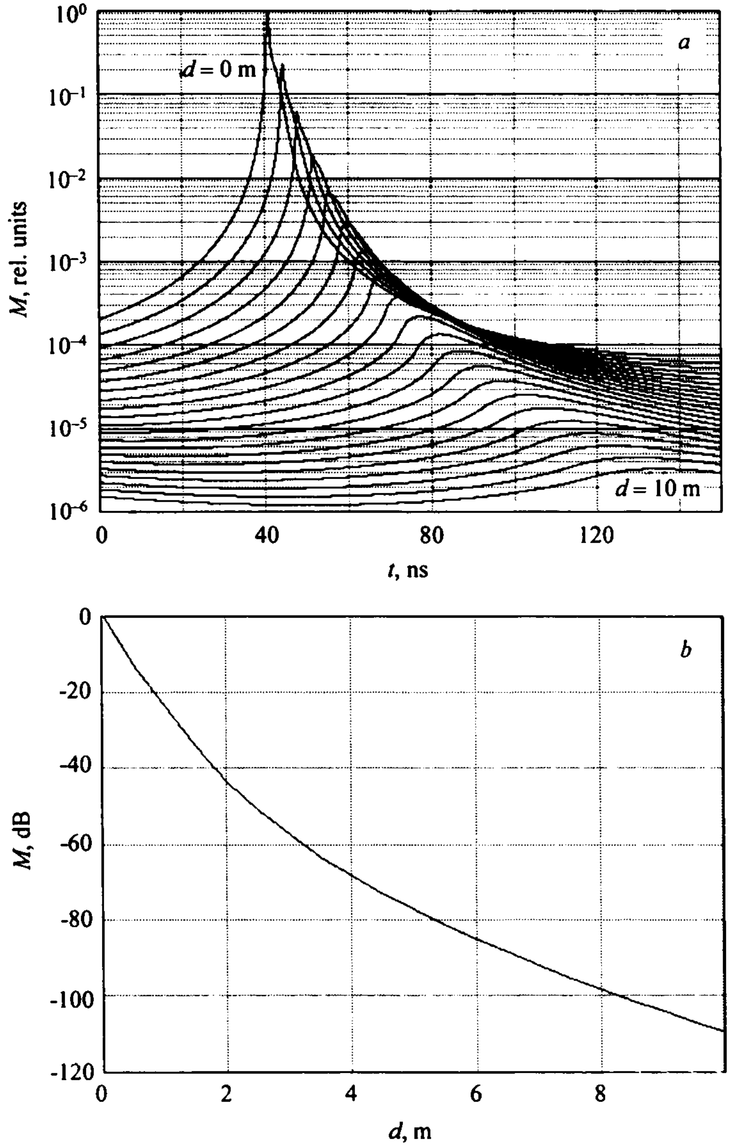

Fig. 6.35. Shape of the UWB pulse envelope (*a*) and attenuation of its maximum (*b*) depending on the penetration depth into the oil-bearing stratum.

The calculations employed a so-called balanced optimal signal, for which

$$S_x(t) = S_0\left(\frac{t}{T}\right)^p \left\{\exp\left(-\frac{t}{T}\right) - m^{p+1}\exp\left(-m\frac{t}{T}\right)\right\},\ t \ge 0,$$

$$T_0 = T\frac{p+1}{m-1}\ln(m).$$

T_0 is the duration of the first (short) lobe of the pulse at the zero level. We set $T_0 = 1$ ns and $p = m = 6$.

It can be seen that the attenuation per unit length decreases smoothly from 25 dB/m at the surface to a value of 5 dB/m at a depth of 10 m. This is caused by the rapid rate of absorption with depth of the high-frequency components compared to the slower attenuation of the low-frequency components. In the case of radio-sounding of a petroleum reservoir directly from the water-injection borehole, the strongest influence on the reflection of waves comes from the boundary of the borehole itself. The weighted differential technique (WDT) for extraction of weak signals from deep layers involves extracting the contribution of the boundary reflection $|Y(t)|$ from

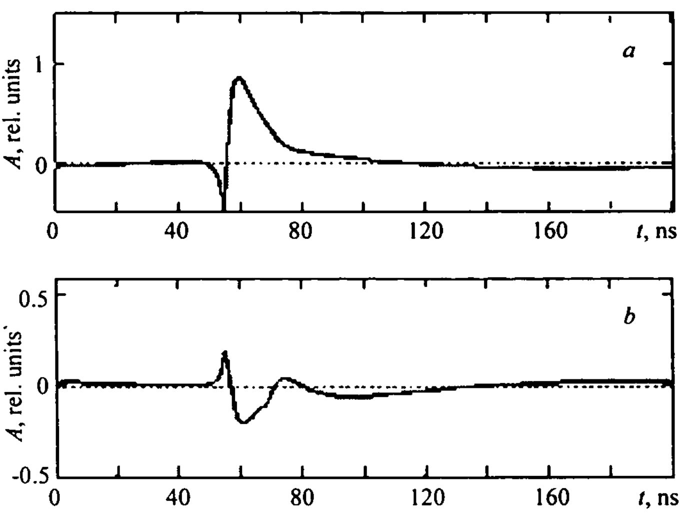

Fig. 6.36. Shape of reflected pulse after weighted differential processing for the oil-bearing stratum at 1-m depth for sounding of the petroleum reservoir in the downward (*a*) and upward (*b*) direction.

the integral signal $|Y(t)|$ and normalizing. That technique reduces to calculating the following quantity

$$A(t) = \frac{y(t)}{|Y(t)|} \approx \frac{|S(t)|}{|Y(t)|} - 1 .$$

This technique makes it possible to clearly delineate the difference between upward and downward sounding (Fig. 6.36), which is especially important for navigating the drilling equipment as well as tomographic reconstruction of the three-dimensional structure of the media in a petroleum–gas reservoir. In the final analysis, the obtained result delivers a positive response to the question of the realistic applicability of UWB techniques to radio-wave well-logging for exploitation of hydrocarbon fields.

6.6. Summary

The methods and approaches considered in this chapter demonstrate the efficiency of UWB tomography techniques for georadar research. The suggested approaches enhance the accuracy of current techniques and provide new efficient methods, e.g., for sounding of the media in a petroleum–gas reservoir and navigating the drilling equipment in horizontal and angular drilling.

Not without practical interest is random and incomplete scanning as well as scanning techniques over a curved surface. All results are confirmed by numerical simulation and comparison with experimental data. The results on practical radio sounding of soils at depths down to 6 m in combination with contact measurements of the vertical profile parameters are important.

Chapter 7

ULTRA-WIDEBAND TOMOGRAPHY OF LAND COVERS

The contents of this chapter generalize the results of papers [1–16].

7.1. Forest tomography

In recent years, interest in boreal forests, which are the lungs of the Earth accumulating carbon, has risen significantly. Hence, there is an increased interest in the development of methods for remote monitoring of the condition of forest covers. Radio-engineering space-based assets in the microwave range are especially efficient for forest sounding. These are all-weather high-performance systems. For an adequate assessment of forest conditions, an unambiguous correspondence between radiophysical measurements and the results of conventional methods for measuring forest parameters must be established. The potential for accuracy of the method identified by experimental research on a UWB radar functional prototype has become a subject of interest.

The authors carried out tests of the pulsed locator (radar) prototype to acquire measurements of the parameters of a normal larch forest in the test field of the Forest Institute, Siberian Branch of the Russian Academy of Sciences (Pogorelki Village, Krasnoyarsk Region). The exterior of the antenna system and a block diagram of the UWB locator prototype for forest tomography are presented in Fig. 7.1.

For testing of forest areas a pulse driver with a 50-ps edge was developed and tested (see Fig. 7.2). The bandwidth of the radiated signal, extending from 500 MHz to 17 GHz, overlapped the frequency band of forest semi-transparency.

The transverse resolution of the UWB locator is defined by its directivity pattern (DP). Results of the actual DP evaluation, obtained from the signal reflected from a corner reflector, are presented in Fig. 7.3 (curve *1*). The amplitude of the corresponding analytical signal was used. Curve *2* plots the approximation, which as used in subsequent tomographic processing. The full width at half maximum (FWHM) of the DP locator was 4–5°. The snail-type UWB antennas described in Chapter 2 (Figs. 2.4 and 2.5) were used as feedhorns for the transmitting and receiving antennas to provide the required bandwidth.

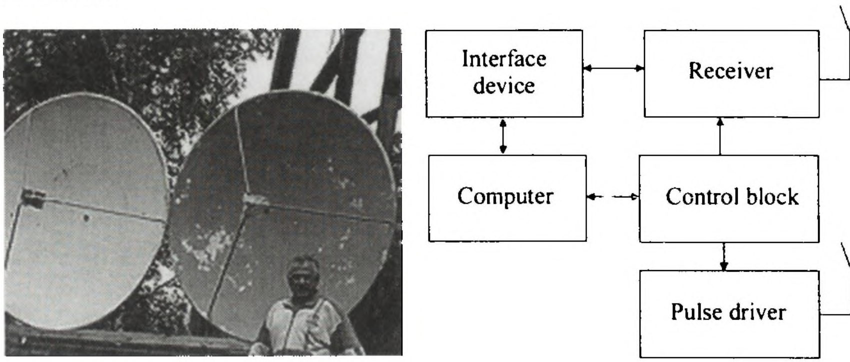

Fig. 7.1. External view of antenna system and block diagram of the UWB locator for the forest tomography.

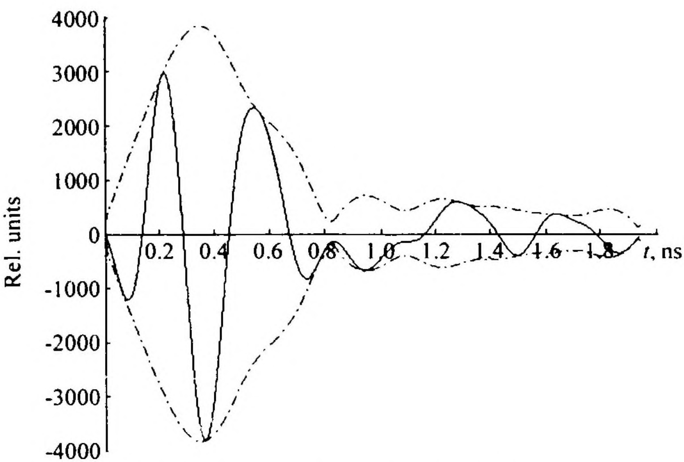

Fig. 7.2. The waveform of radiated pulses.

In forest tomography, it should be taken into account that the forest is simultaneously the object of sounding and the medium for radiation propagation as well. It can be assumed in the first approximation that wave scattering arises on certain forest inhomogeneities (trunks, branches, leaves and needles), but direct and reflected radiation penetrates the forest canopy with multiple attenuation. This means that the amplitude of the reflected signals will decay exponentially with distance from the scattering point. A graph of the experimental dependence of the amplitude of the analytical signal, which corresponds to the azimuth-averaged radar response, is presented in Fig. 7.4. The slanting dashed line describes the exponential attenuation averaged over multiple angles.

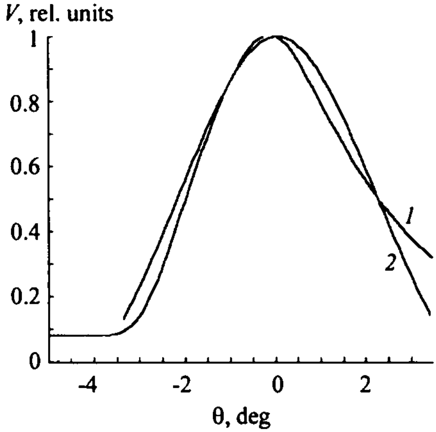

Fig. 7.3. Evaluation of the UWB Locator DP.

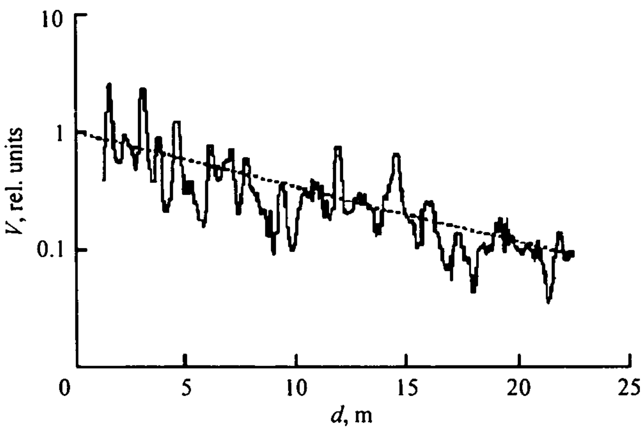

Fig. 7.4. Attenuation of the UW radiation.

It follows that the first operation of forest tomogram reconstruction is to align the multi-angle radar data by renormalizing them with respect to their average dependence. The second operation is compression of the radar response over time (distance). This is a quite routine procedure, which is realized using matched filtering. It results in a maximum increase in the signal-to-noise ratio: the contributions of individual inhomogeneities become more localized and the noise is averaged out. The third, and less conventional, operation is deconvolution, i.e., the operation of removing image blurring over the azimuth (bearing angle) due to the finiteness of the antenna directivity pattern. Here, the approximating antenna DP is used, which was mentioned in the previous section. Deconvolution is performed using Wiener filtering with regularization.

Forest sounding was performed by scanning the azimuth (bearing angle) over the range from $-10°$ to $+10°$ and the elevation angle over the range from $0°$ to $15°$. The reconstructed tomogram of the forest test area is presented in Fig. 7.5 as a grayscale plot. The circles indicate the locations of trees in the landscape plan of the survey area. Figure 7.5 demonstrates good agreement of the obtained results with the landscape plan even up to the positions of individual trees. Such agreement was achieved in 70% of cases. Besides the marked trees, some additional inhomogeneities are visible in the tomogram, which seem to be large branches of the forest canopy.

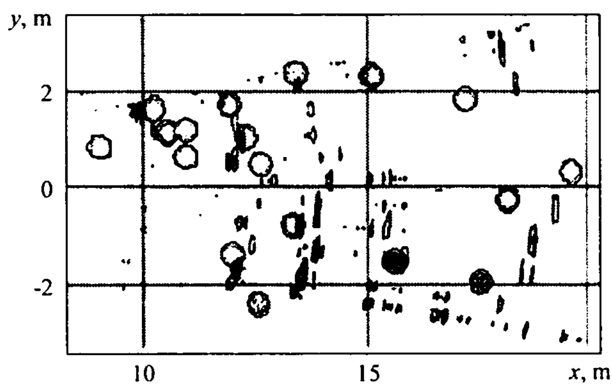

Fig. 7.5. Forest landscape plan (circles) and forest tomogram.

Further increase in spatial resolution can be obtained (see Section 7.3) if we take into account the possibility of transforming from multi-angle measurements of the distribution of the forest radar response to the equivalent spatial frequency spectrum. With the help of the Fourier transform, this spectrum is brought into a one-to-one correspondence with the spatial field distribution in an equivalent transverse aperture. The spatial field distribution reconstructed in this way can then be used for computer-aided focusing of the recorded field at any required distance and angle using the synthetic large aperture technique. The larger the inhomogeneity that is located at the focusing point, the more intense the response will be. By varying the location of the focusing point it is possible to achieve full scanning of the sounded area so that a tomogram of the inhomogeneous medium (the forest in our situation) can be obtained. Of course, the proposed procedure works only within the limits of the Fresnel diffraction zone.

7.2. Tomography of wooden constructions

This section discusses results of field tests of the nanosecond radar which were obtained in collaboration with personnel of the Department of Physical Problems, Buryat Scientific Center, SB RAS (Ulan-Ude). The testing was conducted at an arbitrarily chosen site with a corner reflector inserted into the scene as a test object.

The nanosecond radar developed at IHCE SB RAS (Tomsk) radiated short pulses with a duration of 10 ± 2 ns, with a peak power of 40 W, and a pulse repetition rate of 5 kHz on a carrier frequency of 10 GHz. The width of the DP of this radar was $\alpha = 2.5°$. These characteristics provided range resolution of objects which are larger than 1.5 m in size. A logarithmic amplifier was used to increase the dynamic range of the radar. The radar orientation system allows to scan over a large angular range both in azimuth (bearing angle) and elevation angle. The waveform of the received pulse was recorded using a Tektronix digital oscilloscope with a sample rate of 10 GS/s and then processed on a NoteBook computer in MathCad.

A nondescript field on one of the test sites of BSC SB RAS near Istomino village was selected as the test area. This field was situated at a distance of 60 m behind a wooden fence on uneven ground covered with scanty vegetation. The only object located on this wasteland was an unfinished wooden house. A trihedral corner reflector (CR) with an edge size of 30 cm situated at a height of 2 m was used for the purpose of calibration. During the measurements, one corner reflector was placed inside the house in a window opening, the other one – outside the house, on the green. Constant visual contact between the radar and the CR ensured accurate alignment of the optical axis of the CR with the direction to the radar.

Tomographic measurements were preceded by measurements of the attenuation of the response with distance to the CR and measurements of the radar directivity pattern. It was confirmed that the amplitude of the radar response A fell off inversely as the square of the distance d^2 up to the target against the background of which a relatively small interference contribution was observed due to the effect of the Earth's surface. It was shown that although the FWHM of the DP was not large ($\alpha = 2.5°$), the contribution of the sidelobes was significant due to the extended dynamic range of the radar even when the radar antenna axis is raised above the horizon.

Tomographic measurements of the test site involved recording the radar response as a function of the azimuth angle α with a step of 1° within a range of ±13° relative to some average direction. Per its elevation angle, the antenna axis of the radar was oriented precisely toward the CR. Each recorded response matched the position of a corresponding reflection point in the Cartesian system:

$$x = d\cos\alpha,\ y = d\sin\alpha\,,$$

where $d = c\tau/2$ and τ was the corresponding signal time delay. The radar was taken to be located at the origin of the coordinate system. The resulting two-dimensional radar image $A(x, y)$ for transformation to the tomographic image S was renormalized for geometrical attenuation with range:

$$S(x, y) = d^2 \cdot A(x, y)\,.$$

That procedure had already been used previously for forest tomography (Section 7.1). A tomographic image, reconstructed in that way, is presented in Fig. 7.6 in grayscale using the Contour Plot option in MathCad. The actual positions of the objects are marked off here with dashed lines. Locations of two corner reflectors (objects *2*) are shown as triangles. The entire image is bounded in bearing angle and range by the scanning area.

Let us discuss the obtained result. In Fig. 7.6, object *1*, corresponding to the wooden fence, has a straight-lined shape kinked at the point $x = 0$ m, $y = 57$ m, as can be easily identified in the image. The position of the back post clearly rising up above the fence is marked by a circle. Two CR's (objects *2*) are imaged quite distinctly and are localized both in range d and in azimuth α. The front wall (object *3*) of the unfinished house, which faces the radar is visible in the image. Object *4* corresponds to a reflection from some hill with quasi-sinusoidal channels which are parallel to the fence on the test site. This hill was covered by the radar sidelobes. Objects *5* and *6* are manifestations of the effect of multipath propagation of radio-waves. This is proven by the fact that they are located at exactly the same azimuth as object *4* and they are nearly equidistant, consequently they are the result of double-hop and triple-hop reflections of signal *4* from the fence *1*.

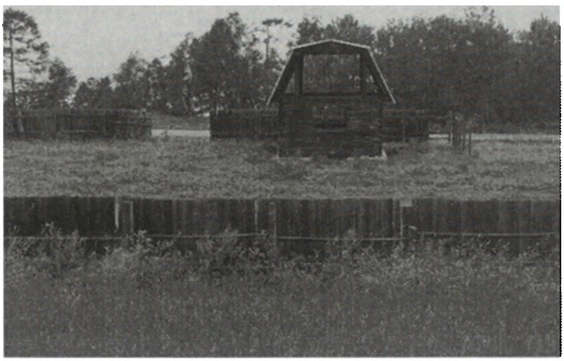

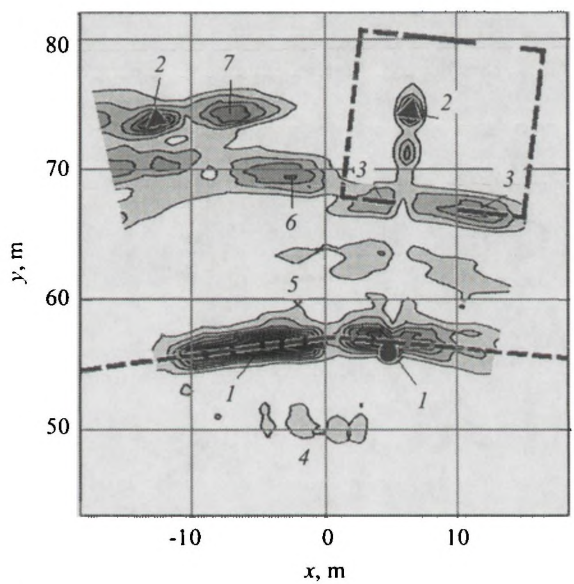

Fig. 7.6. Photograph and radio-tomographic image of objects in the test area: *1* – fence; *2* – corner reflectors; *3* – wooden house.

Object *7* is of the greatest interest. First, there were no visible objects at this point at the test site. Second, the observed distance between the radar and object *7* is close to the distance to the adjacent corner reflector. This suggests that the phantom object *7* belongs to the actual corner reflector *2*. The low dependence of the radar response of the CR on its orientation within the range ±45° (Fig. 7.7) is key to understanding these phenomena. The situation arises in this regard, when the signal transmitted by the radar to the point 7 is scattered over the edge of the fence 1 and propagates to the corner reflector 2, which reflects the signal directly back (Fig. 7.8*a*). The scattering diagram

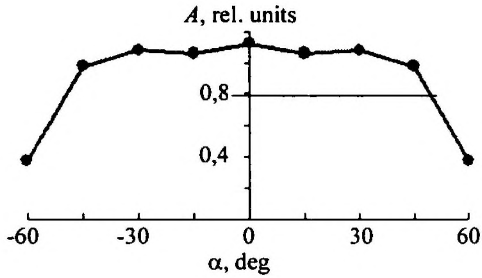

Fig. 7.7. Dependence of the reflectivity of the corner reflector on its azimuthal orientation.

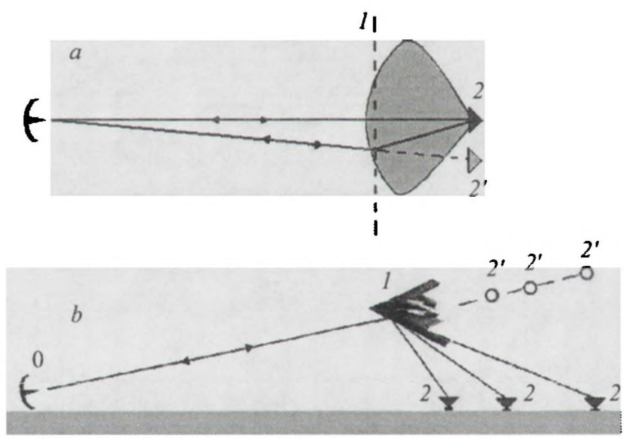

Fig. 7.8. Generation of false images (phantoms) of corner reflectors: *a* – on the test site (top view), *b* – in quasi-bistatic location of low-reflective targets (side view).

of the CR is filled-in in gray in Fig. 7.8*a*. Next, the signal returns to the radar from the initial direction. This results in the phantom 7 (shown in Fig. 7.6), which is represented as object *2'* in Fig. 7.8*a*.

One possible application of the discovered effect connected with the scattering characteristics of the CR is of interest. The idea here is the possible application of passive illumination for low-reflective target detection, e.g., stealth aircraft (Fig. 7.8*b*). The idea is to use the spatially distributed field from the corner reflectors *2*, which is set up on the approach to a radar-protected zone. In this case, the absence of direct reflections from the radiolocation (radar) target *1* can be compensated by secondary signals of the corner reflector, which makes it possible without large losses to, in fact, realize bistatic radiolocation using a single-position radar. The phantom objects *2'* will be observed to lie along the direction to the actual low-reflective target. The chain of phantoms *2'* allows one to detect the actual target and determine the direction to it.

The work presented above confirms the potential of using the considered nanosecond radar for sounding the environment and for verifying the data of aerospace sounding.

7.3. Refocusing method

Further increase of spatial resolution can be achieved if the possibility of transforming from multi-angle measurements of the distribution of a forest radar response to the equivalent spatial frequency spectrum is taken into account. With the help of the Fourier transform, this spectrum is put into one-to-one correspondence with the spatial field distribution in some equivalent transverse aperture (Fig. 7.9). After the spatial field distribution is reconstructed, the synthetic aperture technique can be used and the recorded field can be focused at any predefined distance and angle within the Fresnel diffraction zone, of course, where possible.

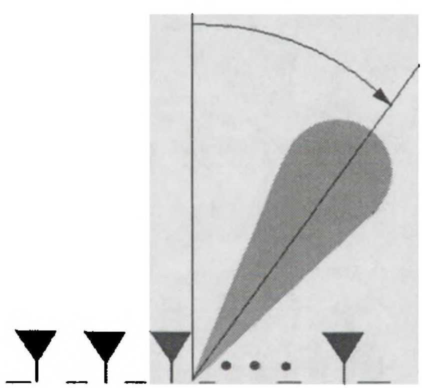

Fig. 7.9. Directivity pattern and equivalent aperture of an antenna.

Let us consider, element by element, how this can be done. Let the field distribution be defined as $\Gamma(\boldsymbol{\rho})$ over a finite aperture of the antenna system. From this distribution, the Fourier transform delivers the spectrum of spatial frequencies $\mathbf{u} = (u_x, u_y)$ of the radiated field:

$$\tilde{\Gamma}(\mathbf{u}) = \int_{-\infty}^{\infty}\int_{-\infty}^{\infty} \Gamma(\boldsymbol{\rho})\exp(i\mathbf{u}\boldsymbol{\rho})(d^2\boldsymbol{\rho}),$$

and, conversely, the field distribution over the aperture can be obtained from the spatial frequency spectrum using the inverse Fourier transform:

$$\Gamma(\boldsymbol{\rho}) = (2\pi)^{-2}\int_{-\infty}^{\infty}\int_{-\infty}^{\infty} \tilde{\Gamma}(\mathbf{u})\exp(-i\mathbf{u}\boldsymbol{\rho})(d^2\mathbf{u}),$$

where $(d^2\boldsymbol{\rho}) = dxdy$ and $(d^2\mathbf{u}) = du_x du_y$ are the integration elements. For radiation with wave number k, the spatial frequencies are related to the direction of wave propagation defined by the angular variable relations

$$u_x = k\sin\vartheta\cos\varphi,\ u_y = k\sin\vartheta\sin\varphi,\ u_x = k\cos\vartheta.$$

Taking this into account, we can write

$$(d^2\mathbf{u}) = k^2\cos\vartheta(\sin\vartheta d\vartheta d\varphi) = ku_z d\Omega,$$

where $\sin\vartheta d\vartheta d\varphi = d\Omega$ is the solid angle element. Thus, it is possible to write

$$\Gamma(\boldsymbol{\rho}) = \int_{-\infty}^{\infty}\int_{-\infty}^{\infty} \tilde{\Gamma}(\mathbf{u})ku_z\exp(-i\mathbf{u}\boldsymbol{\rho})d\Omega = \int\int R(\vartheta,\varphi)\exp(-i\mathbf{u}\boldsymbol{\rho})d\Omega.$$

Here the following quantity should be taken as the diagram function of the antenna $R(\vartheta,\varphi)$

$$R(\vartheta,\varphi) = \tilde{\Gamma}(\mathbf{u})ku_z.$$

After normalization to the maximum of the modulus, this function is the directivity pattern of the antenna, i.e., the field distribution over the angular variables.

This latter equation establishes a connection between the complex diagram function of the spatial distribution of the field and the spectrum of its spatial frequencies. If the angular distribution of the field is known, the spatial frequency spectrum can always be recovered by renormalization

$$\tilde{\Gamma}(\mathbf{u}) = R(\vartheta,\varphi)/ku_z$$

and then, the distribution of currents over the aperture $\Gamma(\boldsymbol{\rho})$ will be recovered by the inverse Fourier transform. This pertains to definite spectral frequency $f = ck/2\pi$.

If the distribution of currents over the aperture is known, it can be focused on an arbitrarily assigned point in space $\mathbf{r}$ (Fig. 7.10). For this purpose, it suffices to sum up in-phase all values of the current relative to the point $\mathbf{r}$, which is written as

$$E(\mathbf{r}) = \int_{-\infty}^{\infty}\int_{-\infty}^{\infty} \Gamma(\boldsymbol{\rho})\exp(-ik|\boldsymbol{\rho}-\mathbf{r}|)(d^2\boldsymbol{\rho}).$$

In the case when the receiver and the transmitter are collocated (the radiolocation case), this is written as

$$E(\mathbf{r}) = \int_{-\infty}^{\infty}\int_{-\infty}^{\infty} \Gamma(\boldsymbol{\rho})\exp(-2ik|\boldsymbol{\rho}-\mathbf{r}|)(d^2\boldsymbol{\rho}).$$

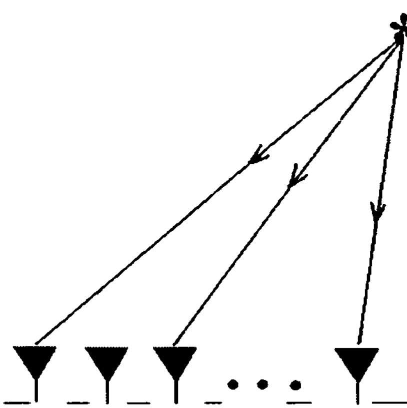

Fig. 7.10. Synthetic and focused radiation at a given point.

If there is an actual inhomogeneity at the focusing point, the intensity of the response will be directly proportional to the degree of non-uniformity. If there is no inhomogeneity, i.e., scatterer, at the focusing point, the response will be close to zero. By varying the position of the focusing point it is possible to scan the entire sounded area so that the tomogram of the inhomogeneous medium (the forest in our situation) can be obtained. The procedure proposed here is computer-based, and is equivalent to the synthetic large aperture technique [1–16]. The transverse spatial resolution of inhomogeneities can be markedly improved. In the first approximation, the resolution in the focusing area achieved by using a synthetic aperture radar system is estimated as

$$\Delta x = 2\lambda z / 2D ,$$

where λ is the wave length; z is the distance from the aperture to the focusing point, and $2D$ is the size of the synthetic aperture. This estimate is the distance between the first zeros.

It is obvious that the proposed procedure works only within the Fresnel diffraction zone (the near field zone), which is defined by the condition

$$z \le z_D ,$$

where $z_D = D^2/\lambda$ is the diffraction length of the light beam for a wave beam with radius D (the aperture radius in our situation) and λ is the wavelength of the radiation [8]. In other words, z_D is the distance within which the phase difference from the center to the edge of the aperture is significant enough to be measured. Generally, this zone is called the Fresnel diffraction zone. For example, for the wave length $\lambda =$ 0.3 m and the aperture width $D = 3$ m, the diffraction length z_D is estimated as 30 m. For $\lambda = 0.1$ m it increases to $z_D = 90$ m. For the frequency equal to 7.1 GHz ($\lambda = 0.04$ m) and the aperture width $D = 1.5$ m, the diffraction length $z_D = 53$ m. This latter distance covers the entire extent of exponential attenuation of the field in forests as measured in units of the attenuation length.

A scanning system having a directivity pattern with a width of 3° in the azimuthal plane (Fig. 7.11) was numerically simulated to validate the efficiency of the proposed approach. Such a directivity pattern is realized for the aperture $2D =$ 6 m and the wave length $\lambda =$ 0.5 m. Eighty points inside the aperture were used in the calculation, which implies a discretization step of 7.5 cm (0.15 λ).

Angular scanning was performed in the range (–90°, +90°) under the assumption that one corner reflector was placed at the point $x = 5$ m, $y = 6$ m.

The angular spectrum so obtained was recalculated to the spatial frequency spectrum and then to the equivalent field distribution over the aperture. The above-described focusing technique was applied to the obtained equivalent field distribution. The focusing of the field in the vicinity of the focusing point achieved in this way is displayed in grayscale in Fig. 7.12. The boundary of the DP of the antenna for sounding from the point $x = 0$, $y = 0$ is indicated by dashed lines.

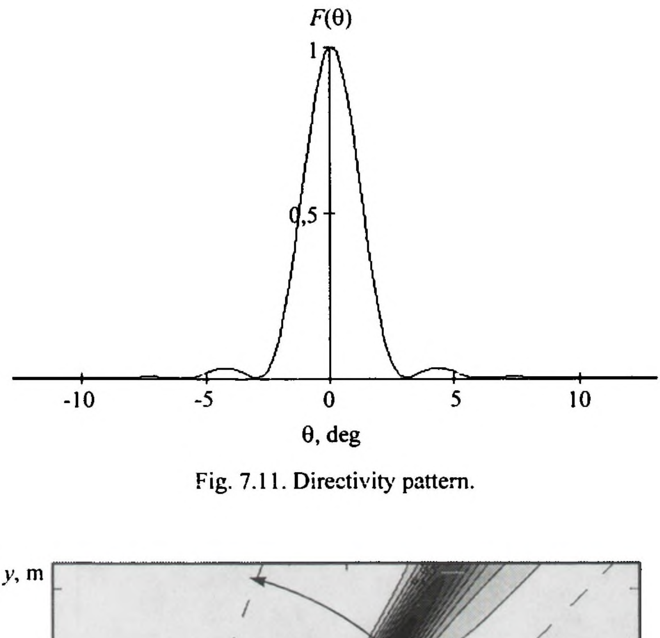

Fig. 7.11. Directivity pattern.

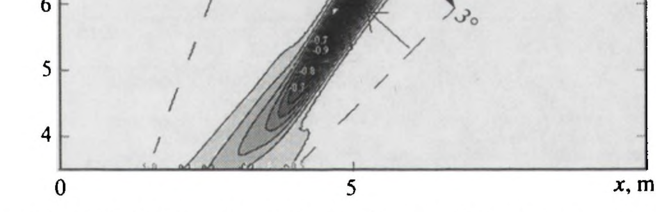

Fig. 7.12. Field amplitude distribution around the focusing point.

It can be seen that the best focusing of the field (indicated by the arrows) is realized at the position of the corner reflector. The size of the focused field is estimated as 0.5 m (FWHM) while the energy spread width calculated from the DP at this distance is estimated as 3.7 m. Thus, the resolution has been improved by roughly sevenfold thanks to the focusing effect. Note that the distance between the first zeros in this region is somewhat greater – by about 1 m; however, it is preferable to use the FWHM value as the estimate.

Using pulsed radiation and matched filtering, it is possible to obtain the 2D tomogram, i.e., the spatial distribution of inhomogeneities in the sounding plane. For this purpose it is sufficient to focus at all frequencies of the pulsed signal spectrum:

$$S(\mathbf{r},\tau)=\int S_0(f)E(\mathbf{r},f)\exp\{i2\pi f\tau\}\,df\,,$$

where $S_0(f)$ is the spectrum of the sounding pulse, and $\tau = 2r/c$.

In this way, additional scanning over range will be achieved and the overall spatial resolution of inhomogeneities will be improved. Figure 7.13 displays an example of reconstruction of a tomogram of three scatterers using the above-described procedure for a pulse with a duration of 100 ps. The spatial distribution of the function $|S(\mathbf{r},\tau=2r/c)|$ is the tomogram.

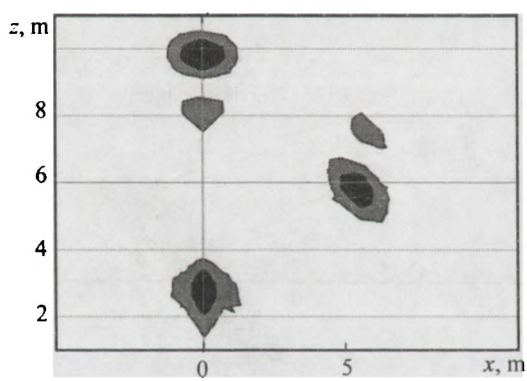

Fig. 7.13. Tomogram of three inhomogeneities using pulsed radiation.

Thus, employing the equivalence between angular radar scanning and measurements of the spatial frequency spectrum of the scattered field makes it possible to realize controlled spatiotemporal focusing using the synthetic large aperture technique for radio-wave tomography of a distribution of scatterers and enables an improvement of the transverse spatial resolution by not less than sevenfold within the limits of the Fresnel diffraction zone.

The proposed method is not described in the literature as it is a new technique for tomographic processing of radar measurements. Its implementation will increase the accuracy of tomographic processing in the realization of angular measurements by several-fold. Based on the proposed approach, new mobile scanning systems can be developed which operate in real time and under conditions of strict size and weight limitations, such as in forested areas. Such systems can also be used for monitoring of large traffic flows and also for security purposes in airports, subway stations, and stadiums.

7.4. Summary

Pulsed radio-wave scanning can be used to realize tomography of the natural environment, e.g., forests or various structures. Radio-wave tomography enables the reconstruction of forest landscapes.

Tomographic processing of radar data is based on either the well-known technique of removing point blur or the focusing method proposed here. These techniques are used to increase the transverse resolution. A shorter wavelength and/or a wider bandwidth must be used to increase the longitudinal resolution.

The proposed refocusing method works only within the limits of the Fresnel diffraction zone and provides a sevenfold improvement of the transverse resolution.

Chapter 8

ULTRAWIDEBAND INCOHERENT TOMOGRAPHY

8.1. Statement of the problem

Incoherent tomography is taken to mean tomography in the case when the radio-wave transmitter and receiver are not synchronized so that the relative phase difference between the transmitted and received signals cannot be measured. A number of widely used methods are available for reconstructing the radar images from incoherent radiation.

The method based on using a narrow-beam antenna or large-aperture antenna array is one of the most popular of such methods. A directional antenna allows one to measure the amplitude of the waves coming in from a certain direction, and also to reconstruct a two-dimensional radio-image with high angular resolution. Multi-position measurements of the angular distribution of the amplitude of the field are required to obtain three-dimensional images. The three-dimensional image reconstruction techniques, in this case, are very similar to algorithms used in X-ray tomography. It should be noted that active as well as passive tomography is used for this purpose – the waves can be emitted by an outside source or the test objects themselves can act as radio-wave sources. For example, stars, particle clouds, and the relict background radiation are considered as wave sources in radio astronomy [1]. From 2001 to 2009, the NASA WMAP (Wilkinson Microwave Anisotropy Probe) space vehicle sent back data from orbit and enabled the construction of a celestial map with a resolution of 12 ang. min. in various frequency ranges between 23 and 93 GHz [2, 3].

Another radio tomography technique applied to incoherent radiation is based on the use of the radio-holographic principle for reception [4–6]. This method measures the amplitude of the interference field of the direct wave (reference wave) from the transmitter $E_0 = A_0 \exp\{i\varphi_0\}$ and the wave scattered by the test object (object wave) $E_1 = A_1 \exp\{i\varphi_1\}$ with the help of a non-directive antenna. Generally, the amplitude of the reference wave is far larger than the amplitude of the object wave: $A_0 \gg A_1$. It turns out that the amplitude of the interference pattern in this case is directly related to one of the quadratures of the object wave field:

$$A = |E_0 + E_1| = \sqrt{A_0^2 + 2A_0A_1\cos(\varphi_1 - \varphi_0) + A_1^2} \approx \\ \approx A_0 + A_1\cos(\varphi_1 - \varphi_0). \tag{8.1}$$

The cosine field quadrature can be estimated as

$$C_1 \equiv A_1\cos(\varphi_1 - \varphi_0) = A - A_0. \tag{8.2}$$

The phase is determined accurately to within a constant, namely the phase of the reference wave. This constant phase shift does not affect the focusing. This is all that is needed to apply the synthetic aperture technique and perform controlled focusing, and finally, to implement radio-tomographic synthesis. In fact, the presence of a reference wave in a certain sense enables the solution of the so-called phase problem. This technique is important for the terahertz waveband for example, because standard high frequency methods are not applicable for this band, as mixers and waveguide transmission lines require high accuracy in production, but this is very difficult to achieve. This approach is important for incoherent X-radiation as well, where the coherence is provided by stimulated radiation with high pump power. At the same time, phase reconstruction promises to deliver an increase in spatial resolution. The proposed approach is analyzed in more detail below.

For the sake of evenhandedness, we note that in the case when only the amplitude of the object wave is measured and use of the two above-mentioned techniques (with narrow-beam radiation and analysis of the interference field of the reference and object signals) is impossible, iterative algorithms have been proposed in the literature to reconstruct the amplitude-phase field distribution [7, 8]. The Gerchberg–Saxton iterative algorithm is a good example of this [7]. The problem of reconstructing the image of the object from measurements of the amplitude of the scattered field in some region at some distance from the object is considered. The approximate shape of the scattering object is used in the initial step of the algorithm. Then, the wave field propagated from this object is calculated, whose intensity (or amplitude) is assigned on the basis of the shape of the scattering object and whose phase is determined by the phase of the incident radiation. Thus, the field in the measurement region is calculated, but its amplitude differs from the measured amplitude because of inaccuracies in the initial approximation; however, a phase distribution is obtained. Next, the amplitude of the calculated field is replaced by the measured amplitude, after which the inverse problem of reconstruction of the image of the scattering object is solved. The next iteration is performed on the basis of the obtained solution. The iterative process continues until the calculated amplitude coincides with the measured one. This algorithm converges under certain conditions. In practice, this algorithm is hardly ever used.

The chapter is based on summary results of papers [8–14].

8.2. Spatial clocking with unfilled aperture

Radio holographic methods are considered to be a promising development of radio tomographic systems in the terahertz and subteraherz bands because they require measurements of only the field intensity and do not require any measurements of the phase. Phase measurements in these frequency bands are a complex technical problem. Nevertheless, phase information is needed to reconstruct images with resolution near the diffraction limit. However, in radio holographic systems partial preservation of the phase information in the intensity of the interference image is possible due to interference of the reference and object signals. This makes it possible to reconstruct the radio-image with the highest possible resolution as shown in papers [9, 10]. One of the problems related to the use of the radio holography method according to the Nyquist–Shannon–Kotelnikov theorem is the need to measure the field amplitude with intervals of half a wavelength, which requires a significant amount of measuring time under conditions of mechanical scanning or the use of expensive filled sensor arrays. A method that enables the use of sparse measurements of the field amplitude and does not result in artefacts and secondary maxima [11] will be covered in this section. This radio-holographic method for reconstructing radio-images is based on sparse measurements of the amplitude of the interference field of the object signal and different reference signals (from different sources). Minimization of the level of artefacts and secondary maxima is assumed to obtain as a result of optimal placement of the radiating elements with respect to the measurement range.

The problem of narrowband radio holography based on sparse measurements of the field intensity using several reference sources is considered (see Fig. 8.1). Intensity measurement points are marked with circles in Fig. 8.1 and sources are marked with stars. It is assumed that the measurement points are located in a plane at a distance h_2 from the plane where the transmitters (sources) have been placed. The test object in the shape of a stepped polygon is placed at a distance h_1 from the plane with the transmitters. The transmitters are considered to be point-sources and isotropic. The number of transmitters can be varied. The more transmitters that are used, the more accurate the information about the scattering object that can be obtained. It is assumed that the transmitters are not working simultaneously, but in sequence, clocked, i.e., only one transmitter is working in a given time slice. As a result, different interference patterns will be obtained for different transmitters in the measurement plane.

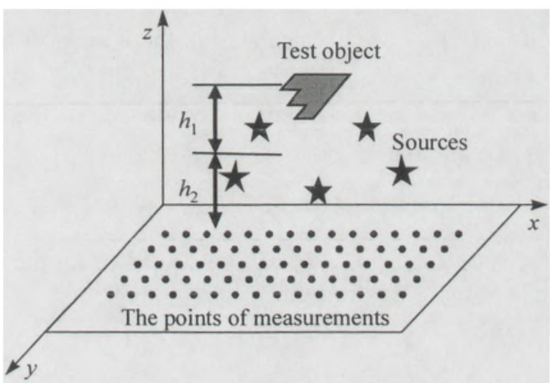

Fig. 8.1. Layout of measurements.

To validate the feasibility of the proposed approach, we performed a numerical simulation of this problem for a predefined distribution of transmitting $\mathbf{r}_0$ and receiving $\mathbf{r}$ elements (Figs. 8.2 and 8.3). A stepped polygon with a step size of 10 cm was used as the test object. The distance from the receiving array to the test object was 70 cm while the distance between the array of transmitters and the test object was 50 cm. The radiation frequency was 20 GHz.

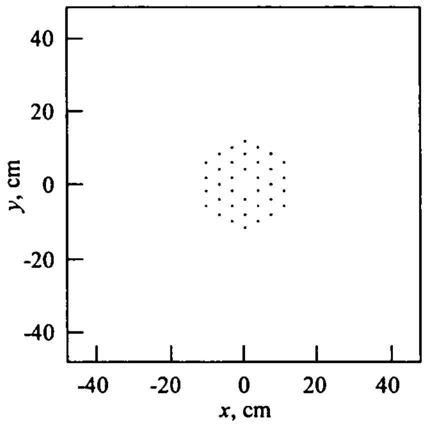

Fig. 8.2. Matrix composed of 36 radiating elements.

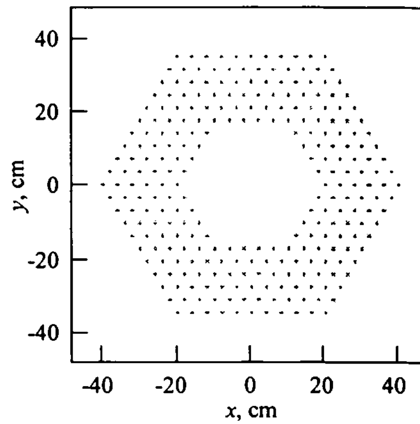

Fig. 8.3. Matrix composed of 270 receiving elements.

The scattered field $E_1(\mathbf{r})$ was calculated in the Kirchhoff approximation. The reference wave was assigned as the field of a point source $E_0(\mathbf{r}) = G_0(\mathbf{r} - \mathbf{r}_0)$. Thus, the information component of the resultant field according to Eqs. 8.1 and 8.2 is equal to

$$C_1 = |E_0 + E_1| - |E_0|.$$

The tomography inverse problem can be solved using the inverse focusing technique according to the formula:

$$U(\mathbf{r}_F) = \sum_m \sum_n M(\mathbf{r}_F, \mathbf{r}_m, \mathbf{r}_{0,n}) E(\mathbf{r}_m, \mathbf{r}_{0,n}), \tag{8.3}$$

where $C_1(\mathbf{r}_m, \mathbf{r}_{0,n})$ is substituted for $E(\mathbf{r}_m, \mathbf{r}_{0,n})$, and the focusing function is defined as before as

$$M(\mathbf{r}_F, \mathbf{r}_m, \mathbf{r}_{0,n}) = \exp\left\{-ik\left(|\mathbf{r}_F - \mathbf{r}_m| + |\mathbf{r}_F - \mathbf{r}_{0,n}|\right)\right\}.$$

Her, $\mathbf{r}_m$ и $\mathbf{r}_{0n}$ are the transmitting and receiving points, and $\mathbf{r}_F$ is the target focusing point.

Figure 8.4*a* displays the test object for only one transmitter connected. Secondary maxima are observed due to the sparsity of the measuring matrix. Applying formula 1.12, the image was obtained for the case in which all 36 radiation sources are active (Fig. 8.4*b*). No secondary maxima are evident, and the object image can be identified unambiguously. Increasing the image quality depends on overlaying interference images from different sources. This ensures in-phase addition of the central maximum and incoherent addition of the secondary maxima in the summation of images provided by different sources according to formula 1.12. The focusing plane was taken to be coincident with the plane of test object placement.

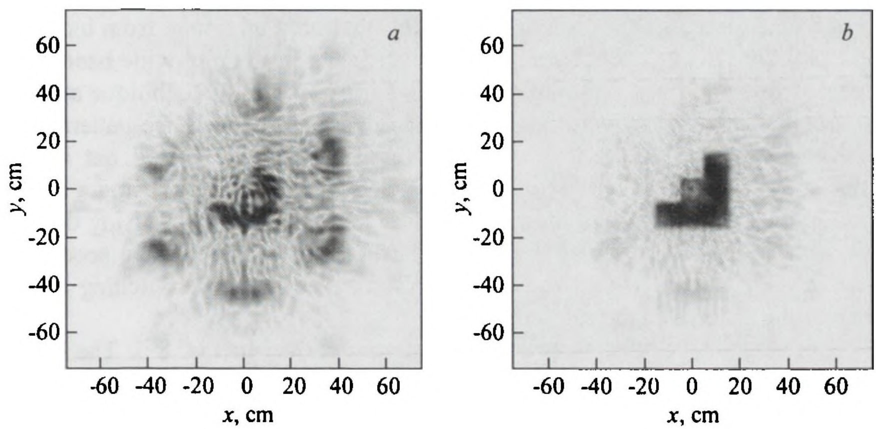

Fig. 8.4. Reconstruction of the image of the test object:
a – using one source, *b* – using 36 sources.

Notice that the resolution of the image obtained is close to the diffraction limit for the system with the aperture considered here, and is equal to 1.5 cm.

8.3. Frequency clocking

As it was described in previous chapters, the most quality 3D image with the resolution close to the diffraction limit can be obtained with the SAR technology using the ultrawideband signals. Consider the summary of the technique studied in the current chapter for obtaining the image from the incoherent radiation using the set of frequencies distributed within the ultrawide band. The idea of such approach is the concept of using the amplitude technique on each frequency followed by addition of obtained interference images according to 1.13 a. It is supposed that sounding is clocked on different frequencies. This can be achieved by using a set of bandpass filters to isolate required frequency bands, or by using the dispersion prisms, which convert the time spectrum into the spatial wave spectrum. In our case, it can be realized by the step frequency switching of the backlight generator (the reference source).

As was described in previous chapters, the highest-quality 3D image with a resolution close to the diffraction limit can be obtained with SAR technology using ultrawideband signals. We consider a generalization of the technique considered in the present chapter for obtaining an image from incoherent radiation using a set of frequencies distributed in the ultrawide band. The idea of this approach is based on the use of the amplitude technique at each frequency with subsequent addition of the obtained interference patterns according to Eq. (1.13a). It is assumed that sounding is carried out in the clocked regime at different frequencies. This can be done by using a set of bandpass filters to isolate the required frequency bands, or by using dispersion prisms, which convert the time spectrum into a spatial wave spectrum. In our case, it can be realized by step (clocked) frequency switching of the backlight generator (the reference source).

Let us consider the measurement diagram shown in Fig. 8.5. The transmitting and receiving antennas are placed at the fixed distance d from each other and together form a transceiver. It is moved with a certain step in the XOY plane and enables measurement of the amplitude at different frequencies. The transmitting antenna is connected to the tunable monochromatic signal generator. It emits radio waves in the direction of the test object and in the direction of the receiving antenna. The wave reflected from the object (object wave) interferes with the direct wave from the source (the reference wave). A detector diode is connected to the receiving antenna and together with an analog-to-digital converter measures the amplitude of the combined signal. The measurements are performed upon emission of the monochromatic signal. Then the frequency of the monochromatic signal is changed and the measurements are repeated. In this way broadband radio-holographic measurements are realized. The proposed variant of sounding can be realized with a dual-axis scanner as shown in Fig. 8.5.

The frequency clocking technique proposed in this section was numerically simulated for the frequency range 5–10 GHz in the spatial region $1\times1\times1$ m. In the calculations it was assumed that the transmitter and the receiver were placed 10 cm apart and are moved within an area of 1×1 m with a step of 4 mm. The investigated inhomogeneity, a stepped polygon with a step size of

5 cm (Fig. 8.6), was placed at a distance of 30 cm from the scanning area. The result of radio tomogram synthesis at that distance is presented in Fig. 8.6.

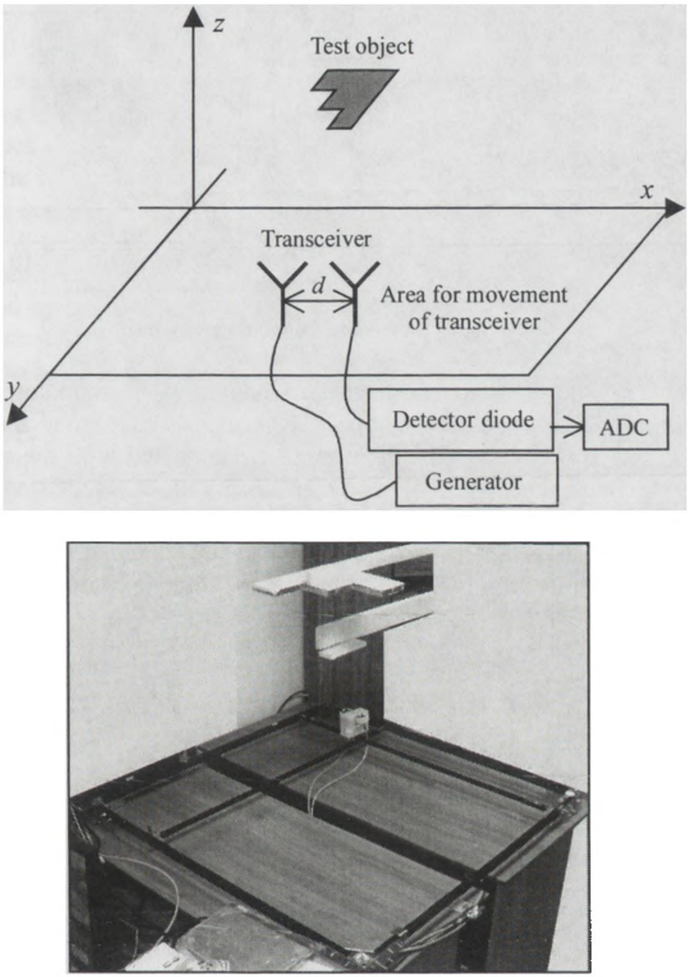

Fig. 8.5. Diagram and experimental setup for measurements with frequency clocking.

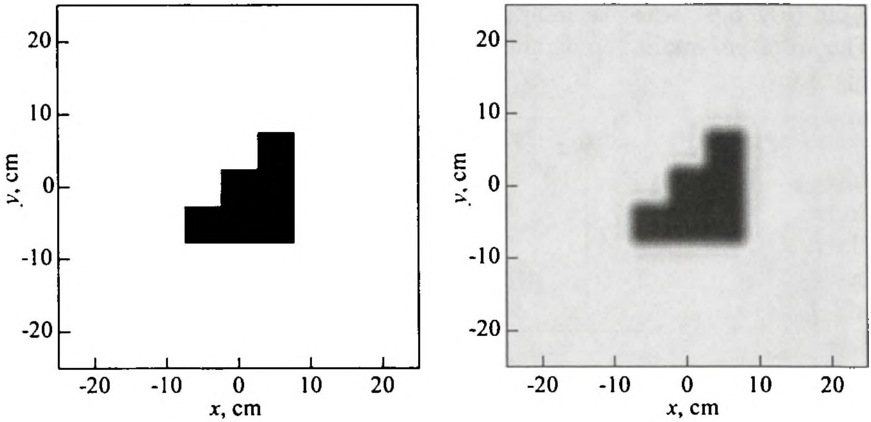

Fig. 8.6. Test object and its radio tomogram.

Figure 8.7 displays the result of image scanning at the sounding depth in the center of the test object position. The image was normalized to the maximum at zero distance. This maximum is connected with the reference signal in the source data. It can be seen that the test object is localized near the assigned value (30 cm), and the resolution obtained is close to the diffraction limit for systems with synthetic aperture in the UWB range: 1.5 cm in the transverse direction, and 6 cm in the longitudinal direction (along the z axis).

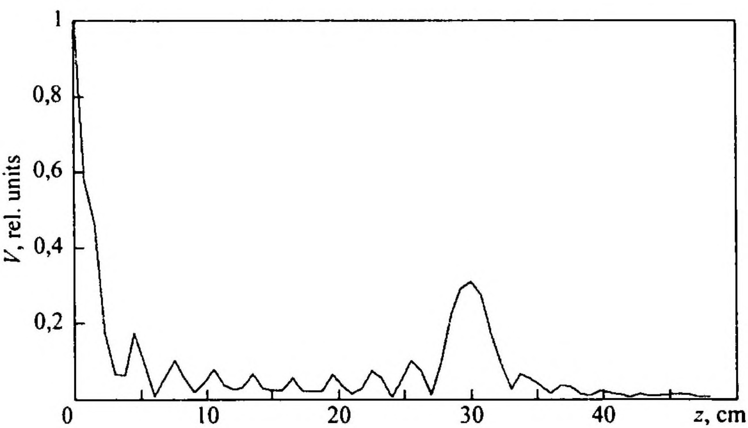

Fig. 8.7. Image scanning of test object at the scanning depth.

This latter value depends on the clocked frequency band at 5 GHz. It should be noted that the aperture is completely filled there, and the proposed solution was realized using FFT-based fast algorithms at each frequency.

Thus, numerical simulation demonstrated the fundamental feasibility of frequency clocking. The experimental scanning was performed over an area of 80×80 cm with a step of 1 cm. A dual-axis mechanical scanner was used which consisted of a square frame with dimensions 110×110 cm that included a moving carriage guided in two mutually perpendicular directions by steel ropes connected to the stepper motors. Each stepper motor controlled one of the two guide ropes. The transceiver module consisting of two UWB antennas separated by a distance of 5 cm from each other was fixed to the carriage at the cross-point of the guide ropes. One antenna was used for signal transmission, the other one – for receiving the signal. The antennas were separated by an aluminum plate with a hole to reduce the direct signal from the transmitter to the receiver. However, the direct signal remained strong enough to be used as the reference signal.

Measurements were performed at 512 frequencies within the range from 8 to 18 GHz with a uniform step. Two stepped objects were used as the test object. The first one was a plaster object with a step size of 5 cm at a distance of 36 cm from the plane of transceiver movement (scanner plane). The second one was a metallic object with a step size of 10 cm at a distance of 56 cm from the scanner plane. Measurements at frequencies of 10 GHz and 15 GHz are presented in Fig. 8.8.

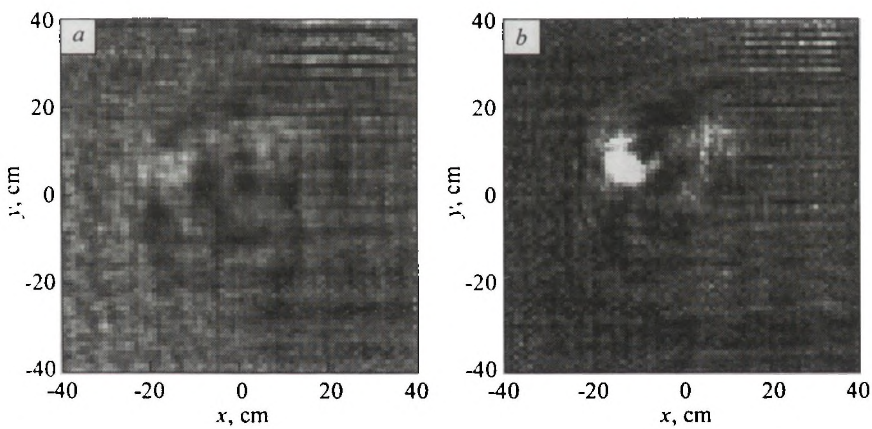

Fig. 8.8. Field amplitude measurements at a frequency of 10 GHz (a) and 15 GHz (b).

A complex interference image is displayed there suggesting that the measurement data contain information about the phase of the object wave.

Reconstruction of images based on the experimental data was performed in two stages. Firstly, the reference signal amplitude was subtracted from the measured amplitude of the interference field. The next stage is to provide the inverse focusing and receive the three-dimensional radio-image.

The results of reconstructed images from a plaster and a metallic object are presented in figure 8.9. The image of the plaster object was recovered with lower quality than the image of the metallic object. It depends on the relatively low reflection factor of plaster by contrast to metal. The shadow from the plaster object is visible on the image of the metallic object placed at the longer range. As the plaster object is semi-transparent for waves of the chosen frequency band the metallic object placed behind it can be visualized anyway.

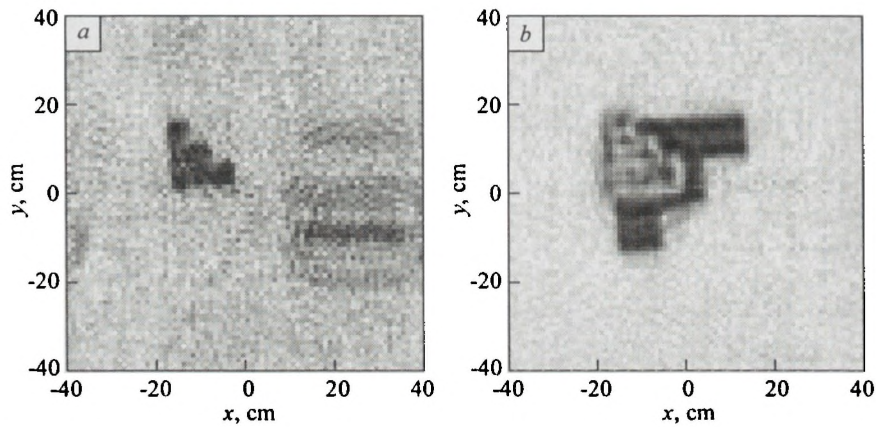

Fig. 8.9. Reconstructed images of test objects: *a* – object of plaster, 15×15 cm in size at the distance of 36 cm; *b* – metallic object, 30×30 cm in size, 56 cm apart from scanner plane.

The resolution of the images obtained is close to the diffraction limit for this frequency band and is about 1 cm. Moreover, there is the range resolution in the obtained 3D image as evidenced by the distinct vision of both objects which were placed at different range. The evaluation of the range resolution in theory is 3 cm for the frequency band of 8-18 GHz.

An experiment with a stepped metallic object with the step size of 5 cm was also conducted, when the object was placed 46 cm apart from the scanner plane. Figure 8.10 shows the recovered image of the single test object.

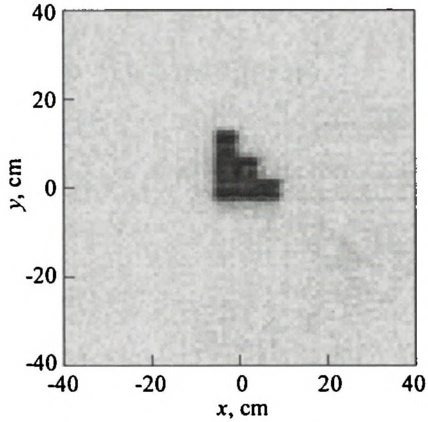

Fig. 8.10. Tomogram of metallic test object at distance of 46 cm.

8.4. Summary

The work described in this chapter has revealed the potential of radio-wave tomosynthesis with incoherent radiation. The efficacy of using spatial and frequency clocking of the measurements has been demonstrated.

This is important since this method makes it possible to exceed the spatial resolution of conventional methods of incoherent tomography by several orders of magnitude. To realize the proposed approach, it is sufficient to provide interference of the reference and object fields and record the amplitude of the interference field. In the final analysis, it provides information about the relative phase of the object wave and ensures the possibility of focusing, which is needed for the radio tomography of test objects using the method of tomosynthesis.

Chapter 9

TOMOGRAPHY OF NONLINEARITIES

The problem analyzed in this chapter pertains to a process that is referred to as nonlinear radio-location (detection), when nonlinear inclusions or their absence in the monitored field are to be detected by distortions of the scattered field during sounding. In the first approximation all sounded regions are linear, which underlies the linearity of the constitutive equations. However, this linearity breaks down if the transmitted power is increased. As a rule, this happens in regions filled with semiconductor electronic parts (diodes, transistors, microchips, etc.) or at bad electrical contacts between metal structures. The first-mentioned situations usually result in the appearance of even-order harmonics while the latter typically lead to the appearance of odd-order harmonics. This is the basis for technologies of nonlinear element detection [1–8].

9.1. Current state of the problem

Let us look at the current state of the solution to the problem of nonlinear radio location (detection) (ND). At the present time, the main task of ND is to answer the question of how to provide countermeasures against industrial and economic espionage. Modern transmitters and recorders are so small that they can be carried and hidden nearly anywhere, being placed inside different household appliances, interior items, and building structures. Extended long-life batteries allow them to function for months or even years. Such "bugs" are hard to detect from their radio emissions because many of them are turned off remotely.

To assist with this problem, nonlinear radio detectors come to the fore [1–7]. The wide range of modern nonlinear radio detectors available in world and domestic markets today allows you to choose a detector that best meets your needs.

Back in the early 70's a ND method was developed in Russia based on an analysis of harmonic emissions caused by an illuminating signal when it is reflected off a target. A few years later, this method was used by the Superscout Nonlinear Junction Detector (NLJD) system, which was the first commercially available and patented NLJD. The instrument typically includes an antenna, a transceiver, an indicator unit, and a power supply. The signal emitted by the NLJD antenna causes any currently known electronic device to generate a response signal.

The NLJD remains the only way to localize non-radiating electronic devices, including defective devices or devices with burned-out semiconductor junctions, apart from the possibility of occasional detection as a result of physical searching or detection by means of X-ray equipment.

The principle of NLJD operation is based on flooding the suspect area or object with a monochromatic microwave signal. The test object re-emits the harmonics of the radar signal. This phenomenon is tied up with the fact that the induced potential difference on the nonlinear object gives rise to a nonlinear current which contains harmonics. The induced alternating current generates a re-emitted electromagnetic field, which contains these harmonics. Usually, the appearance of such harmonics indicates the presence of nonlinearities.

Nonlinear properties are more strongly expressed in semiconductor *p-n* junctions and in pressed metallic contacts as well. The current-voltage (I-V) characteristics of most semiconductor junctions included in all electronic devices are close to a square law. These are the elements that are the main target for nonlinear junction detectors. The I-V characteristics of dissimilar metals in contact with one another as well as those of metal-oxide–metal contacts resulting from corrosion are approximated by a cubic polynomial. These contacts are commonly referred to as *false* junctions. When a radiodetector irradiates a semiconductor junction, the resulting second harmonic is stronger than the third harmonic. If a metal contact is irradiated, on the contrary, the third-harmonic response is much stronger than that of the second-harmonic. High-quality NLJDs have the capability to compare the received signal intensity of both the second and third harmonics, so they assist the operator in discriminating between true semiconductor junctions and false junctions. This feature typically results in a much more expensive NLJD because it means that the unit has two receivers with well-isolated channels (frequencies).

Nonlinear radio detection of objects is similar to the conventional detection of objects with active response in the identification mode. Thus, the power of the nth harmonic response (and the detection efficiency as well) depends directly on the power of the radiation emitted by the detector and inversely on the square of the frequency and the order of the received harmonic. The lower the radiation frequency of the NLJD, the lower the signal attenuation and the response from the object.

Thus, the frequency of the radiation emitted by the detector is one of the fundamental parameters of ND. It is around 915 MHz for most NLJDs (the second harmonic is 1830 MHz and the third harmonic is 2745 MHz). The frequency of 888 MHz is rarely used (for which the second harmonic is 1776 MHz and the third harmonic is 2664 MHz). Generally speaking, detectors operate at one fixed frequency. However, some detectors operate at multiple frequencies. As detectors with a limited frequency band often find themselves in conflict with other electronic devices, NLJDs with a wide frequency band and automatic free channel (frequency) selection are preferred. For example, in the US, NLJDs could interfere with mobile phone signals in the frequency band at 888 MHz.

Although the radiation power significantly increases the detection capability, the receiver sensitivity is equally important. NLJDs with low power output, but with a sensitive receiver can have higher performance than high-power NLJDs with an insensitive receiver. Moreover, high-power NLJDs can damage electronics and have an adverse effect on people's health.

The modality of radiation is directly related to the power. Most NLJDs operate in the continuous mode, and their output power hardly exceeds 3 W. A 2-watt nonlinear detector can detect an eavesdropping device through several inches of concrete or buried not too deep in the ground. Lower-power units (50–100 mW) will detect eavesdropping devices only an inch from the antenna.

Some domestic nonlinear detectors use pulsed mode and correspondingly have a number of advantages. Such NLJDs consume far less electric power, which reduces their power supply requirements. Moreover, when operating in pulsed mode with a peak power of 300 W, the mean power of irradiation of the operator (the specific absorption rate (SAR)) is very low — far lower than in continuous mode with a power level of 3–5 W.

The three main functions of NLJDs are detection, position location, and identification.

Detecting is successful if the response amplitude exceeds a threshold level. A visual or auditory signal keeps the user informed that the suspect object is located within the antenna illumination range. Location of the position of the object is performed through a comparison of the amplitude with the response bearing. The amplitude of the response signal increases as the antenna gets closer to the signal source during the search. The anisotropy of the directivity pattern allows the user to determine the direction to the source of the response signal from its maximum level.

Object identification is performed according to an analysis of the response signal from the object located within the antenna radiation range. In those NLJD models that simultaneously receive a response from the object in the second and third harmonics of the radiated signal, identification is realized by comparing the signals of both receive paths by monitoring the linear indicator lights. Usually, objects with semiconductor junctions return a second harmonic signal that is 20–40 dB stronger than that of the third harmonic. Noisy metal contacts, in contrast, generate a third harmonic signal exceeding the signal of the second harmonic by 20–40 dB. NLJDs receiving only the second harmonic response require additional actions from the user to identify the object. The problem here is that there are a number of objects containing nonlinear metal contacts. These include reinforced concrete structures, different types of supports, furniture springs in contact with screw heads, nails contacting metallic object inside a wall, electrical switches, contacts of fluorescent tubes, paper clips, etc. Such objects give false alarms on the odd-numbered harmonics, but sometimes they produce even-numbered harmonic responses as well. Since these contacts are mechanically unstable, their current–voltage characteristic is unstable as well and is highly dependent on the mechanical state and history of the contacts. If low physical vibration is applied to a false junction, the crystal texture of corroded and bimetallic junctions may be destroyed, which leads to modulation of the response signal with the frequency of vibration. Vibration does not affect the *p*-*n* semiconductor junctions. The operator should test the search field, for example, by tapping the ground with a small rubber hammer using both the indicator and the headphones. In this case, the response from electronic devices will not change, and no sound will be generated in the headphones. Metallic sources upon tapping will cause disordered unstable display readings and noise (crackling) in the headphones.

Exploration with a NLJD usually starts with slow scanning, with the radiation switched off, of every surface in the search area. The operator should scan all surfaces thoroughly including walls, the floor, the ceiling, equipment, etc. This is quite a time-consuming procedure (usually its rate is 0.2–0.4 m^2/min), its aim is to detect devices that generate electromagnetic fields.

Then, with the irradiating signal switched on, walls and other surfaces should be scanned, holding the antenna at least 2–3 m away from the surface. This allows the operator to detect and isolate those objects that cause noise in the headphones. After removing these objects from the search area the distance to the NLJD is reduced to 1–1.5 m, and the scanning procedure should be repeated. Finally, the distance should be reduced to 0.5 m or to immediate contact with the object. Then a number of scanning operations are performed while gradual increasing the NLJD power from its lowest possible level up to its maximum value.

Scanning of flat surfaces is performed with a rate of 0.03 m^2/s, complex surfaces are scanned at a slower rate. So, scanning of a small office (no more than 20 m^2) takes about 2–3 h, a medium-sized office will take 3–4 h, but scanning of a large building demands 6–8 h or even several days.

Nonlinear detection technology is applicable to the remote detection of small-sized objects such as radio-controlled devices, equipment for industrial espionage, small arms and light weapons, aircraft wreckage, portable transceivers including ones that are switched off, etc. The search objects can include special nonlinear markers which are used for secret marking of different objects and terrains (for precision guided weapons) and also for people (e.g., lifeguards in inaccessible areas). Experiments have shown that the optimal frequency for remote detection of nonlinear objects should not exceed 1 GHz, and it is reasonable to use high-power pulses with low duty cycle ratio to extend the detector coverage range. If the pulse peak power is 50 kW and the duty cycle ratio is 1/1000, the airborne detection range for small-sized objects is 300–350 m. If an object is buried 0.1–0.2 m deep in the ground, the detection range is about 80–100 m.

The basic characteristics of the best-known models of modern NLJD are presented in Table 9.1. Nonlinear junction detectors are considered to be the optimal devices for detecting unauthorized information collecting devices. The use of pulsed UWB technology for nonlinear detection has received but scant attention in the scientific literature thus far. The key reason for this is that their low pulse power simply does not enable detection of nonlinear inclusions.

Table 9.1

Nonlinear junction detectors

Model (Manufacturer, Country)	Radiation Mode	Radiating Power, W, min/max	Radiation Frequency, MHz	Receiving Frequency, MHz	Sensitivity, dBm	Polarization	Supply Voltage, V	Price, Thous. USD.
Orion NJE-4000 (REI, USA)	Contin.	0.01/1	915	1830, 2745	–130	Circular	7.2	15
SuperBroom Plus (Audiotel, UK)	Contin.	0.001/3	885.5	1777, 2665.5	–	–	12	30
«Rodnik-2» (CSRRTI, Russia)	Contin.	0.4/2	910	1820	–145	Linear	220/12	3.5
«Rodnik-2K» (modification)	Contin.	0.8	980	1960	–137	–	220/12	–
«Rodnik 23» (CSRRTI, Russia)	Contin.	2	910	1820, 2730	–145	Linear	220/12	8.3
NR900E (Engineering-Commercial Multiprofile Center-1, Russia)	Pulse	25/150	900	1800, 2700	–115	Circular	220/12	6.5
NR900M (Engineering-Commercial Multiprofile Center-1, Russia)	Pulse	25/150	900	1800	–115	–	220/12	4.5
NR-m (Engineering-Commercial Multiprofile Center-1, Russia)	Contin.	2	680	1360, 2040	–150	–	220/6	–
«Ob'» (Mascom Ltd, Russia)	Contin.	0.25	1000	2000	–145	–	220/12	–
«Envis» (Russia)	Contin.	0.04/0.8	910	1820, 2730	–	–	220/12	–
NR-900-20K (Russia)	Pulse	150	900	1800	–115	–	220/12	–
NR-900-E (Russia)	Pulse	150	900	1800, 2700	–115	–	220/12	–
«Octava» (Russia)	Pulse	–	885–895	1770	–	–	220/12	–
«Lux» (Russia)	Pulse	> 14	435	870	–	–	220/12	–
«Onega-3M» (Russia)	Pulse	100	910	1820, 2730	–	–	220/12	6.7
«Cyclone-M1A» (Russia)	Pulse	300	680	1360	–110	Circular	220/12	–

9.2. UWB tomography of nonlinearities

The present section is aimed at research into the possibility of using UWB signals for nonlinear detection. The well-known Luxembourg effect (LE) is assumed to lie at the basis of such an approach. The main idea underlying this effect consists in the occurrence of cross-modulation when radio waves propagate in nonlinear media. Cross-modulation is the phenomenon that arises when a receiver tuned to a station on a broadcast frequency f_1 simultaneously receives signals from a high-power broadcast station operating at the carrier frequency f_2 (far enough removed from f_1). This effect was observed for the first time in 1933 in Eindhoven (the Netherlands), where the high-power Radio Luxembourg station, located in line with a Swiss station, could be heard during the Swiss broadcast. A similar phenomenon was observed in Gorki (Russia), where high-power Moscow stations could be heard during the reception of radio stations located to the west of Moscow. The depth of such cross-modulation of the radio waves of both stations can reach 10 % or even more, but it usually does not exceed 1–2 %. The Luxembourg effect is a source of interference in radio reception.

The theory of the Luxembourg effect was developed by the Australian physicists V. Bailey and D. Martyn (1934–1937), the Soviet physicist V.L. Ginzburg (1948), and others. The possible effect of cross-modulation in the ionosphere was mentioned first by the Soviet scientist M.A. Bonch-Bruyevich in 1932. The cause of the LE is as follows: a high-power wave "heats up" (perturbs) a region where another wave propagates transmitting information. Both waves experience cross-modulation, i.e., they *see* each other. It is based on the nonlinear modulation effect. At the physical level, it is similar to the mixing of two signals in a solid-state mixer.

Let us consider how this effect can be applied to the UWB detection of nonlinear inclusions. Let $E_0(t)$ be a pulsed UWB signal which irradiates a nonlinear inclusion. Then, to within a constant factor, the scattered field can be written as

$$E_{\text{scat}}(t) = E_0(t) + g\left[E_0(t)\right],$$

where $g(x)$ is the nonlinearity. Generally, it can be assumed that

$$E_{\text{scat}}(t) \approx E_0(t).$$

If we add a high-power monochromatic illuminating wave

$$E_1(t) = A\sin(\omega t + \varphi_1)$$

to the UWB field, then the total scattered field can be represented as

$$E_{\text{scat}}(t) = E_0(t) + A\sin(\omega t + \varphi_1) + g\left[E_0(t) + A\sin(\omega t + \varphi_1)\right].$$

The phase of the monochromatic illuminating signal is not correlated with the UWB signal, so after averaging we can write

$$\left\langle \tilde{E}_{\text{scat}}(t, A)\right\rangle = E_0(t) + \frac{1}{2\pi}\int_{-\pi}^{\pi} g\left[E_0(t) + A\sin(\varphi)\right]d\varphi .$$

This means that a nonlinear inclusion appears as an averaged scattered pulsed signal! This effect does not occur at a low level of illumination:

$$\left\langle \tilde{E}_{\text{scat}}(t, A \ll |E_0|)\right\rangle \approx E_0(t).$$

The difference between the obtained signals is the information value to identify the type of nonlinearity. This conclusion was confirmed by numerical simulation. The proposed method is based on this effect.

It should be emphasized that although the harmonics are not recorded in contrast to the conventional method of nonlinear detection, the nonlinearity is manifested in the distortion of the shape of the UWB pulse. Conceptually, this corresponds to the Luxembourg effect. The proposed method is covered by a Russian Federation Patent [9].

Figure 9.1 shows typical shapes of signals received during UWB sounding of a D20 diode with illumination (curve *1*) and without illumination (curve *2*) as well as the differential signal (curve *3*). The diode was not connected to a

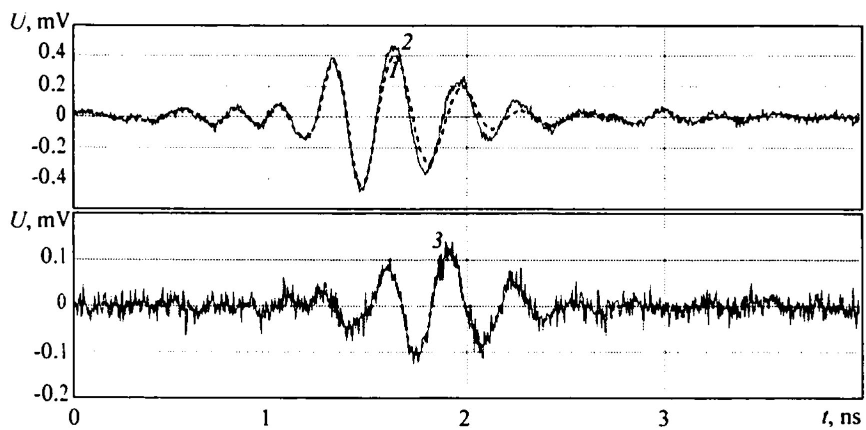

Fig. 9.1. Signal shapes in the UWB sounding of a D20 diode with illumination (curve *1*) and without (curve *2*), and the differential signal (curve *3*).

circuit, it was just a free standing factory-made unit. The frequency of the illumination signal was $f = 850$ MHz, and a focused UWB signal with a duration of 0.2 ns was used for sounding.

The illumination signal power at the output of the transmitting antenna was 30 W. As the figure shows, the differential signal stands at 20–25 %, which is quite a significant value. There is a certain inertia (delay) of the nonlinear diode response. Similar characteristics are observed for other nonlinear inclusions as well.

9.3. Processing program and results of the UWB tomography of nonlinearities

A program chart of the experimental setup is presented in Fig. 9.2. This program was applied within the framework of the Volnorez (Breakwater) project.

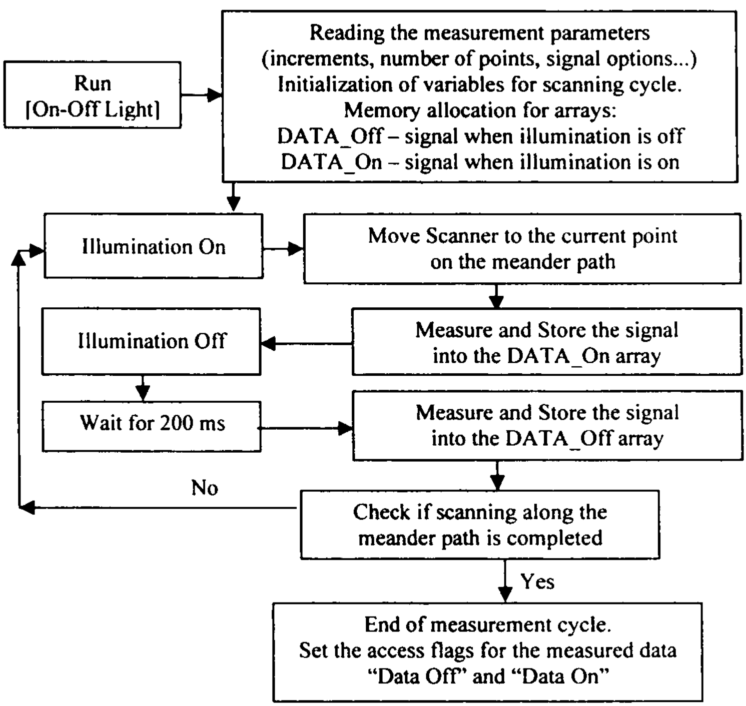

Fig. 9.2. Program flowchart.

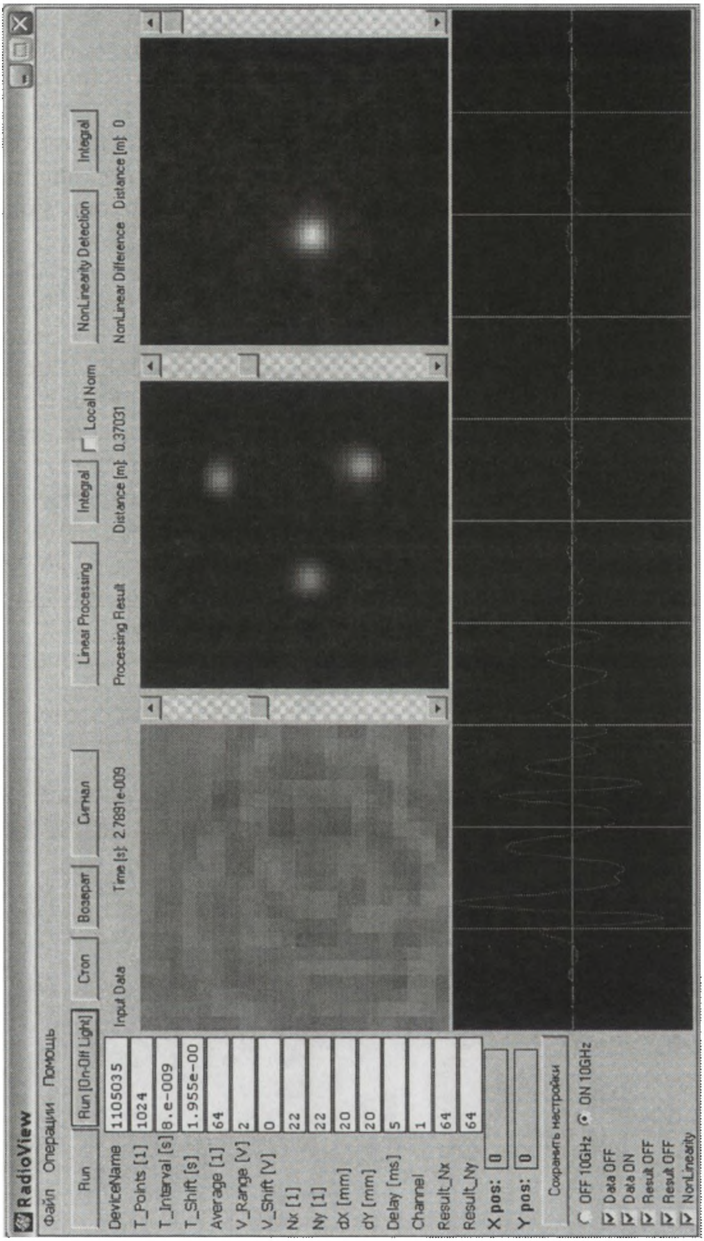

Fig. 9.3. Interface of the program RadioView.

The program workflow is sequential UWB scanning of the test area with an assigned step. Sounding is performed in two sequentially activated modes: with illumination and without illumination by high-power monochromatic radiation.

Scanning is realized according to the program by automatic movement of the antenna unit. The collected arrays are sent to the program for tomographic processing and detection of nonlinearities. The program's main window is illustrated in Fig. 9.3.

Layer-by-layer images of the sounded area are displayed in the pop-up windows. The source sounding data are shown in the first window. The waveform of the signal at a selected point is displayed at the bottom. The middle frame displays the tomogram of all the detected inhomogeneities at different depths. The right-upper window displays a tomogram of the detected nonlinearity or nonlinearities. Images are displayed layer-by-layer in grayscale. Layer-to-layer transfer is performed interactively with the scrollbar: slider up – for near layers, slider down – for far layers. The depth of each layer (m) is displayed below. There was just one nonlinear inhomogeneity in the given example (a microwave diode). Other inhomogeneities were 2×2 cm square-shaped pieces made of aluminium foil. Each object was taped to the foam plastic surface with adhesive tape.

The experiments confirmed the feasibility of the proposed solution.

9.4. Summary

Using UWB radiation for radio tomography of nonlinearities of artificial origin creates numerous opportunities for their 3D tomography. In contrast to the conventional nonlinear detection method, it does not use the detection of harmonics to achieve this end. However, UWB radiation requires an external high-power microwave source to detect nonlinearities.

The proposed method of nonlinear detection is covered by a Russian Federation Patent.

Chapter 10

CONTACTLESS ULTRASONIC TOMOGRAPHY

Electromagnetic radiation interacts with electrophysical inhomogeneities in the propagation medium. In contrast to electromagnetic radiation, acoustic radiation interacts mainly with density contrasts in the sounding medium [1–2]. In this context, using ultrasound in the tomography of inhomogeneous media provides additional opportunities, in particular for detecting the type of material that the hidden objects are made of. Integration of radio- and acoustic sounding provides opportunities, e.g., for the detection of explosives.

A search on remote ultrasonic sounding techniques reveals that most industrial methods are based on contact measurements. The principal reason for this is that ultrasound attenuation in air is quite high. Ultrasound is used in Parktronic systems for car parking, and for control of industrial robots. The ultrasound system (echolocation) used by bats is perhaps the only ultrasonic ranging system actually effective in air (see Fig. 10.1).

Fig. 10.1. Bats are effective ultrasonic stations in air.

Some insects also use ultrasound, but rather for active jamming of bats' sounding. There is no doubt in the efficiency of ultrasound for sounding in liquids and through immersion liquids. This applies in the fields of industrial metal working, medicine, and submarine echolocation. In nature this also pertains to dolphins and fish. However, ultrasound can be efficiently used for tomography in air in safety systems and in non-destructive testing. If the object is radiopaque, radiation can hardly penetrate it, and only acoustic radiation will allow the recovery of its internal structure.

The overall purposes of the present chapter are: the development of physico-mathematical models of a system for reconstruction of images of inhomogeneous media based on tomographic processing of multi-angle measurements of scattered acoustic radiation, the development of the key elements of a simulation system and the development of experimental measuring techniques, and finally, an evaluation of the potential and actual characteristics of an acoustic wave tomograph in different measurement and sounding schemes. The chapter summarizes the results of papers [3–5].

10.1. Experimental results

From a mathematical perspective, acoustic wave propagation is similar to the propagation of electromagnetic waves. From a physical point of view, electromagnetic and acoustic oscillations are fundamentally different. To a first approximation, the difference lies in the fact that an electromagnetic wave is a vector transverse wave, while an acoustic wave is a scalar longitudinal wave. It is important that the phase velocity of electromagnetic waves is lower in a more condensed material while the phase velocity of acoustic waves is higher in air. Moreover, the attenuation of electromagnetic waves in a water-filled medium is rapid (exponential) unlike acoustic waves, which hardly attenuate in such a medium as water is practically incompressible and transmits acoustic oscillations without significant attenuation. And most importantly, electromagnetic waves can propagate through a vacuum while acoustic waves cannot.

A common factor is that both electromagnetic and acoustic waves are described by wave equations, and both give rise to reflection, scattering, and diffraction effects when the wave interacts with inhomogeneities in the medium. In this respect, all of the mathematical methods and results elaborated in previous chapters are applicable for ultrasound.

The simplest setup for our experiments in ultrasound tomography is shown in Fig. 10.2. Standard piezoceramic transmitters and ultrasound receivers with a resonant frequency of 40 kHz are set on an x-y recorder, and a computer sound card can be employed as a signal generator and receiver. A Creative Audigy SE PCI SB0570 sound card enables signal generation and recording with a sample rate up to 96 kHz. An MA40S4R ultrasonic transmitter was used as well as an EM9767 electret microphone. The object of sounding (a toy gun) was placed at a certain distance from the transmitter. Scanning was performed through a simple computer-aided controller.

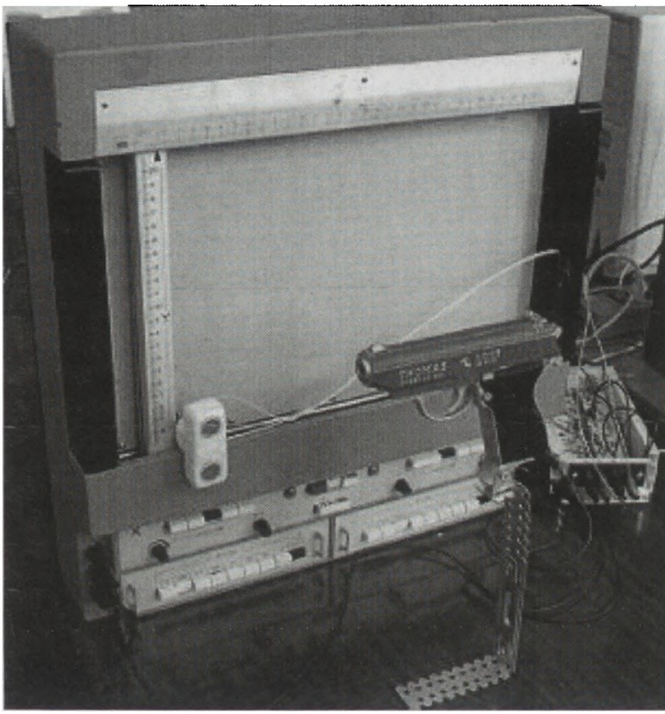

Fig. 10.2. Experimental setup for ultrasonic tomography.

A broadband ultrasonic scanner setup was built and used to experimentally recover the ultrasonic image of the toy gun. The result is presented in Fig. 10.3, which demonstrates variations of the real part of the complex amplitudes at different frequencies of the spectrum of the measured signal.

Typical wave images of an ultrasonic field scattered by a test object are clearly apparent in this figure.

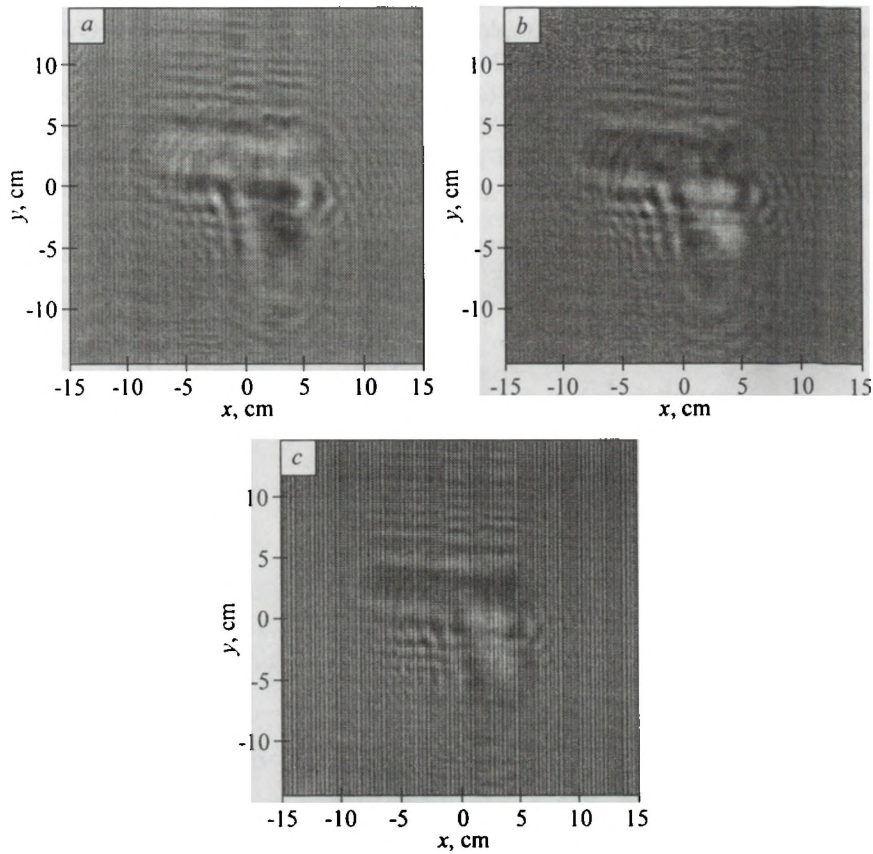

Fig. 10.3. Ultrasonic echo of a toy gun located at a range of 12 cm at frequencies of: 37 kHz (*a*), 40 kHz (*b*), and 43 kHz (*c*).

To recover the images of an object, the inverse focusing was used in the frequency domain at three different frequencies according to Eq. (1.13). The restored image of the test object is presented in Fig. 10.4. The image of a gun can be clearly distinguished in the result of single-frequency sounding; however, there are minor artefacts. The number of artefacts was markedly decreased when the sounding was performed at all frequencies within the frequency band 37–43 kHz. It should be noted that in air a wavelength of 8.3 mm corresponds to a frequency of 40 kHz, which makes it possible to distinguish fine details in the image.

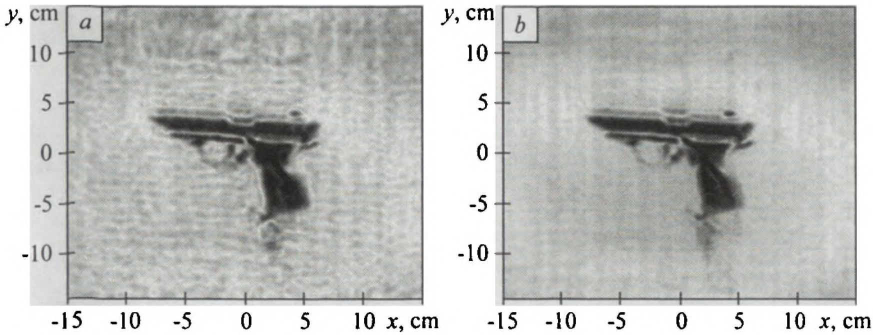

Fig. 10.4. Recovered image of the object (tomogram): at a frequency of 40 kHz (*a*), within the frequency band 37–43 kHz (*b*).

The resolution of details improves as the distance to the object is decreased. This is because the condition of Fresnel diffraction is being met more precisely (Fig. 10.5). The result of sounding of a test object in the form of a stepped triangle with a hole is displayed in Fig. 10.6. The resolution in this case is close to the radiating wavelength and even higher.

The reported results confirm the efficacy of the use of ultrasound in location (detection) tomography of small-sized objects. Furthermore, no special permit is required to use ultrasound, so it can be used for covert surveillance.

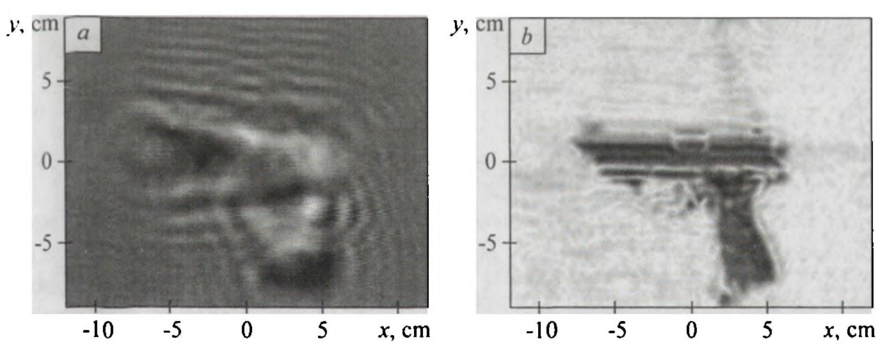

Fig. 10.5. Plastic gun in air at a distance of 10 cm: measured data (*a*) and result of focusing (*b*).

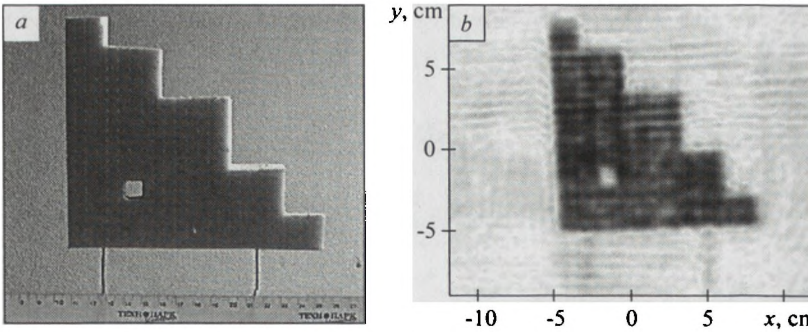

Fig. 10.6. Stepped triangle in air at a distance of 10 cm: photograph (*a*) and the result of ultrasonic imaging (*b*).

Objects can visualized which are hidden behind opaque but acoustically transparent screens (Fig. 10.7). The image is blurred of course, but it remains recognizable. The resolution could be improved significantly with the use of multiple frequencies.

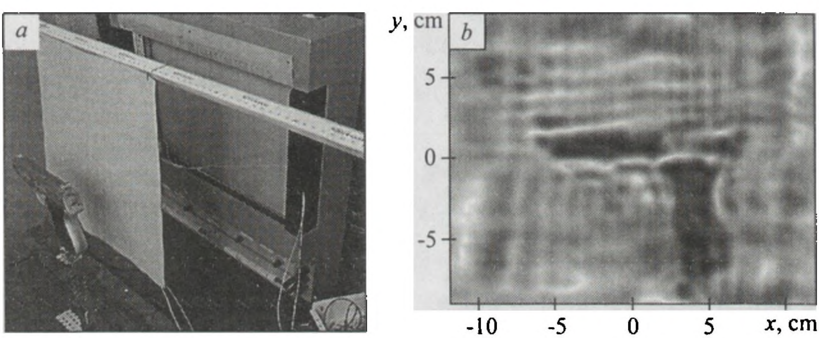

Fig. 10.7. Plastic gun behind a curtain at a distance of 10 cm: photograph of experimental setup (*a*) and the result of focusing (*b*).

Mechanical scanning of an acoustic field requires up to several tens of minutes and the object must remain motionless, which is unattainable, e.g., when screening people. Thus, it would be interesting to consider how sounding could be speeded up by electronic switching of the transmit/receive arrays. In the view of the authors, cross-shaped sounding systems are of interest. A demo setup of a sonar was therefore developed that included 32 ultrasonic transmitters and 32 receivers arranged in the form of a cross, situated 1 cm apart from each other (Fig. 10.8).

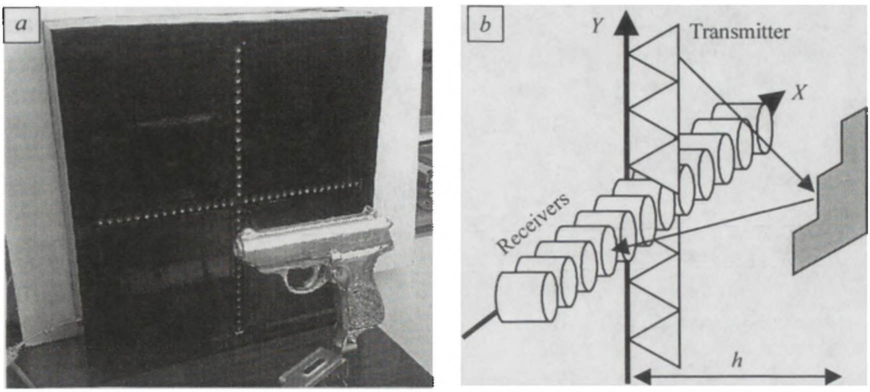

Fig. 10.8. Sonar for contactless ultrasonic imaging: external view (*a*), configuration scheme (*b*).

Measurements were carried out in the clocked mode. The time for a complete measurement, data processing, and visualization of the results on a standard computer does not exceed 2 s, which is acceptable for many applications. An image obtained using the sonar demo setup is presented in Fig. 10.9.

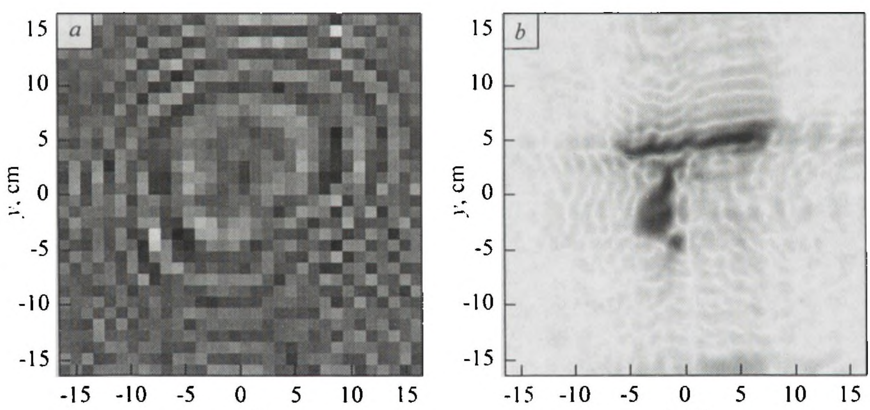

Fig. 10.9. Testing results of sonar demo setup: measured field (*a*), recovered image (*b*).

10.2. Integration of radio- and ultrasonic tomography

Ultrasonic radiation mostly is scattered at the inhomogeneities of the density ρ. In remote sounding, it provides the information about the material an inhomogeneity is made of. Using electromagnetic waves in sounding makes it possible to monitor the electrophysical properties of matter. The integration of electromagnetic and acoustic waves for sounding enables us to distinguish solid and liquid media. The following empirical relation is true for solids:

$$\rho = 2(n-1)\text{, or } n = [\rho/2+1],$$

where ρ is the density and $n=\sqrt{\varepsilon}$ is the refractive index of the material. A plot of the refractive index versus the density is shown in Fig. 10.10, where the sloped line plots the abovc dependence.

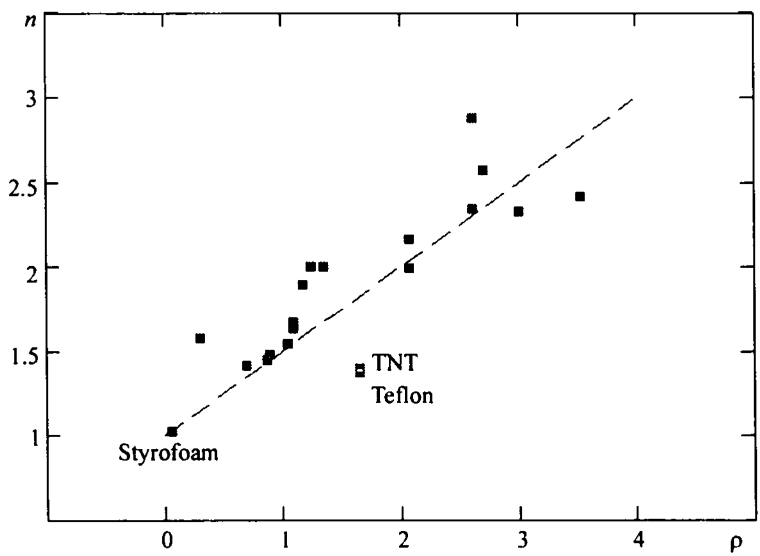

Fig. 10.10. Refractive index – density diagram of several solid materials.

The values for certain solids are indicated with dots. Each value is listed in Table 10.1. Materials of higher density have a higher refractive index.

Note that that TNT, which is distinctly different from other materials, takes a very low position in the diagram. The position of fluoroplastic (Teflon) is close to the that of TNT. This means that Teflon can be used to simulate TNT in the laboratory; in real practice it is necessary to use reconstruction of the shape of such objects to distinguish these materials.

Table 10.1

Refractive index and density of solids

Material	Density, g/cm^3	Refractive Index
Foam plastic (Styrofoam)	0.06	1.022741
Wood	0.3	1.581139
Paper	0.7	1.414214
Paraffin	0.87	1.449138
Polyethylene	0.9	1.48324
Polystyrene	1.05	1.549193
Asphalt	1.1	1.637071
Amber	1.1	1.67332
Plexiglas	1.18	1.897367
Fabric-reinforced laminate	1.25	2
Vinyl plastic (PVC)	1.35	2
Fluoroplastic (Teflon)	1.65	1.378405
TNT	1.654	1.4
Quartz	2.07	2.165641
Sulfur	2.07	1.994994
Marble	2.6	2.880972
Phlogopite	2.6	2.345208
Slate	2.7	2.569047
Glass	3	2.32379
Diamond	3.515	2.42

The refractive index in liquids is generally higher than in solids (see Table 10.2). Liquids are easily identified in the diagram. Furthermore, the electrophysical parameters of liquids have a definite temperature dependence that can be used for their identification.

One way or another, integration of ultrasonic sounding with radio waves provides additional information about a material and is therefore considered to be a promising direction for research. Moreover, the use of ultrasound is harmless to human health and it requires no special permit to be used. That is why the development of technology based on the SAR technique is considered to be important for ultrasonic tomography of inhomogeneous media and objects. Problems arising in this context and their possible solutions are discussed in the current section.

Table 10.2

Refraction index and density of liquids

Liquid	Density, g/cm³	Refractive Index
Ethanol	0.7894	25.8
Methanol	0.7915	31.2
Acetone	0.792	26.6
Oil	0.86	2.13
Benzene	0.879	2.29
Flaxseed oil	0.94	3.35
Castor oil	0.96	4.67
Water	0.9982	81.1
Nitrobenzene	1.229	2.41
Glycerin	1.26	56.2
Nitroglycerin	1.601	2.196

A large-sized scanner, where the radio- and ultrasonic elements are combined in a transceiver head, is shown in Fig. 10.11.

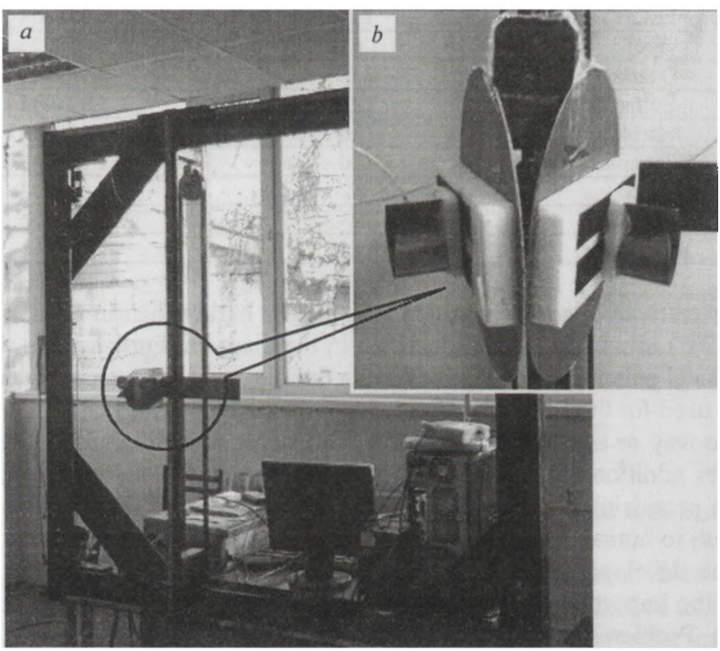

Fig. 10.11. Radio- and ultrasonic scanner (*a*), and scanner detector head (*b*).

A series of experiments with different objects was carried out (Figs. 10.12–10.14). The ultrasound frequency was tuned within the band of 35–45 kHz, and the duration of the UWB pulses was 200 ps.

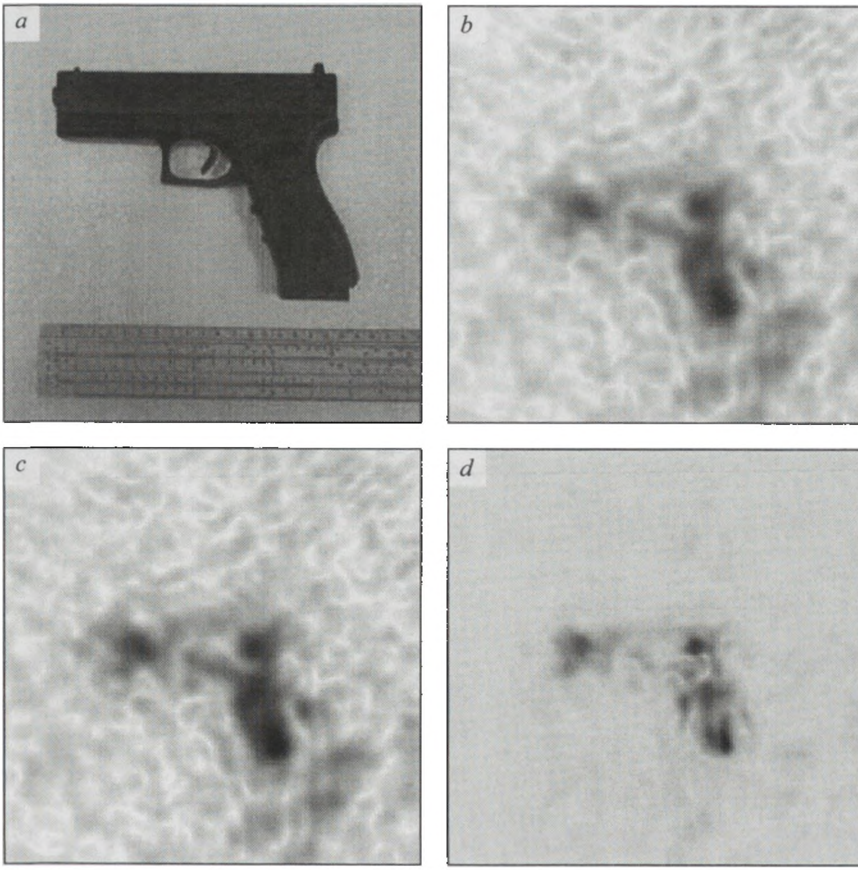

Fig. 10.12 Image of a plastic gun: photograph (*a*), ultrasonic image (*b*), UWB image (*c*), image from integrated tomography (*d*).

It was established that the images of metallic objects in radio-wave tomography have more contrast than in ultrasonic tomography. Apparently, the reason for this is that a part of the energy is spent to excite secondary waves in the metal and behind it. On the contrary, radio waves have weaker reflection from dielectrics, and penetrate into dielectric objects. This was clearly demonstrated in experiments with a metallized grid (the reflection coefficient of radio waves was 0.9 whereas for ultrasonic waves it was 0.1) and with a foam-plastic object (where the radio waves did not reflect, and the reflection coefficient of ultrasound was 0.7).

Ultrasound provided higher resolution (of 2–3 mm) than the radio waves (1–2 cm) at identical distances (<1.2 m) to the test object.

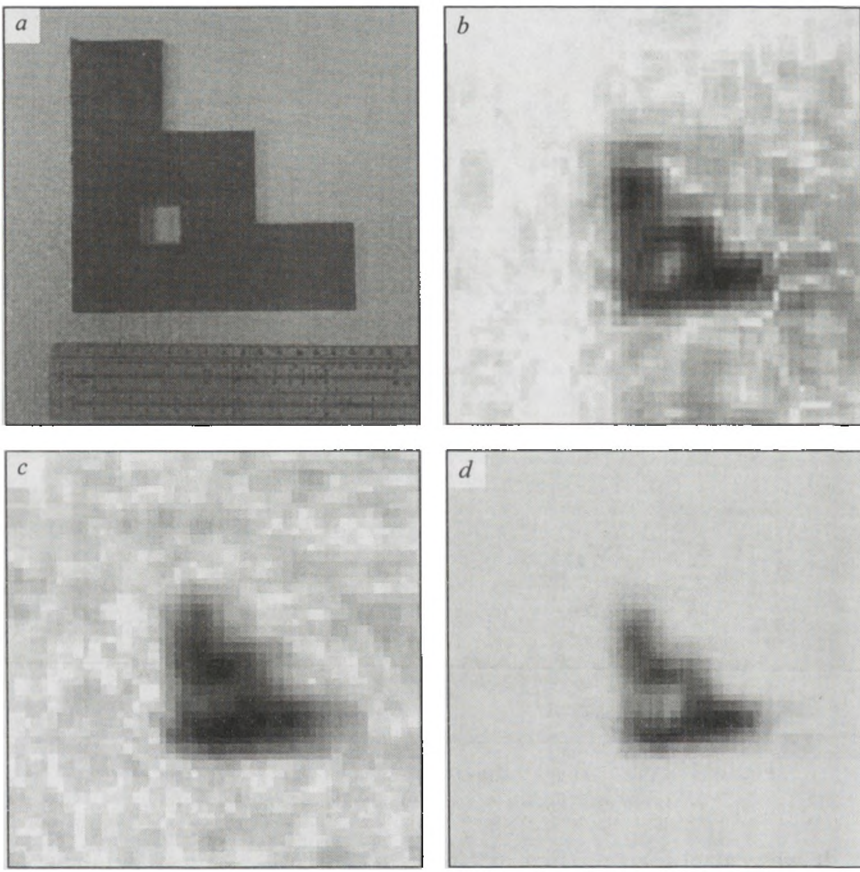

Fig. 10.13. Image of a stepped triangle made of plasterboard: photograph (*a*), ultrasonic image (*b*), UWB image (*c*), image from integrated tomography (*d*).

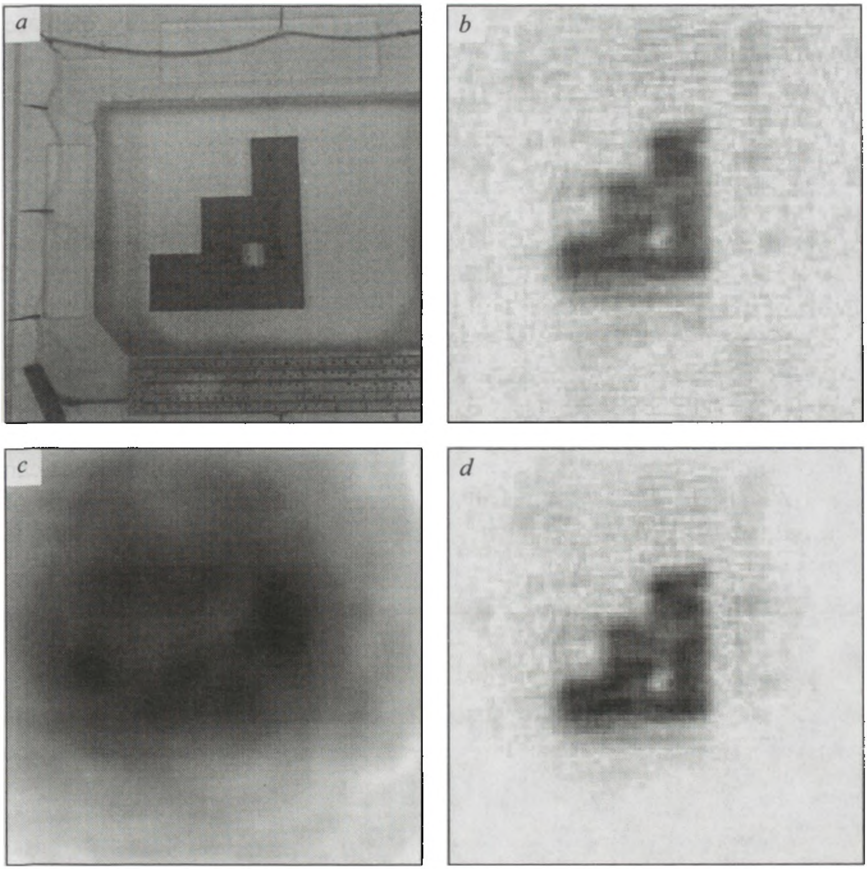

Fig. 10.14. Image of a stepped triangle made of plasterboard behind a metallized grid: photograph (*a*), ultrasonic image (*b*), UWB image (*c*), image from integrated tomography (*d*).

The reason for this is the difference between the average operating wavelength for ultrasound (8 mm) and for a radio wave (2 cm). It is important here that the Fresnel zone (the focusing region) for ultrasound has about twice the diameter as for radio waves given the same size of synthetic aperture.

Overlaying the radio-wave image and the ultrasonic image of the test object in a false-color combined image makes it possible to judge the material of the test object without additional processing. A similar effect is observed in an element-by-element multiplication of images with a significant increase of the resolution as well.

10.3. Ultrasonic tomography of small-sized flaws in metal items

Another area of ultrasonic tomography that deserves our attention is contactless tomography of flaws in metal structures. If a stimulator (source of ultrasonic vibrations) is set up on a metal surface or some other sound-conducting structure, then propagating waves are excited in it. When these waves encounter non-uniformities in their path (cuts, flaws, sags, etc.), they are scattered and reradiated at all angles and into the air. The edges (boundaries) of the object can also reradiate. Considering these non-uniformities as sources of ultrasonic waves, a tomographic visualization of such sources can be performed using inverse focusing. As a result, the position and shape of even the small faults will be reconstructed without contact. An example is displayed in Fig. 10.15.

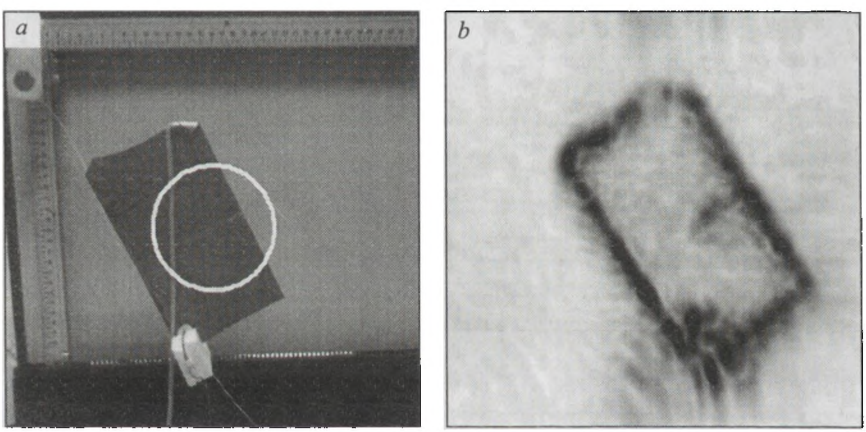

Fig. 10.15. A cut in a thin metal sheet (*a*) and its ultrasonic image (*b*).

A similar experiment was carried out with a large metal sheet (Fig. 10.16).

If a sound-conducting object is excited by an external stimulator, e.g., by impact, the distribution of faults as well as the position of the stimulator,

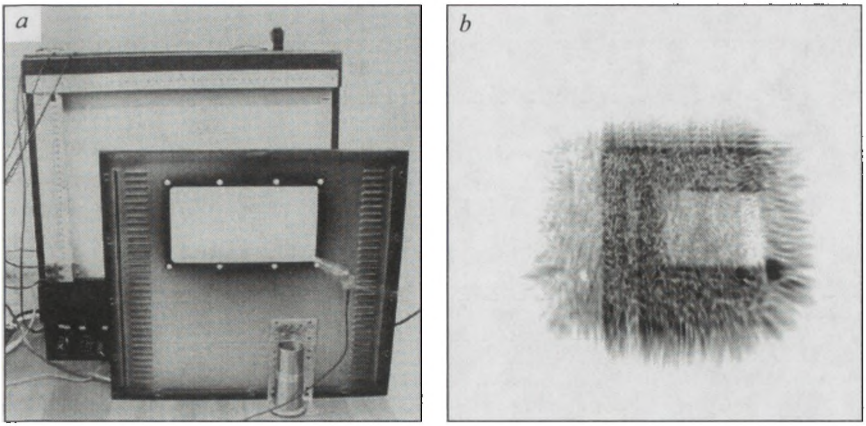

Fig. 10.16. Holes in a metal sheet (*a*) and its ultrasonic image (*b*).

even in the other half-space, can be reconstructed by the secondary acoustic field generated by this object. A stimulator in the form of an electric micromotor with an eccentric, mounted to a fiberglass plate with dimensions 15×11 cm, is shown in Fig. 10.17. The frequency of rotation was about 23 kHz. The size of the area for monitoring the distribution of ultrasonic oscillations was 40×40 cm. The result of tomograpahic processing of the recorded field is shown in Fig. 10.18. When using a wide spectrum of recorded frequencies, good localization of the radiation source is observed, and the shape of the plate is also reconstructed.

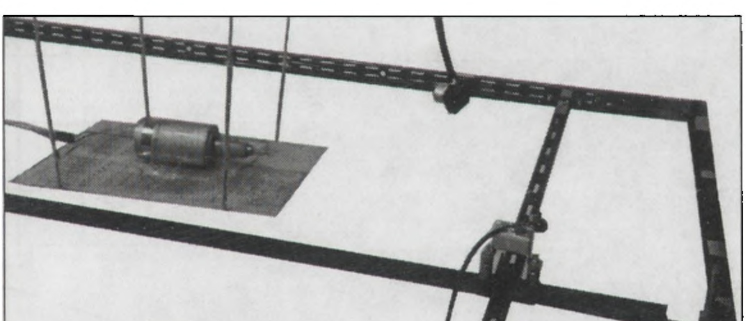

Fig. 10.17. Stimulator of fiberglass plate (electric micromotor).

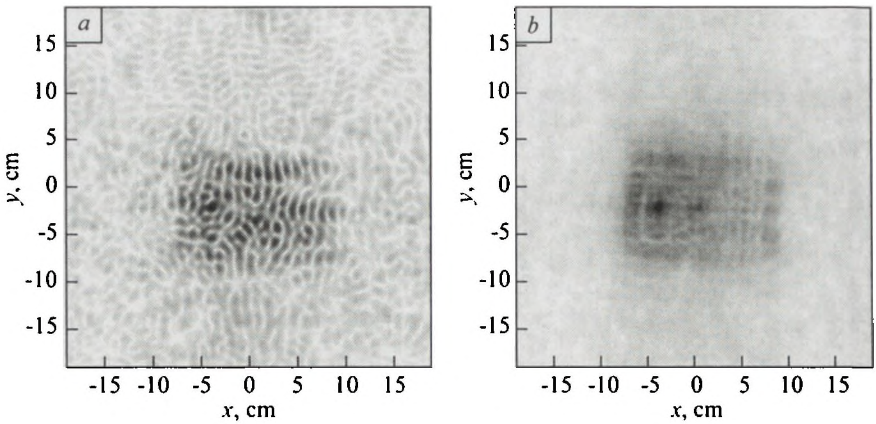

Fig. 10.18. Reconstructed image of a fiberglass plate: at a frequency of 23 kHz (*a*), at 32 frequencies in the range 10–30 kHz (*b*).

The obtained result demonstrates the potential of this method for acoustic introscopy, e.g., of metal parts (doors, safes, etc.). Field measurements of the acoustic signals can be performed quite rapidly using a two-dimensional array of 256 EM9767 microphones arrayed over a hexagonal grid with a 1-cm step (see Fig. 10.19).

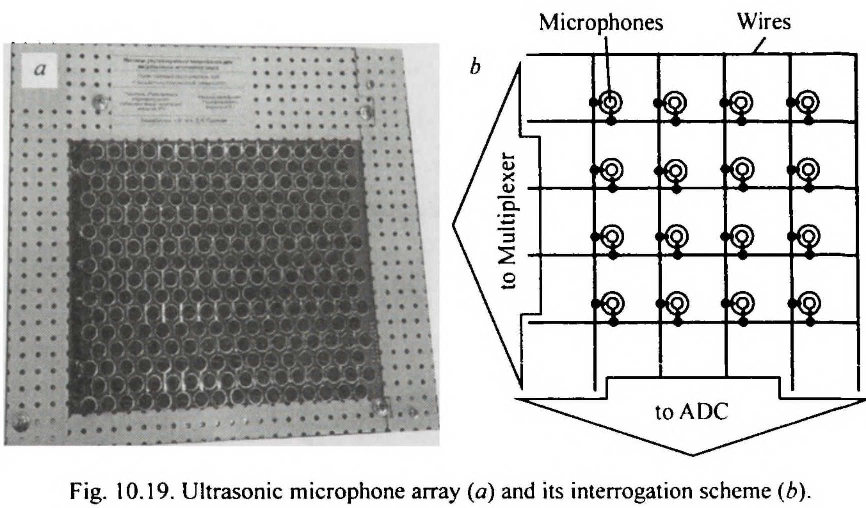

Fig. 10.19. Ultrasonic microphone array (*a*) and its interrogation scheme (*b*).

10.4. Summary

The combined use of radio waves and ultrasound enables an increase in the information content of the obtained images both in resolution and in the possibility of identifying the material that the sounded object is made of. Radio waves provide penetrating power, for example, under clothing, and ultrasound increases the accuracy of identification of the material of the hidden object. A complete discovery of the possibilities of this approach would require individual study of a wide array of materials using the neural network method. In this case, the larger will be the size of the accumulated data bank, the higher will be the probability of valid identification of the material. The use of ultrasound tomography is of interest in its own right, for example, in the introscopy of metal parts (doors, safes, etc.), and to detect cavities and defects in them. For internal and near-surface introscopy of sound-conducting objects or fragments of them, contact-free ultrasound tomography with additional coherent stimulation can be effective. For tomographic processing of secondary-radiation data the technology of large aperture synthesis can be used. The system is a development of known foreign and domestic technologies, but it does not require disassembly of the object for inspection or immersion in an immersion liquid. In this case both x-rays and radio waves are simply ineffective.

Chapter 11

SPECIAL ASPECTS OF LOW-FREQUENCY MAGNETIC INDUCTION TOMOGRAPHY

Magnetic and magnetic induction methods were almost entirely worked out in the twentieth century and now offer a comprehensive range of feasible solutions. These methods are not subjected to revision in the present chapter but they are supplemented with respect to their use for magnetic tomography.

Eddy current flaw detection is based on the induction of an alternating current in a metal test object by an external magnetic field. Induction currents give rise to a distortion in the external field, which is detected by an induction coil. Depending on the electrophysical properties of the metal and the origin of the flaw, the induction currents have different amplitude and phase distributions, which underlies the use of eddy currents for flaw detection. The source and receiver coils can be combined.

There is a wide selection of eddy current flaw detectors of different modifications available at the present time. These include, for example, VD-12NFM, VD-26P (Research and Production Company "Ultracon"»), VD-89R (Municipal Scientific and Production Association "Spektr"), D-95 "Expert" ("AKA") (0.5–128 kHz), etc. Eddy current flaw detectors mainly make use of a single transmitter-receiver module which functions as a sensor of the alternating magnetic field. They measure the signal phase and amplitude in the receiver coil. Flaw detection is based on an analysis of the signal amplitude and phase. A special feature of eddy current flaw detectors is magnetic field confinement due to the small size of the induction coils (about 5 mm). This provides more accurate flaw detection, but decreases the operating range of the detector. The operating range of eddy current flaw detectors is comparable to the size of the sounding coil.

Metal detectors make use of the same physical phenomena as do eddy current flaw detectors. They make use of large-size magnetic coils (about 30 mm) to provide an increase in the range of metal object detection. In this regard it should be noted that the detection range of objects buried in the ground depends on the signal frequency. The higher the frequency, the smaller is the penetrating depth because of losses in the conductive medium. And conversely, if the frequency is low, the penetration depth is greater, but the detection sensitivity of small inhomogeneities is decreased. Metal detectors used at depths of about 1 m operate at low frequencies (about 1 kHz).

Metal detectors can differ in their design: some of them contain a source coil and a receiver coil, other use a single transmitter-receiver coil. The use of signals of different types – harmonic, multifrequency, frequency-modulated, compound pulse signals, etc. is possible. Object detection is based on an analysis of the signal level in the receiver coil. Or, in the case of a single transmitter-receiver coil, the coil is integrated into an oscillating LC-circuit, whose frequency is known in the absence of inhomogeneities. In the presence of an inhomogeneity, the resonant circuit frequency changes, which signals the presence of a metal object, i.e., it is detected.

This chapter summarizes the results of papers [1–4].

11.1. Secondary eddy currents and their fields

Unlike microwaves, low-frequency magnetic fields have a high penetrating power and can penetrate even a conductive medium. However, the components of the magnetic field have a narrow spatial spectrum far from the source, so measurements with a high dynamic range and high signal-to-noise ratio are required to obtain high-resolution images from sounding with low-frequency magnetic fields.

Let us analyze the measurement scheme displayed in Fig. 11.1. The external coil generates an alternating magnetic field in the test region. If there are conductive inclusions in this region, eddy currents will be induced in them, generating secondary magnetic fields. The total contribution of the secondary magnetic fields is recorded by a scanning receiving coil or by a commutated coil system. The ultimate purpose of magnetic tomography is to measure the spatial distribution of the induced eddy currents. The measurements are performed at some distance from these currents, e.g., at ground level, whereas the metal inclusions are buried. The eddy current distribution provides information about the presence of metal-containing objects within the test region and about their shapes as well. An important point here is that the currents induced in conductive objects are usually displaced to the object's surface, so the current distribution should duplicate the shape of the objects.

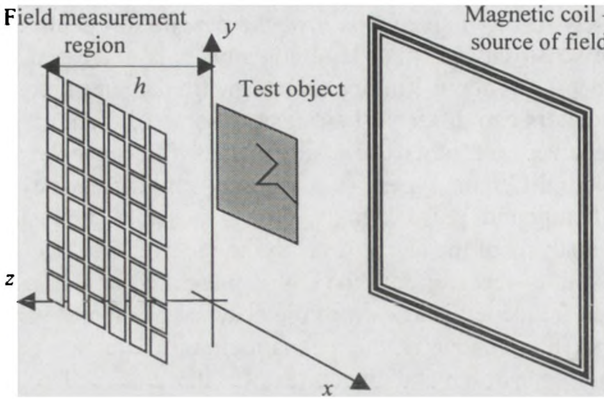

Fig. 11.1.Measurement scheme.

Methods of magnetic tomography and introscopy can be used for diagnostics of conductive objects as well as for detecting conductive objects behind dielectric barriers. Moreover, alternating magnetic fields penetrate through metal barriers, making it possible to detect objects hidden behind them [1, 2]. As mentioned above, one of the main problems of magnetic tomography is poor confinement of the magnetic field at some distance from the source, which results in low resolution of the reconstructed tomographic images.

Let us consider a method of reconstructing the spatial distribution of the current density using measurements of the z-component of the magnetic field only [4].

If $\mathbf{j}(\mathbf{r}_1)$ is the eddy current density vector expressed as a function of the coordinates in the volume V_1, then, applying the Stratton–Chu formula, the magnetic field generated by these currents is written as

$$\mathbf{H}(\mathbf{r}) = \iiint_{V_1} [\mathbf{j}(\mathbf{r}_1), \nabla_1 G_0(\mathbf{r}_1 - \mathbf{r})] d^3\mathbf{r}_1, \tag{11.1}$$

where $G_0(\mathbf{r}) = \exp(ik|\mathbf{r}|)/4\pi|\mathbf{r}|$ is the Green's function of a point source in the background medium, which can be rewritten as $G_0(\mathbf{r}) \approx 1/4\pi|\mathbf{r}|$ in the quasi-static approximation. Equation (11.1) is similar to Eq. (1.4) for wave tomography.

If the measurement of the magnetic field $\mathbf{H(r)}$ is performed in some plane that is perpendicular to the Oz axis (Fig. 11.1), the normal component of the magnetic field $H(\mathbf{r}) \equiv \mathbf{e}_z\mathbf{H(r)}$ is determined by the components of the eddy current that are parallel to the measurement plane:

$$H(\mathbf{r}) = \mathbf{e}_z \iiint_{V_1} [\mathbf{j}_\perp(\mathbf{r}_1), \nabla_1 G_0(\mathbf{r}_1 - \mathbf{r})] d^3\mathbf{r}_1 . \tag{11.2}$$

Here $\mathbf{e}_z$ is the normal unit vector in the direction of the Oz axis. Here it is taken into account that the values of the normal component of the current do not contribute to the normal component of magnetic field. The normal projection of the magnetic field is chosen since it can be measured more easily.

After some transformations, the integral expression for the observed test field [Eq. (11.2)] can be rewritten as

$$H(\mathbf{r}) = \mathbf{e}_z \operatorname{rot} \iiint_{V_1} \mathbf{j}_\perp(\mathbf{r}_1) G_0(\mathbf{r}_1 - \mathbf{r}) d^3\mathbf{r}_1 .$$

In the special case of a DC current I in the closed loop L, the following expression is obtained

$$H(\mathbf{r}) = I \oint_L \frac{\mathbf{e}_z[\mathbf{r}_1 - \mathbf{r}, d\mathbf{r}_1]}{4\pi(\mathbf{r}_1 - \mathbf{r})^3} .$$

The closed loop L can be divided into a sum of rectilinear conductors, thus

$$H(\mathbf{r}) = I \sum_j \int_{L_j} \frac{\mathbf{e}_z[\mathbf{r}_1 - \mathbf{r}, d\mathbf{r}_1]}{4\pi(\mathbf{r}_1 - \mathbf{r})^3} .$$

Each of these integrals can be calculated analytically.

Figure 11.2 displays the calculated field distribution for two loops shifted diagonally relative to each other. It is demonstrated that the generated magnetic field is distributed but the center of gravity of this distribution coincides with the geometric center of the system of loops. A similar result is observed in the experimental measurements.

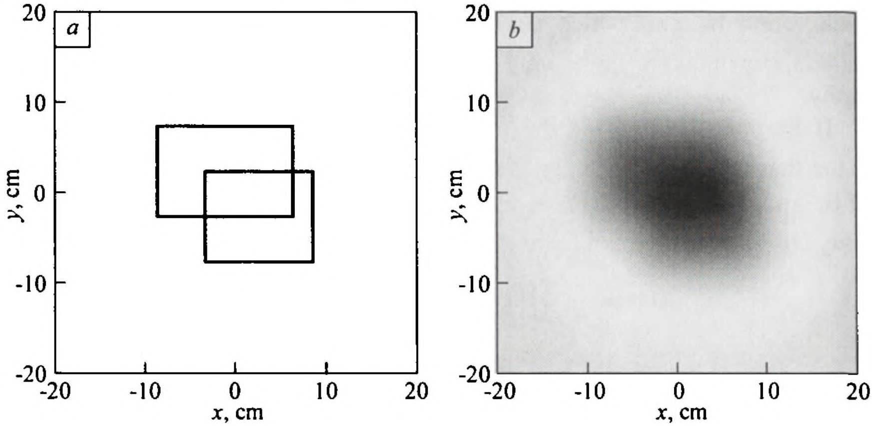

Fig. 11.2. Simulation of the magnetic field of two current loops: simulated object (a), z-component of the magnetic field at a distance of 5 cm (b).

11.2. Inverse problem of reconstructing the eddy current distribution

If the observed point lies at a distance z from the xOy plane (Fig. 11.1), where $\mathbf{r}=(x,y,z)$ and $\boldsymbol{\rho}=(x,y)$, the corresponding two-dimensional spatial frequency spectrum can be written as

$$H(\boldsymbol{\kappa}_\perp,z)\equiv\iint H(\boldsymbol{\rho},z)\exp\{-i\boldsymbol{\kappa}_\perp\boldsymbol{\rho}\}d^2\boldsymbol{\rho}\,.$$

According to the Weyl formula, this spectrum can be written as

$$H(\boldsymbol{\kappa}_\perp,z)=-\frac{\exp\{i\kappa_z z\}}{2\kappa_z}\mathbf{e}_z\left[\boldsymbol{\kappa},\mathbf{j}_\perp(\boldsymbol{\kappa})\right].$$

Here, $$\mathbf{j}_\perp(\boldsymbol{\kappa})\equiv\iiint\limits_{V_1}\mathbf{j}_\perp(\mathbf{r}_1)\exp\{-i\boldsymbol{\kappa}\mathbf{r}_1\}d^3\mathbf{r}_1$$

is the spatial frequency spectrum of the eddy current density vector in the volume V_1. The spatial frequency vector has following components:

$$\boldsymbol{\kappa}=(\kappa_x,\kappa_y,\kappa_z)\,,\ \boldsymbol{\kappa}_\perp=(\kappa_x,\kappa_y)\,,\ \kappa_z=\sqrt{k^2-\kappa_x{}^2-\kappa_y{}^2}=\sqrt{k^2-\kappa_\perp{}^2}\,.$$

Thus, in the pre-exponential terms we can set

$$\kappa_z = \sqrt{k^2 - \kappa_x{}^2 - \kappa_y{}^2} = \sqrt{k^2 - \kappa_\perp{}^2} \approx i|\kappa_\perp|,$$

and thus

$$H(\kappa_\perp, z) = i\frac{\exp\{i\kappa_z z\}}{2}\mathbf{e}_z\left[\frac{\kappa_\perp}{|\kappa_\perp|}, \mathbf{j}_\perp(\kappa)\right].$$

Multiplication of both sides of this equation by the vector $\mathbf{e}_z$ reconstructs the z-component of the magnetic field vector. Performing vector multiplication, the following equation is obtained

$$i[\kappa, \mathbf{e}_z]H(\kappa_\perp, z) = i[\kappa_\perp, \mathbf{e}_z]H(\kappa_\perp, z) = -\frac{\exp\{i\kappa_z z\}}{2}\left[\kappa_\perp\left[\frac{\kappa_\perp}{|\kappa_\perp|}, \mathbf{j}_\perp(\kappa)\right]\right].$$

We resolve the double vector product by taking into account that the charge conservation law in the quasistatic approximation

$$\operatorname{div}\mathbf{j}_\perp(\mathbf{r}) = 0$$

is rewritten in the spectral representation as follows:

$$i[\kappa, \mathbf{j}_\perp(\kappa)] = i[\kappa_\perp, \mathbf{j}_\perp(\kappa)] = 0.$$

In this approximation we obtain

$$i[\kappa_\perp, \mathbf{e}_z]\mathrm{H}(\kappa_\perp, z) = |\kappa_\perp|\frac{\exp\{i\kappa_z z\}}{2}\mathbf{j}_\perp(\kappa) = |\kappa_\perp|\frac{\exp\{-|\kappa_\perp|z\}}{2}.$$

Hence, the solution for the eddy current spectrum is given by

$$\mathbf{j}_\perp(\kappa) = \exp\{|\kappa_\perp|z\}2i\left[\frac{\kappa_\perp}{|\kappa_\perp|}, \mathbf{e}_z\right]H(\kappa_\perp, z). \tag{11.3}$$

On a formal level, this is the solution of the inverse problem, it is sufficient simply to take the inverse Fourier transform over spatial frequencies. However, two aspects should be borne in mind.

First, in the presence of measurement noise, which is always present, the exponential factor in expression (11.3) leads to divergence of the obtained expression. This situation can be overcome by using Wiener filtering and regularization via the substitution

$$\exp\{|\kappa_\perp|z\} \to \frac{\exp\{-|\kappa_\perp|z\}}{\exp\{-2|\kappa_\perp|z\} + \alpha},$$

where α is a regularization parameter which is usually estimated empirically.

Second, if there is an eddy current flowing in the *xOy* plane, then we must make the substitution $\mathbf{j}_\perp(\mathbf{r}_1) = \mathbf{j}_S(\boldsymbol{\rho}_1)\delta(z_1)$ and thus we obtain $\mathbf{j}_\perp(\boldsymbol{\kappa}) = \mathbf{j}_S(\boldsymbol{\kappa}_\perp)$.

Taking these two facts into account, we write the final solution of the inverse problem as

$$\mathbf{j}_S(\boldsymbol{\rho}) \equiv \frac{1}{(2\pi)^2}\iint \mathbf{j}_S(\boldsymbol{\kappa}_\perp)\exp\{i\boldsymbol{\kappa}_\perp\boldsymbol{\rho}\}d^2\boldsymbol{\kappa}_\perp,$$

where
$$\mathbf{j}_s(\boldsymbol{\kappa}_\perp) = 2i\left[\frac{\boldsymbol{\kappa}_\perp}{|\boldsymbol{\kappa}_\perp|},\mathbf{e}_z\right]H(\boldsymbol{\kappa}_\perp,z)\frac{\exp\{-|\boldsymbol{\kappa}_\perp|z\}}{\exp\{-2|\boldsymbol{\kappa}_\perp|z\}+\alpha}. \tag{11.4}$$

Solution (11.4) is written in the quasistatic approximation. It is a complete analog of the solution obtained by the tomosynthesys method in Section 1.3. It should be noted that all of the indicated transformations can be performed using FFT and IFFT algorithms.

Solution (11.4) for the model problem corresponding to the data shown in Fig. 11.2 successfully reconstructs the eddy current distribution. The distribution of the magnitude of the reconstructed current $j_S(\boldsymbol{\rho}) \equiv |\mathbf{j}_S(\boldsymbol{\rho})|$ is presented in Fig. 11.3*b*. Considering that the calculated distribution of the generated secondary magnetic field is quite blurry (Fig. 11.2*b*), the reconstructed current distribution is entirely acceptable.

The displayed result was obtained by numerical simulation. The result of a real experiment is shown in Fig. 11.4. Two rectangular loops not connected to each other were used. The loops were made of copper wire 1.5 mm in diameter. The resolution obtained was lower than the theoretically predicted value; however, the reconstructed object is entirely recognizable.

The experimental setup included a test object (two closed loops taped to a foam-plastic board with a rectangular exciting coil wound around the perimeter, Fig. 11.5*a*) and a scanning measuring probe for measuring the magnetic field (which was translated by an XY plotter, Fig. 11.5*b*). The measuring probe was in the form of a rectangular coil 2×2 cm in size. The test object was placed 5 cm away from the sensor plane. AC current in the exciting coil with a frequency of 5 kHz was generated by a computer sound card. The same sound card was used to sample signals from the measuring probe. Both field quadratures were measured.

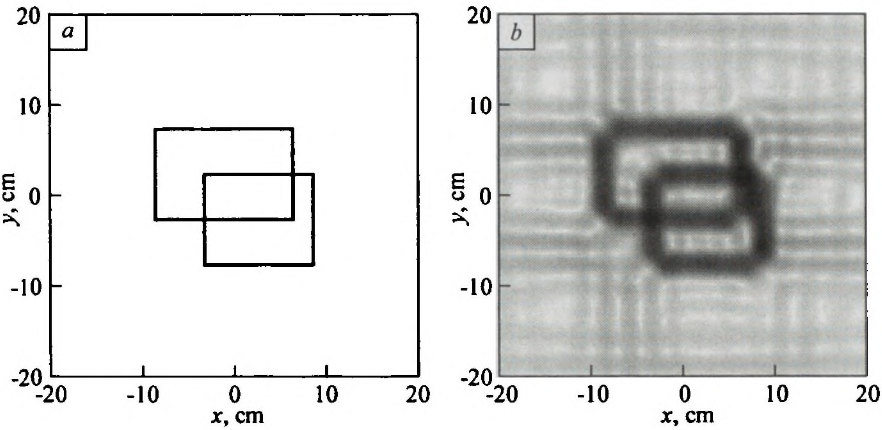

Fig. 11.3. Predefined (a) and reconstructed (b) current distribution in the form of rectangular loops – numerical simulation.

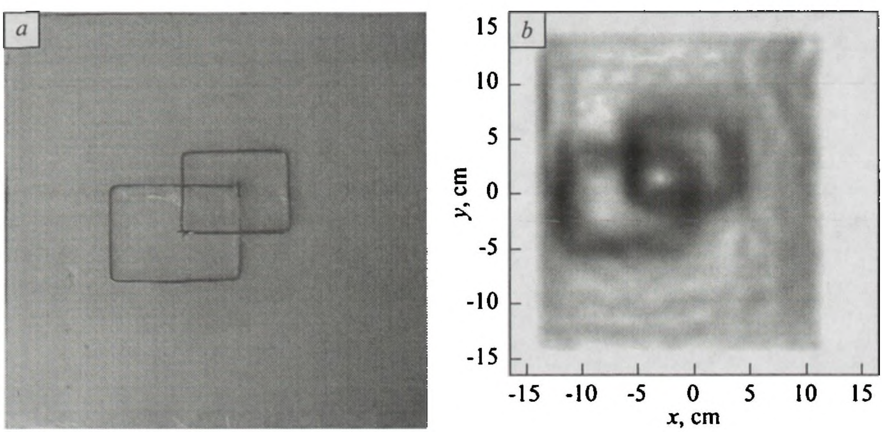

Fig. 11.4. Predefined (a) and reconstructed (b) current distribution in the form of rectangular loops – actual experiment.

Measurements were carried out in two stages: first, the spatial distribution of the magnetic field without the test object was measured, then with the object. The measured distributions were differenced. In this way the field generated by the eddy currents was extracted.

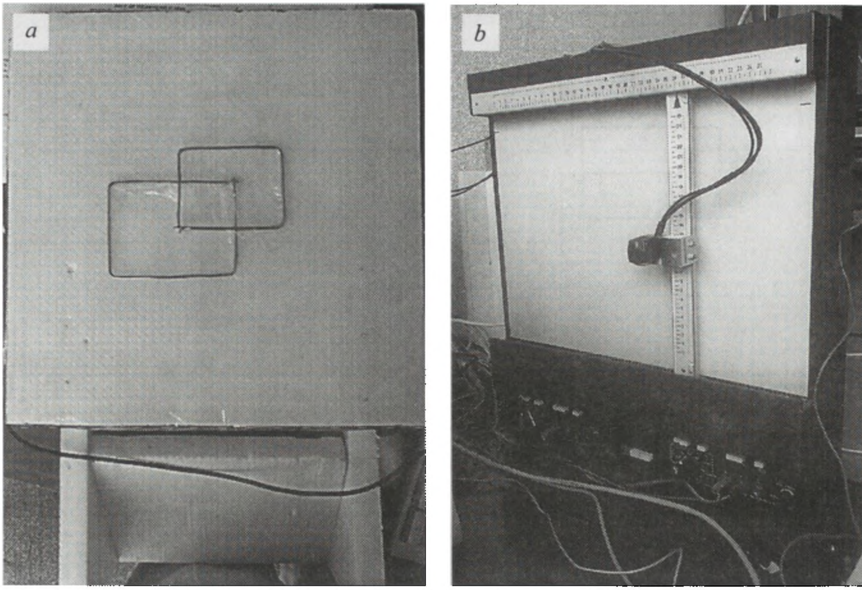

Fig. 11.5. Experimental setup: test object (a) and scanning measuring probe (b).

The accuracy of the measurements increased rapidly as the measuring probe was moved closer to the test object. According to the Eq. (11.4), as $z \to 0$ the measured magnetic field should essentially replicate the current distribution giving rise to it. This is explained by the fact that the magnetic field falls off with distance as $\sim 1/r^2$.

11.3. Self-compensated sensing coil and reconstruction of the shape of metal objects

It is possible to increase the accuracy of measurement by moving the sensing coil closer to the test object. However, the most significant impact on the measurement accuracy is achieved by subtracting out the background value of the magnetic field (the value without the test object), which is far larger than the value of the secondary magnetic field.

In this section, we shall discuss the possible use of self-compensated sensing coils to visualize conductive objects [6]. As a self-compensated source of the magnetic field, it is proposed to use two flat spiral coils of different size located in the same plane with a common center, so that they create opposite magnetic induction vectors at this common center (Fig. 11.6). The sensing coil is placed at the center. Thus, if there is no field distortion due to objects in the medium, an induction current will not be induced in the receiving coil. We call the proposed system of coils a self-compensated sensing coil (SCSC).

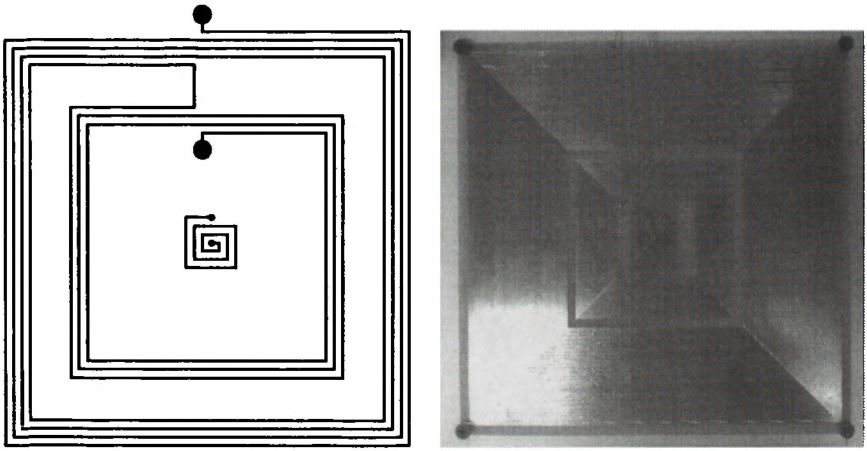

a *b*

Fig. 11.6. Self-compensated sensing coil: connection diagram (*a*) and printed circuit (*b*).

A self-compensated magnetic coil was printed on a circuit board (Fig. 11.6*b*) for the purpose of these experiments. The external coil had 100 turns, the internal one – 42 turns, and the sensing coil in the center had 18 turns. The helix pitch distance was 500 μm. The two outer coils (one circuit) comprised the source coil, and the innermost coil – the sensing coil – comprised the receiving coil (for a schematic depiction of this arrangement, see Fig. 11.6*a*). The size of the circuit board was 20×20 cm, and the thickness of the conductors was 250 μm. Calculation of the size and number of turns was based on the Biot–Savart law. First, the field of the rectilinear conductors was calculated by integration. Then, the fields of all the rectilinear conductors were summed up. As the source coil consisted of a single wire, the current in it was the same along all segments. The number of turns was determined to meet the condition that the magnetic field be equal zero at the center of the system.

An SB Creative Audigy SE PCI SB0570 sound card was used as the generator and the recorder. The SCSC circuit board was moved by a dual-axis scanner. During the experiments the test objects were situated at a distance of 1 cm from the scanning plane.

The first test object was made of three aluminum foil strips of different length: 5, 10, and 15 cm; they were 30 μm in thickness and 5 cm in width. There was an air gap of 1 mm between the strips and no electrical contact between them. In the experiments the cosine and sine quadratures of the output signal of the receiver coil at a frequency of 40 kHz were measured for different positions of the SCSC with a step of 5 mm over an area of 40×40 cm. The result of the amplitude measurements is displayed in Fig. 11.7*a*, where the darker regions correspond to higher values of the amplitude. A plot of the cosine quadrature of the measured signal is shown in Fig. 11.7*b*.

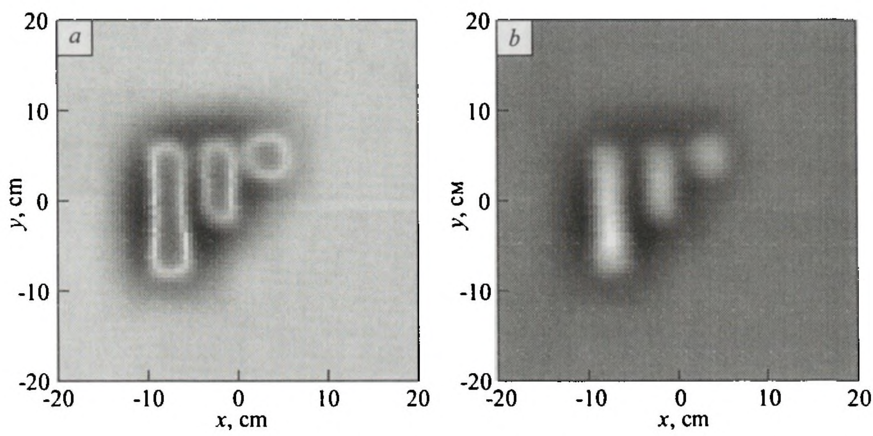

Fig. 11.7. Measurements of an object consisting of three aluminum strips: amplitude (*a*), cosine quadrature (*b*).

All of the strips are clearly distinguishable even though the gap between them is just 1 mm. This means that the system is sensitive to the absence of electrical contacts. The cosine quadrature image demonstrates that the signal phase reverses sign when crossing the boundary of a metal object, which enables an accurate detection of object outlines.

To demonstrate the possibility of visualizing objects composed of several layers with different distributions of conductive regions, an experiment was carried out in which two layers of aluminum strips, each configured in the shape of the previous object, were overlaid crosswise with respect to each the other. The result of measurements is displayed in Fig. 11.8, from which it is possible to distinguish the structure of the object.

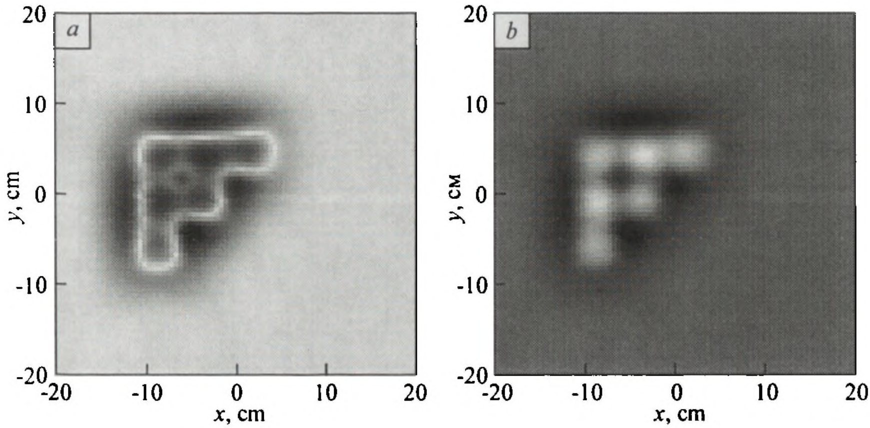

Fig. 11.8. Measurement result for the object consisting of two layers of crossed aluminum strips: amplitude (*a*), cosine quadrature (*b*).

Next, an experiment was carried out with five flat objects taped to a flat piece of Styrofoam (Fig. 11.9*a*). The first object was a square with a side length of 5 cm. The second object was a square with a side length of 5 cm and a notch 4.5 cm long down the center. The notch creates a break in the contour along the perimeter of the square-shaped object, which should decrease the level of inductive currents. The third object was a square with a side length of 2.5 cm. This object should demonstrate a substantial decrease in the level of induction currents due to a decrease in its outer contour. The fourth object was a square with a side length of 5 cm with a square piece cut out of its middle, of such size that the width of the remaining square metal outline was 5 mm. This object should demonstrate that retaining the outer contour while removing the inner part only insubstantially decreases the level of induction currents. The fifth object consisted of four aluminum strips 50 mm long and 5 mm wide, placed 5, 10, and 15 mm apart.

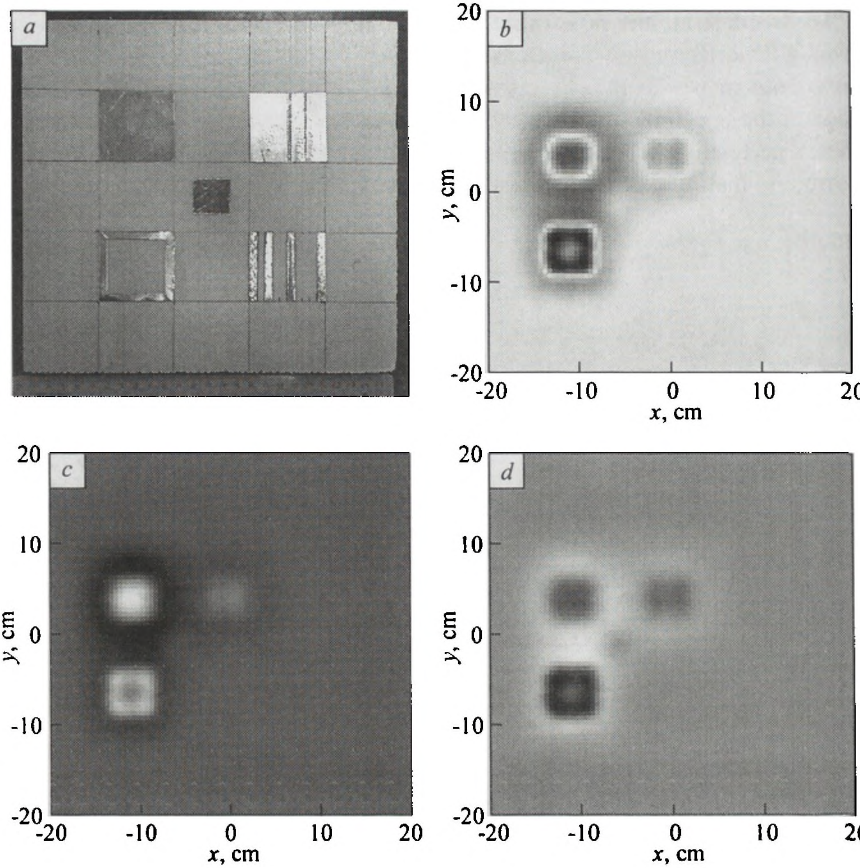

Fig. 11.9. Measurement results for the object composed of five elements: external view (*a*), amplitude (*b*), cosine quadrature (*c*), sine quadrature (*d*).

The results of the experiment demonstrated that

- the object with a large piece cut out of its center generates a signal comparable to the signal of the corresponding intact object, i.e., the greatest contribution to the signal comes from the outer contour of the conductive region;

- a notch in the outer contour substantially decreases the signal level;

- objects whose outer contours circumscribe a small area are not visualized.

To evaluate the possibility of fault detection, specifically detection of defects in the form of a notch, an experiment was carried out with a brass plate having dimensions of 12×7.5 cm and 0.5 mm in thickness, in which an oblique cut was incised (Fig. 11.10). Measurements were performed at a frequency 40 kHz at an offset distance of 1 cm.

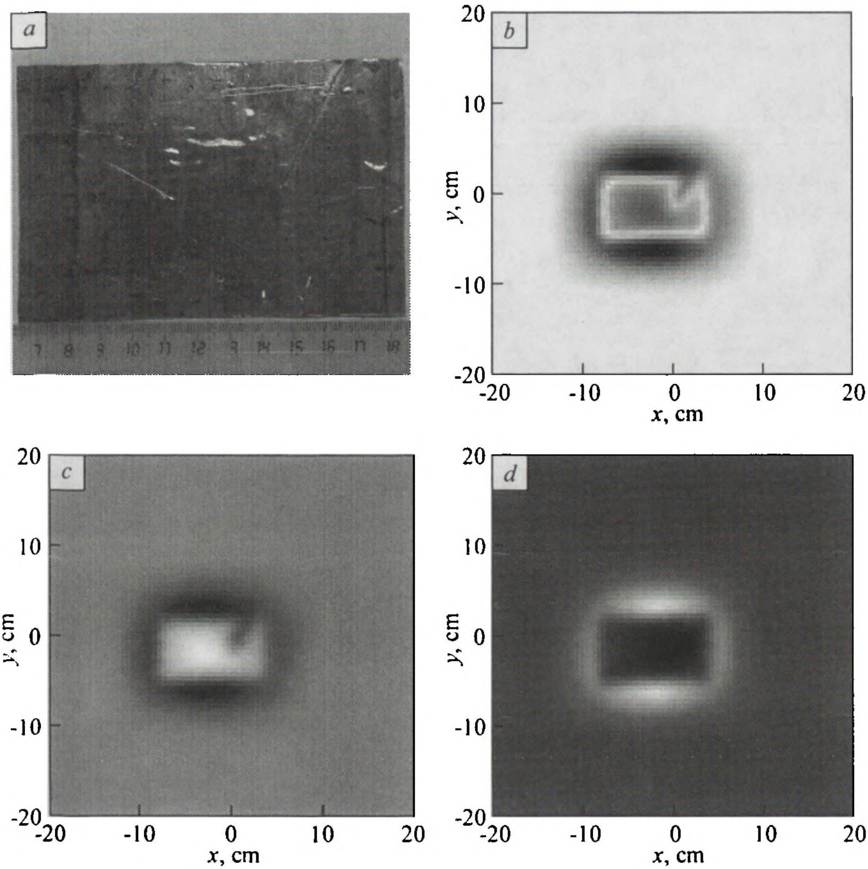

Fig. 11.10. Measurements on a brass plate: external view (*a*), amplitude (*b*), cosine quadrature (*c*), sine quadrature (*d*).

The region of the notch (cut) is clearly visualized in the displayed images. The induction current skirts the cut so it can be visualized by the SCSC.

11.4. Tomography of metal objects hidden behind metal screens

A series of experiments with an SCSC was carried out to evaluate the possibility of detection of metal objects hidden behind conductive screens. A study of the possibility of detecting a metal object hidden behind a metal screen was conducted in the course of those experiments.

Aluminium, copper, and steel sheets were used as the metal screens. As the objects to be detected we used brass, aluminium and steel plates.

An experiment on detection of a brass plate hidden behind a copper screen was carried out in which a fiberglass sheet covered with copper foil on both sides was employed as the metal screen (Fig. 11.11*a*). The brass plate was placed 1 cm above the screen, which, in turn, was hung 2 cm above the plane of translation of the SCSC.

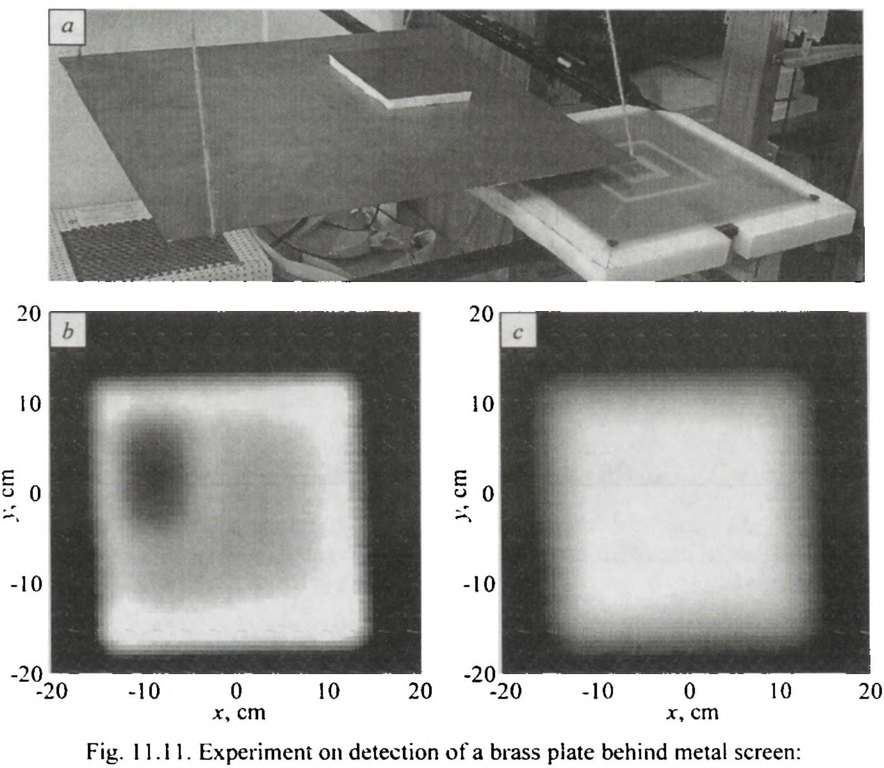

Fig. 11.11. Experiment on detection of a brass plate behind metal screen: external view of setup (*a*), cosine quadrature (*b*), sine quadrature (*c*).

Figures 11.11*b* and *c* display the results of measurements at a frequency of 5 kHz. The image of the cosine quadrature of the measured signal reveals an inhomogeneity having the shape of the brass plate. Thus, an object hidden behind a barrier was detected. Since the barrier was thin, the alternating magnetic field was only insignificantly attenuated, which made it possible to detect objects behind a barrier. In the given case, the hidden object was visualized in the cosine quadrature better than in the amplitude since the phases of the fields of the induction currents are different for different objects.

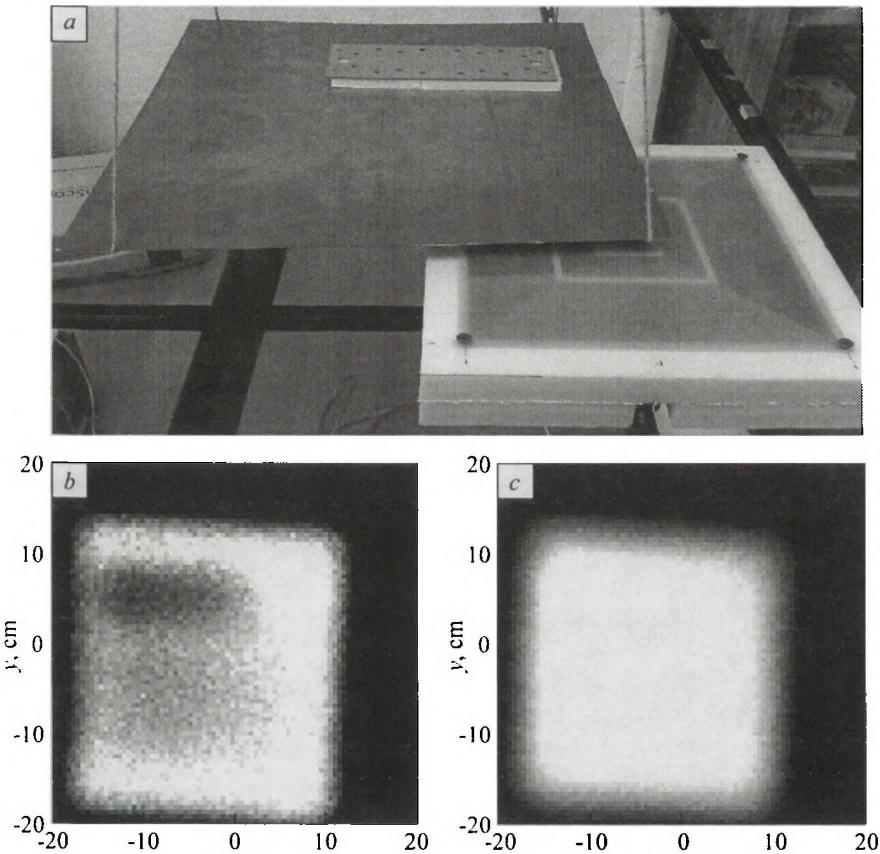

Fig 11.12. Experiment on detection of a steel plate behind a copper screen: external view of setup (*a*), cosine quadrature (*b*), sine quadrature (*c*).

A similar experiment was carried out with a steel plate 1 mm in thickness with dimensions of 65×180 mm. The steel plate was placed behind the copper screen (Fig. 11.12). Measurements were performed at a frequency of 3 kHz.

Similar results were also obtained for an aluminum plate behind the copper screen. When the copper screen was replaced by a thin aluminum screen the result remained the same, but when the screen thickness was increased, the detection effect was lowered. Detection was not achieved behind an iron screen. This fact can be explained by the ferromagnetic properties of iron, which concentrate the magnetic field lines, thereby shielding the oscillating magnetic fields.

11.5. Summary

Low-frequency magnetic fields can be used in the tomography of flat metal objects. The basis of its use consists in measurements of secondary magnetic fields generated by eddy currents induced on the object's boundaries.

Scanning with a self-compensated sensitive coil is considered to be a promising tool for measurements. The SCSC should be placed very close to the test object since the secondary magnetic field generated by this object attenuates rapidly with distance.

Metal objects and their flaws are clearly detected when they are placed behind dielectric screens, and also behind thin nonmagnetic metal screens.

Chapter 12

VISUALIZATION TECHNIQUES FOR TOMOGRAPHIC IMAGES

One task of radio-wave and ultrasonic tomography is to generate three-dimensional (3D) bitmap images of test objects. However, there are no currently available displays that are capable of presenting three-dimensional bitmap images on the screen. As a consequence of this fact, it is necessary to develop techniques for presenting 3D bitmap images in two-dimensional displays.

12.1. Visualization of 3D tomogram by a polyscreen

One technique for displaying 3D images is to construct a polyscreen. A polyscreen is a two-dimensional bitmap image composed of a set of images corresponding to different cross sections of the sounded volume along a predefined direction. One advantage of such a visualization scheme is the simplicity inherent in it of interpretation of the displayed data. In such a scheme, the distribution of inhomogeneities inside the test object (e.g. cavities and flaws) becomes accessible for detection and analysis. A similar visualization technique is used in medical computer-aided diagnostics.

The tomogram for a numerically simulated image of a stepped test object is presented in Fig. 12.1. The polyscreen presents images of 16 layers with a 0.5-cm increment in range (depth). The first layer corresponds to a depth of 0.5 cm, the last layer corresponds to a depth of 8 cm. The dark areas correspond to higher values of the amplitude . As is readily obvious, the test object is located in the ninth level, corresponding to a depth of 4.5 cm.

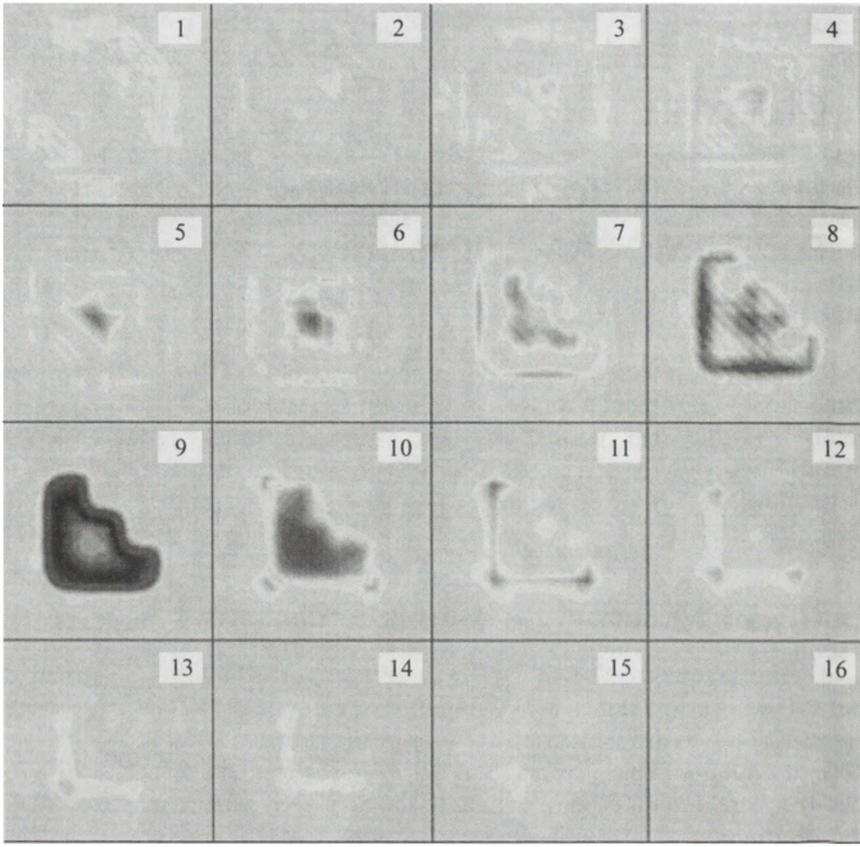

Fig. 12.1. Test object tomogram.

12.2. 3D tomogram visualization by equipotential surfaces

The contouring of equipotential surfaces is one of the techniques that are available for visualization of 3D images. The result of contouring is a three-dimensional surface, which can be visualized by the standard techniques of three-dimensional polygon graphics. But this scheme requires multi-staged processing of the 3D image: first, the polygonal model must be constructed, then this polygonal model must be visualized, which requires additional computing resources.

The backward ray tracing method is proposed as a means for displaying equipotential surfaces of 3D images. Each image point is obtained by scanning the 3D image with a direct ray originating from the observer. The intersection point of the ray and the equipotential surface is indicated in the display.

Figure 12.2 displays images of the equipotential surface of a numerically simulated radio-image (tomogram) of a test object of stepped shape.

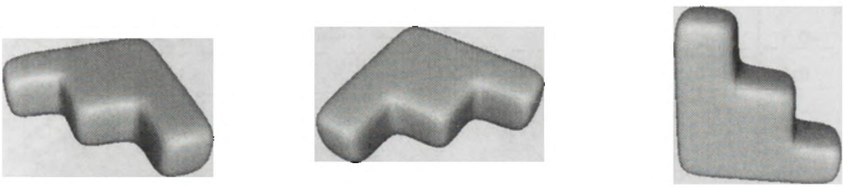

Fig. 12.2. Equipotential surface of 3D field as seen from different angles.

An advantage of the backward ray tracing method as compared with the polygonal technique is a more accurate display of the equipotential surface and simplicity of the corresponding imaging algorithms.

12.3. Visualization of a 3D tomogram with orthogonal cross sections

The basic form for presenting three-dimensional images in geolocation and radio tomography is a three-dimensional cube. This cube is constructed using data from the sounded volume and is composed of six planar surfaces, each of which is orthogonal to the next one. In this way we can fully visualize the sounding data of interest to us (Fig. 12.3). The cross sections can be made at any angle and direction.

To make the 3D image more readily understandable, we construct the cross sections of the cube in three orthogonal planes: X, Y, and Z, which correspond to the use of a Cartesian coordinate system. The number of cross sections of the cube and the spacing between them can be selected arbitrarily. The result of cross sections of the cube for each of the planes is recorded into a separate video file.

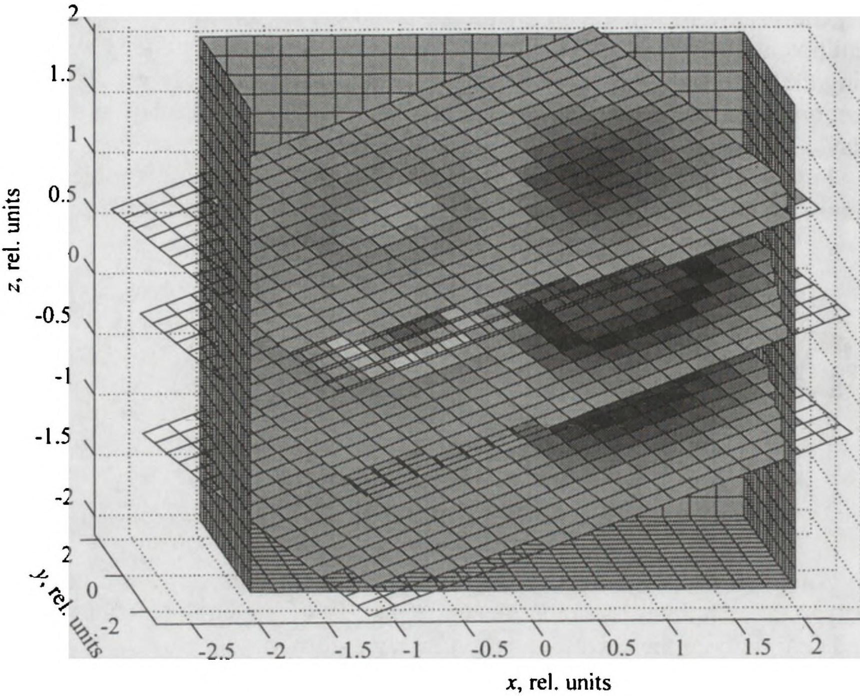

Fig. 12.3. Three-dimensional cube and its cross section sections.

Figure 12.4 shows cross sections in the *X*, *Y* and *Z* planes. These cross sections were obtained from processing of actual experimental data. A complete three-dimensional picture of the test volume can be assembled by scanning the recorded video files.

The given test scene contains several localized objects (inhomogeneities), whose positions and dimensions can be estimated. The circled object most likely represents a metal pipe. The coordinates of starting point of this object are 1.7, 0.8, –1.6 m and this object ends at the point with coordinates 3.9, 2.8, –2.0 m.

The advantage of this latter method is its ease of realization, good visual presentation, and the ability to easily scan the recorded video files by means of various MATLAB applications.

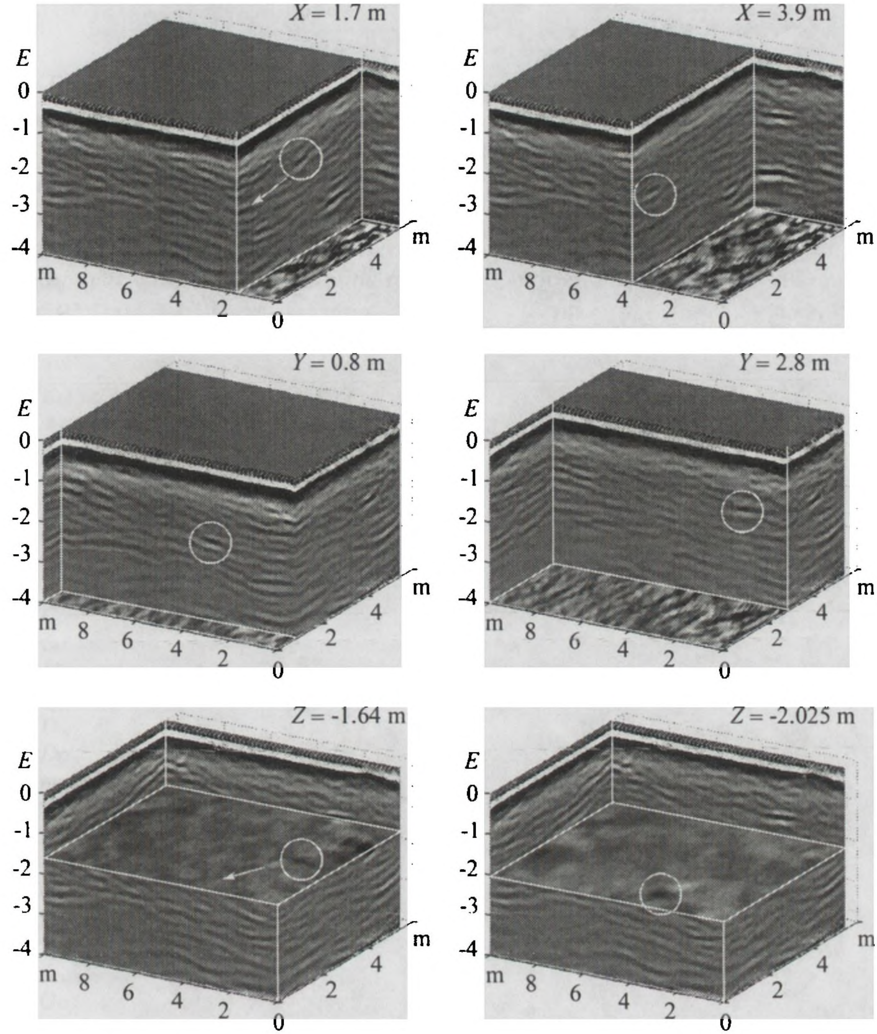

Fig. 12.4. Orthogonal crpss sections of the cube in the X, Y, Z planes at various distances.

12.4. Summary

The proposed techniques for visualization of 3D tomograms entail the presentation of results as a polyscreen, equipotential surfaces, and orthogonal cross sections in the form of bitmap images.

However, the results of 3D tomography in the form of two-dimensional bitmap images can be displayed in a visually more accessible form as a video record or an animation built up from successive sections, layers, or records of camera motions around the object. Cartoon animation technology is required in this case. Applications for 3D game developers, such as Blender 2.59, can be considered as possible options as well.

REFERENCES

Introduction

1. *Barrett H.H.* Optical processing in Radon space // Opt. Lett. – 1982. – V. 7. – No. 6. – P. 248–250.
2. *Baum C.E.* Introduction to SEM // IEEE Group Antennas Propagat. Int. Symp. Dig. – 1973. – V. 11. – P. 459–462.
3. *Baum C.E.* The singularity expansion method: Background and developments // IEEE Antennas Propagat. Soc. Newsletter. – 1986. – V. 28. – No. 4. – P. 14–23.
4. *Berni A.J.* Target identification by natural resonance estimation // IEEE Trans. Aerospace and Electronic Sistems Propagat. – 1975. – V. 11. – No. 2. – P. 147–154.
5. *Chiang Be-S. et al.* Spatial resolution in industrial tomography // IEEE Transactions on Nuclear Science. – 1983. – V. NS-30. – No. 2. – P. 1671–1676.
6. *Cordaro J.T. and Davis W.A.* Time-domain techniques in the singularity expansion method // IEEE Trans. Antennas Propagat. – 1981. – V. 29. – No. 3. – P. 534–538.
7. *Cormack A.M.* Representation of a function by its line integrals, with some radiological application // J. Appl. Phys. – 1963. – V. 34. – No. 9. – P. 2722–2727.
8. *Moffatt D.L. and Kennaugh E.M.* The axial echo area of a perfectly conducting prolate spheroid // IEEE Trans. Antennas Propagat. – 1965. – V. 13. – No. 3. – P. 401–409.
9. *Daniels D.J.* Surface-Penetrating Radar. – London, UK: IEE, 1996. – 300 p.
10. *Dolph C.L. and Cho S.K.* On the relationship between the singularity expansion method and the mathematical theory of scattering // IEEE Trans. Antennas Propagat. – 1980. – V. 28. – No. 6. – P. 888–897.
11. *Felsen L.B.* Comments on early time SEM // IEEE Trans. Antennas Propagat. – 1985. – V. 33. – No. 1. – P. 118–119.
12. *Gaunaurd G.C., Uberall H., Nagl A., and Subrahmanyam J.V.* SEM poles and creeping-wave transients on conductors of simple shapes // IEEE Int. Antennas Propagat. Symp. – 1982. Dig. – V. 20. – P. 16–17.
13. *Joaquim. F.-G.* A Novel 3-D Subsurface Radar Imaging Technique // IEEE Trans. on Geosciences and Remote Sensing. – 2002. – V. 40. – No. 2. – P. 443–452.
14. *Kennaugh E.M. and Cosgriff R.L.* The use of impulse response in electromagnetic scattering problems // IRE National Convention Record. – 1958. – March. – P. 72–77.
15. *Marin L.* Natural-mode representation of transient scattering from rotationally symmetric bodies // IEEE Trans. Antennas Propagat. – 1974. – V. 22. – No. 2. P. 266–274.
16. *Mittra R. and Pearson L. W.* A variational method for efficient determination of SEM poles // IEEE Trans. Antennas Propagat. – 1978. – V. 26. – No. 2. – P. 354–358.

17. *Moffatt D.L. and Mains R.K.* Detection and discrimination of radar targets // IEEE Trans. Antennas Propagat. – 1975. – V. 23. – No. 3. – P. 358–367.
18. *Mohan R., Rothenberg L., Reinstien L., and Ling C.C.* Imaging in three-dimensional conformal radiation therapy // Int. J. Imaging Systems Technol. – 1995. – V. 6. – No. 1. – P. 14–32.
19. *Morgan M.A.* Singularity expansion representations of fields and currents in transient scattering // IEEE Trans. Antennas Propagat. – 1984. – V. 32. – No. 5. – P. 466–473.
20. *Munk W.H.* Oceanic acoustic tomography: a scheme for large monitoring // Deep-Sea Res. – 1979. – V. 26. – No. 2A. – P. 123–161.
21. *Nagl A. and Uberall H.* Transient radar scattering analyzed in terms of creeping waves // IEEE Int. Antennas Propagat. Symp. Dig. – 1982. – V. 20. – P. 18–20.
22. *Pearson L.W.* A note on the representation of scattered fields as a singularity expansion // IEEE Trans. Antennas Propagat. – 1984. – V. 32. – No. 5. – P. 520–524.
23. *Pearson L.W. and Roberson D.R.* The extraction of the singularity expansion description of a scatterer from sampled transient surface current response // IEEE Trans. Antennas Propagat. – 1980. – V. 28. – No. 2. – P. 182–190.
24. *Ramm A.G.* Theoretical and practical aspects of singularity and eigenmode expansion methods // IEEE Trans. Antennas Propagat. – 1980. – V. 28. – No. 6. – P. 897–901.
25. *Richards M.A.* SEM representation of the early and late time fields scattered from wire targets // IEEE Trans. Antennas Propagat. – 1994. – V. 42. – No.4. – P. 564–566.
26. *Sahiner B. and Yagle A.E.* Iterative inversion of the Radon transform using image-adaptive wavelet constraints to improve image reconstruction // IEEE Engineering in Medicine and Biology. – 1996. – V. 8. – No. 7. – P. 395–397.
27. *Sarkar T.K., Weiner D.D., Jain V.K., and Diant S.A.* Impulse response determination in the time domain-theory // IEEE Trans. Antennas Propagat. – 1982. – V. 30. – No. 4. – P. 657–663.
28. *Stolt R.H.* Migration by Fourier transform // Geophysics. – 1978. – V. 43. – No. 1. – P. 23–48.
29. *Swith W.E. and Barrett H.H.* Radon transform and band width compression // Opt. Lett. – 1983. – V. 8. – No. 7. – P. 395–397.
30. *Tesche F.M.* On the analysis of scattering and antenna problems using the singularity expansion technique // IEEE Trans. Antennas Propagat. – 1973. – V. 21. – No. 1. – P. 53–62.
31. *Tseng F. and Sarkar T.K.* Experimental determination of resonant frequencies by transient scattering from conducting spheres and cylinders // IEEE Trans. Antennas Propagat. – 1984. – V. 32. – No. 9. – P. 914–918.
32. *VanBlaricum M.L. and Mittra R.* A technique for extracting the poles and residues of a system directly from its transient response // IEEE Trans. Antennas Propagat. – 1975. – V. 23. – No. 6. – P. 777–781.
33. *Ultra* wideband radar. Applications and design / Edited by James D. Taylor. – New-York: Crc Press, 2012. – P. 536.
34. *Handbook* of ultra-wideband short-range sensing: theory, sensors, applications by Jurgen Sachs. – Wiley-vch, 2012. – P. 844.
35. *Oliver C. und Quegan S.* Understanding Synthetic Aperture Radar Images. – SciTech Publishing, Inc., 2004.

36. *Astanin L.Y.* Ultrawideband signals – A new step in radar development // IEEE AES Syst. Mag. – 1992. – March, 12–15.
37. *James D. Taylor.* Advanced Ultrawideband Radar: Signals, Targets, and Applications. – CRC Press, 2016. – 476 p.
38. *Astanin L.Y. and Kostylev A.A.* Ultrawideband Radar Measurements Analysis and Processing, EE, London, 1997.
39. *Baum C.E.* Emerging Technology for Transient and Broad-Band Analysis and Synthesis of Antennas and Scatterers // Proc. IEEE. – V. 64. – P. 1598–1616.
40. *Kostylev A.A., Astain L.Yu., Zinoviev J.S., and Pasmurov A.Ya.* Radar Characteristics of Aircraft. – CRC Press, Boca Raton, FL, 1994.
41. *Kunitsyn V.E., Tereshchenko E.D.* Ionospheric tomography (with 88 figures, including 16 color plates). – Berlin: Springer-Verlag, 2003. – 260 p.
42. *Herman G., and Natterer F.* Mathematical Aspects of Computerized Tomography. – Berlin: Springer-Verlag, 1981.
43. *Nebabin V.G.* Methods and Techniques of Radar Recognition. – Boston: Artech House, 1995. – 248 p.
44. *Daniels D.J.* Ground Penetrating Radar. – 2nd edition. – London, UK: Institute of Engineering and Technology, 2004.
45. *Jol H.M.* (ed.) Ground Penetrating Radar Theory and Applications. – Amsterdam, the Netherlands: Elsevier, 2009.

Chapter 1

1. *Borden B. and Cheney M.* Synthetic-aperture imaging from high-Doppler-resolution measurements // Institute of Physics Publishing Inverse Problems. Inverse Problems. – 2005. – V. 21. – P. 1–11. DOI:10.1088/0266-5611/21/1/001.
2. *Yakubov V.P. and Masharuev M.L.* Method of Double Focusing for Microwave Tomography // Microw. Opt. Technol. Lett. – 1996. – V. 13. – No. 4. – P. 187–189.
3. *Brekhovskikh L.M.* Waves in Layered Media. – 2nd ed. – New York: Academic, 1980.
4. *Yakubov V.P., Sukhanov D.Ya., Sklarczyk K.G., et al.* // Russian Physics Journal. – 2008. – V. 51. – No. 10. – P. 1064–1082.
5. *Sukhanov D.Ya., Yakubov V.P.* Application of linear frequency modulated signals in three-dimensional tomography // The Russian Journal of Applied Physics. – 2010. – V. 55. – No. 4. – P. 546–550.
6. *Shipilov S.E.* Aperture synthesis method in 3d radio tomography // Russian Physics Journal. – 2014. – V. 56. – No. 9. – P. 1062–1068.
7. *Yakubov V.P., Mirontchev A.S., Andretsov A.G., Ponomaryova I.O.* Artificial materials and radio tomography // Russia Physics Journal. – 2011. – V. 53. – No. 9. – P. 895–899.
8. *Yakubov V.P., Sklyartchik K.G., Pintchuk R.V., et al.* Radiowave tomography of hidden objects for safety systems // Russian Physics Journal. – 2008. – V. 51. – No. 10. – P. 1064–1082.
9. *Yakubov V.P., Telpukhovskiy E.D., Tsepelev G.M., et al.*. Radiowave tomography of inhomogeneous media // Russian Physics Journal – 2006. – V. 49. – No. 9. – P. 923–928.

10. *Yakubov V.P., Telpuchovski E.D., Zepelev G.M., et. al.* Radar tomography // Proceedings of SPIE – The International Society for Optical Engineering. – 2006. – V. 6522.

Chapter 2

1. *Satarov R.N., Kuzmenko I.Yu., Muksunov T.R., et al.*. Switched ultrawideband antenna array for radio tomography // Russian Physics Journal. – 2013. – V. 55. – No. 8. – P. 884–889.
2. *Sukhanov D.Y., Zav'yalova K.V.* 3D radio tomography of objects hidden behind dielectrically inhomogeneous shields // The Russian Journal of Applied Physics. – 2015. V. 60. – No. 10. – P. 1529–1534.
3. *Yakubov V.P., Shipilov S.E., Sukhanov D.Ya., Razinkevich A.K.* Ultrabroad-band tomography of remote objects // Russian Journal of Nondestructive Testing. – 2012. – V. 48. – No. 3. – P. 191–196.
4. *Yakubov V.P., Mirontchev A.S., Andretsov A.G., Ponomaryova I.O.* Artificial materials and radio tomography // Russian Physics Journal. – 2011. – V. 53. – No. 9. – P. 895–899.
5. *Yakubov V.P., Shipilov C.E., Satarov R.N.* Ultra-wideband sensing behind dielectric barriers // Russian Physics Journal. – 2011. – V. 53. – No. 9. – P. 887–894.
6. *Shipilov S., Satarov R., Fedyanin I., Balzovsky E., Yakubov V.* Positioning for people behind barriers in real time with uwb pulse sensing // MATEC Web of Conferences 7. Ser. "7th Scientific Conference with International Participation "Information-Measuring Equipment and Technologies", IME and T 2016". – 2016. – P. 01079.

Chapter 3

1. *Yakubov V.P. and Slavgorodsky S.A.* Microwave tomography – experimental model // VIII Joint International Symposium "Atmospheric and Ocean Optics. Atmospheric Physics". Symposium Proceedings / ed. by V.A. Banakh and O.V. Tikhomirova. – Tomsk: Institute of Atmospheric Optics SB RAS, 2001. – P. 128–129.
2. *Yakubov V.P. and Slavgorodsky S.A.* Model radiowave tomography // Journal Radioelectroniks. – 2001. – No. 10. http://jre.cplire.ru/win/oct01/6/text.html
3. *Yakubov V.P., Masharuev M.L.* Method of Double Focusing for Microwave Tomography // Microwave and Optical Technology Letters. – 1996. – V. 13. – No. 4. – P. 187–189.
4. *Yakubov V.P., Tarabrin Yu.K., Masharuev M.L.* Regularization of inverse problems of microwave tomography in medicine // Proceedings SPIE. – 1995. – V. 2570. – P. 332–335.
5. *Sukhanov D.Y., Murav'eva A.A.* Monochromatic ultrasonic transmission tomography // Optoelectronics, Instrumentation and Data Processing. – 2015. – V. 51. – No. 3. – P. 247–253.
6. *Yakubov V.P., Telpukhovskiy E.D., Tsepelev G.M., et al.* Radio-wave tomography of inhomogeneous media // Russian Physics Journal. – 2006. – V. 49. – No. 9. – P. 923–928.

Chapter 4

1. *Koshelev V.I., Shipilov S.E., Yakubov V.P.* Reconstructing the shape of an object in the narrow range-of-view superwideband radio location // Journal of Communication Technology and Electronics. – 1999. – V. 44. – Issue 3. – P. 281–284.
2. *Yakubov V.P., Losev D.V., Maltsev A.I.* Wave tomography of absorbing media // Journal of Communication Technology and Electronics. – 2004. – V. 49. – Issue 1. – P. 54–57.
3. *Yakubov V.P., Shipilov S.E., Ponomarev S.V.* Dual software and hardware refocusing of satellite reflectors // CriMiCo 2014 – 2014 24th International Crimean Conference Microwave and Telecommunication Technology, Conference Proceedings, art. no. 6959522. – P. 549–550.
4. *Yakubov V.P., Shipilov S.E., Sukhanov D.Ya.* Microwave tomography of radiopaque objects // Russian Journal of Nondestructive Testing. – 2011. – V. 47. – Issue 11. – P. 765–770.
5. *Yakubov V.P., Shipilov S.E., Sukhanov D.Ya., Razinkevitch A.K.* Ultrabroad-band tomography of remote objects // Russian Journal of Nondestructive Testing. – 2012. – V. 48. – Issue 3. – P. 191–196.
6. *Koshelev V.I., Sipilov S.E., Yakubov V.P.* Shape reconstruction in small-angle surepwideband radar using genetic functions // Journal of Communication Technology and Electronics. – 2000. – V. 45. – Issue 12. – P. 1333–1338.
7. *Klokov A.V.,Yakubov V.P., Shipilov S.E., Yurchenko V.I..* Development of the vision systems based on radiowave using a Luneburg lens focusing for robots // SPIIRAS Proceedings. – 2016. – V. 2. – Issue 45. – P. 130–140.

Chapter 5

1. http://www.produktinfo.conrad.com/datenblaetter/500000-524999/502371-da-01-en-RADAR_BEWEGUNGSMELDER_RSM_1700.pdf
2. *Skolnik M.* Radar Handbook / McGraw-Hill Education; 3 edition (February 12, 2008). – 1328 p.
3. *Petrou M., Petrou C.* Image Processing: The Fundamentals / Wiley; 2 edition (May 17, 2010). – 818 p.
4. *Kuzmenko I.Yu., Muksunov T.R., Yakubov V.P.* LFM locator for hidden objects tomography // (2014) CriMiCo 2014 – 2014 24th International Crimean Conference Microwave and Telecommunication Technology, Conference Proceedings, art. no. 6959738. – P. 1013–1014.
5. *Satarov R.N., Kuz'menko I.Y., Muksunov T.R., et al.* Switched ultrawideband antenna array for radio tomography // Russian Physics Journal. – 2013. – V. 55. – No. 8. – P. 884–889.
6. *Sukhanov D.Y., Murav'eva A.A.* Monochromatic ultrasonic transmission tomography // Optoelectronics, Instrumentation and Data Processing. – 2015. – V. 51. – No. 3. – P. 247–253.
7. *Sukhanov D.Y.* Bistatic Multipositional Wave Tomography // Russian Physics Journal. – 2015. – V. 58. – No. 1. – P. 26–34.

8. *Sukhanov D.Y., Zav'yalova K.V.* 3D radio tomography of objects hidden behind dielectrically inhomogeneous shields // Technical Physics. – 2015. – V. 60. – No. 10. – P. 1529–1534.
9. *Sukhanov D., Zavyalova K.* Radiotomography Based on Monostatic Interference Measurements with Controlled Oscillator // (2016) MATEC Web of Conferences, 79, art. no. 01040.
10. *Kuzmenko I.Yu, Yakubov V.P., Muksunov T.R.* Relief Restoration of Complicated form Objects by Monochromatic Microwave Radiation // (2016) MATEC Web of Conferences, 79, art. no. 01047.
11. *Fedyanin I.S., Yakubov V.P., Antipov V.B., Kuz'Menko I.Yu., Muksunov T.R.* Using of movement microwave detector for radiovision tasks // (2014) CriMiCo 2014 – 2014 24th International Crimean Conference Microwave and Telecommunication Technology, Conference Proceedings, art. no. 6959394. – P. 282–283.
12. *Yakubov V., Shipilov S., Parvatov G., Antipov V., Muksunov T.* Complex Security System for Premises under Conditions of Large Volume of Passenger Traffic // (2016) MATEC Web of Conferences, 79, art. no. 01007.
13. *Kuzmenko I., Yakubov V., Muksunov T.* Relief Restoration of Complicated form Objects by Monochromatic Microwave Radiation // (2016) MATEC Web of Conferences, 79, art. no. 01047.

Chapter 6

1. *Groenenboom J. and Yarovoy A.G.* Data processing for a landmine detection dedicated GPR // Eighth Int. Conference on Ground Penetrating Radar. – 2000. – P. 367–371.
2. *Ulaby F.T., Moore R.K., and Fung A.K.* Microwave Remote Sensing: Active and Passive. V. 3 From Theory to Applications. – Norwood: Artech House, 1986. – 2162 p.
3. *Yilmaz Oz.* Seismic Data Analysis: Processing, Inversion, and Interpretation of Seismic Data. V. 1 / ed. Stephen M. Doherty. – Tulsa: Society of Exploration Geophysicists, 2001. – P. 2027.
4. *David J. Daniels.* Ground Penetrating Radar. Vol. 1. – IET, 2004. – 726 p.
5. *Persico R.* Introduction to Ground Penetrating Radar: Inverse Scattering and Data Processing (IEEE Press Series on Electromagnetic Wave Theory) 1st Edition. Wiley-IEEE Press; 1 edition (June 9, 2014) // IEEE Press Series on Electromagnetic Wave Theory. – 392 p.
6. *Hough P.V.C.* Method and means for recognizing complex patterns. – U.S. Patent 3,069,654, Dec. 18, 1962.
7. *Harry M. Jol.* Ground Penetrating Radar Theory and Applications. – Elsevier, 2009. – 525 p.
8. *Skolnik M.* Radar Handbook, Third Edition 3rd Edition / McGraw-Hill Education; 3 edition (February 12, 2008). – 1328 p.
9. *Yakubov V.P., Sukhanov D.Y., Klokov A.V.* Radiotomography from Ultra-Wideband Monostatic Measurements on an Uneven Surface // Russian Physics Journal. – 2014. V. 56. – No. 9. – P. 1053–1061.

10. *Yakubov V.P., Omar A.S., Sukhanov D.Y., et al.* New Fast SAR Method for 3-D Subsurface Radiotomography // Tenth International Conference on Ground Penetrating Radar, 21–24 June, 2004, Delft, The Netherlands. – P. 103–106.
11. *Klokov A., Zapasnoy A., Shipilova S.* // Jitter in Geolocation Data Processing. (2016) MATEC Web of Conferences, 79, art. no. 01022.
12. *Durán-Ramírez V., Martínez-Ríos A., Guerrero-Viramontes J., et al.* Measurement of the refractive index by using a rectangular cell with a fs-laser engraved diffraction grating inner wall // Opt. Express. – 2014. – V. 22. – P. 29899–29906.
13. *Sukhanov D.Ya., Yakubov V.P.* Inclined focusing method in subsurface radar // Technical Physics. The Russian Journal of Appled Physics. – 2006. – V. 51. – No. 7. – P. 882–886.
14. *Sukhanov D.Ya., Yakubov V.P.* Determining the refractive index of the background medium in subsurface tomography // Radiophysics and Quantum Electronics. – 2007. – V. 50. – No. 5. – C. 381–387.
15. *Yakubov V.P., Shipilov S.E., Sukhanov D.Y.* Microwave tomography of radiopaque objects // Russian Journal of Nondestructive Testing. – 2011. – V. 47. – No. 11. – P. 765–770.
16. *Epov M.I., Yakubova O.V., Telpukhovskii E.D., et al.* Method od ultrawideband radiopulse logging of horizontal wells // Russian Physical Journal. – 2008. – V. 51. – No. 9. – P. 949–957.
17. *Kochetkova T.D., Zapasnoy A.S., Klokov A.V., Shipilov S.E., Yakubov V.P., Yurchenko A.V.* Ultra-wideband tomography of land cover // (2014) Proceedings of SPIE – The International Society for Optical Engineering, 9292, art. no. 929250.
18. *Yakubov V.P., Sukhanov D.Ya.* Solution of a subsurface radio-imaging inverse problem in the approximation of a strongly refractive medium // Radiophysics and Quantum Electronics. – 2007. – V. 50. – No. 4. – P. 299–307.
19. *Yakubov V.P., Sukhanov D.Y., Klokov A.V.* Radiotomography from Ultra-Wideband Monostatic Measurements on an Uneven Surface // Russian Physics Journal. –2014. – V. 56. – No. 9. – P. 1053–1061.
20. *Klokov A.V., Zapasnoy A.S., Mironchev A.S., Yakubov V.P., Shipilova S.S.* A comprehensive study of underground animals habitat // Journal of Physics: Conference Series. – 2016. – V. 671. – No. 1, art. no. 012028.

Chapter 7

1. *Klokov A., Yakubov V., and Sato M.* Ultra Wideband Radiolocation of a Forest // Proc. of the 2010 IEICE GENERAL CONFERENCE. The Institute of Electronics, Informanion and Communication Engineers. – March 16–19, 2010. – P. 298.
2. *Mironov V.I., Yakubov V.P., Telpukhovsky E.D., and Novik S.N.* Height Dependence of Electromagnetic Field inside the Forest Canopy at Meter and Decimeter Wavelengths // Proc. IGARSS. – Denver, Colorado, USA, 2006. – V. VI. – P. 2962–2964.
3. *Mironov V.L., Novik S.N., Klokov A.V., et al.* Space – Time and Frequency – Polarization Variations in the Electromagnetic wave Interacting with the Forest Curtains // Proc. IGARSS. – Barcelona, Spain, 2007. – P. 200.

4. *Mironov V.L., Yakubov V.P., Telpukhovsky E.D., et al.* Spectral study of microwave attenuation in a larch forest stand for oblique wave incidence // Proc. IGARSS'05, Seoul, Korea, 2005. – V. V. – P. 3204–3207.
5. *Telpukhovskiy E.D., Yakubov V.P., Mironov V.L., et al.* Wideband radar phenomenology of forest stands // IEEE International Geoscience and Remote Sensing Symposium: Proceedings. July 21–25, 2003, Toulouse, France. – P. 4265–4267.
6. *Yakubov V.P., Telpukhovskiy E.D., Mironov V.L., et al.* Measured spectrum and polarization of wideband radar signal from forest stand // IEEE Int. Geoscience and Remote Sansing Symposium. – USA, 2004. – P. 1235–1238.
7. *Yakubov V.P., Telpukhovskiy E.D., Sarabandi K., et al.* Attenuation and depolarization data measured for scattered field inside larch canopy // IEEE International Geoscience and Remote Sensing Symposium: Proceedings. July 21–25, 2003, Toulouse, France. – P. 4195–4197.
8. *Wood R. Williams.* Physical Optics. – Nabu Press, 2010. – 582 p.
9. *Mironov V.L., Yakubov V.P., Telpukhovskiy E.D., et al.* Spectral study of microwave attenuation in a larch forest stand for oblique wave incidence // (2005) International Geoscience and Remote Sensing Symposium (IGARSS), 5, art. no. 1526522. – P. 3204–3207.
10. *Yakubov V.P., Telpukhovskiy E.D., Tsepelev G.M., et al.* Measured spectrum and polarization of wideband radar signal from forest stand // (2004) International Geoscience and Remote Sensing Symposium (IGARSS), 5. – P. 3471–3473.
11. *Magazinnikova A.L., Yakubov V.P.* Dual mechanism of radio wave propagation in forests // Radiotekhnika i Elektronika. –1999. – V. 44. – No. 1. – P. 5–9.
12. *Telpukhovskiy E.D., Yakubov V.P., Mironov V.L., et al.* Wideband Radar Phenomenology of Forest Stands // (2003) International Geoscience and Remote Sensing Symposium (IGARSS), 7. – P. 4265–4267.
13. *Magazinnikova A.L., Yakubov V.P.* Attenuation of coherent radiation in forest regions // Microwave and Optical Technology Letters. – 1998. – V. 19. – No. 2. – P. 164–168.
14. *Magazinnikova A.L., Yakubov V.P.* Dual mechanism of radio wave propagation in forests // Bandaoti Guangdian/Semiconductor Optoelectronics. – 1998. – V. 19. – No. 6. – P. 5–10.
15. *Yakubov V.P., Telpukhovskii E.D., Tsepelev G.M.* Pulse sensing of a forest canopy // Russian Physics Journal. – 2003. – V. 46. – No. 8. – P. 784–790.
16. *Mironov V.L., Telpukhovsky E.D., Yakubov V.P., et al.* Space-Temporal and frequency-Polarization variations in the electromagnetic wave interacting with the forest canopy // (2007) International Geoscience and Remote Sensing Symposium (IGARSS), art. no. 4423370. – P. 2574–2576.

Chapter 8

1. *Kraus J.D.* Radio Astronomy. – Cygnus-Quasar Books, 1986. – 719 p.
2. *Afshordi N., Lin Y.-T., Sanderson A.J.R.* Wilkinson microwave anisotropy probe constraints on the intracluster medium // The Astrophys. J. – 2005. – V. 629. – No. 1 I. – P. 1–14.

3. *Finkbeiner D.P.* Microwave interstellar medium emission observed by the Wilkinson microwave anisotropy probe // The Astrophys. J. – 2004. – V. 614. – No. 1 I. – P. 186–193.
4. *Wang S. and Zhang X.-C.* Pulsed terahertz tomography // J. Phys. D: Appl. Phys. – 2004. – V. 37. – No. 4. – P. 1–36.
5. *Bespalov V.G. and Gorodetsky A.A.* THz pulse holography // J. Holograph. Speckle. – 2009. – V. 5. – No. 1. – P. 62–66.
6. *Kitayoshi Hitoshi.* Applied radio holography for EMC and instrumentation // IEEE International Symposium on Electromagnetic Compatibility. – 1994. – P. 803.
7. *Gerchberg R.W. and Saxton W.O.* A practical algorithm for the determination of the phase from image and diffraction plane pictures // Optik. – 1972. – V. 35. – P. 237–246.
8. *Sukhanov D.Y., Zav'yalova K.V.* Reconstruction of 3D radio images from multifrequency holographic measurements // Technical Physics. – 2012. – V. 57. – No. 6. – P. 819–823.
9. *Shipilov S., Satarov R., Fedyanin I., et al.* Positioning for People behind Barriers in Real time with UWB Pulse Sensing // MATEC Web of Conferences. – 2016. – V. 79. – Art. no. 01079.
10. *Yakubov V.P., Shipilov S.E., Satarov R.N., Yurchenko A.V.* Remote ultra-wideband tomography of nonlinear electronic components // Technical Physics. – 2015. – V. 60. – No. 2. – P. 279–282.
11. *Sukhanov D., Erzakova N.* Visualization of Broadband Sound Sources // MATEC Web of Conferences. – 2016. – V. 79. – Art. no. 01001.
12. *Sukhanov D., Zavyalova K.* Radiotomography Based on Monostatic Interference Measurements with Controlled Oscillator // MATEC Web of Conferences. – 2016. – V. 79. – Art. no. 01040.
13. *Sukhanov D.Y., Zav'yalova K.V.* 3D radio tomography of objects hidden behind dielectrically inhomogeneous shields // Technical Physics. – 2015. – V. 60. – No. 10. – P. 1529–1534.
14. *Sukhanov D.Y., Zav'yalova K.V.* Ultrabroadband 3D radio holography in a stratified medium // Technical Physics. – 2014. – V. 59. – No. 12. – P. 1854–1858.

Chapter 9

1. *Johns T.* An Overview of Non-Linear Junction Detection Technology for Countersurveillance. – URL: http://www.ccmeinc.com/pdfs/ORION_NLJDTech.pdf
2. *Zharov A.A., Stolbov M.B., Gudkov S.A., Danilov V.M.* Ustroystvo dlya obnaruzheniya signalov / Patent № 2140656. reg. Pussian Pat. Off. 27.10.99. (in Russian)
3. *Perenosnoy* detector nelineynykh perekhodov «NR-900EK» / User manual. UTDN 468 165 003 РЭ. – «Gruppa zashtchity – UTTA» Ltd. (in Russian)
4. http://www.detektor.ru
5. http://www.findpatent.ru/patent/247/2474840.html
6. http://www.t-ss.ru/lokator.htm
7. http://www.arms-expo.ru/049048052052124057049054.html

8. *Yakubov V.P., Losev D.V., Maltsev A.I.* Diagnostics of nonlinearities using scattered field disturbances // Radiophysics and Quantum Electronics. – 2000. – V. 43. – Issue 7. – P. 645–651.
9. *Yakubov V.P., Shipilov S.E., Sukhanov D.Ya.* Sposob obnaruzheniya skrytykh nelineynykh radioelectronnykh elementov / Patent RF. Appl: № 2012131727, from 24.07.2012. (in Russian)

Chapter 10

1. *Brekhovskikh L.M.* Waves in Layered Media. – 2nd ed. – New York: Academic, 1980.
2. *Greguss P.* Ultrasonic Imaging: Seeing by Sound Focal Press, 1980. – 224 p.
3. *Yakubov V.P., Shipilov S.E., Sukhanov D.Ya.* Radio and ultrasound tomography of hidden objects // Russian Physics Journal. – 2013. – V. 55. – No. 8. – P. 878–883.
4. Sukhanov D.Ya., Kalashnikova M.A. Remote ultrasonic defectoscopy of sound radiating objects through the air // Acoustical Physics. – 2014. – V. 60. – No. 3. – P. 304–308.
5. *Sukhanov D.Ya., Barysheva K.V.* Transmission incoherent ultrasonic imaging of planar objects // Acoustical Physics. – 2010. – V. 56. – No. 4. – P. 501–505.

Chapter 11

1. *Sukhanov D.Y., Sovpel' E.S.* A magnetic-induction introscope for flaw detection of metal objects // Russian Journal of Nondestructive Testing. – 2015. – V. 51. – No. 5. – P. 308–314.
2. *Sukhanov D.Ya., Berzina E.S.* Magnetic induction introscopy using the scanning matrix of induction coils // CriMiCo 2014 – 2014 24th International Crimean Conference Microwave and Telecommunication Technology, Conference Proceedings. – 2014. – Art. no. 6959710. – P. 952–953.
3. *Mook G., Simonin J.* Surface and subsurface material characterization using eddy current arrays, 19th World Conference on Non-Destructive Testing, 13.–17. Juni 2016, München, DGZfP-Proceedings BB 158, We.2.C.2.
4. *Peng X.* A new differential eddy current testing sensor used for detecting crack extension direction / X. Peng, H. Songling, Z. Wei // NDT&E International 44. – 2011. – P. 339–343.

Appendix 1

Divergent and convergent waves

The Helmholtz equation for the Green's function of a point source is written as

$$\Delta G(\mathbf{r}) + k^2 G(\mathbf{r}) = -\delta(\mathbf{r}).$$

As is well known, the fundamental solutions of this equation are represented by the two functions

$$G_0(\mathbf{r}) = \exp(ik|\mathbf{r}|)/4\pi|\mathbf{r}|,$$

$$G_*(\mathbf{r}) = \exp(-ik|\mathbf{r}|)/4\pi|\mathbf{r}|,$$

where the first function corresponds to a divergent spherical wave, and the second one, to a convergent spherical wave. The origin of the coordinate system corresponds to the position of the point source.

We assume that the coordinates of the sources of the convergent wave and the divergent wave are different. Then, from the Helmholtz equation we can write

$$\begin{aligned} &G_0(\mathbf{r}-\mathbf{r}_1)\Delta G_*(\mathbf{r}-\mathbf{r}_2) - G_*(\mathbf{r}-\mathbf{r}_2)\Delta G_0(\mathbf{r}-\mathbf{r}_1) = \\ &= G_*(\mathbf{r}-\mathbf{r}_2)\delta(\mathbf{r}-\mathbf{r}_1) - G_0(\mathbf{r}-\mathbf{r}_1)\delta(\mathbf{r}-\mathbf{r}_2). \end{aligned}$$

If the first and second source are found inside some volume V, then after integration over this volume and application of Green's theorem we can write

$$\begin{aligned} &G_*(\mathbf{r}_1-\mathbf{r}_2) - G_0(\mathbf{r}_2-\mathbf{r}_1) = \\ &= \oiint_S \left\{ G_0(\mathbf{r}_S-\mathbf{r}_1)\frac{dG_*(\mathbf{r}_S-\mathbf{r}_2)}{dn} - G_*(\mathbf{r}_S-\mathbf{r}_2)\frac{dG_0(\mathbf{r}_S-\mathbf{r}_1)}{dn} \right\} dS. \qquad (1) \end{aligned}$$

The integration is performed over the surface S bounding the volume V, and the outer normal to the volume is taken.

The left-hand side of the equation is the function

$$G_*(\mathbf{r}_1-\mathbf{r}_2) - G_0(\mathbf{r}_2-\mathbf{r}_1) = \frac{1}{2i}\delta_k(|\mathbf{r}_1-\mathbf{r}_2|),$$

where we have introduced the notation

$$\delta_k(|\mathbf{r}_1 - \mathbf{r}_2|) \equiv \frac{\sin(k|\mathbf{r}_1 - \mathbf{r}_2|)}{\pi|\mathbf{r}_1 - \mathbf{r}_2|}.$$

This function is the *blurred* δ-function, which in the limit $k \to \infty$ transforms to the usual Dirac δ-function with all of its characteristics:

$$\lim_{k\to\infty} \delta_k(|\mathbf{r}_1 - \mathbf{r}_2|) = \delta(|\mathbf{r}_1 - \mathbf{r}_2|).$$

As δ_k approaches the δ-function, the two integral terms become equal, and the integrand in Eq. (1) reduces to the form

$$\delta_k(|\mathbf{r}_2 - \mathbf{r}_1|) = \frac{4}{i} \oiint_S \left\{ G_0(\mathbf{r}_S - \mathbf{r}_1) \frac{dG_*(\mathbf{r}_S - \mathbf{r}_2)}{dn} \right\} dS.$$

The equation so obtained can be interpreted as the orthogonality relation for the divergent and convergent waves. The function $G_0(\mathbf{r}_S - \mathbf{r}_1)$ can be considered as the divergent field of the point source located at the point $\mathbf{r}_1$ observed on the surface S. The second function, having the form

$$W(\mathbf{r}_2, \mathbf{r}_s) \equiv \frac{4}{i} \cdot \frac{dG_*(\mathbf{r}_s - \mathbf{r}_2)}{dn} = W(\mathbf{r}_s - \mathbf{r}_2),$$

is a focusing function, multiplication by which upon integration over the closed surface gathers the field of the divergent wave back to the point $\mathbf{r}_2$:

$$\oiint_S \{ G_0(\mathbf{r}_S - \mathbf{r}_1) W(\mathbf{r}_S - \mathbf{r}_2) \} dS \Rightarrow \delta_k(|\mathbf{r}_2 - \mathbf{r}_1|).$$

Appendix 2

Derivation of detection Green's function

The detection Green's function for a point source is defined as $[G(\mathbf{r})]^2$, where $G(\mathbf{r}) = \exp(ik|\mathbf{r}|)/4\pi|\mathbf{r}|$ is the ordinary Green's function which describes a divergent spherical wave and obeys the Helmholtz equation

$$\Delta G(\mathbf{r}) + k^2 G(\mathbf{r}) = -\delta(\mathbf{r}).$$

The function $[G_0(\mathbf{r})]^2$ can be represented as the product of two functions: $G_2(\mathbf{r}) \equiv \exp(i2k|\mathbf{r}|)/4\pi|\mathbf{r}|$ and $G_0(\mathbf{r}) \equiv 1/4\pi|\mathbf{r}|$, the first one of which is the Green's function for the wave field at the double frequency, and the second one of which is the Green's function at zero frequency, which is the solution of the Laplace equation.

We write an expression for application of the Laplace operator to the Green's function

$$\Delta G^2(\mathbf{r}) = \Delta\left[G_2(\mathbf{r})G_0(\mathbf{r})\right] =$$
$$= G_0(\mathbf{r})\Delta G_2(\mathbf{r}) + 2\nabla G_0(\mathbf{r})\nabla G_2(\mathbf{r}) + G_2(\mathbf{r})\Delta G_0(\mathbf{r}).$$

Next, by direct calculation for $\mathbf{r} \neq 0$ we obtain

$$\Delta G_2(\mathbf{r}) = -4k^2 G_2(\mathbf{r}),\ \Delta G_0(\mathbf{r}) = 0,$$

$$\nabla G_2(\mathbf{r})\nabla G_0(\mathbf{r}) = -G_2(\mathbf{r})G_0(\mathbf{r})\left(2ik - \frac{1}{|\mathbf{r}|}\right)\frac{1}{|\mathbf{r}|}.$$

As a result, we can finally write

$$\Delta G^2(\mathbf{r}) = \Delta\left[G_2(\mathbf{r})G_0(\mathbf{r})\right] = G^2(\mathbf{r})\left\{-4k^2 - \frac{2}{|\mathbf{r}|}\left(2ik - \frac{1}{|\mathbf{r}|}\right)\right\}.$$

Hence, in the limit $k|\mathbf{r}| \to \infty$ the following asymptotic expression is obtained:

$$\Delta G^2(\mathbf{r}) = \Delta\left[G_2(\mathbf{r})G_0(\mathbf{r})\right] = -4k^2 G^2(\mathbf{r})\left\{1 + O\left(\frac{1}{k|\mathbf{r}|}\right)\right\},$$

or

$$\Delta G^2(\mathbf{r}) \approx -(2k)^2 G^2(\mathbf{r}).$$

ABBREVIATIONS

ACP	–	access control point
ADC	–	analog-to-digital converter
BPF	–	blurring point function
BS	–	building structure
CF	–	characteristic function
CR	–	corner reflector
CVC	–	current –voltage characteristics
DP	–	directivity pattern
FFT	–	the fast Fourier transform
FS	–	the Fourier synthesis
IFFT	–	the inverse fast Fourier transform
IFT	–	inverse focusing technique
LE	–	the Luxembourg effect
LFM	–	linear-frequency modulation
ND	–	nonlinear detection
RMM	–	Radar based motion detection module
RWTS	–	radio-wave tomosynthesis
SAR	–	synthetic aperture radar
SCSC	–	self-compensated sensing coil
SIF	–	system instrument function
SP	–	shadow projection
SS	–	spatial spectrum
UWB	–	ultrawideband (signal)
WDM	–	weighted difference method
TEM-antenna	–	antenna with transverse electromagnetic wave

CONTENTS

PAGE INTENTIONALLY LEFT BLANK

PAGE INTENTIONALLY LEFT BLANK

Scientific Publication

Yakubov, Vladimir Petrovitch
Shipilov, Sergey Eduardovitch
Sukhanov, Dmitry Yakovlevitch
Klokov, Andrey Vladimirovitch

WAVE TOMOGRAPHY

Editor *P. Shipnik*
Design, Proof: *D. V. Fortes*

"Scientific Technology Publishing House", Co. Ltd.
634050, Tomsk, Ploshchad' Novosobornaya 1, tel. (3822) 533-335

Submitted for printing 20.02.2017. Format 60 × 84 $^1/_{16}$. Offset paper.
Offset print. Times font. Circulation 500 copies. Order No. 10.

Printed at M-Print Typography, Tomsk,
per. Dobrolyubova, 10, st. 3, tel. (3822) 258-279

ISBN 978-5-89503-588-7